INSA CENTRE VAL DE LOIRE

ÉCOLE DOCTORALE MATHÉMATIQUES, INFORMATIQUE, PHYSIQUE THÉORIQUE ET INGÉNIERIE DES SYSTÈMES

LABORATOIRE PRISME

THÈSE présentée par :

Ruipeng CHEN

Soutenance prévue Juin 2020

pour obtenir le grade de : **Docteur de l'INSA Centre Val de Loire**

Discipline/ Spécialité : Robotique

Design Methodology for Electromagnetic Microrobotic Platforms

THÈSE dirigée par :

Antoine FERREIRA	Professeur des Universités, INSA Centre Val Loire

RAPPORTEURS :

Li ZHANG	Professor, Chinese University of Hong-Kong
Samer MOHAMMED	Professor, Université Paris-Est Créteil

JURY :

Li ZHANG	Professor, Chinese University of Hong-Kong
Samer MOHAMMED	Professor, Université Paris-Est Créteil
Christine PRELLE	Professor, Université Technologique de Compiègne
Antoine FERREIRA	Professeur des Universités, INSA Centre Val Loire, Directeur
David FOLIO	Maitre de Conférences, INSA Centre Val Loire, Co-Encadrant

Contents

List of Figures

List of Tables

Nomenclature

Common rules

Notations	Description
x lower case	a scalar
$\mathbf{v}$ bold lower case	a vector
$\mathbf{M}$ bold upper case	a matrix or a vector field
$\mathbf{f}$	a force vector
$\mathbf{t}$	a torque vector
$\mathbf{M}^\intercal$	the transpose of matrix $\mathbf{M}$
$\mathbf{M}^{-1}$	inverse of matrix $\mathbf{M}$
$\mathbf{M}^{+}$	pseudo-inverse of matrix $\mathbf{M}$
$\mathbb{0}_{n\times m}$	a zero matrix or null matrix of dimension $n \times m$
$\mathbb{1}_{n\times m}$	identity matrix of dimension $n \times m$

Unless explicitly stated otherwise, throughout this document the values will be stated in SI units.

List of symbols

Symbol	Description	Unit
d_w	The distance to the workspace center	$[\,\mathrm{m}\,]$
$\mathbf{p}$	Position vector	$[\,\mathrm{m}\,]$
Ω	The workspace: $\Omega \subset \mathbb{R}^3$	$[\,\mathrm{m}\,]$
$\mathbf{D}$	Electric flux density	$[\,\mathrm{C/m^2}\,]$
$\mathbf{E}$	Electric field	$[\,\mathrm{V/m}\,]$
$\mathbf{H}$	Magnetic field strength	$[\,\mathrm{A/m}\,]$
$\mathbf{i}$	Electric current	$[\,\mathrm{A}\,]$
$\mathbf{J}$	Electric current density	$[\,\mathrm{A/m^2}\,]$
$\mathbf{B}$	Magnetic field flux density: $\mathbf{B} = \mu_0\mu_r\mathbf{H}$	$[\,\mathrm{T}\,]$

Symbol	Description	Unit
$\nabla \mathbf{B}$	Magnetic field gradient	$[\,\mathrm{T/m}\,]$
$\mathbf{m}$	The magnetic moment	$[\,\mathrm{A\,m^2}\,]$
$\mathbf{M}$	Magnetization or magnetic polarization of a magnetic material, that correspond to the volumetric density of magnetic moment: $\mathbf{M} = \frac{\mathbf{m}}{V_m}$, with V_m the volume of magnetic material.	$[\,\mathrm{A/m}\,]$
$\boldsymbol{m}$	Magnetization strength: $\|\mathbf{M}\| = \boldsymbol{m}$	$[\,\mathrm{A/m}\,]$
μ_r	Relative magnetic permeability, that is the ratio of the permeability of a specific medium to the permeability of free space: $\mu_r = \mu/\mu_0$	–
μ_0	Magnetic permeability of the free space: $\mu_0 = 4\pi \times 10^{-7}$	$[\,\mathrm{H/m}\,]$
μ	Magnetic permeability	$[\,\mathrm{H/m}\,]$
ρ	Volume charge density	$[\,\mathrm{C/m^3}\,]$
$\mathcal{A}$	Actuation matrix	–
$\mathbf{f}_\mathrm{m}$	Magnetic force	$[\,\mathrm{N}\,]$
$\mathbf{t}_\mathrm{m}$	Magnetic torque	$[\,\mathrm{N\,m}\,]$
R_e	Reynold number that corresponds to the ratio of inertial forces to viscous forces within a fluid	–
g	Gravitational acceleration. On Earth objects fall with an acceleration between $9.764\,\mathrm{m/s^2}$ and $9.834\,\mathrm{m/s^2}$, with a typical value of $\mathrm{g} = 9.80\,\mathrm{m/s^2}$	$[\,\mathrm{m/s^2}\,]$
M	Mass of object	$[\,\mathrm{kg}\,]$
$\langle\varphi\rangle$	The average index of a vector field φ defined as the arithmetic mean.	–
κ	The matrix conditioning number, given by eq. (III.12).	–
Γ_ξ	The global performance indexes, given by eq. (III.15).	–
γ	The uniformity index of a vector field φ, given by eq. (III.6).	$[\,\%\,]$
w	The manipulability index, given by eq. (III.7)	–

Acronyms

ABF artificial bacteria flagella.

DOF degrees of freedom.

EMA Electro-Magnetic Actuation.

ETH Swiss Federal Institute of Technology in Zurich, in German: Eidgenössische Technische Hochschule Zürich (`http://www.ethz.ch`).

FEM finite element method.

MIS Minimally Invasive Surgery.

MRI Magnetic Resonance Imaging.

RMS root mean square.

SPIO super paramagnetic iron oxyde.

STD standard deviation.

SVD singular value decomposition.

VH vitreous humor.

Introduction

Magnetic actuation techniques and microrobots have attracted great interest since they have potential in biomedicine applications. Interventional techniques have emerged as a tool to handle a wide range of minimally invasive operations. However, current interventional procedures are constrained by the limitation of manual operation by surgeon. Thus, various microrobotic solutions including magnetic navigation systems have been proposed for minimally invasive surgery (Minimally Invasive Surgery (MIS)), which carries many potential benefits such as reduced incision, less intraoperative hemorrhaging and postoperative pain, and faster recovery time. Recently, many electromagnetic actuation (EMA) systems have been reported and even involved to general surgery. The magnetic field and gradient generated by EMA system can be used to induce magnetic torque and force, respectively, for microrobot manipulation within workspace. Similar to other control systems, EMA system must be adapted to the given control object and customized for the application. The EMA system allows generate efficiently magnetic source for microrobot control when its specifications are further investigated and satisfied for the desired application.

Despite the large research effort on manipulating objects magnetically, few studies are carried out on the analysis and optimization of EMA systems requiring a minimum number of electromagnets necessary to perform magnetic manipulation at small scales. The most common force-based position control setup applies a static field in one direction, to magnetize or align the object, and uses three gradient fields to apply forces for position manipulation. These designs commonly use as few as three electromagnets and as many as eight electromagnets. However, these designs do not follow a generic rule to handle microrobotic constraints related to the application, such as limited workspace, number of degree of freedom, manipulability, unexpected singularities, stabilization, gravity. Theoretical approaches to analyze these magnetic system performances are not well understood and developed at the pre-design stage.

In this dissertation, we will demonstrate a design methodology for performant electromagnetic micromanipulation platforms. The various specifications and configurations of EMA systems have been comprehensively estimated and analyzed. An innovative robotized EMA platform named OctoRob is finally proposed by utilizing the methodology for singular-free 5 degrees of freedoms (DOFs) control of microrobot. The main components consist of magnetic generation parts, robotic arms and external equipment, that must be well designed and considered. The considered design enables reconfigurable structure for more effective magnetic control with translating and rotating electromagnets by externally generated rotational robotic arms. The designed OctoRob can be used for wireless navigation, oriented control and other specified actions to improve surgical procedures, especially for ophthalmic MIS. System characterization has validated

the underlying assumption. Through the investigation of full simulation, the built platform following the methodology has great potential to achieve precise control of micromanipulation tools. Furthermore, the reconfigurable design allows the magnetic control more effective, flexible and resourceful. In order to make clinic testing become a reality, experimental assessments must be thereafter implemented to evaluate the performance of the built system.

Chapter I

State of the Art

Chapter contents

Introduction

Minimally Invasive Surgery (MIS) encompasses surgical techniques that limit the size of incisions needed and so lessen wound healing time, associated pain and risk of infection. MIS procedures have been enabled by the advance of various medical technologies. In particular, several surgical robotics systems have been developed. Such robotic platforms already play a significant role to improve patient care, though it increases surgical preparation, cost and risk of the MIS approach compared with traditional open surgery [1]–[14]. For example, there are the well-known da Vinci® surgical assistance robots [7], [8], [11], developed by Intuitive Surgical[1], which improves the surgeon technical skills. Historically, such medical robotics topic is the main concern of the Robotics team from the PRISME Laboratory[2]where this PhD thesis has been conducted. Actually, researchers from the Robotics team have developed solutions like robotized tele-echography to provide skilled medical care to isolated patients [15], [16]. Moreover, unlike the dependence on using rigid instruments with dexterous distal wrists, it is commonly more attractive to use flexible or adaptive robotic tools that access internal anatomy with few skin incisions [14], [17]–[21]. Especially, the mechanical parts of existing medical robotic devices are still relatively large and rigid to access and treat major inaccessible parts of the human body (e.g. in robot-assisted surgery). In parallel, the various medical robotics solutions have been developed to improve the acceptance of the use of robotics systems in clinical practices. In the meanwhile, microrobotic has also emerged as an attractive technology to introduce novel microsystems to further reduce trauma, create new diagnoses tools and therapeutic procedures. Indeed, designing miniaturized and versatile (micro)robotic systems would allow accessing throughout the whole human body; leading to new procedures down to the cellular level; and offering localized diagnosis and treatment with greater precision and efficiency. For example, untethered microscopic devices, with size of less than a millimeter, may navigate within the body for targeted therapies [22]–[24]. Among the various actuation of microrobots, *magnetic actuation* is considered to be the most promising method [13], [22]–[51]. To this aim, numerous Electro-Magnetic Actuation (EMA) systems have been proposed to control untethered magnetic microrobots for biomedical applications [30], [43], [49], [50], [52]–[79]. The development of magnetic microrobotic systems circumvents the need to embed power within the microdevice [13], [22], [23], [26], [47], [80]. Magnetic microrobot can be then remotely powered and actuated precisely by the use of external electromagnetic fields. This enables untethered microrobots to assist the surgeon to increase precision and dexterity of the MIS procedure [13], [14], [22], [26], [47], [58], [79].

This PhD thesis aims to deal with the design, simulation and optimization of magnetic robotic system to improve MIS procedures. The magnetic manipulation of microrobots is one of the most interesting areas for researchers to improve many common biomedical applications as presented in figure I.1, where the electromagnetic sources could be set either in a two-dimensional (2D) or three-dimensional (3D) arrangements, and then applies properly to the different parts of the human body. As illustrated in figure I.1(A), the 2D placement of magnets could be useful for surface operations such as angioma or cosmetic treatments. In the meanwhile, most MIS interventions require a 3D workspace, hence, the EMA system should be arranged in 3D above I.1(B) or around I.1(C) the workspace. Certainly, the EMA system has great potential to remotely control the untethered medical device to complete the difficult traditional surgical operation. For

[1]Intuitive Surgical Inc. `https://www.intuitivesurgical.com`, `http://www.davincisurgery.com`

[2]Laboratoire Pluridisciplinaire de Recherche en Ingénierie des Systèmes, Mécanique, Énergétique (Multidisciplinary in the general domain of engineering sciences): `http://www.univ-orleans.fr/fr/prisme`

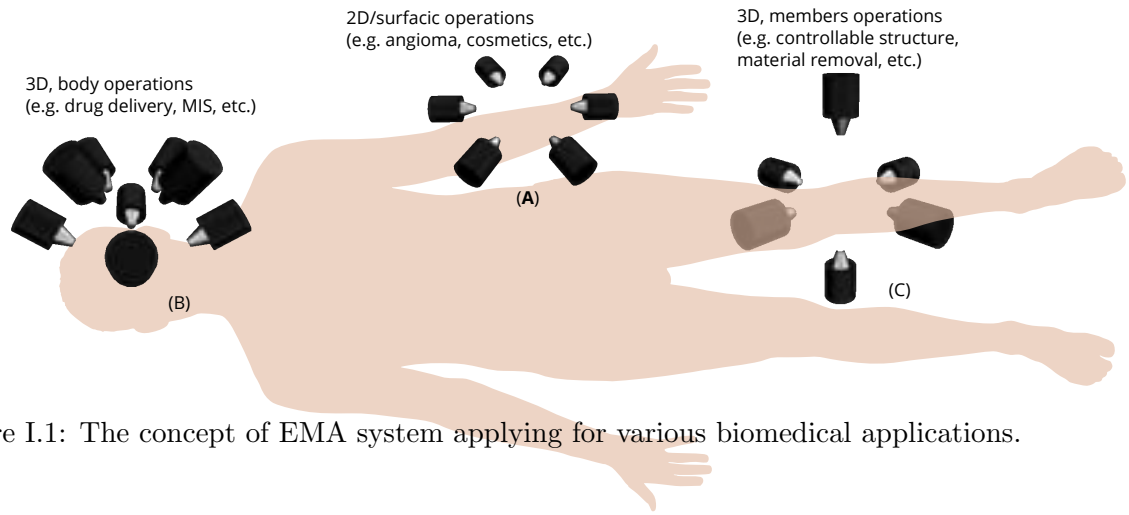

Figure I.1: The concept of EMA system applying for various biomedical applications.

instance, the eye surgery requires high sensitive manipulations that are constrained by the limits of human performance and requires forces below the threshold of human perception. In addition, current ophthalmic surgical techniques typically require a vitrectomy to gain access to the retina, which can result in postoperative complications [81]. Thus, the traditional ophthalmic surgery below the microscale is truly difficult to operate, and novel magnetic microrobotic solution can significantly enhance the procedure. To address this objective of designing proper EMA system for a given application, the first chapter presents the background of the magnetic microrobots for minimally invasive medicine and further describes the state of the art. To this aim, the chapter is organized as follows. Section I.1 demonstrates the challenge of MIS procedure, and explores the potential impact of biomedical magnetic microrobot. Next, since the design of magnetic microrobotic system is the main motivation of this PhD research work, it is important to investigate the basic principle of magnetic propulsion of microrobots, and the various magnetic microrobots that can be considered for biomedical applications. These studies are carried out in Section I.2. To enable the magnetic actuation of microrobots, it is mandatory to use and control magnetic field sources. Section I.3 introduces the different magnetic sources that can be considered, as well as the basic principles of classical coils investigated by scientists. An overview of the different EMA platforms developed by researchers is then presented in Section I.4. On the basis of this state of the art, in Section I.5, the objective of this PhD thesis is defined as the design of innovative magnetic actuation setup for microrobotic biomedical applications to improve MIS procedure.

I.1 Untethered microrobot for biomedical tasks

This section will provide a comprehensive survey of the state-of-the-art in biomedical robotics, and the impact and potential of untethered microrobots.

Nowadays, there are two broadly known and useful robotic systems in clinical applications: Intuitive Surgical's da Vinci and the capsule endoscopy for gastrointestinal diagnosis [7], [8], [11], [82], [83]. The main motivation of the da Vinci medical robot is to assist the surgeon with high precision and full dexterity technology, especially in MIS applications. Minimally invasive procedures bring many advantages from reduction of recovery time, medical complications and postoperative pain to increase quality of care [1]–[14]. Hence, many researchers have investigated over the past decades the use of microrobots for innovative biomedical applications [13], [22]–[51].

For instance, Jeon *et al.* [34] report that magnetic microrobots can be used to transport colorectal carcinoma cancer cells to tumor microtissue in a body-on-a-chip, which comprised an *in vitro* liver-tumor and micro-organ network. The magnetic microrobots can also be controlled in a mouse brain slice and rat brain blood vessel. Moreover, the potential of microrobots for the culture and delivery of stem cells has been also demonstrated [34], [39]. Therefore, the wireless microrobots have the great potential to revolutionize many aspects of biomedical applications [84]–[86]. This is made possible thanks to the advances in micro/nanoscale sciences and technologies allowing creating tiny tools able to operate in very small spaces. Therefore, untethered microrobots are envisioned to perform surgical tasks with precise and flexible procedure in many internal locations of the body that are either inaccessible or hard to reach. These additional locations in the human body would become available with wireless intervention for MIS procedure. For instance, the biomedical microrobot can navigate within natural pathways (such as the vascular network, urinary system, central nervous system.) enabling intervention with minimal trauma [13], [22], [38], [40].

To design a reliable and efficient medical microrobot, a good comprehension of the biomedical applications and theirs constraints must be achieved. First, the environment in which the microrobot will operate, affects its locomotion capabilities. When the microrobot performs a task in a fluid, as the Reynolds number[3] decreases ($R_e \ll 1$), gravity and velocity become less relevant, and the fluid viscosity and surface effects have to be taken into account [87]. Thus, the type of the wireless microrobot (size, shape, materials, etc.) is mainly determined with respect to the media of workspace. Obviously, the biomedical tasks that need to be achieved will also determine the design of the microrobotic system. Generally, the microrobot will likely perform relatively basic functions. Some of these tasks should be realized in autonomous way to allow robustness, adaptability and precision. In more advanced procedures, supervision and tele-operation directed by a practitioner allow offering more reliability and safety. It is foreseeable that as technology advances, the microrobotic system will be able to take more and more complex tasks.

In the following, the most relevant and envisioned biomedical tasks for untethered microrobot are introduced, also depicted in figure I.2.

Targeted therapy

The targeted therapy is a useful and most promising application for untethered microrobot. The microrobot could cargo and deliver chemical and biological substances only to the desired locations. For instance, the given drug can be applied to the specific cells, genes or other regions of interest thanks to therapeutic microrobots [22], [35], [38], [39], [88]–[90]. Similarly, the microrobot carrying higher concentration of radioactive materials could navigate near to the unwanted cells to kill them better [91]. These localized methods can reduce the risk of side effect in the rest of the body.

Material removal

The medical microrobot can be applied to remove material by mechanical means. For example, when a fatty deposit exists on the inner walls of blood vessels, the microrobot can be used to ablate it by scraping or a resonating mechanical structure [47], [78]. Beside, the microrobot can also be used to excise a tissue sample from the human body, that is biopsy, for the *in vitro* analysis [92]. Thus, the microrobot can be actuated with rotational motion to remove or get

[3]Reynold number that corresponds to the ratio of inertial forces to viscous forces within a fluid

- Hyperthermia and thermoablation refer to the local delivery of heat energy to destroy unwanted cells (27). Hyperthermia involves moderately raising temperature for extended periods of time, typically to the range of 40–45°C, to improve the effectiveness of other therapies; thermoablation involves raising the temperature to the point of cell death, which is typically above 50°C (28). The most promising methods for wireless heat delivery include high-frequency magnetic fields (27) and ultrasonic-resonating mechanical structures.

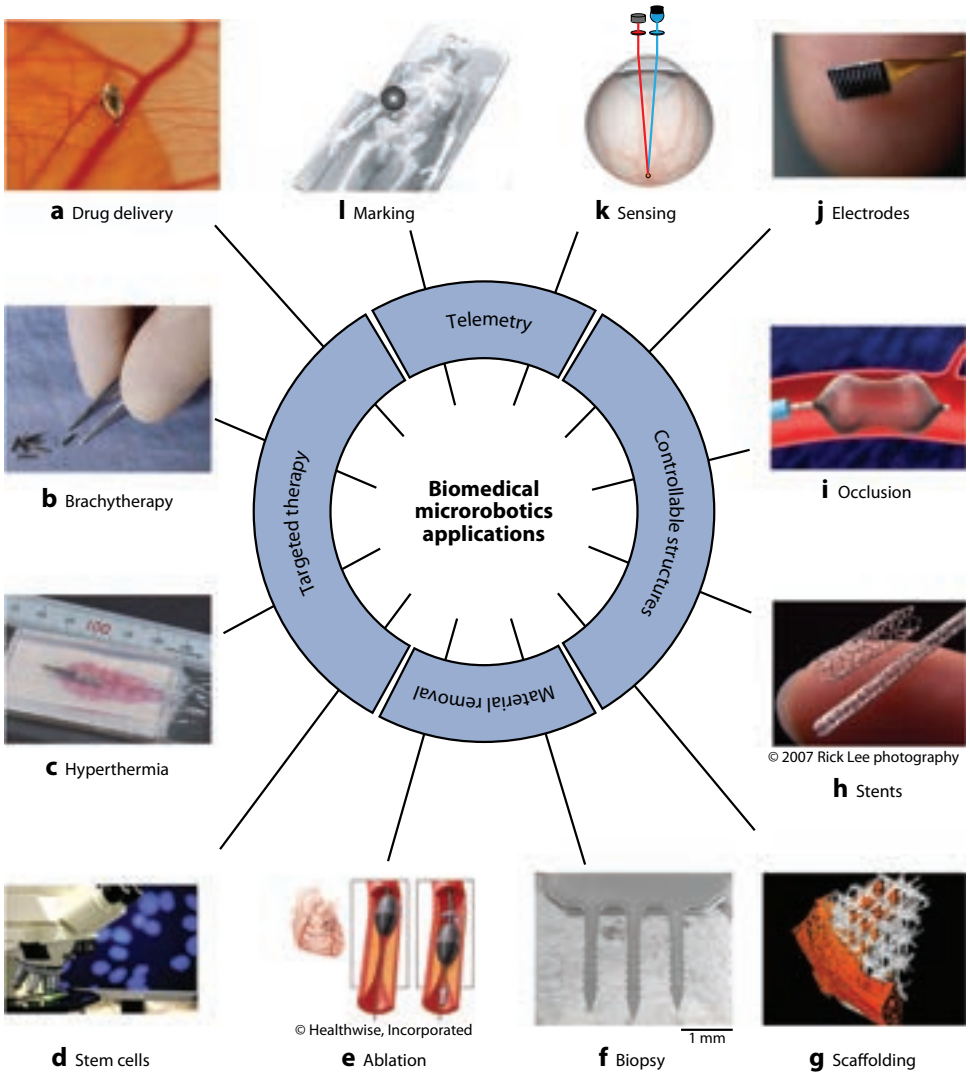

Figure I.2: Principal biomedical tasks for microrobots, targeted therapy, material removal, controllable structures, and telemetry [22].

the desired parts. Likewise, the microrobot can destroy the unwanted objects by the emitted ultrasonic pressure waves.

Controllable structure

The microrobots can act as simple static structures whose positions and direction are controllable. For example, the scaffold-type microrobots can act as cell support frames on which nerves can be regenerated, artificial organs developed, and blood vessels regrown [35], [93]. Moreover, the microrobot can serve as the stent or occlusion to dredge or block a passageway in the location of interest. For instance, the use of a microrobot to keep blood flowing through a clogged vessel, or to clog a blood vessel that nourishes a tumor [94], [95].

Telemetry

Due to the limitations of imaging detection position, there are some areas of the body (such as the brains, the microvasculature system.) where the information may be difficult or impossible to obtain. The untethered microrobot is capable of transmitting such information by using radio, fluorescent marker or other methods near the desired areas for remote sensing. For example, magnetic microrobot can transmit the time history of a physical signal of interest or transmit the status of the analyzed object with a simple digital signal. In addition, if the remote sensing is combined with marking, the microrobot can be used to localize unknown internal phenomena that detects the location of interest and transmit the obtained information to the external setup [95], [96].

Discussions

Combining the above functionality, the biomedical microrobot could be used to fully perform specific MIS procedures, for instance, in ophthalmic interventions [13], [22]–[51]. As example, injecting untethered microrobots directly into the retina avoids vitrectomy, reduces the invasiveness of the procedure, and improves the health of the eye after the procedure by maintaining a more natural state [13], [14], [22], [41], [60]. To achieve such objective and to propel and control the untethered medical microrobot, the use of externally applied magnetic fields are the most envisioned solution [30], [43], [49], [50], [52]–[79]. Magnetic actuation is the most preferred thanks to its main advantages: insensitivity to biological substances, remote control, and precise positioning ability. Electromagnetic field that is generated externally for energy transfer and propulsion can provide reliable and efficient solution required for the *in vivo* tasks. Automatic control also plays an important role in modern medical MIS [13], [14], [22], [41]. For example, when ophthalmic procedure involves hand-held manipulation systems, for force and position exerted by the practitioner on the surgical tool, it can be processed and adapted [41]. Such systems obviously improve the efficacy, flexibility and accuracy for retinal MIS. Thus, the accurate manipulation of medical microrobots can be increased thanks to their automatic control in the therapies. Specifically, Yesin *et al.* [50] have investigated untethered biomedical microrobots guided through external magnetic fields inside the human body, with a particular attention for the retina intervention. In [89], the authors have proved the feasibility of targeted retinal drug delivery with wireless magnetic microrobots. These early works demonstrate the relevance of magnetic actuation to achieve suitable wireless control of biomedical microrobots in the eye. Moreover, different kinds of magnetic microrobots designs have been considered in biomedical applications [13], [22]–[51].

All these considerations make the use of untethered magnetic microrobot to perform innovative MIS procedures very promising. However, with the various applications of the magnetic technology, we must be acutely aware of the working principle of the EMA platform and their magnetic sources, the magnetic propulsion together with the microrobots design. In addition, the advantages or limitations of the different magnetic setups, including the classical electromagnetic coil configurations, have to be investigated for the further selection of design parameters. These aspects are addressed in the following sections.

I.2 Magnetic microrobotic system

The biomedical magnetic microrobots provide a promising alternative approach for many clinical procedures. The complete magnetic microrobotic system is mainly composed of an EMA platform and magnetic microrobot. These different components of the magnetic microrobotic system must also be further investigated to be able to fully comprehend either their capabilities or limitations. Indeed, the status, behavior or configuration of the microrobot can be changed by applying an electromagnetic field. To do so, different types of microrobots (e.g. diverse size, shape, materials.) can be designed for the particular tasks with various principles of locomotion.

This section introduces the basic principles of magnetic actuation that makes the microrobot move in the desired workspace. In addition, the various types of magnetic microrobots will be introduced and compared.

I.2.1 Magnetic actuation

The basic principle of magnetic actuation is to manipulate microrobots with the use of electromagnetic fields to induce forces and/or torques on it. Basically, any magnetized objects can be subjected to forces and torques within an externally-imposed electromagnetic field. The magnetic forces and torques developed on a magnetized object are usually expressed as follows [97]:

$$\mathbf{f}_{\mathrm{m}} = V_m \ (\mathbf{M} \cdot \nabla)\, \mathbf{B} \tag{I.1}$$

$$\mathbf{t}_{\mathrm{m}} = V_m \ \mathbf{M} \times \mathbf{B} \tag{I.2}$$

where V_m is the magnetic volume of the object; $\mathbf{M}$ denotes its magnetization (A/m); and $\mathbf{B}$ indicates the magnetic field flux (T). It is also possible to describe the applied magnetic field by the magnetic field intensity $\mathbf{H}$ (A/m), where $\mathbf{B} = \mu_0 \mu_r \mathbf{H}$, with $\mu_0 = 4\pi \times 10^{-7}$ H/m, the magnetic permeability of the free space, and μ_r the relative magnetic permeability. Obviously, magnetic torque $\mathbf{t}_{\mathrm{m}}$ is a function of the magnetic field $\mathbf{B}$, while the magnetic force $\mathbf{f}_{\mathrm{m}}$ is related to the magnetic gradient $\nabla \mathbf{B}$ (T/m).

A basic solution to magnetically propel a microrobot is to use solely the magnetic gradient $\nabla \mathbf{B}$, and such simple technique is commonly referred as *bead pulling*. Figure I.3 shows examples of microrobots relying on the bead pulling. Other propelling schemes can be obtained using magnetic torques and/or forces. These different schemes are introduced hereafter.

I.2.2 Magnetic microrobots and their motion

Numerous microrobot designs and types of mobility have been investigated by researchers [13], [22]–[51], [98]–[105]. For instance, Solovev *et al.* [99] have proposed a chemically propelled design corresponding to a microtubular jet. With the OctoMag system, a nickel (Ni) microrobot shown in figure I.3b is pulled by a three dimensional (3D) magnetic field gradient with 5 DOFs motion [60]. Among others, we can notice the colloidal magnetic swimmer [98], the magnetic thin-film helical swimmer [106], the microhelix microrobot with magnetic head [100], and so on. Moreover, some microrobots can be actuated by biohybrid approaches including the artificially-magnetotactic bacteria [107], the magnetically sperm-driven organism, magnetically steered microrobots [108], and the chemotactic steering of bacteria-propelled microbeads [109], etc. For example, Alapan *et al.* [27] report biohybrid microrobots composed of bio-engineered motile bacteria and erythrocytes loaded with anticancer drugs and super paramagnetic iron oxyde (SPIO) particles. This biohybrid

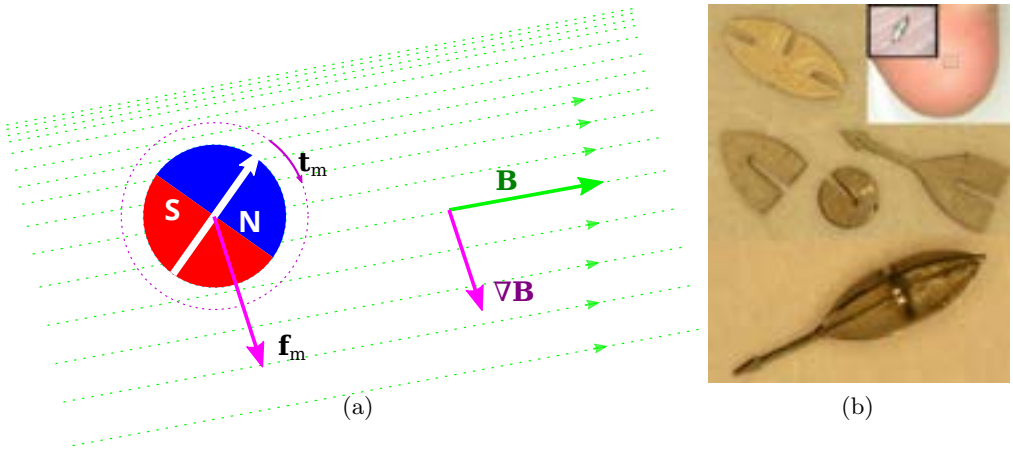

(a) (b)

Figure I.3: Magnetic bead pulling: (a) a schematic representation of its principle; and (b) Ni microrobot components and an assembled microrobot [49].

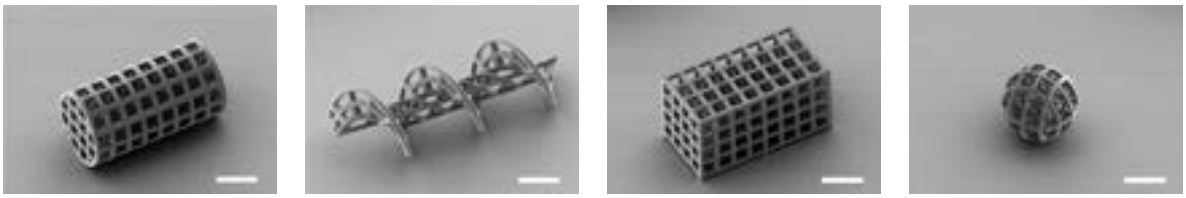

(a) (b) (c) (d)

Figure I.4: The scanning electron microscopy images of scaffold-type microrobots [34]: (a) cylindrical scaffold-type microrobot; (b) helical scaffold-type microrobot; (c) hexahedral scaffold-type microrobot; (d) spherical scaffold-type microrobot. Scale bars are 40 µm.

microrobot provides autonomous propulsion, untethered magnetic steering, and efficient drug encapsulation and release. Likewise, Du Nguyen *et al.* [36] propose a tumor targeting cell-based microrobot that performs similar function for active drug delivery to tumors. Thus, various types of motion or swimming have been investigated, and particularly for magnetic microrobots. Since the microrobot has great potential to operate efficiently tasks in the microworld, the magnetic microrobot is the envisioned method to perform biomedical applications with small scale. Therefore, the microrobot actuated by electromagnetic field and gradient with different methods will be discussed in the following.

I.2.2.1 Magnetic bead pulling of microrobot

One most basic principle of magnetic actuation relies on the use of the magnetic force Eq. (I.1), commonly referred as bead pulling. On this basis, Yesin *et al.* [49], [50] have fabricated a 3D structure built by microassembly of individual parts as illustrated in figure I.3b. The winged-ellipsoid shape has an axis of symmetry along the long axis of the ellipsoid. The microrobot can be aligned to the desired direction by an external magnetic field $\mathbf{B}$ and pulled along the direction of magnetic gradient $\nabla\mathbf{B}$, as represented in figure I.3. Likewise, Figure I.4 shows the scanning electron microscopy (SEM) images of fabricated cylindrical, hexahedral, helical, and spherical scaffold-type microrobots, respectively [110]. Different shapes of microrobots exhibit

various modes of operations when magnetic fields and gradients are applied. The cylindrical and hexahedral microrobots are pulled by using an external magnetic field gradient $\nabla \mathbf{B}$. In [35], the manipulation of the cylindrical and hexahedral scaffold microrobots using magnetic force by the gradient field is shown to be not optimal. Thus, the drilling motion by a rotating magnetic field could induce more efficient and controllable motion of microrobots in a confined *in vivo* microfluidic environment.

I.2.2.2 Microrobot with swimming

A first alternative is to apply a magnetic torque $\mathbf{t}_\mathrm{m}$ (I.2) on the microrobot. Next, to enable a motion, it must be basically placed in a rotating magnetic field, whose strength and rotational frequency have to be flexibly controlled to enable an efficient swimming. Obviously, the shape of the microrobot plays a significant role in the swimming condition, and different swimming principles are investigated. A basic design relies on the use of helical microswimmer, as illustrated in figure I.5. Hence, inspired by bacterial flagella, microrobots with helical propeller have been investigated by many researchers [25], [26], [34], [37], [44], [64], [100], [111]–[123]. As example, figure I.6 shows some realizations of such helical microswimmer. The helical microrobots can perform 3D locomotion in various mediums with a sub-micrometer precision under rotating magnetic field. Especially, the helical propulsion is likely a proper choice in comparison to other methods when considering the limitation in generating strong controlled magnetic gradient field. Compared to basic bead-pulling, the helical motion also brings supernumerary advantages including the high swimming velocity, particularly in strong viscous fluid. The helical microswimmer can be steered by a low strength rotating magnetic field with micrometer positioning precision [114]. Since magnetic field with low strength is harmless to cells and tissues [45], the magnetic helical microrobot is a promising tool for many biomedical applications, such as cell manipulation, targeted therapy and intraocular MIS procedures. It can be shown that the head size and the tail length, turns, etc. notably affect the swimming properties (e.g. velocity) of the helical microrobot. In order to optimize locomotion property, these designs and shape parameters have to be investigated with respect to the envisioned biomedical application. In this regard, Zhang *et al.* [100] have evaluated quantitatively some metrics of the locomotion of helical microswimmer.

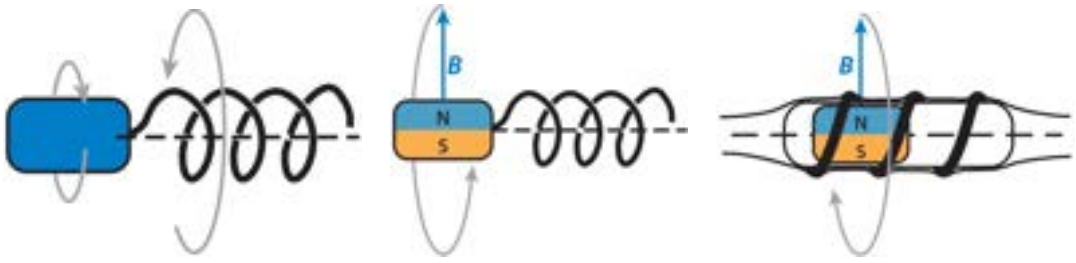

(a) (b) (c)

Figure I.5: Representation of the principle of the helical microswimmer concept: (a) a rotary actuator turns the propeller with respect to the microrobot body; (b) a propeller rigidly attached to the microrobot body, which is rotated by a magnetic field $\mathbf{B}$; and (c) a capsule type magnetic microrobot with helical propulsion to crawl through lumens or tissues. [22] N and S indicate the north and south poles of the magnetic body.

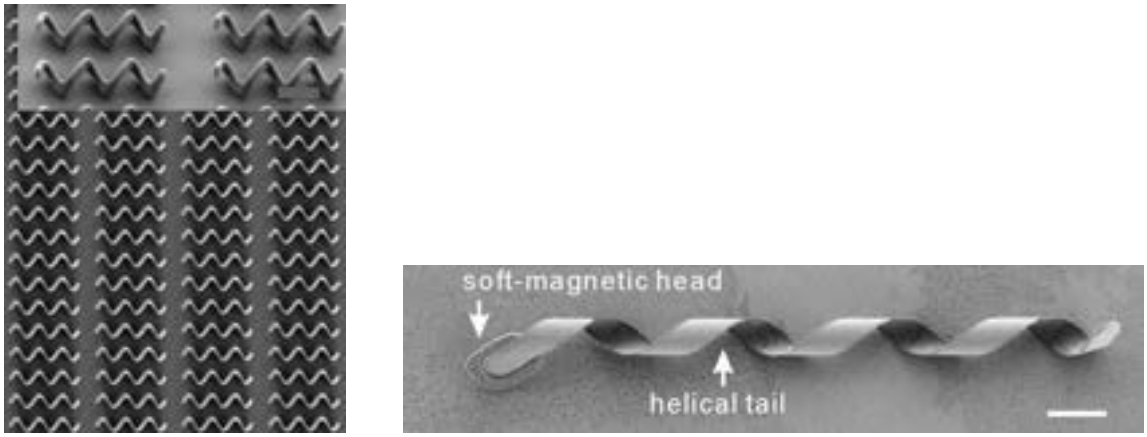

(a) (b)

Figure I.6: Example of fabricated artificial bacteria flagella (ABF) helical microswimmers: (a) a horizontal array of helical swimming micromachines [116]; (b) a photograph of an untethered artificial bacterial flagella (scale bar=4 µm) [113].

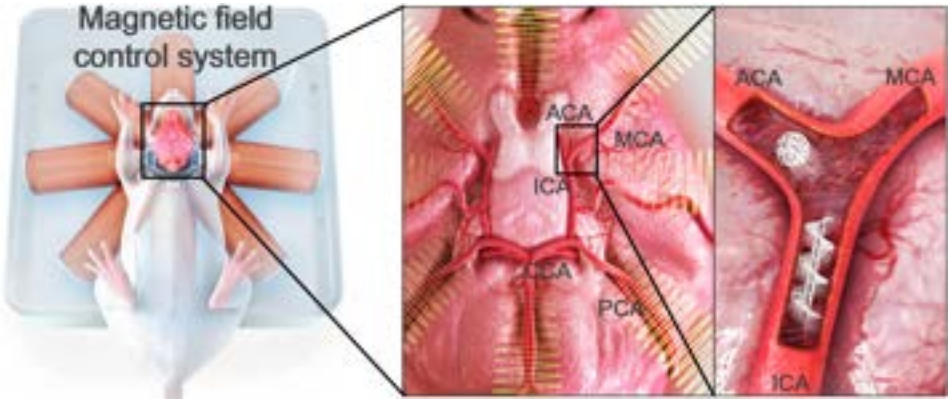

Figure I.7: *In vivo* model of a brain blood vessel and MiniMag system [34], [61].

Thus, the adoption of integrating a rotary motor to the passive flagellum is an easy method for microrobot actuation, as illustrated in figure I.5a. However, miniaturizing a running motor system is difficult below the millimeter scale [22]. The figure I.5b illustrates a helical microrobot, which is rotated by a magnetic field. On this basis, Sendoh *et al.* [124] have fabricated an endoscope that is composed of a capsule case, a tube-shaped neodymium (NdFeB) magnet inside it, and a spiral structure, as illustrated in figure I.5c. The designed capsule microrobot can be rotated and propelled remotely by applying an external rotating magnetic field, requiring neither battery nor wire as a power supply. In addition, the authors also mention the less possibility of the breakdown of the actuator due to its simple structure. Such design of microrobot has great potential for remote manipulation of the capsule endoscope. Jeon *et al.* [34] have also investigated the biomedical use of helical swimmer. Specifically, spherical scaffold-type microrobots are developed and characterized for targeted delivery of stem cells in rat brain using a rotating magnetic field generated by a MiniMag system [61]. Figure I.7 shows a schematic of the experimental setup for helical and spherical microrobots manipulation in the blood vessel of a rat brain. Similarly, Lee *et al.* [37] have fabricated a magnetic drilling microrobot optimized to operate in a confined

(a) (b)

Figure I.8: Drilling microrobot: (a) fabrication procedure of the magnetic drilling actuator; (b) conceptual schematic of the designed microrobot as an intravascular driller in a 3D vascular network. [37]

fluid medium, such as a vasculature network. The structure of the proposed microrobot is a spiral-shaped with 3 mm in diameter and 9 mm in length. A Nd magnet is inserted in the cylindrical inner space (0.5 mm diameter, 5 mm length), as illustrated in figure I.8a. Figure I.8b shows a conceptual schematic diagram of thrombosis treatment (i.e. a material removal task) using the drilling microrobot in a vascular network. The designed microrobot can precisely navigate to a desired location and then drill through the thrombus to open the pathway for recirculating blood. This type of biomedical microrobot can be controlled with 5 DOFs by using the OctoMag system [60]. Likewise, Tottori *et al.* [116] have proposed a simple magnetic helical microstructure illustrated in figure I.4b. Li *et al.* [39] have designed a microrobot loaded with targeted cells that could be automatically controlled to reach a desired site by using a magnetic gradient field. The cell-cultured magnetic microrobot with a burr-like porous spherical structure has been evaluated *in vivo* for cargo transport in zebrafish embryos [39], [125]. In [25], [111], the authors have added a head to the microswimmer that comprises either a permanent magnet or soft magnetic materials to steer the microrobot by mean of external magnetic field. In the same way, Zhang *et al.* [100], [113] investigate an artificial bacteria flagella (ABF) consisting of a helical tail mimicking a natural flagellum and a soft-magnetic metal head in the shape of a thin square plate that is shown in figure I.6b. The proposed ABF helical tail is made of InGaAs/GaAs/Cr. But different materials are candidates for helical tail fabrication, including semiconductors, metals, and polymers [120]–[122]. Using rigid propeller instead of compliant helical one, the direction of microrobot motion can be then reversed simply by reversing the rotation direction. Thus, rigid propeller is capable of both pushing and pulling helical microrobot. Barbot *et al.* [28] have designed the rotating helical microrobots with conical structure at both ends. They have demonstrated that the control of the rotation of their microrobots inside microchannel can be achieved.

I.2.2.3 Discussions

Literature proposes many different solutions and designs to magnetically propel a microrobot. Commonly, the choice of the microrobots depends on the considered procedure, as well as the targeted environments (networks: vascular, urinary, nervous, cavities: brain, eye, bladder, etc.). Indeed, the medium in which microrobot operates is significantly different than that of conventional robotic systems. In particular, biomedical microrobot is manipulated typically in fluids at the low Reynolds-number regime (e.g. $R_e \ll 1$), where viscous drag significantly

dominates over inertia [87]. External magnetic field manipulation should provide physicians with a direct way of controlling and steering medical microrobot inside patients. Actually, the direction of the microrobots' movements will alter in response to change in the direction of the magnetic field. However, magnetic forces (I.1) decay exponentially with distance, and very high magnetic gradient field will be required to translate the microrobot deep inside the human body [23]. As example, in the context of retina intervention, the microrobot will navigate in the vitreous humor. The vitreous humor is a complex biofluid (e.g. water with salts, sugars, collagens.) exhibiting a non-Newtonian rheological properties giving it a gelatinous consistency [81]. Hence, in such physiological condition, helical microswimmers are one of the most efficient methods [44], [100], [113]–[115], [119].

From the first literature review, it can be shown that the magnetic microrobot can be efficiently actuated by the utilization of magnetic field. This field **B** should be generated from an EMA platform, that must obviously comprises some electromagnetic sources. The magnetic sources could be produced by either permanent magnets [30], [52]–[57] or electromagnets [43], [49], [50], [58]–[79], that should be selected according to the specified biomedical application. Various EMA setups could generate the proper magnetic field or gradient. We review in the following the different principles that are actually used in the generation of the magnetic fields for the propulsion of magnetic microrobots.

I.3 Magnetic field and its gradient generation

In this section, the generation of magnetic field and its gradient are investigated. Generally, magnetic sources can be produced by either either permanent magnets or electromagnets. This section will mainly focus on the classical electromagnetic coils, such as Helmholtz coils, Maxwell coils and saddle-shaped coils. In the end, the simulations of generated magnetic field will be presented.

I.3.1 Magnetic field sources

I.3.1.1 Permanent magnet sources

To design a magnetic microrobotic system, a key issue remains on the magnetic actuation of the microrobot. Commonly, either permanent magnets [30], [52]–[57] or electromagnets [43], [49], [50], [58]–[79] are used to generate the magnetic field and magnetic gradient field required for the manipulation tasks. The main advantage of using permanent magnets to induce an external magnetic field is that no extra heat is diffused in the human tissues. Secondly, without the need of power supply, permanent magnets allow significantly reducing the energy demand for the magnetic manipulation system [53]. For instance, in [30] the authors have developed a robotic magnetic navigation system with permanent magnets to control a video capsule in the gastrointestinal tract. Mahoney and Abbott [54] have explored a 5 DOFs manipulator system to control a magnetic capsule endoscopy in fluid using a single permanent magnet. Amokrane *et al.* [57] have developed an EMA platform consisting of two permanent magnets shown in figure I.9. The proposed magnetic platform is allowed to control magnetic microrobot in the inner ear with good stability and robustness. Classically, permanent magnets are suitable for large-sized workspace thanks to their large magnetic field strength with respect to the volume

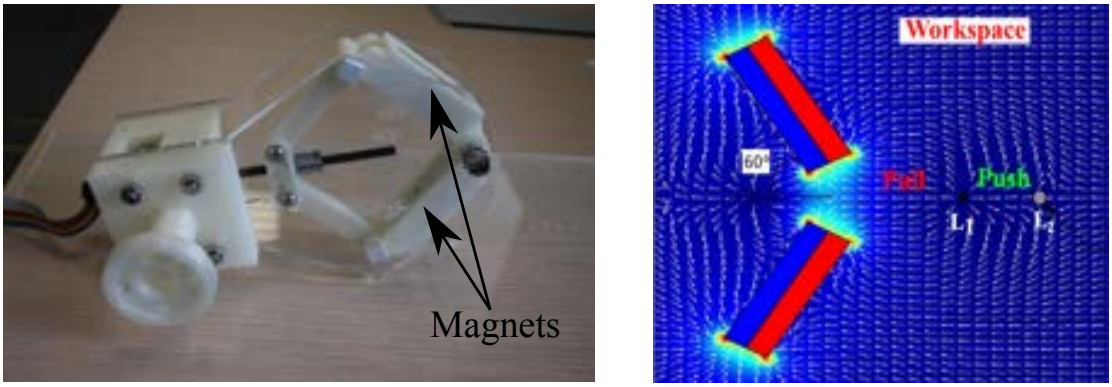

(a) (b)

Figure I.9: Example of a robotic magnetic system composed of two permanent magnets [57]: (a) a photograph of the magnets; and (b) a simulation of the magnetic field of the two magnets.

ratio. However, the magnetic fields generated by permanent magnets can not be accurately adjusted or switched off [55]. This can cause potential risks for precise and safe MIS procedure.

I.3.1.2 Electromagnet sources

In contrast, the magnetic field induced by electromagnets can be regulated by controlling the input electric currents, and it can thus be stopped. Basically, electromagnets usually consist of wire wound into a coil, also termed as a solenoid. When the magnetic microrobots need to be translated and/or rotated, the magnetic fields and/or their gradients have to be changed continuously. Thereby electromagnets can generate appropriate and flexible magnetic fields to efficiently control the motion of microrobots. The simplest electromagnet is wrapped around an air-filled core, as the one depicted in figure I.10. In such case, the magnetic fields or their gradients can be uniformly defined in the workspace, and linear relationship can be expressed with their input currents. However, in such case, the magnetic field strength is usually weaker than using permanent magnet on an equivalent volume. To improve the magnetic strength, a magnetic core with a high magnetic permeability can be added within the coil to confine and guide the magnetic fields. Thus, the magnetic fields are related to the current running through the electromagnetic coil as well as the magnetic core. Nevertheless, the corresponding electromagnetic fields usually possess a nonlinear behavior when the magnetic core is involved.

I.3.1.3 Stationary and mobile sources

Furthermore, the magnetic manipulation systems can be divided into stationary and mobile. Stationary magnetic sources commonly use Helmholtz, Maxwell and saddle coils [62]–[66], [68], [70], [72], [75], [126], as in Magnetic Resonance Imaging (MRI) system [59], [127]–[129], to induce magnetic fields and gradients that only are controlled by the current flowing into the electromagnetic coils. With such stationary configurations, the magnetic manipulation of the microrobot together with the workspace geometry remains limited by the stationary coils arrangement. Conversely, mobile magnets actuated by a robotic system can obviously move around the target to improve the dexterity of microrobots [130], [131]. As the magnetic

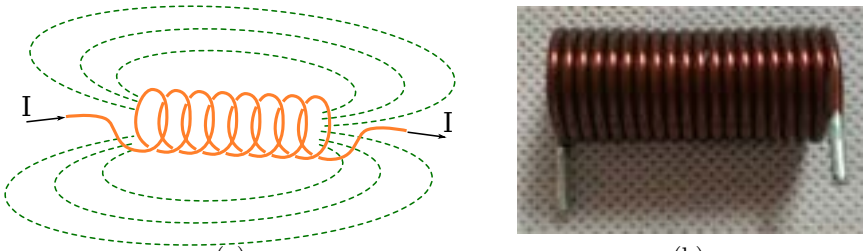

(a) (b)

Figure I.10: An example of a simple air-filled electromagnet: (a) illustration of the basic principle of a solenoid; and (b) an example of realization.

sources usually remain close to the microrobot, the moving coils also reduce the energy demand. Furthermore, they are able to change the local magnetic field distribution by modifying the positions and/or orientations of the magnets [61], [74].

(a) (b)

Figure I.11: Examples of magnetic manipulation systems with moving permanent magnets: (a) conceptual image of a rotating-permanent-magnet manipulator proposed by Fountain *et al.* [52], and (b) the Stereotaxis Niobe® consisting of two robotically-controlled magnets next to the table.

As shown in figure I.11a, Fountain *et al.* [52] propose the use of nonuniform magnetic fields emanating from a single rotating-permanent magnet manipulator for the control of magnetic helical microrobots, where the robotic arm bringing the magnet closer to the patient, and the axial and radial controls cause the local magnetic field to change. Stereotaxis[4] Inc. has developed and commercialized the Niobe® robotic magnetic navigation system presented in figure I.11b. Niobe® uses two permanent magnets mounted on pivoting arms and positioned on opposing sides of the operating table to control proprietary catheters and guidewires that have very small magnets at their distal tips. To circumvent the uncontrollability of the magnetic field generated by permanent magnet, Véron *et al.* [130] investigate a robot-assisted magnetic manipulation system with several mobile electromagnetic coils as represented in figure I.12a, where a robotic system keeps full dexterity for the use of electromagnetic coils while reducing energy consumption by a nearer manipulation. Also, Yang *et al.* [131] demonstrate an electromagnetic manipulation system with three parallel mobile coils named DeltaMag and represented in figure I.12b. The proposed EMA system can remotely control the magnetic untethered devices in an enlarged

[4]Stereotaxis Inc., St. Louis, MO, USA, `http://www.stereotaxis.com`

(a)

(b)

Figure I.12: Examples of magnetic manipulation systems with moving electromagnets: (a) the robot-assisted magnetic manipulation proposed by Véron *et al.* [130], and (b) the DeltaMag system consisting of three parallel mobile coils [131].

workspace, moreover, the electromagnetic coils are actuated through the parallel mechanism to achieve the flexibility of their placement. Thus, the DeltaMag system proves that the mobile source generated by moving electromagnets can improve the manipulability of localization to close the vicinity of the desired area and bring the good space utilization.

I.3.2 Classical electromagnetic coils configurations

One basic way to design a magnetic source relies on the use of electromagnets usually consisting of wire wound into a coil. The induced electromagnetic field can be simply regulated by controlling the input electric currents. When a current flows in such solenoid coil, the magnetic flux intensity can be modeled by a distant vector from a center according to Biot-Savart theory, and is directly proportional to the flowing current [97]. Hence, the magnetic field can be commonly approximated by: $\mathbf{B} = ki$, where the parameter k depends on the type and shape of the electromagnetic coil, and i is the electric current flowing through it. We investigate the expressions of the magnetic fields for common electromagnetic coil configurations in the following.

Remark 1 *Some further details on the basic electromagnetic theory are presented in the Chapter II.*

I.3.2.1 Helmholtz coils

One basic electromagnets arrangement follows the Helmholtz coils configuration. Indeed, the Helmholtz coils are commonly used to generate a uniform magnetic field $\mathbf{B}$ in a given workspace. Hence, Helmholtz electromagnets are useful to induce the magnetic torque $\mathbf{t}_{\mathrm{m}}$ Eq. (I.2) to align the microrobot magnetic moment. To do so, the Helmholtz set includes two solenoids with a radius r_h that equals the distance between the two coils: $l = 2r_h$, as shown in figure I.13. The currents flowing in an Helmholtz coil pair have same intensity and phase, that is: $i_h = i_{h\mathrm{left}} = i_{h\mathrm{right}}$. The magnetic field intensity $\mathbf{H}_h$ of Helmholtz coils can be the computed as follows:

$$\mathbf{H}_h = \begin{pmatrix} d_h x & 0 & 0 \end{pmatrix}^{\mathsf{T}} \tag{I.3}$$

$$d_h = \left(\frac{4}{5}\right)^{\frac{3}{2}} \frac{i_h}{r_h} \tag{I.4}$$

where x is the axis of the Helmholtz pair. Since a pair of Helmholtz coils can induce a uniform magnetic flux along its axis, two pairs of Helmholtz coils are basically orthogonally placed in the same plane to generate a uniform magnetic field in the 2D plane.

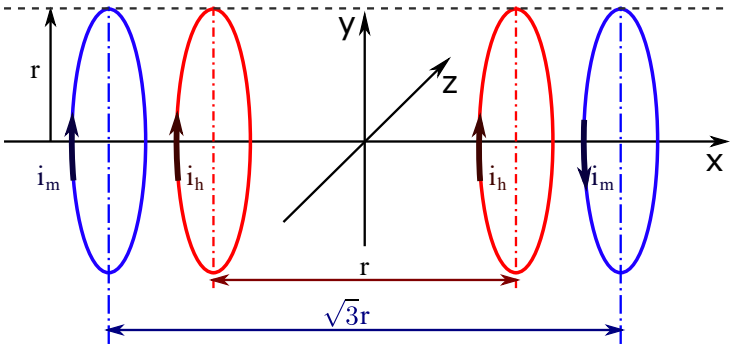

Figure I.13: Representation of an Helmholtz (inner red) and Maxwell (outer blue) coils pair.

Figure I.14 shows simulation results where the Helmholtz coils pair generates the uniform magnetic field along x-axis direction. The figure I.14(a) presents the magnetic field vectors in the 3D workspace, and figure I.14(b)-(d) show the magnetic fields in xy-plane, xz-plane, yz-plane, respectively. There is no vectors in the figure I.14(d) because the magnetic field component does not exist in xy-plane.

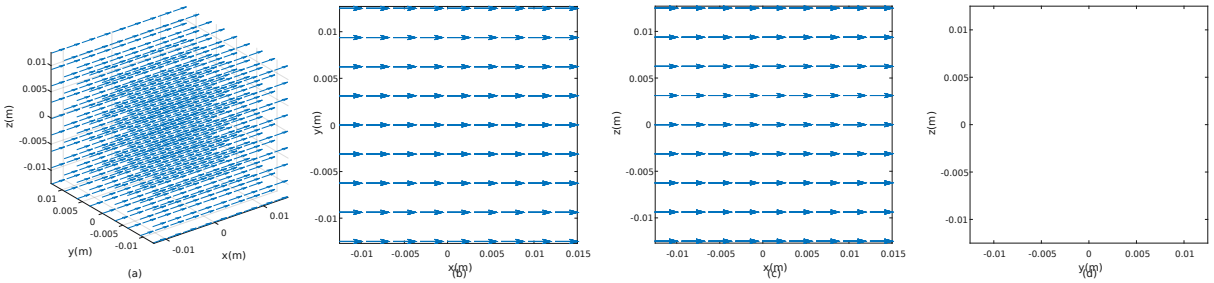

Figure I.14: The magnetic fields of Helmholtz coils: (a) 3D workspace, (b) xy-plane, (c) xz-plane, (d) yz-plane.

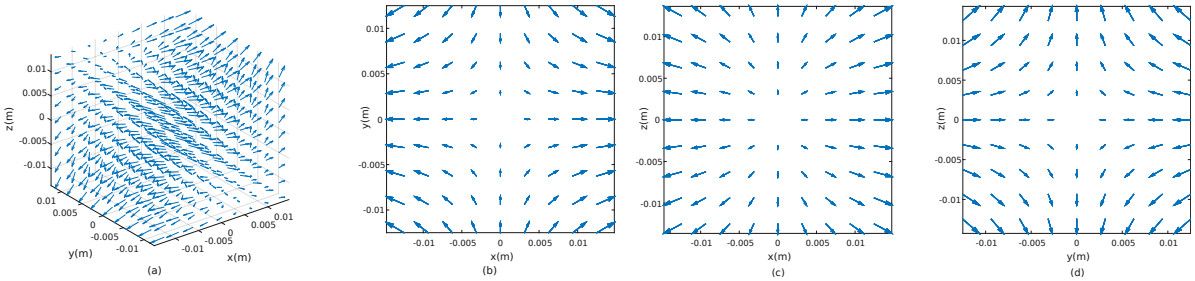

Figure I.15: The magnetic fields of Maxwell coils: (a) 3D workspace, (b) xy-plane, (c) xz-plane, (d) yz-plane.

I.3.2.2 Maxwell coils

The second basic electromagnets arrangement follows the Maxwell configuration. The Maxwell coils set is classically used to generate a uniform magnetic gradient $\nabla \mathbf{B}$ in a given workspace for providing a force $\mathbf{f}_{\mathrm{m}}$ (I.1) to propel the microrobot with bead pulling. The Maxwell coil consists of a pair of solenoid coils of radius r_m, separated with a distance $l = \sqrt{3}r_m$, as illustrated in figure I.13. The intensities of current have the same magnitude, but are flowing in opposite phases, that is: $i_{m\mathrm{left}} = -i_{m\mathrm{right}}$. The magnetic gradient is generated along the x-axis by Maxwell coil. As previously, the magnetic field intensity produced by Maxwell coil is defined as:

$$\mathbf{H}_m = \begin{pmatrix} g_m x & -0.5 g_m y & -0.5 g_m z \end{pmatrix}^{\intercal} \tag{I.5}$$

$$g_m = \frac{16}{3}\left(\frac{3}{7}\right)^{\frac{5}{2}} \frac{i_m}{r_m^2} \tag{I.6}$$

where $i_m = |i_{m\mathrm{left}}| = |i_{m\mathrm{right}}|$ denotes the current following into the Maxwell coils. Since the Maxwell coil induces magnetic gradient, it can provide propulsion force on microrobot located near the center of the workspace.

The magnetic gradient is the rate of change of magnetic field with spatial displacement. For EMA system, the Maxwell coils pair is responsible for producing a uniform gradient field. The distribution of magnetic field in an arbitrary direction of propulsion force has been illustrated in figure I.15. The magnetic gradient is mathematically verified to be uniform.

I.3.2.3 Saddle-shaped coils

Besides the well-known and used circular-shaped Helmholtz and Maxwell coils, saddle-shaped coils is one of most considered design for electromagnetic manipulations. In particular, their opened designs find interesting use in MRI systems. Based on this idea, Jeong *et al.* [62] have developed saddle-shaped coils referred as uniform and gradient saddle coils. Figure I.16 shows the basic configurations of these saddle coils. As for Helmholtz and Maxwell coils arrangements, saddle-shaped coils can be employed to induce either uniform magnetic fields or magnetic gradients, and will be presented in the following paragraphs.

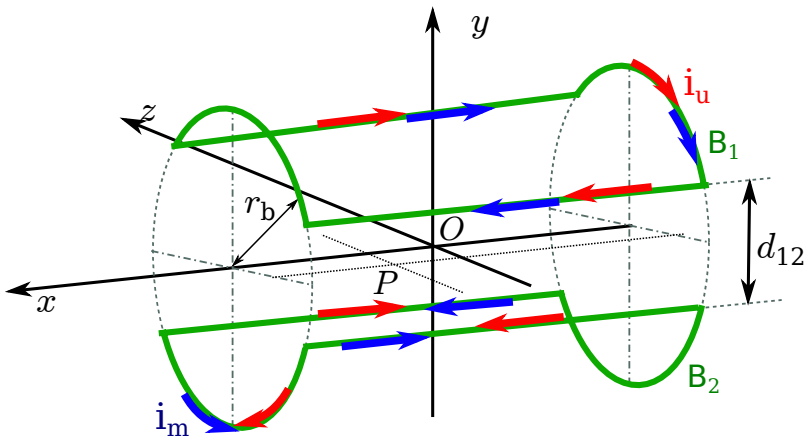

Figure I.16: Representation of saddle-shaped coils: with same current i_u flowing in uniform saddle coil, and current i_g in phase opposite for gradient saddle coil.

The uniform saddle coils

The uniform saddle coils pair is able to perform same functions as the Helmholtz coils pair, that is produce a quasi-uniform magnetic field within a given workspace. The uniform saddle coil generates homogeneous magnetic field near the center which can be expressed as the following equations [68]:

$$\mathbf{H}_u = \left(0, d_u, 0\right)^\intercal \tag{I.7}$$

$$d_u = 0.6004 \frac{i_u}{r_u} \tag{I.8}$$

where i_u is the current following the uniform saddle coil, and r_u radius of the saddle coil ($r_u = r_b$, in figure I.16). Similar to the Helmholtz coils, the specific geometrical relationship of saddle coil allows generating uniform magnetic gradient. Thus, the uniform saddle coils pair plays the similar role as the Helmholtz coils pair to produce uniform magnetic field as represented in figure I.17.

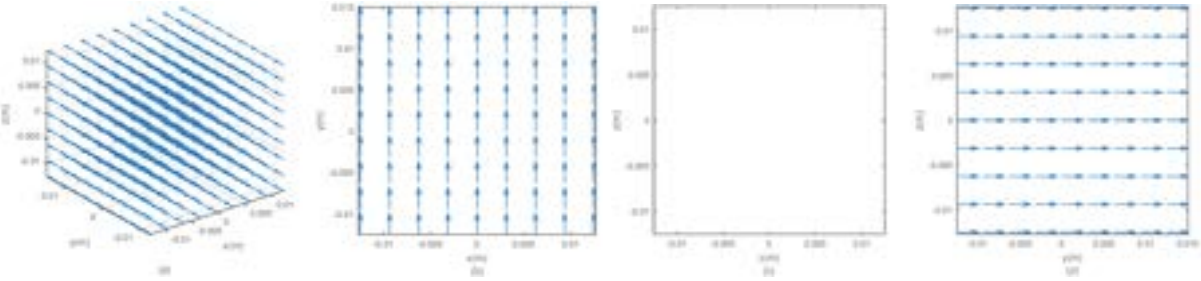

Figure I.17: The magnetic fields of uniform saddle coils: (a) 3D workspace, (b) xy-plane, (c) xz-plane, (d) yz-plane.

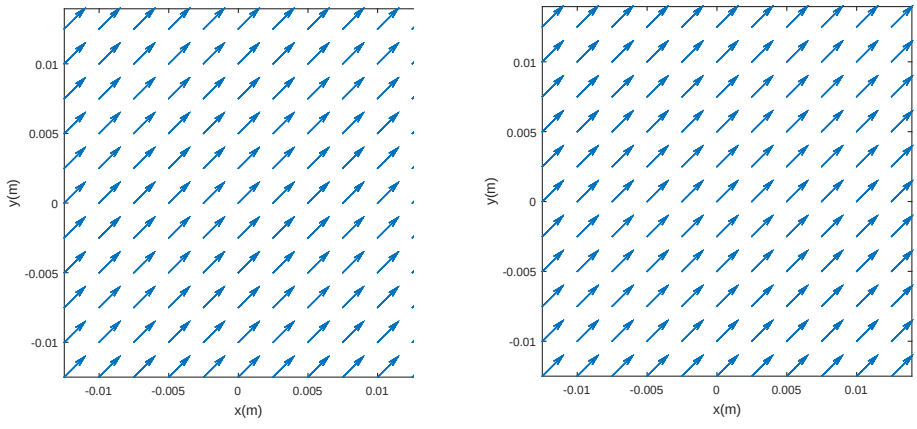

Figure I.18: (a) shows the magnetic field generated by two pairs of Helmholtz coils at the 45°; and (b) shows the magnetic field generated by one pair of Helmholtz coils and one pair of uniform saddle coil.

To illustrate such similarity, two configurations cases are simulated: (i) the magnetic field is applied to angle 45° by two pairs of Helmholtz coils (see figure I.18a), and (ii) the magnetic field generated by the Helmholtz and uniform saddle coils pairs (see figure I.18b). The results confirm that the both coils can generate uniform magnetic field, thereby providing appropriate magnetic torque to align microrobot in a desired direction.

The gradient saddle coils

The gradient saddle coil presents same function as the Maxwell coil that produces a quasi-uniform magnetic gradient field within a given workspace. The linearized magnetic field intensity of gradient saddle coil near the center can be expressed as follows[68]:

$$\mathbf{H}_g = \begin{pmatrix} g_g x & -2.4398 g_g y & 1.4398 g_g z \end{pmatrix}^{\mathsf{T}} \tag{I.9}$$

$$g_g = \cos^{-1}\left(1 - \frac{3}{2a^2}\frac{16}{3\pi}\left(\frac{3}{7}\right)^{\frac{5}{2}}\frac{i_g}{r_g^2}\right) \tag{I.10}$$

where i_g is the current following the gradient saddle coil, r_g is its radius ($r_g = r_b$, in figure I.16), and the value of a equals to 1.2015.

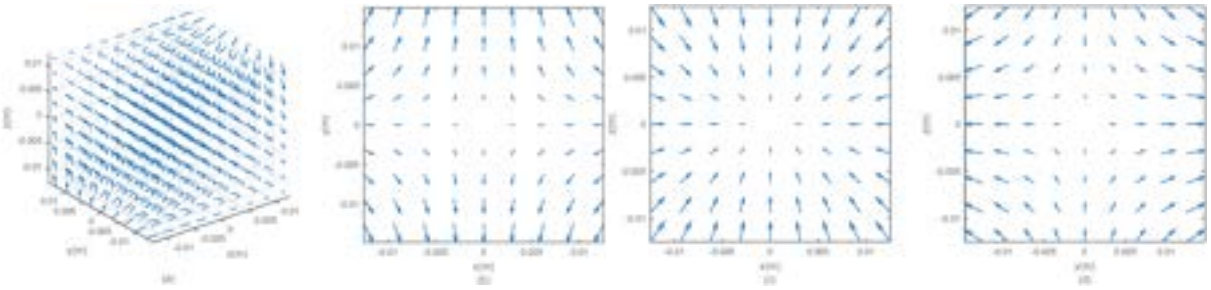

Figure I.19: The magnetic fields for gradient saddle coils: (a) 3D workspace, (b) xy-plane, (c) xz-plane, (d) yz-plane.

The figure I.20a presents the magnetic field produced by the two pairs of Maxwell coils, and the figure I.20b shows the magnetic field induced by one pair of Maxwell coils and one pair of gradient saddle coils as depicted in figure I.26a. Once again, these simulations verify that the magnetic gradient fields $\nabla \mathbf{B}$ of the Maxwell and gradient saddle coils are similar. From these results, it is confirmed that the Maxwell coils and gradient saddle coils both can produce a uniform magnetic gradient in any desired direction once the flowing currents meet the following Eqns. (I.16), (I.17), (I.23) and (I.24).

I.4 Electromagnetic actuation setups

As stated previously, a wide variety of EMA platforms has been proposed by researchers [30], [43], [49], [50], [52]–[79]. We present a brief overview of different EMA setups in the following paragraph. These platforms can be divided into two-dimensional and three-dimensional manipulations. The status of electromagnetic coils could be stationary or mobile.

The functions of designed magnetic platform vary according to the configuration of electromagnets. It is clear that the magnetic field generated by the combination of a Helmholtz coils

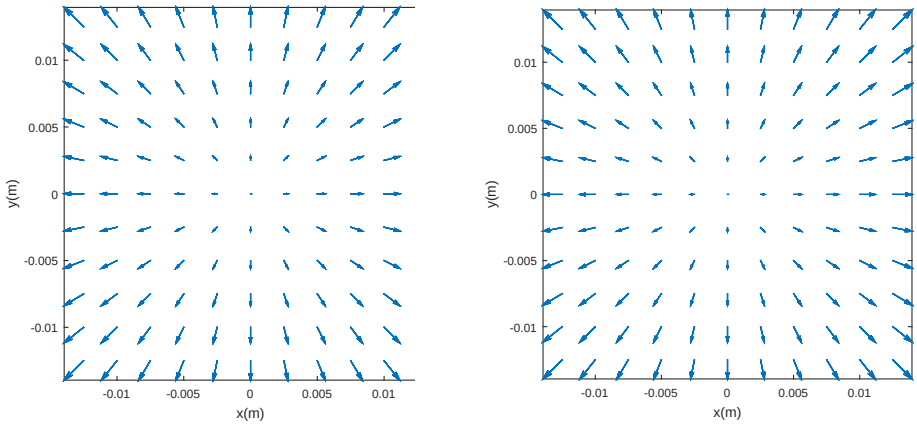

Figure I.20: Simulation of the magnetic gradient field generated by: (a) two pairs of Maxwell coils; and (b) one pair of Maxwell coils and one pair of gradient saddle coils.

pair and a Maxwell coils pair is different from that produced by two Helmholtz coils pairs. Hence, the different configurations of platform composed of different coils pairs will be investigated. To make it easier to name each magnetic platform, we introduce the abbreviation to identify them with the nomenclature provided in table I.1. In this section, various configurations of EMA setups will be discussed.

Table I.1: ElectroMagnetic Actuation system nomenclature

Symbol	Description	Symbol	Description
H	Helmholtz coils	M	Maxwell coils
U	Uniform saddle coils	G	Gradient saddle coils
E	Electromagnet	C	single coil pair
2D	two-dimensions	3D	three-dimensions
r	rotational		

I.4.1 Two-dimensional manipulation

I.4.1.1 Platform HMr

Yesin *et al.* [50] propose a simple EMA system consisting with one Helmholtz and one Maxwell coils pairs. The coils sets are designed to surround the same rotating axis, as shown in figure I.21. Figure I.21a illustrates the schematic diagram of the proposed EMA system. The rotating Helmholtz coils allow aligning the magnetic moment of the microrobot to the desired direction. Maxwell coils are then used to directly translate the microrobot in the aligned direction. Thereby the microrobot is actuated in 2D space thanks to the manipulation plane obtained by rotating a straight line around the axis of rotation.

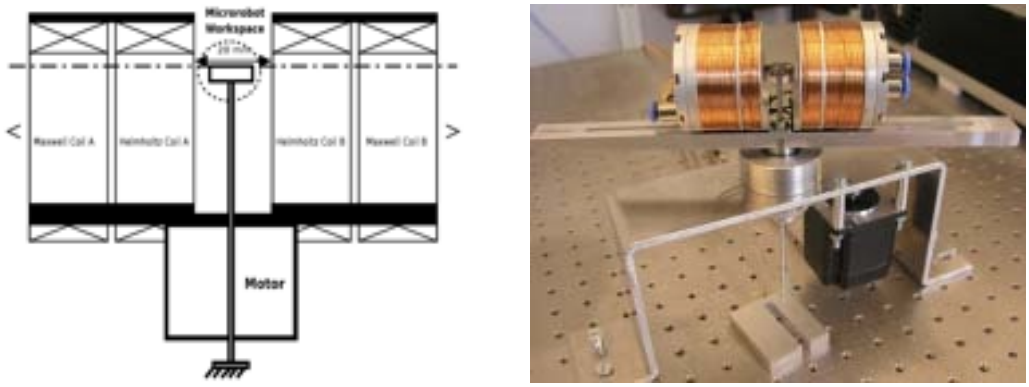

(a) (b)

Figure I.21: HMr EMA platform developed by Yesin *et al.* [50]: (a) scheme of the concept; and (b) a photograph of the magnetic steering system.

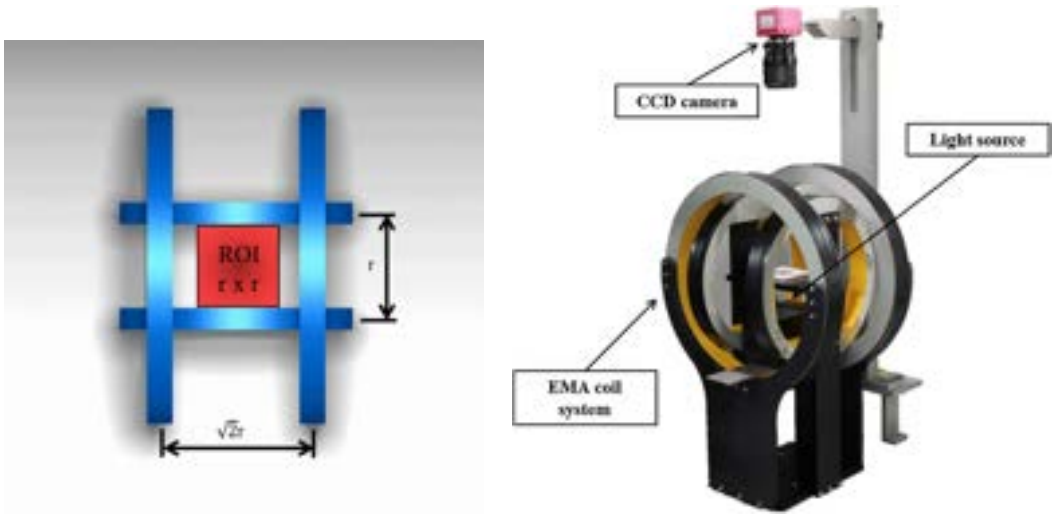

(a) (b)

Figure I.22: 2C EMA platform developed by Park *et al.* [71]: (a) scheme of the concept; and (b) a photograph of the built system.

I.4.1.2 Platform 2C

Go *et al.* [71] propose an EMA system comprising of two stationary pairs of electromagnetic coils to steer microrobot within 2D plane, and is depicted in figure I.22a. The microrobot can be aligned and steered to a desired location by controlling the currents flowing through each electromagnetic coil. With such simple configuration, the proposed EMA system requires less power consumption and smaller volume. After all, to actuate microrobot, the proposed system needs specific control algorithm of the currents through their coils. Thus, the authors demonstrate real time positioning through the magnetic field control of a calibrate field at the edge of the workspace. Thereby, the method allows microrobot move accurately along desired paths with less positioning error.

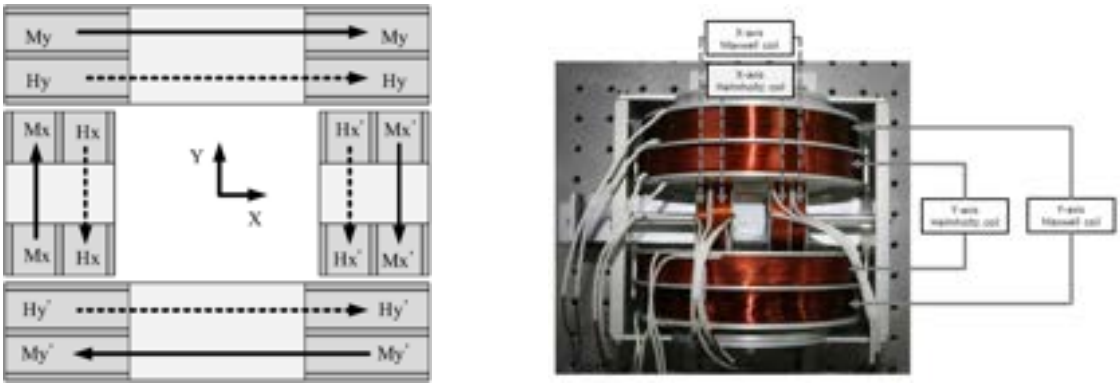

(a) (b)

Figure I.23: 2H2M EMA platform developed by Choi *et al.* [66]: (a) scheme of the concept; and (b) a photograph of the built system.

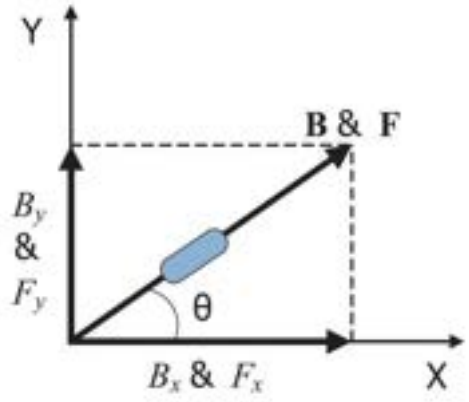

Figure I.24: Schematic diagram of the two-dimensional manipulation of microrobot.

I.4.1.3 Platform 2H2M

Choi *et al.* [66] also use Helmholtz and Maxwell coils. The difference is that they are designed by using four sets of fixed coils, as represented in figure I.23. Two Helmholtz coils are placed perpendicular to each other in the xy-plane. By adjusting the current ratio between the two pairs of Helmholtz coils, a steerable uniform magnetic field can be generated to drive the magnetic moment of microrobots. Two Maxwell coils are also placed perpendicular to each other in the xy-plane. By applying different current ratios between the two pairs of Maxwell coils, the direction of the magnetic force (I.1) can be adjusted.

Specifically, the magnetic torque, $\mathbf{t}_\mathrm{m}$, aligns the magnetic moment of the microrobot to the desired direction defined by the magnetic field. For a given alignment angle as shown in figure I.24, from the relation (I.2), the magnetic torque generated by the two pairs of Helmholtz coils is derived as:

$$t_{m,z} = V_m \left(m_x b_y - m_y b_x\right) \tag{I.11}$$

where m_x and m_y represent the 2D magnetization along the x and y-axis, respectively; b_x and

b_y denote the magnetic field components in the corresponding direction. Magnetic torque value tends to be zero when the microrobot is aligned to desired angle θ (cf. figure I.24). Also, the magnetization of microrobot can be rewritten as $m_x = \boldsymbol{m}\cos\theta$ and $m_y = \boldsymbol{m}\sin\theta$, that is $\|\mathbf{M}\| = \boldsymbol{m}$. Thus, from Eqns. (I.3) and (I.4), the above relation (I.11) is rearranged as:

$$\mu_0\mu_r\boldsymbol{m}\left(\frac{4}{5}\right)^{\frac{3}{2}}\left(\cos\theta\frac{i_y}{r_y} - \sin\theta\frac{i_x}{r_x}\right) = 0 \tag{I.12}$$

$$\frac{i_y}{r_y} = \frac{i_x}{r_x} \tag{I.13}$$

where i_x, i_y, r_x and r_y represent the currents and the radius of coils fixed on the x- and y-axis, respectively. Assuming the radii of all Helmholtz coils are identical, to control the direction θ of the magnetic moment of a microrobot, the currents flowing through the coils should satisfy:

$$\frac{i_x}{i_y} = \tan\theta \tag{I.14}$$

Furthermore, the Maxwell coils fixed in xy plane are used for generating magnetic gradient to propel microrobot, as shown in figure I.24. Similarly, the magnetic force can be derived from Eqns. (I.1), (I.5) and (I.6) as follows:

$$\begin{pmatrix} f_x \\ f_y \end{pmatrix} = \mu_0\mu_r V_m \begin{pmatrix} \boldsymbol{m}\cos\theta\,(g_x - 0.5g_y) \\ \boldsymbol{m}\sin\theta\,(g_y - 0.5g_x) \end{pmatrix} \tag{I.15}$$

Hence, the magnetic microrobot can be moved to the direction θ, when the magnetic force meet the following expression:

$$\frac{f_y}{f_x} = \tan\theta = \frac{\mu_0\mu_r V_m\ \boldsymbol{m}\cos\theta\,(g_y - 0.5g_x)}{\mu_0\mu_r V_m\ \boldsymbol{m}\sin\theta\,(g_x - 0.5g_y)} \tag{I.16}$$

$$g_x = g_y \tag{I.17}$$

Next, considering Eqns. (I.5) and (I.6), the relation of currents flowing through the Maxwell coils can be derived as $i_m = i_x = i_y$. This means the two pairs of Maxwell coils should produce the same magnetic gradient by inputting the same current strength.

I.4.1.4 Platform 2H1M

Choi *et al.* [65] have proposed another stationary EMA system for 2D locomotion of microrobot. The designed EMA system consists of two pairs of Helmholtz coils, and a sole pair of Maxwell coils, that is illustrated in figure I.25. Similarly, the two pairs of Helmholtz coils arranged perpendicularly induce a homogeneous magnetic field that can be aligned to a given direction θ in a 2D xy-plane. The additional pair of Maxwell coils is placed orthogonally to the existing Helmholtz 2D plane. Although the strength of magnetic gradient in xy plane is less than the magnetic gradient along the z-axis, this EMA setup can move microrobot in 2D xy-plan.

For the EMA platform given in [66], magnetic torque is also calculated by Eqns. (I.12) and (I.13). The magnetic force is here computed from one pair of Maxwell coils to provide the actuation force. Assuming the orientation of microrobot is θ set by the magnetic torque shown in figure I.24, the relation between the magnetic force components can be derived from Eqns. (I.1), (I.5) and (I.6) as:

$$\frac{f_y}{f_x} = \tan\theta = \frac{-0.5\mu_0\mu_r V_m\ \boldsymbol{m}\cos\theta g_z}{-0.5\mu_0\mu_r V_m\ \boldsymbol{m}\sin\theta} \tag{I.18}$$

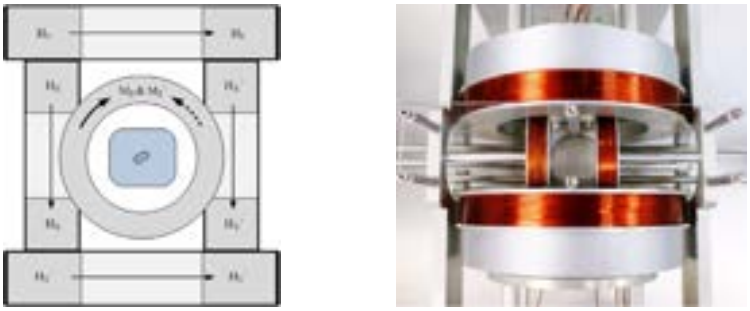

(a) (b)

Figure I.25: 2H1M EMA platform developed by Choi *et al.* [65]: (a) scheme of the concept; and (b) a photograph of the built system.

$$g_x = g_y g_z \tag{I.19}$$

Thereby the magnetic force is steered in the same direction as the orientation of the microrobot. Hence, the considered stationary EMA system can provide a magnetic field to align the microrobot in desired direction, and can also produce the magnetic gradient to propel it in the aligned direction. However, due to the weak magnetic gradient in the workspace, more powerful current suppliers are necessary to control efficiently microrobots.

I.4.1.5 Platform HMUG

Jeon *et al.* [63] have developed a stationary EMA system composed of one pair of conventional Helmholtz and Maxwell coils, and one pair of uniform and gradient saddle coils as represented in figure I.26. The proposed EMA system is capable of controlling the 2D locomotion of magnetic microrobot. The geometric shape of saddle coils also brings the convenience for manipulation, and especially allows increasing the accessibility to the workspace. Authors point out that the proposed system is geometrically compact to allow a patient to lie down and magnetically efficient compared with the conventional coils which has two pairs of Maxwell and Helmholtz coils.

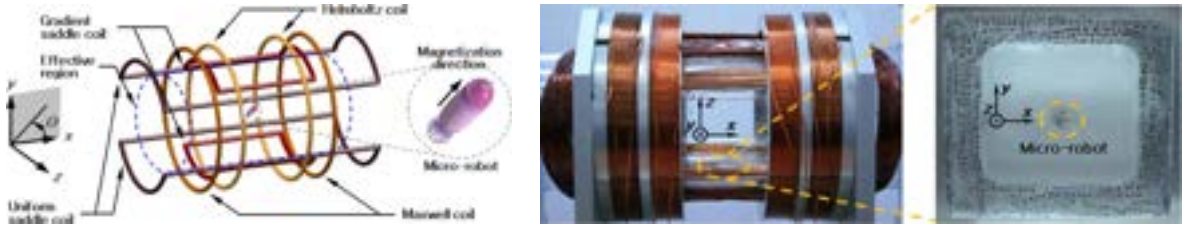

(a) (b)

Figure I.26: HMUG EMA platform developed by Jeon *et al.* [63]: (a) scheme of the concept; and (b) a photograph of the built system.

Once again, the uniform and gradient saddle coils play the same functions of Helmholtz coil and Maxwell coil. Thus, the desired uniform magnetic field is produced by the pairs of Helmholtz and uniform saddle coils to generate magnetic torque aligning the orientation of microrobot in

the xy-plane. The magnetic field generated can be derived from Eqns. (I.3), (I.5), (I.7) and (I.9) as follows:

$$\mathbf{B} = \mu_0 \mu_r \begin{pmatrix} d_h + (g_g + g_m)\, x \\ d_u - (2.4398 g_{gs} + 0.5 g_m)\, y \\ (1.4398 g_g - 0.5 g_m)\, z \end{pmatrix} \tag{I.20}$$

Since the uniform magnetic field exists only in the xy-plane, the microrobot is rotated within xy-plane. The currents of Helmholtz coils and uniform saddle coils should satisfy the following requirements to produce desired magnetic torque:

$$\frac{b_x}{b_y} = \frac{\mu_0 \mu_r d_h}{\mu_0 \mu_r d_u} \tan\theta \tag{I.21}$$

$$i_u = 1.1917 \tan\theta \frac{r_{us}}{r_h} i_h \tag{I.22}$$

Assuming that the orientation of the microrobot is controlled to be aligned at the angle θ as shown in figure I.24, the magnetic gradient is then induced by the pairs of Maxwell and gradient saddle coils to steer the magnetic microrobot along this direction. The currents flowing through the Maxwell and gradient saddle coils are required to satisfy the following relations:

$$\frac{f_y}{f_x} = \frac{\mu_0 \mu_r V_m\, \boldsymbol{m} \sin\theta\, (-2.4398 g_g - 0.5 g_m)}{\mu_0 \mu_r V_m\, \boldsymbol{m} \cos\theta\, (g_g + g_m)} = \tan\theta \tag{I.23}$$

$$i_m = -1.1751 \left(\frac{r_m}{r_g}\right)^2 i_g \tag{I.24}$$

Obviously, the magnetic force on microrobot is always in the direction of magnetization with a constant magnitude regardless of its direction when currents meet Eq. (I.24). Therefore, this EMA system can provide pointing and positioning control of microrobot.

I.4.2 Three-dimensional manipulation

In this section, we discuss the different EMA systems designed for 3D motion. Classically, 3D trajectory of a microrobot can be obtained by direct 3D manipulation control [75], or rotating the 2D manipulation plane [62], [68].

I.4.2.1 Platform 3DMH

In [75] authors present an EMA system composed of three sets of electromagnets, as shown in figure I.27a. The three pairs of coils are placed perpendicularly to generate the magnetic field in the three directions of Cartesian coordinate system. Accordingly, the setup can produce an oriented 3D magnetic gradient field to directly 3D manipulate microrobot. Similarly, the three sets of coils can also provide propulsion force to move the microrobot by the proper control of their currents. Hence, by the combination of Helmholtz and Maxwell coils in each set, the proposed EMA system can provide a simple approach for the 3D actuation of the microrobot in low fabrication cost, that is represented in figure I.27b. The authors report that this EMA platform could generate the necessary magnetic field and gradient to perform suitable control of a microrobot on a defined trajectory [75].

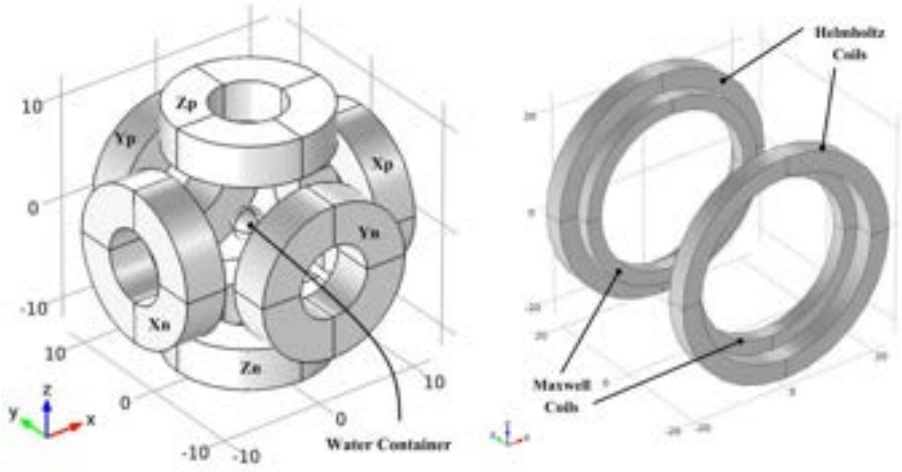

(a) (b)

Figure I.27: 3DMH EMA platform developed by Dadkhah *et al.* [75]: (a) representation of the concept; and (b) the design of a set of electromagnets for a given axis that combines a pair of Helmholtz and Maxwell coils.

I.4.2.2 Platform 2H2Mr

It is also possible to simply obtain 3D motion control by moving the stationary 2D manipulation plane. For instance, Jeong *et al.* [62] propose an EMA system for 3D locomotion of intravascular microrobot by the controlling the rotational plane. The considered system is composed of a stationary Helmholtz–Maxwell coil pairs and a rotational Helmholtz–Maxwell coil pairs, as shown in figure I.28a. Two pairs of the Helmholtz coils align the microrobot to the desired direction, and two pairs of the Maxwell coils steer the microrobot on the aligned direction. Figure I.28a shows the stationary Helmholtz–Maxwell coils located in the x-axis, and the other rotational Helmholtz–Maxwell coils that are set along the x-axis. Moreover, the stationary coils pairs are arranged inside the rotational coils pairs. Thus, in the workspace, when a microrobot is not aligned in the desired direction, the two pair of Helmholtz coils generate a uniform magnetic field to align the microrobot in the desired orientation. The magnetic torque can be then calculated from Eqns. (I.2) and (I.11). The magnetic torque becomes zero until the microrobot is aligned in the given direction. Specifically, the currents flowing through the Helmholtz coils have to meet Eq. (I.13) to allow aligning the microrobot in the desired direction. The uniform gradient magnetic field generated by the two pairs of Maxwell coils induces the propulsion force to propel the microrobot. As shown in figure I.28a, the rotational Maxwell coil pairs behave similarly to the rotational Helmholtz coil pairs. Thus, the microrobot can be rotated and translated in the same manipulation plane. The ratio of the stationary and rotational components of the magnetic force should match the Eqns. (I.16) and (I.17) to steer the microrobot in the aligned direction.

In particular, when a microrobot has to be aligned and propelled to the angle α (see also figure I.29), the ratio between the x-axis and the y-axis components of the magnetic fields generated by the Helmholtz coils should be equal to $\tan(\alpha)$. Besides, the magnetic field generated by the Maxwell pairs should be same strength when the influence of gravity is not considered. Though the microrobot is actuated in 2D plane, the 2D manipulation plane can be expanded

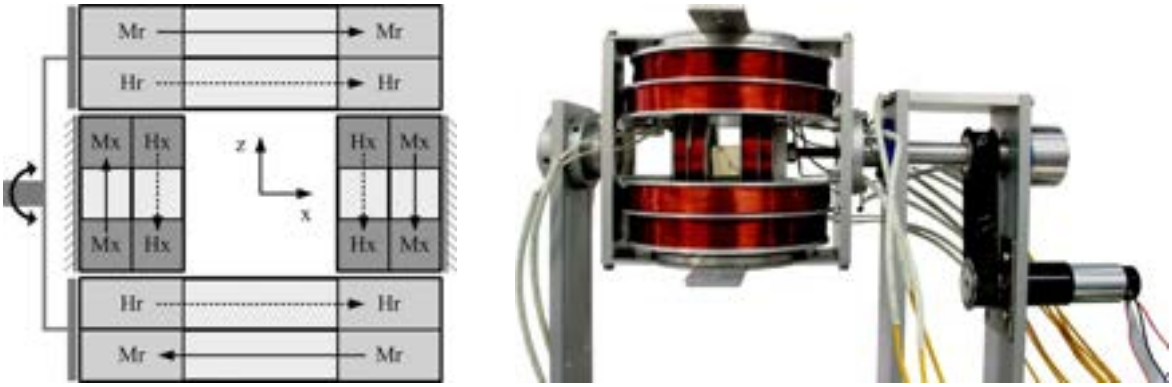

(a) (b)

Figure I.28: 2H2Mr EMA platform developed by Jeong *et al.* [62]: (a) scheme of the concept; and (b) a photograph of the built system.

to 3D space by rotating determined plane by rotational coils pairs revolving about the x-axis. Therefore, the considered EMA system can achieved 3D manipulation.

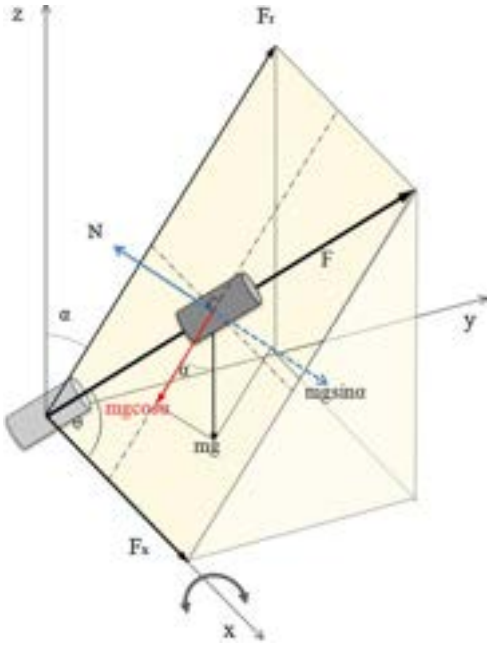

Figure I.29: Schematic principle of the 3D locomotion of magnetic microrobot.

When the object gravity reaches a sufficient magnitude, the gravity factor should be considered. Based on the rotational angle α as shown in figure I.29, the gravitational force can be divided into a normal ($Mg\sin\alpha$) and a tangential ($Mg\cos\alpha$) components. The normal component is an offset by the supporting force N from platform as represented in figure I.29. The left component of gravity is superimposed accordingly to the applied magnetic force. Hence, the currents flowing through the Maxwell coils should be regulated to generate a proper magnetic gradient that can compensate the gravity force of microrobot. The x-r plane is the actuation surface of

the microrobot. Besides, f_x and f_r indicate the magnetic force generated by the stationary coil pairs and the rotational coil pairs respectively, as illustrated in figure I.29. The relation Eq. (I.16) should be modified to compensate additional gravity force. For a given rotational angle α of manipulation plane, the relation of magnetic force components and gravitational force components are rearranged as:

$$\frac{f_r - M\mathrm{g}\cos\alpha}{f_x} = \tan\theta = \frac{\mu_0\mu_r V_m \ \boldsymbol{m}\sin\theta\,(g_r - 0.5g_x) - M\mathrm{g}\cos\alpha}{\mu_0\mu_r V_m \ \boldsymbol{m}\cos\theta\,(g_x - 0.5g_y)} \tag{I.25}$$

$$g_r = g_x + \frac{2M\mathrm{g}\cos\alpha}{3V_m \ \boldsymbol{m}\sin\theta} \tag{I.26}$$

Hence, the relation of the currents flowing through the stationary and rotational coils is derived as:

$$i_r = i_x\frac{r_r^2}{r_x^2} + 1.04\frac{r_r^2 \ M\mathrm{g}\cos\alpha}{V_m \ \boldsymbol{m}\sin\theta} \tag{I.27}$$

where the g denotes gravitational acceleration, and M represents the mass of the microrobot. Therefore, the microrobot can be propelled along the direction with the angle θ on the manipulation plane that is rotated to angle α. Obviously, Eq. (I.26) becomes Eq. (I.24) when the angle equals to $\alpha = 90°$.

I.4.2.3 Platform HMUGr

Generally, the EMA system constructed from Helmholtz and Maxwell coils takes up a large space. In order to get a smaller volume of actuation system and less consumption of driving energy, in [63], [68] the authors have developed an EMA system based on uniform and gradient saddle coils for the 3D locomotion of a microrobot. As stated, the uniform and gradient saddle coils perform the same function as Helmholtz and Maxwell coils, respectively. Thus, referring to structure given in [68], the pair of Maxwell-Helmholtz coils and the pair of the uniform-gradient saddle coils are perpendicularly fixed (see also figure I.30a), and the arranged configuration can thereby realize 2D locomotion of a microrobot.

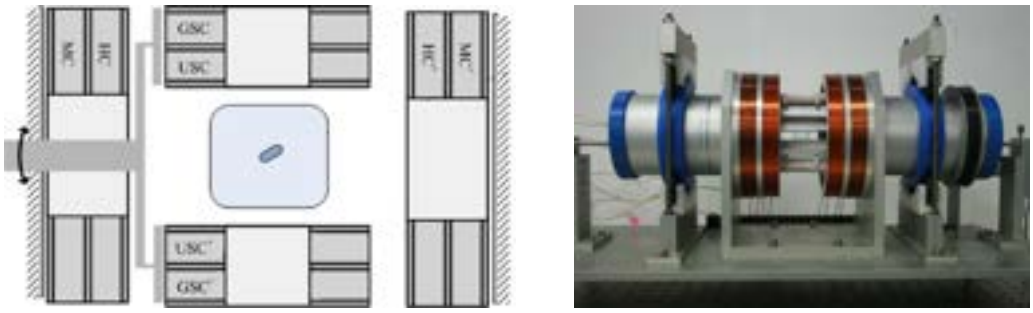

(a) (b)

Figure I.30: HMUGr EMA platform developed by Choi *et al.* [68]: (a) scheme of the concept; and (b) a photograph of the built system.

Similarly, the designed EMA system expands 2D to 3D actuation by rotating saddle coil pairs instead of conventional Helmholtz–Maxwell coil pairs rather than the previous 2H2Mr platform

developed by Jeong *et al.* [62]. With such structure of rotating saddle coils, the considered system provides a more flexible and accessible workspace. In the figure I.30a, the 2D control of orientation of microrobot is realized by using one pair of Helmholtz coils fixed along x-axis, and one pair of uniform saddle coils placed around the x-axis. Assuming the applied magnetic field aligning at angle β, the currents flowing through the coils should satisfy the condition given by Eq. (I.22). Once the microrobot is aligned along the angle β, the pairs of Maxwell and gradient saddle coils produce the necessary propulsion force owing to the induced magnetic gradient. For a given propulsion direction, the relation of the current applied to the Maxwell and gradient saddle coils has to satisfy Eq. (I.24).

Once again, the 3D locomotion of the microrobot can be achieved by the rotational 2D actuation mechanism, and the desired actuation plane is determined by the pairs of rotational saddle coils. In case of significant gravitational force exerted on the microrobot, the HMUGr EMA setup has to generate the necessary magnetic gradient field in the weight. When an arbitrary rotational angle α is given, as illustrated in figure I.29, only the tangential component ($M\mathrm{g}\cos\alpha$) of the gravitational force needs to be compensated by magnetic force due to the reaction force already offsetting the normal component ($M\mathrm{g}\sin\alpha$). The applied magnetic gradient field should then induce a propulsion force to satisfy an equilibrium of all components. Thereby, Eq. (I.23) can be rewritten as:

$$\frac{f_r - M\mathrm{g}\cos\alpha}{f_x} = \tan\theta = \frac{\mu_0\mu_r V_m\ \boldsymbol{m}\sin\theta\,(-2.4398g_r - 0.5g_x) - M\mathrm{g}\cos\alpha}{\mu_0\mu_r V_m\ \boldsymbol{m}\cos\theta\,(g_x + g_y)} \tag{I.28}$$

$$g_r = -\frac{M\mathrm{g}\cos\alpha}{3.4398V_m\ \boldsymbol{m}\sin\theta} - 0.4361g_x \tag{I.29}$$

where the f_r is generated by the gradient saddle coil pairs and the g_r is produced by the Maxwell coil pairs. Thus, the relation of the inputting currents flowing through the saddle coils and Maxwell coils can be precomputed from Eq. (I.29) as follows:

$$i_r = -1.37i_x\frac{r_r^2}{r_x^2} - \frac{r_r^2 M\mathrm{g}\cos\alpha}{0.7028V_m\ \boldsymbol{m}\sin\theta} \tag{I.30}$$

It is reported in [63], [68], [132] that the system with structure of saddle coil allows less power consumption with a more compact setup. Moreover, such structures are suitable for the actuation of medical microrobot *in vivo*.

I.4.2.4 Platform H2US-MUG

Jeon *et al.* [64] have proposed an EMA system composed of one pair of Helmholtz coils, two pairs of uniform saddle coils, one pair of Maxwell coils and one pair of gradient saddle coils, that is illustrated in figure I.31. The Maxwell and gradient saddle coils pairs are nested into other coils. Authors demonstrate that their EMA system can perform helical and translational motions of a microrobot in several organs of the human body such as the central nervous system, the urinary system, the eye and blood vessel. The EMA setup is able to generate rotating magnetic fields thanks to the Helmholtz and uniform saddle coils for the helical motion of the microrobot; and can also provide uniform magnetic gradient field to pull the microrobot along the axial direction, thanks to the Maxwell and gradient saddle coils pairs. Thus, the considered EMA system can provide the sufficiently precise corkscrew motions to a spiral-type microrobot using a precalculated range of rotating frequency of magnetic field. Moreover, transverse movement

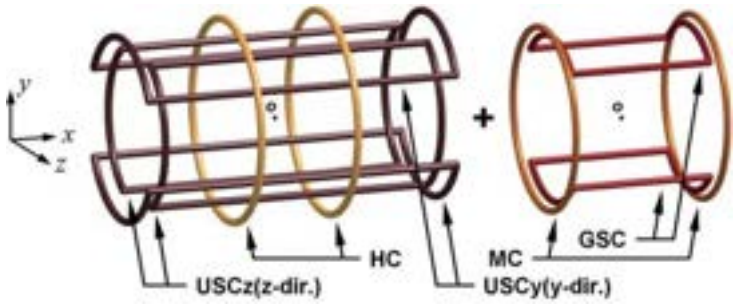

Figure I.31: Schematic diagram of the investigated H2US-MUG EMA system developed by Jeon *et al.* [64].

of the microrobot along the axial direction is produced by magnetic gradient in the workspace, which can apply for several organs of human body such as the urinary system, the eye or the nervous system.

I.4.2.5 Platform 3DH

Mahoney *et al.* [118] have developed an EMA system consisting of three nested Helmholtz coil pairs, as illustrated in figure I.32. The three pairs of Helmholtz coils are arranged perpendicularly to allow generating an uniform magnetic field whose orientation can be controlled in the 3D workspace. The authors have also proposed an open-loop algorithm for velocity control with gravity compensation for helical microrobot. To steer the microswimmer, the 3D rotating magnetic field is generated by each pair of Helmholtz coils in the workspace. Assuming the microswimmer always rotating in synchronization with the applied field, the central axis of the microswimmer is asymptotically converging on the rotation axis of the magnetic field. The desired velocity of the microrobot is provided with a precalculated frequency of the rotating magnetic field. Thus, such EMA configuration can be used to actuate remotely the medical microrobot for performing tasks, such as targeted therapy, tissue removal and remote sensing, by controlling its orientation and rotation speed intuitively, especially in low-Reynolds-number environment.

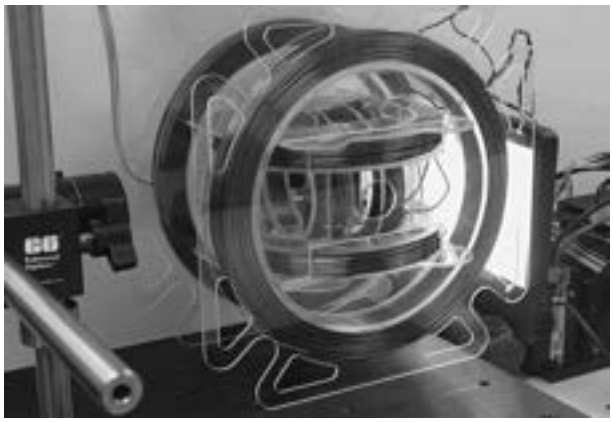

Figure I.32: Photograph of the 3DH EMA setup developed by Mahoney *et al.* [118].

I.4.3 Independent control of multiple microrobots

Classically, only a single microrobot can be controlled with most of the proposed 2D and 3D EMA platforms. This leads to an important limitation to enable the control of multiple microrobots simultaneously. To overcome this constraints, some dedicated EMA systems for magnetic manipulation of microparticles have been investigated [73], [133]–[137].

I.4.3.1 2D independent manipulation

For 2D independent operations, there are two main methods that can achieve the independent control of multiple microrobots: i) localized selective trapping [133]; and ii) design by using heterogeneous microrobots [134]–[136].

Platform 3H2M

Go *et al.* [134], [135] have investigated an EMA system with three stationary pairs of Helmholtz coils on each direction, and two stationary pairs of Maxwell coils fixed on xy plane as shown in figure I.33. For selective control of the microrobots, the authors have used the thermally responsive microclampers that are composed of pNIPAm hydrogel[5]. For the selective activation of microclampers, microheater with electrode arrays was introduced.

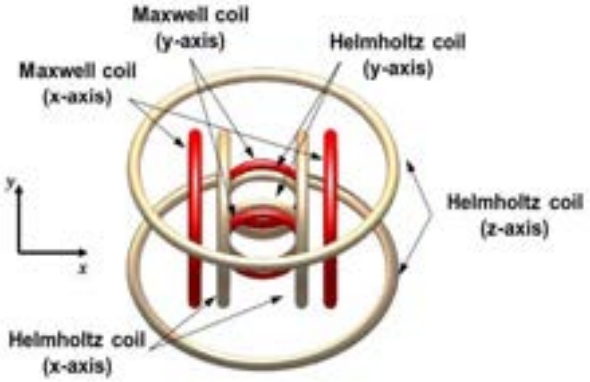

Figure I.33: Schematic configuration of EMA system coils developed proposed by Park *et al.* [134].

Platform 6E

Diller *et al.* [73], [136], [137] have proposed a method to control multiple untethered magnetic microrobots using an EMA system consisting of six independent air-core electromagnetic coils. Actuated by the applied external magnetic field, multiple microrobots are steered to arbitrary goal positions, and limited path following is also achievable. Hence, the proposed EMA system has the potential to control independently the locomotion of multiple microrobots for different manipulation tasks.

I.4.3.2 3D independent manipulation

However, the limitation of the control on 2D surface remains a significant limitation, especially in medical applications, such as cell manipulation, drug delivery, tissue assembly. Commonly,

[5]pNIPAm is the abbreviation of poly-N-isopropylacrylamide, which is a temperature-responsive polymer.

magnetic microrobot can be manipulated in a 3D workspace by the two following methods: i) tail rotation to provide swimming motion, and ii) propelling by magnetic gradient directly [73], [137]. For microswimmer, the generation of forward thrust is produced by a magnetic torque spinning an asymmetric structure such as a helix [32], [113]. For translational movement, the magnetic gradient directly induces the net propulsive force on microrobots that can achieve the motion with three translational DOF [60], [138]–[140]. However these methods have also not been used to achieve independent positioning of multiple microrobots. The main difficulty of control multiple microrobots is typically due to the uniformity of the magnetic field and gradient in the workspace. Thereby, all microrobots receive identical control signal. For independently controlling each microrobot, in [73], [137] the authors report that the heterogeneous microrobot designs are the most viable way to perform independent control in a 3D workspace. Motion differentiation is then accomplished through the use of geometrically or magnetically distinct microrobots which behave different magnetization direction in a rotating or oscillating magnetic field [137]. Besides, if each microrobot is processed by a different magnetic strength or rotational fluid drag coefficient, arbitrary forces could also be exerted independently and simultaneously on each microrobot [73].

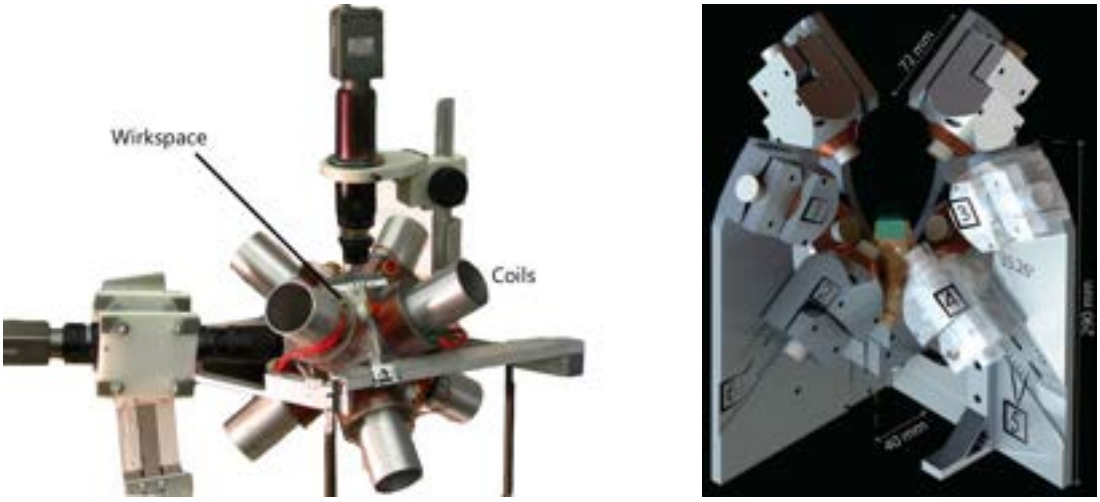

(a) (b)

Figure I.34: EMA platform developed with independent control: (a) a photograph of the EMA system comprising of eight electromagnetic coils [73]; and (b) a photograph of the nine-coils EMA system [141].

Platform 8E

Base on these considerations, an EMA system including eight independent iron-core electromagnetic coils has been developed [73]. Figure I.34a illustrates the proposed setup, where the iron-core electromagnets are all pointing to the common workspace center. The 3D motions of microrobots are directly actuated using magnetic gradient generated by the eight completely independent coils. The differentiation of magnetic forces applied to each microrobot is accomplished by inducing the unique viscous drag on each microrobot when placed in a rotating magnetic field. The different rotational responses result in the different orientations of microrobots, and thence the forces are generated in different directions. Therefore, the proposed EMA system allows for

different magnetic forces to be exerted on the microrobots, that is capable of enabling independent remote control and path following of multiple microrobots along arbitrary 3D trajectories. The proposed EMA system of multiple microrobot control and strategy can be used to expand the microrobot techniques for clinical manipulation, drug delivery, remote sensing and localized therapy in microfluidic channels or in the human body.

Platform 9E

Ongaro *et al.* [141] have investigated the design of an EMA system composed of nine electromagnetic coils that is capable of independently controlling identical and nonidentical microrobots in the 3D workspace, and named BatMag as illustrated in figure I.34b. The independent control is achieved by exploiting the inhomogeneity of the strong fields that the system can generate. The control strategy for independent 6 DOFs control of microrobots has been tested and evaluated. Also, a thermal management technique is developed and quantitatively analyzed to prevent overheating during continuous operation. In fact, the Joule heat occurred by large input current flowing the coil is an important safety factor for EMA setups. This nine-coil EMA system with independent control could be used for precise collaborative tasks in MIS field, microassembly, micromanipulation, tissue engineering, and labon-a-chip applications.

I.4.4 Discussions

From the various developed magnetic setups, the uniform magnetic field can be generated by Helmholtz coils pair and the uniform saddle coils pair, while the uniform gradient can be produced by Maxwell coils pair and the gradient saddle coils pair with the different settings, respectively. The such electromagnetic coils form the EMA system with different desired functions. The four stationary coils pairs, such as two pairs of Helmholtz coils and two pairs of Maxwell coils, can control a magnetic microrobot in 2D workspace. The same function of control is also achieved by the four pairs of saddle coils or combination of four coils pairs with the correct configuration. Meanwhile, only two rotating coils pairs can control the 2D motion of microrobot. The one rotating Helmholtz and one rotating Maxwell coils pairs can contribute a 2D position and orientation control. Similarly, the two rotating saddle coils pairs also can provide the same control with a suitable setting. When the workspace is expanded to the 3D, at least six stationary independent electromagnetic coils are required. If the coils pair is able to be rotated, the number of coils pair could be reduced. For instance, two pairs of Helmholtz coils and two pairs of Maxwell coils can actuate 3D locomotion of microrobot where one Helmholtz coils pair and one Maxwell coils pair are rotatable along a same axis for rotating 2D manipulation plane into 3D workspace. When an electromagnetic coil is used to generate both magnetic field and gradient by adjusting the current, the number of stationary coils pairs can be further reduced to three pairs. In addition, the number and type of coils also depends on the manipulated microrobot. The motion of the microswimmer only requires three pairs of coils that generate uniform magnetic field throughout the 3D workspace.

The independent manipulation of multiple microrobots has been also investigated. It requires either complicated control strategy or special design of the microrobots. Such as, the eight independent electromagnetic coils are responsible for generating the common magnetic gradient to propel the multiple microrobots in the workspace. With the unique viscous drag due to the specific microrobots, their responses are independent to obtain their control. Basically, the electromagnetic actuation system is useful for various manipulation tasks with different

configurations of electromagnetic coils under adjustable current input and efficient control strategy.

I.5 Thesis Objective

Here, we have provided a comprehensive review of the current advances of biomedical microrobot in MIS and a comparison of various EMA systems developed by many researchers. One of the highest potential scientific and societal impact of the untethered microrobot would be the health-care and bio-engineering applications. As the robot size is decreasing to the micro or nano-scale, previously inaccessible body locations would become available for high-resolution *in situ* and *in vivo* operations. Such remotely access will enable an extensive range of MIS operations. To this aim, the untethered microrobot would be wirelessly manipulated by magnetic torque and force induced thanks to an EMA system. To precisely manipulate the biomedical microrobot, a key issue still relies on the design of a suitable EMA platform.

This PhD thesis is devoted to the study of the design of appropriate magnetic microrobotic platform to provide more effective magnetic field and gradient on the microrobot for performing the given medical tasks. Magnetic particles are administered systemically into the blood stream, and external magnets are meant to capture and collect them to a desired target. A first question is whether the applied magnetic field is sufficient to hold particles against blood flow at the target region. The basic idea of our concept, simply depicted in figure I.1, consists of several mobile electromagnets actuated by a robotic system so that they can move around the patient and stay close to the working area. Hence, it keeps full dexterity by making use of electromagnets while reducing energy consumption by a nearer manipulation. Moreover, the robotic system, yet to be properly designed, can be made lighter and less bulky than the existing prototypes, in order to be intrinsically safe to the patient.

Many current EMA systems are composed of electromagnetic coils that can generate the controllable and flexible magnetic field and gradient. To allow the sufficient electromagnetic field, electromagnets with a soft-magnetic core would be preferred in this thesis. For a specific application, the researcher commonly fixes the electromagnets around the workspace, that can control the magnetic field and gradient by the currents flowing through the coils. To the best of current knowledge, the magnetic torque or force may not be controlled at some locations of workspace. Thus, such singular cases should be investigated. A magnetic microrobotic platform with the less singularity lead to an effective and complete control of the microrobot. The singular cases can be pre-evaluated by a mathematical analysis of the simulated electromagnetic field. However, the existing singularity cannot be removed with a fixed arrangement of electromagnets. Intuitively, with a fixed configuration, an EMA system cannot always provide the most efficient and strong magnetic field and gradient simultaneously. Conversely, mobile magnets actuated by a robotic system can obviously move around the target to improve the dexterity of microrobot control [56]. The robotic system is able to change the local magnetic field distribution by modifying the position and/or orientation of the magnets, and then remove some existing singularity. Furthermore, the robotized coils also reduce the energy demand since the magnetic sources usually remain close to the microrobot. Therefore, a novel robotized EMA system called OctoRob is designed in this PhD thesis work for various advanced MIS applications.

The proposed robotic OctoRob system would integrate stationary and mobile electromagnets that can apply a combination of force and torque to the untethered magnetic microrobot. However, to achieve this goal, some key issues must be addressed. Basically, prior to designing an EMA platform, for the given application, designer should consider the following questions:

- How many number of electromagnets should be used in the EMA setup?

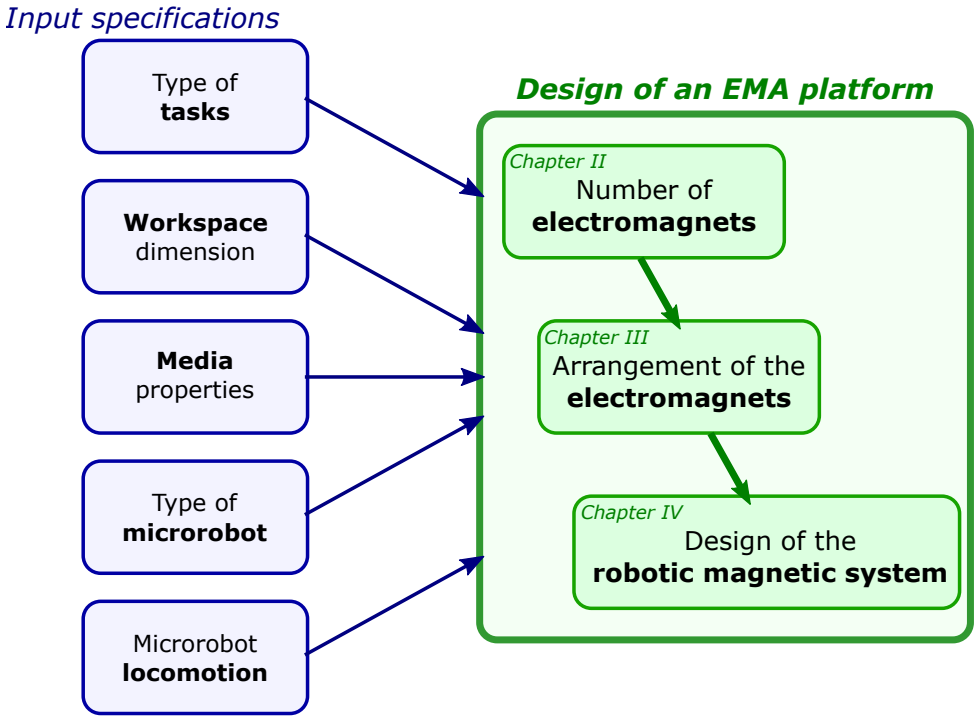

Figure I.35: Illustration of the design process of an EMA system.

- Which kind of electromagnet is suitable for generating the desired magnetic field and gradient?
- Which arrangement or configuration is most efficient for the motion control of the microrobot?
- How many degree of mobility could be added, and how far the electromagnet can be moved in platform? etc.

Commonly, such design parameters are determined by the specifications of the biomedical applications. Figure I.35 shows an overview of the design process of an EMA system allowing fulfilling the mentioned objectives. From the given requirements of the application, the main elements of the specifications are i) the dimensions of the workspace, ii) the environment properties, iii) the considered microrobot, iv) the tasks to be performed, and v) the motions achieved by the microrobot. The desired EMA platform could be designed easily when the number of electromagnetic coils, the size and shape of electromagnets, and arrangement of coils are determined. Therefore, the way to obtain these important design elements of the EMA system according to the given specifications is the principal work of this PhD thesis and would be discussed in the following chapters. As illustrated in figure I.1(A), the magnetic field and gradient on the 2D surface generated by flat-arrangement EMA system are appropriate for the surface or skin operations. For deeper surgical treatment, the EMA system can be utilized to control the medical microrobot to operate on members (e.g. arms, legs) for targeted therapy. This allows increasing the concentration of drugs in the part to be treated and reduces the impact on other parts of the body, that makes treatment more effective and minimize side effects. Therefore, the EMA system could be design to surround the desired workspace as represented in

figure I.1(B) since the applied part could be placed through the setup. Once again, with the requirements of a specific intraocular application, since the magnetic field with a safe intensity is arduous to launch deep into the body tissue providing enough magnetic field and gradient, the coils generating magnetic field placed behind the head would be futile for the eye operation. Hence, the applied coils are all arranged around the eye in the front of head. It is clear that the various EMA systems are utilized for the pertinent biomedical applications in order to perform efficiently their functions.

The investigation of the design of an EMA system is organized as follows. Chapter II presents the theoretical foundation of electromagnetism including the basic principles and necessary equations. From this basis, the electromagnetic manipulation of the untethered microrobot including the magnetic torque and force control is discussed. Moreover, the analysis of the minimum number of electromagnets for an EMA platform is investigated. In particular, singular cases are pointed out when magnetic field and gradient exhibit some linear dependencies. A complete diagram of the specifications for design of an EMA system is provided, where the design specifications for different requirements have been summarized. Chapter III includes the modeling, simulations, comparison and optimization of various arrangements of electromagnetic coils. The different multiple electromagnets configurations are investigated with the defined performance metrics, and the potentially efficient configuration of electromagnets for the selected MIS application is proposed. In chapter IV demonstrates the design of the implemented OctoRob setup that is a specific EMA system for ophthalmic MIS. On the basis of the above proposed investigation, the number of electromagnets and their favorable configuration are clear. Moreover, the type of electromagnet, the optimal rotation angle and the placed position are estimated referring the considered medical application. The overall prototype of the OctoRob EMA system is considered and proposed. The conclusion are thereby presented in the end of the thesis. Since the designed OctoRob EMA platform has been built in our laboratory, the validation of system design and control strategy will be performed in the future. Though the built setup is designed for ophthalmic surgery, the investigation of electromagnet arrangement and control strategy has general validity for the manipulation of microrobot.

Chapter II

Mathematical foundation of Electromagnetic Actuation System

Chapter contents

Introduction

Several promising manipulation systems based on magnetic control have been investigated recently [43], [49], [50], [58]–[79]. Different controls of magnetic field lead to various dynamical movements of microrobots: pulling by magnetic gradient, stick-slip motion by oscillating magnetic field, rolling by rotating magnetic field [79], [142]–[145]. In any of these types of locomotion, the microrobot is dynamically controlled by magnetic torque and force. The torque and force are directly produced through the applied electromagnetic field and its gradient. Hence, the induced magnetic field and its gradient in a desired workspace should be fully modeled and estimated during the EMA system design phase. Especially, the required number of electromagnets should be determined with respect to the application objectives and specifications.

To this aim, firstly, the theoretical foundation of electromagnetism is presented. Electromagnetism is one of the four fundamental interactions in nature. There are numerous mathematical descriptions of electromagnetic field. In Faraday's law, magnetic fields are related to electromagnetic induction and magnetism. The Maxwell's equations describe how electric and magnetic fields are generated and altered by each other and by charges and currents. For analyzing the magnetic field of electromagnet, we use the magnetic dipole to model with the unit-current contribution mapping the electromagnetic coil. Thus, the point-dipole model is proposed. Secondly, the magnetic field and gradient induce the torque and force respectively that control the motion of the magnetic microrobot. The matrices of magnetic torque and force are thereby computed. Thirdly, the minimum number of electromagnets is mathematically analyzed. The number of electromagnetic field and gradient inputs is investigated for different types of motion controls. For reducing the number of inputs, the linear relationships between the field and gradient are analyzed. However, singular cases occur in some linear dependencies that will be estimated in the following sections. Thus, these linear cases for singularities should be avoided. Finally, the minimum numbers of electromagnets of various EMA systems with the required DOFs control are summarized. Also, the suggested design process is illustrated with respect to the application specifications.

II.1 Theoretical foundation of electromagnetism

The aim of this section is to recall the basic principles of electromagnetism that serve as a foundation of our research works.

II.1.1 Maxwell's equations

Maxwell's equations govern the interaction of charged matter, and the behavior of electromagnetic fields. The equations describe how electric and magnetic fields are generated by charges, currents and changes of the fields, which provide a mathematical model for electric, optical and radio technologies. The Maxwell's equations in the time domain are expressed in following differential forms:

$$\nabla \times \mathbf{H} = \mathbf{J} + \frac{\partial \mathbf{D}}{\partial t} \tag{II.1}$$

$$\nabla \cdot \mathbf{B} = 0 \tag{II.2}$$

$$\nabla \times \mathbf{E} = -\frac{\partial \mathbf{B}}{\partial t} \tag{II.3}$$

$$\nabla \cdot \mathbf{D} = \rho \tag{II.4}$$

where $\mathbf{H}$ and $\mathbf{B}$ represent the magnetic parts with the magnetic field strength and magnetic field flux density, respectively; the electric part is described by $\mathbf{E}$ and $\mathbf{D}$ which are referred as electric field strength and electric flux density; $\mathbf{J}$ denotes the current density and ρ specifies the charge density (source charges and free charges in a conducting medium).

II.1.1.1 The magnetic field

For many applications, we can determine the magnetic fields directly from the electromagnetic field equations in the context of magnetostatics where the currents are steady. As illustrated in the figure II.1a, from the Ampere's law Eq. (II.1), the magnetic field is generated outside an infinity long wire carrying a current density $\mathbf{J}$, that can be expressed as:

$$\mathbf{H}_{\varphi}(r) = \frac{\mathbf{i}}{2\pi r} \tag{II.5}$$

where $\mathbf{H}_{\varphi}(r)$ indicates the magnetic field magnitude at a fixed radial position r in the φ direction, and $\mathbf{i} = \mathbf{J}\pi R^2$ is the current in this wire. As $\mathbf{B} = \mu_0 \mathbf{H}$ in free space, the magnetic field can be rewritten as:

$$\mathbf{B}_{\varphi}(r) = \frac{\mu_0 \mathbf{i}}{2\pi r}. \tag{II.6}$$

This consideration can be extended to a long cylindrical coil with N turns and with its axis along the z-axis as shown in figure II.1b, where the $\mathbf{i}$ and L denote the passing current and length of the coil, respectively. Considering a rectangular path with one side of length S along the axis of the coil and the other parallel side just outside the coil, we obtain:

$$\oint_{\text{coil}} \mathbf{H} \cdot dL = N \frac{S}{L} \mathbf{i} \tag{II.7}$$

where the right side of equation is the total current passing through the rectangle. Moreover, the magnetic field equation can be expressed as:

$$\mathbf{B} = \mu_0 \frac{N}{L} \mathbf{i} = k_b \mathbf{i} \tag{II.8}$$

It can be noticed that for a given coil design (ie. fixed length L and turns N), the magnetic field is proportional to electric current $\mathbf{i}$.

II.1.2 Magnetic vector potential

In the previous section, the field is determined by the direct derivation of field equations. However, it is often more convenient to use the vector potential.

The Gauss' magnetism law Eq. (II.2) can be formulated in terms of the vector potential $\mathbf{A}$ to determine the magnetic fields leading to the classical gauge theory:

$$\nabla \cdot \mathbf{B} = 0 \Rightarrow \mathbf{B} = \nabla \times \mathbf{A} \tag{II.9}$$

Using this vector potential $\mathbf{A}$ with Eq. (II.1) we obtain:

$$\nabla^2 \mathbf{A} - \nabla (\nabla \cdot \mathbf{A}) = -\mu_0 \mathbf{J} \tag{II.10}$$

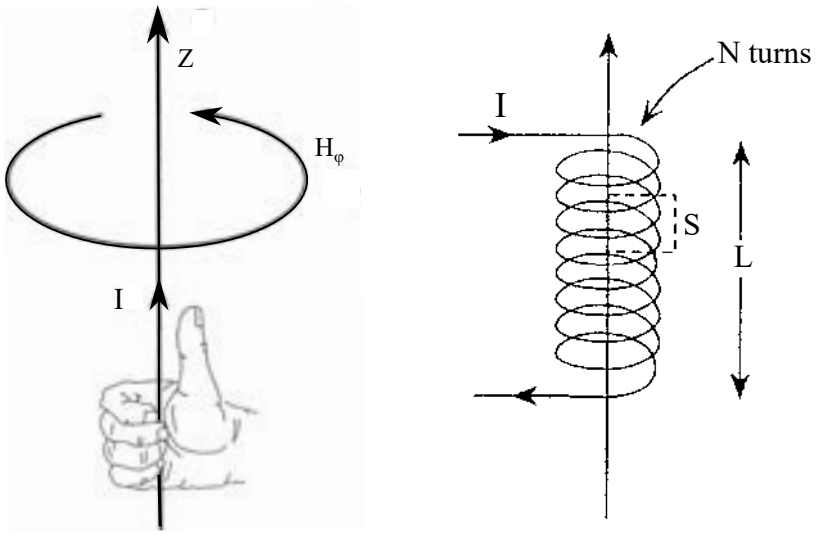

(a) (b)

Figure II.1: Illustration of magnetostatics basic principle: (a) scheme of the long wire [146]; and (b) the model of solenoid.

The equation can be then summarized by imposing the Coulomb gauge condition $\nabla \cdot \mathbf{A} = 0$, and we get:

$$\nabla^2 \mathbf{A} = -\mu_0 \mathbf{J} \tag{II.11}$$

The equation can be expressed in integral form using the free space Green's function for the operator ∇^2, to express the vector potential $\mathbf{A}$.

Otherwise, in classical physics, the magnetic field of a dipole is calculated as the limit of either a current loop or a pair of charges as the source shrinks to a point while keeping the magnetic moment $\mathbf{m}$ constant. For the current loop, this limit is most easily derived for the vector potential. Outside of the source region, this potential is:

$$\mathbf{A}(r) = \frac{\mu_0}{4\pi r^2} \frac{\mathbf{m} \times r}{r} = \frac{\mu_0}{4\pi} \frac{\mathbf{m} \times r}{r^3} \tag{II.12}$$

II.1.2.1 Magnetic field of a magnetic moment

The charge model ia a useful method for analyzing magnetic field. As detailed in [146], the field at a point $\mathbf{p}$ due to a 'point charge' $Q_m(\mathbf{p}')$ at $\mathbf{p}'$ can be calculated from:

$$\mathbf{B}(\mathbf{p}) = \frac{\mu_0}{4\pi} \frac{Q_m(\mathbf{p}')(\mathbf{p} - \mathbf{p}')}{|\mathbf{p} - \mathbf{p}'|^3} \tag{II.13}$$

For instance, let us consider a short thin cylindrical magnet of radius a, length l, and magnetization $\mathbf{M}_s$, as illustrated in figure II.2a. There are surface charges of $-Q_m$ and $+Q_m$ at the two ends of magnet, respectively, where $Q_m = \mathbf{M}_s \pi a^2$. Thus, the field of the corresponding dipole can be obtained as follows:

$$\mathbf{B}(\mathbf{p}) = \frac{\mu_0 Q_m}{4\pi} \left(-\frac{r_1}{r_1^3} + \frac{r_2}{r_2^3} \right) \tag{II.14}$$

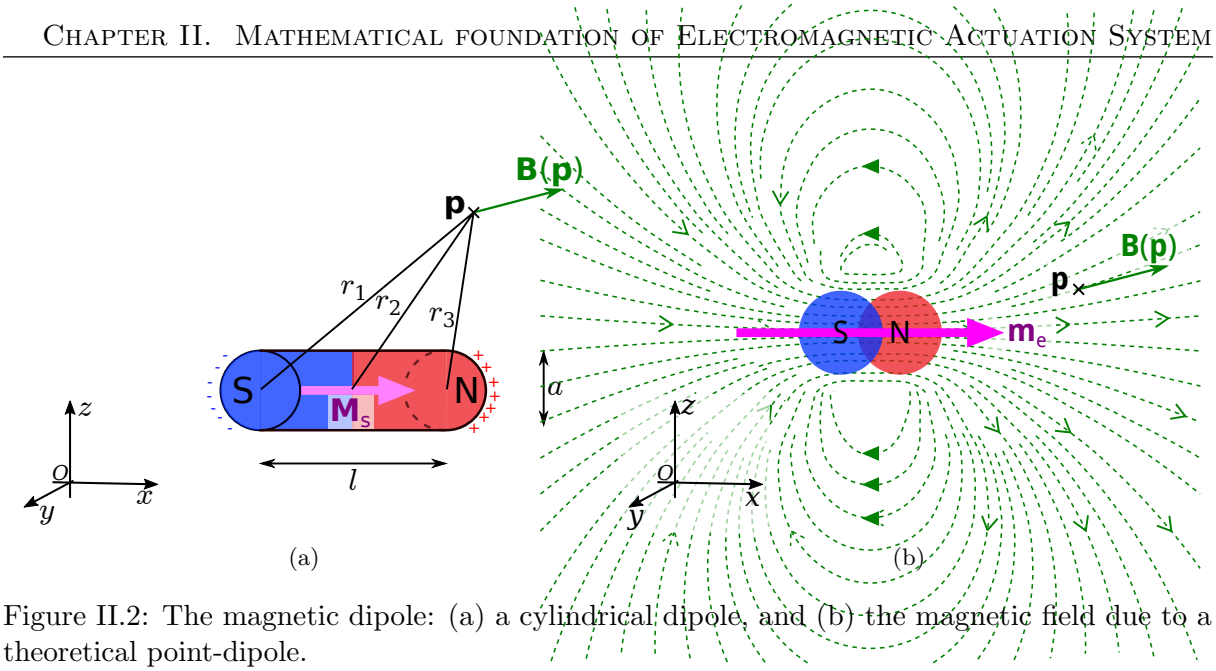

Figure II.2: The magnetic dipole: (a) a cylindrical dipole, and (b) the magnetic field due to a theoretical point-dipole.

The two charges form a magnetic dipole with a magnetic moment given by:

$$\mathbf{m} = Q_m l \tag{II.15}$$

When the length l of magnetic dipole is much smaller than distant r_1 and r_2, we can consider $r_1 \approx r_2 \approx r$, and the magnetic field can be approximated by [146]

$$\mathbf{B}\left(\mathbf{p}\right) = \frac{\mu_0}{4\pi}\left(\frac{3\left(\mathbf{m}\cdot\mathbf{p}\right)\mathbf{p}}{\mathbf{p}^5} - \frac{\mathbf{m}}{\mathbf{p}^3}\right) \tag{II.16}$$

This result can be also retrieved from the magnetic vector potential $\mathbf{A}$.

II.1.3 The point-dipole model

In this work, we use magnetic point-dipole to model the unit-current contribution mapping the each electromagnetic coil as illustrated in figure II.2b. Actually, any electromagnetic source can be seen as a magnetic dipole characterized by its magnetic moment. Thus, the spatial distribution of a magnetic field $\mathbf{B}$ generated by an electromagnetic coil can be approximated from the basic the *magnetic point-dipole model* given by:

$$\mathbf{B}(\mathbf{p}) = \frac{\mu_0}{4\pi|\mathbf{p}|^3}\left(\frac{3\left(\mathbf{m}_e\cdot\mathbf{p}\right)}{|\mathbf{p}|^2} - \mathbf{m}_e\right) \tag{II.17}$$

where $\mathbf{m}_e$ is the equivalent magnetic dipole moment related to the electromagnetic coil source for a unit current input ($i_e = 1$); and the $\mathbf{p}$ is a position vector expressed in a given frame. The green dashed line in figure II.2b depicts an example of the streamlines of the magnetic field calculated with the above point-dipole model.

As reported by Kummer [147], the point-dipole model can fit to the distant portion of the on-axis magnetic field data of the equivalent electromagnet. Although the point-dipole model (II.17) is only valid for location $\mathbf{p}$ along the electromagnet's axis, it remains a suitable approximation of the magnetic field for a small workspace near the axis [60], [147].

II.2 Electromagnetic manipulation of untethered microrobot

The magnetic field and gradient generated by electromagnetic coil in the workspace can be computed and analyzed with the point-dipole model. Placing a magnetized object in the workspace, the magnetic torque or force will be induced on the object. The electromagnetic manipulation can be achieved by the induced torque and force.

As illustrated in figure II.3, the magnetic field and its gradient are generated by the a set of n electromagnets to control the motion of untethered microrobots. The orientation of microrobot tends to be aligned with the direction of magnetic field $\mathbf{B}$, thus the microrobots are rotated by the magnetic torque $\mathbf{t}_\mathrm{m}$. Moreover, the magnetic gradient $\nabla\mathbf{B}$ induces the magnetic force $\mathbf{f}_\mathrm{m}$ as propulsion force to move microrobot. Hence, the magnetic object can be manipulated through the rotation and translation operations using magnetic field and gradient, respectively.

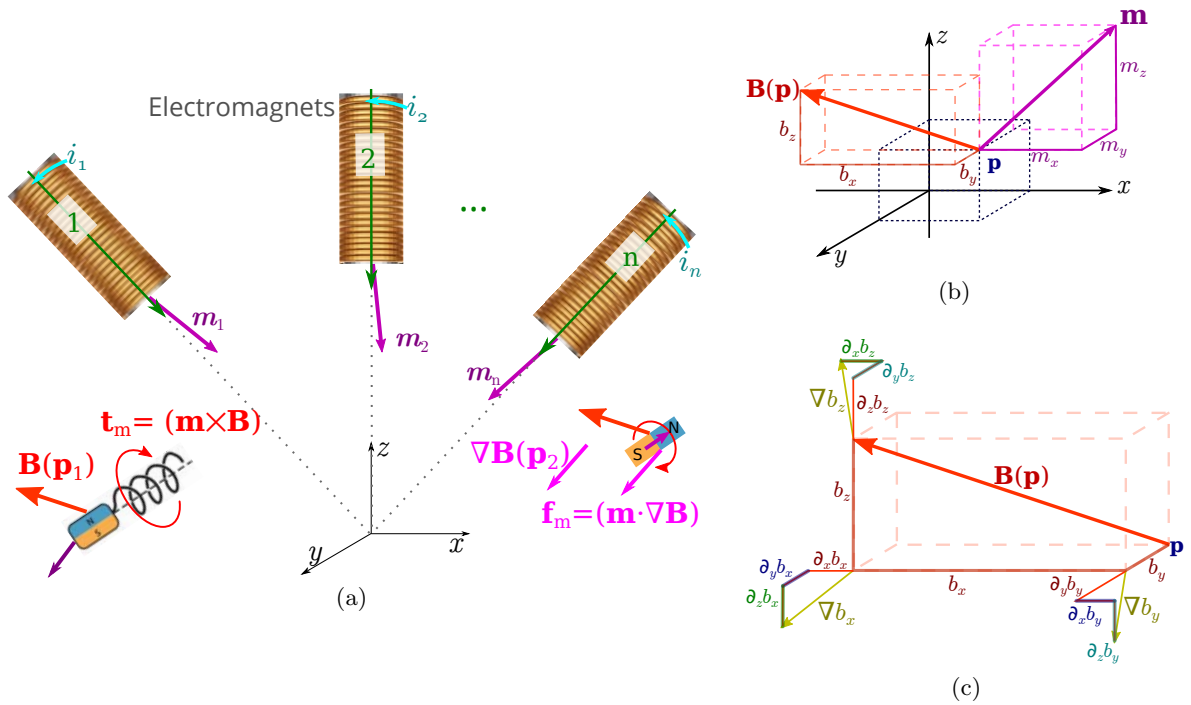

Figure II.3: Electromagnetic manipulation: (a) illustration of the use of the magnetic force and torque on untethered magnetic microrobots; (b) composition of the magnetic field with the magnetic moment of the microrobot; and (c) the different components of the magnetic gradient.

II.2.1 Force and torque on a microrobot in a magnetic field

The locomotion of an untethered magnetic microrobot is basically performed by applying magnetic torque and force through the manipulation of the external magnetic flux $\mathbf{B}$. Starting from the Maxwell's equations (II.1)-(II.4), and assuming that charges are either fixed or move as a steady current $\mathbf{J}$, the governing equation of a *quasi-static magnetic field* can be described by the two following relations [148]:

$$\nabla \cdot \mathbf{B} = 0 \tag{II.18}$$

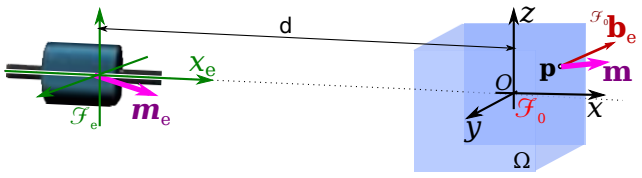

Figure II.4: Schematic representation of a single electromagnet inducing a magnetic flux $\mathbf{B}_e(\mathbf{p})$ within the workspace Ω (blue square box).

$$\nabla \times \mathbf{B} = \mu_0 \mathbf{J} \tag{II.19}$$

Next, assuming that the microrobot is a magnetized body described by its magnetic dipole moment $\mathbf{m}$, that is placed in a magnetic flux $\mathbf{B}$, the induced magnetic force and torque are basically expressed from Eqns. (I.1) and (I.2), and recalled here as [97]:

$$\mathbf{f}_\mathrm{m} = (\mathbf{m} \cdot \nabla)\, \mathbf{B} \tag{II.20}$$

$$\mathbf{t}_\mathrm{m} = (\mathbf{m} \times \mathbf{B}) \tag{II.21}$$

Obviously, $\mathbf{f}_\mathrm{m}$ is related to the magnetic gradient $\nabla \mathbf{B}$, whereas the magnetic torque $\mathbf{t}_\mathrm{m}$ is a function of the magnetic field $\mathbf{B}$. Specifically, the torque tends to align the magnetic moment $\mathbf{m}$ with the applied magnetic field, that is $\mathbf{B}$ can be used to orient the microrobot. Moreover, to actuate the microrobot, the magnetic field must undergo either a spatial change (i.e. exhibit a spatial field gradient), or a temporal change, such as through a rotating magnetic field, oscillation and so on.

Secondly, if we assume there is no electric current flowing through the workspace occupied by the microrobot, Maxwell's equation implies that Eq. (II.19) becomes $\nabla \times \mathbf{B} = 0$. The magnetic force (II.20) can be then rearranged using vector calculus into the following form:

$$\mathbf{f}_\mathrm{m} = \begin{pmatrix} \dfrac{\partial \mathbf{B}}{\partial x} \\ \dfrac{\partial \mathbf{B}}{\partial y} \\ \dfrac{\partial \mathbf{B}}{\partial z} \end{pmatrix} \mathbf{m} = \begin{pmatrix} \dfrac{\partial b_x}{\partial x} & \dfrac{\partial b_y}{\partial x} & \dfrac{\partial b_z}{\partial x} \\ \dfrac{\partial b_x}{\partial y} & \dfrac{\partial b_y}{\partial y} & \dfrac{\partial b_z}{\partial y} \\ \dfrac{\partial b_x}{\partial z} & \dfrac{\partial b_y}{\partial z} & \dfrac{\partial b_z}{\partial z} \end{pmatrix} \mathbf{m} = \mathbf{G}\mathbf{m} \tag{II.22}$$

where $\mathbf{G} \in \mathbb{R}^{3\times3}$ denotes the gradient matrix of the magnetic field $\mathbf{B} = (b_x, b_y, b_z)$. Besides, the subscripts x, y and z explicitly refer to the basis directions of the Cartesian reference frame $\mathcal{F}_0(O : x, y, z)$ linked to the workspace Ω, in which all vectors are expressed (see figure II.4).

The torque on microrobot tends to align the magnetization vector with the magnetic field. To represent vector cross products, the skew-symmetric matrix formed of a vector can be employed, that is:

$$\mathrm{Skew}(\mathbf{m}) = \mathrm{Skew}\begin{pmatrix} m_x \\ m_y \\ m_z \end{pmatrix} = \begin{pmatrix} 0 & -m_z & m_y \\ m_z & 0 & -m_x \\ -m_y & m_x & 0 \end{pmatrix} \tag{II.23}$$

Therefore, the force (II.20) and torque (II.21) applied to magnetic microrobots can be rewritten as:

$$\begin{pmatrix} \mathbf{f}_\mathrm{m} \\ \mathbf{t}_\mathrm{m} \end{pmatrix} = \begin{pmatrix} (\mathbf{m} \cdot \nabla) \\ \mathrm{Skew}(\mathbf{m}) \end{pmatrix} \mathbf{B} \tag{II.24}$$

II.2.2 Electromagnetic control

In our study, the magnetic field is induced by an EMA system consisting of several electromagnets. Hence, with a given set of n electromagnets, each of them creates a magnetic field, $\mathbf{B}_e(\mathbf{p})$, at any location of the workspace: $\forall \mathbf{p} \in \Omega$. From Eqns. (II.8) and (II.19), it can be shown that the magnetic fields and their spatial gradients depend linearly on the currents. When i_e flows through the coils e, the magnetic field can be expressed as: $\mathbf{B}_e(\mathbf{p}) = \widetilde{\mathbf{B}}_e(\mathbf{p})i_e$. The superposition principle is commonly used to compute the overall magnetic field[1], that is:

$$\mathbf{B}(\mathbf{p}) = \sum_{e=1}^{n} \widetilde{\mathbf{B}}_e(\mathbf{p})i_e = \begin{pmatrix} \widetilde{b_{x1}} & \dots & \widetilde{b_{xe}} & \dots & \widetilde{b_{xn}} \\ \widetilde{b_{y1}} & \dots & \widetilde{b_{ye}} & \dots & \widetilde{b_{yn}} \\ \widetilde{b_{z1}} & \dots & \widetilde{b_{ze}} & \dots & \widetilde{b_{zn}} \end{pmatrix} \mathbf{i} = \begin{pmatrix} \mathcal{B}_x(\mathbf{p}) \\ \mathcal{B}_y(\mathbf{p}) \\ \mathcal{B}_z(\mathbf{p}) \end{pmatrix} \mathbf{i} = \mathcal{B}(\mathbf{p})\mathbf{i} \tag{II.25}$$

where $\mathbf{i} = (i_1 \dots i_n)^\intercal$ is the current vector, and $\mathcal{B}(\mathbf{p})$ is a $3 \times n$ matrix mapping the currents to the magnetic fields.
Similarly, the magnetic gradient fields could be expressed as:

$$\frac{\partial \mathbf{B}(\mathbf{p})}{\partial x} = \sum_{e=1}^{n} \frac{\partial \widetilde{\mathbf{B}}_e(\mathbf{p})}{\partial x} i_e = \begin{pmatrix} \dfrac{\partial \mathcal{B}_x}{\partial x} \\ \dfrac{\partial \mathcal{B}_y}{\partial x} \\ \dfrac{\partial \mathcal{B}_z}{\partial x} \end{pmatrix} \mathbf{i} = \mathcal{G}_x(\mathbf{p})\mathbf{i} \tag{II.26}$$

$$\frac{\partial \mathbf{B}(\mathbf{p})}{\partial y} = \sum_{e=1}^{n} \frac{\partial \widetilde{\mathbf{B}}_e(\mathbf{p})}{\partial y} i_e = \begin{pmatrix} \dfrac{\partial \mathcal{B}_x}{\partial y} \\ \dfrac{\partial \mathcal{B}_y}{\partial y} \\ \dfrac{\partial \mathcal{B}_z}{\partial y} \end{pmatrix} \mathbf{i} = \mathcal{G}_y(\mathbf{p})\mathbf{i} \tag{II.27}$$

$$\frac{\partial \mathbf{B}(\mathbf{p})}{\partial z} = \sum_{e=1}^{n} \frac{\partial \widetilde{\mathbf{B}}_e(\mathbf{p})}{\partial z} i_e = \begin{pmatrix} \dfrac{\partial \mathcal{B}_x}{\partial z} \\ \dfrac{\partial \mathcal{B}_y}{\partial z} \\ \dfrac{\partial \mathcal{B}_z}{\partial z} \end{pmatrix} \mathbf{i} = \mathcal{G}_z(\mathbf{p})\mathbf{i} \tag{II.28}$$

where each $\mathcal{G}_{x,y,z}(\mathbf{p})$ is $3 \times n$ matrix mapping the current to the magnetic gradient field in the x, y, and z directions, respectively.

The different mapping matrices $\mathcal{B}(\mathbf{p})$ and $\mathcal{G}_{x,y,z}(\mathbf{p})$ expressions are related to the type and geometry of each electromagnet (e.g. length, radius, numbers of turns.). For instance, the mapping for Helmholtz or Maxwell coils could be easily carried out from the Biot-Savart's law, as presented in section I.3.2. For the other types of electromagnets, especially with a magnetic

[1]For the sake of clarity, we assume in this chapter that the magnetic field is expressed here in the workspace reference frame $\mathcal{F}_0$. The transformation matrices between the different frames will be addressed in the Section III.1.2.

core, the mapping matrices can be calculated either from measures of the magnetic field within the EMA system's workspace or from the simulations of magnetic field using FEM models [60].

Finally, the equations of magnetic force and torque can be rearranged as follows:

$$\begin{pmatrix} \mathbf{t}_{\mathrm{m}} \\ \\ \mathbf{f}_{\mathrm{m}} \end{pmatrix} = \begin{pmatrix} \mathrm{Skew}(\mathbf{m})\mathcal{B} \\ \mathbf{m}^{\intercal}\mathcal{G}_x(\mathbf{p}) \\ \mathbf{m}^{\intercal}\mathcal{G}_y(\mathbf{p}) \\ \mathbf{m}^{\intercal}\mathcal{G}_z(\mathbf{p}) \end{pmatrix} \mathbf{i} = \begin{pmatrix} \mathcal{A}_t(\mathbf{m},\mathbf{p}) \\ \\ \mathcal{A}_f(\mathbf{m},\mathbf{p}) \end{pmatrix} \mathbf{i} = \mathcal{A}(\mathbf{m},\mathbf{p})\mathbf{i} \tag{II.29}$$

where $\mathcal{A}_t(\mathbf{m},\mathbf{p})$ and $\mathcal{A}_f(\mathbf{m},\mathbf{p})$ are the actuation matrices mapping the current vector $\mathbf{i}$ to the torque and force, respectively; and $\mathcal{A}(\mathbf{m},\mathbf{p})$ is the $6 \times n$ actuation matrix mapping to the applied magnetic wrench. These magnetic actuation matrices depend both on the position $\mathbf{p} \in \Omega$, and on the orientation of the dipole moment $\mathbf{m}$ of the microrobot.

According to Eqns. (II.20) and (II.21), each column of the matrix $\mathcal{A}(\mathbf{m},\mathbf{p})$ represents the wrench on the force and torque per current unit created by each electromagnet. If there are greater than $n > 6$ electromagnets, the actuation matrix $\mathcal{A}(\mathbf{m},\mathbf{p})$ leads to a better conditioned matrix, a more isotropic workspace Ω, a reduction of singularity configurations, and lower current requirements [73], [74]. In such cases, $n > 6$, the EMA system could be said "redundant" for the task. Especially, if $\mathcal{A}(\mathbf{m},\mathbf{p})$ is of full rank, for a desired force, ${\mathbf{f}_{\mathrm{m}}}^{\star}$ and torque, ${\mathbf{t}_{\mathrm{m}}}^{\star}$, the actuation currents $\mathbf{i}$ can be calculated from the pseudo-inverse:

$$\mathbf{i} = \mathcal{A}^{+}(\mathbf{m},\mathbf{p}) \begin{pmatrix} {\mathbf{t}_{\mathrm{m}}}^{\star} \\ {\mathbf{f}_{\mathrm{m}}}^{\star} \end{pmatrix} \tag{II.30}$$

If $n < 6$, the pseudo-inverse would be a least-squares approximations. Hence, for a controlled force and torque, the input current can be obtained only if the pseudo-inverse of $\mathcal{A}(\mathbf{m},\mathbf{p})$ exists. This derivation on the controlled current $\mathbf{i}$ can be similarly extended for controllers that require torque and/or force control [58].

II.2.3 Discussions

The well-conditioning of the above magnetic force and torque relies on the location $\mathbf{p}$ and the orientation of the magnetic moment $\mathbf{m}$ of the microrobot within the workspace. Petruska and Nelson [149] have demonstrated that only $n = 7$ stationary coils are required to pull and steer a microrobot. Further details on this aspect is the concern of the following section II.3. But, to avoid some instabilities (e.g. orientation-dependent singularities), an EMA system with at least $n = 8$ static coils is required. It can also been shown that only 5 DOFs can be achieved with the above magnetic manipulation frameworks. Specifically, the microrobot is unable to perform self-rotations (e.g rotation about its main-axis). When the electromagnetic coils arrangement is not fixed, $n = 6$ coils are enough to properly manipulate the magnetic fields [149].

When the rank of matrix $\mathcal{A}_t(\mathbf{m},\mathbf{p})$ is equal to dimension of the workspace, the heading of microrobots system is fully controllable. Furthermore, if the system aims at providing force on the magnetic microrobot in any direction, it requires to control gradient in each direction independently, which means that $\mathcal{A}_f(\mathbf{m},\mathbf{p})$ should be full row rank within the workspace Ω. However, the matrix $\mathrm{Skew}(\mathbf{m})$ has rank of only 2. Hence, there exists a linear dependence between the magnetic field $\mathbf{B}$ and $\mathrm{Skew}(\mathbf{m})$. In other words, there is one item in $\mathbf{B}$ or $\mathrm{Skew}(\mathbf{m})$ that is not necessary. Specifically, as stated, the EMA system can not induce a torque on a dipole

about dipole-moment axis, when the n-electromagnet is in a stationary arrangement. Therefore, the number of magnetic field inputs and gradient inputs, or their linear dependencies should be further investigated in the following section. The number of applied electromagnets will be determined depending on these magnetic inputs.

II.3 Minimum electromagnets for EMA system

One of the motivation of an EMA platform is to provide the necessary DOFs for the manipulation of microrobot, mainly depending on the configuration and the number n of constituting electromagnets. Intuitively, it can be shown that platforms with different arrangements of electromagnet exhibit a wide diversity of operating performances for various manipulation tasks [46], [60] (see also section I.4). In this section, we will rigorously analyze the number of electromagnets that is required for different magnetic manipulations. Commonly, the manipulation of untethered magnetic microrobot includes the control of its orientation and position. As we mentioned in section II.2, the orientation of microrobot can be simply controlled through the magnetic field. In addition, its position is reached using drilling force generated by rotating magnetic field or translating force generated by magnetic gradient. Thus, the efficient remote magnetic manipulation relies on the capability of generating proper magnetic field and gradient. Specifically, the DOFs of wireless microrobot can be evaluated through the magnetic field and its gradient that are generated by the EMA system with a given number of electromagnets.

As demonstrated in [98], [150]–[152] at least $n = 3$ electromagnets are required to achieve 3 DOFs pointing control. Besides, the position control can be effectively realized with at least $n = 4$ magnets in 3D workspace, but up to 8 coils are commonly used to improve the system stability [149]. In fact non-magnetic restoring forces, such as gravity, play also an important role, and should be considered. Moreover, some unexpected singularities involving to force control lead to some holonomic constraints, that will be investigated in the follows.

II.3.1 EMA field manipulation

The quasi-static magnetic fields generated by electromagnets can be defined from the Maxwell's equations (II.18)-(II.19). The magnetic torque and force acting on a microrobot are described following Eq. (II.29). In current free space, Eq. (II.18) constraints the gradient matrix of the vector field $\mathbf{B}$ to have zero trace; and Eq. (II.19) constraints the gradient matrix of the vector field to be symmetric. Hence, the magnetic force Eq. (II.22) can be rearranged as:

$$\mathbf{f}_{\mathrm{m}} = \begin{pmatrix} \frac{\partial b_x}{\partial x} & \frac{\partial b_x}{\partial y} & \frac{\partial b_x}{\partial z} \\ \frac{\partial b_x}{\partial y} & \frac{\partial b_y}{\partial y} & \frac{\partial b_y}{\partial z} \\ \frac{\partial b_x}{\partial z} & \frac{\partial b_y}{\partial z} & \frac{\partial b_z}{\partial z} \end{pmatrix} \begin{pmatrix} m_x \\ m_y \\ m_z \end{pmatrix} = \begin{pmatrix} \frac{\partial b_x}{\partial x} & \frac{\partial b_x}{\partial y} & \frac{\partial b_x}{\partial z} \\ \frac{\partial b_x}{\partial y} & \frac{\partial b_y}{\partial y} & \frac{\partial b_y}{\partial z} \\ \frac{\partial b_x}{\partial z} & \frac{\partial b_y}{\partial z} & -\left(\frac{\partial b_x}{\partial x} + \frac{\partial b_y}{\partial y}\right) \end{pmatrix} \begin{pmatrix} m_x \\ m_y \\ m_z \end{pmatrix} \tag{II.31}$$

This rearrangement allows simplifying the number of magnetic gradient components from nine to five. It is obvious that the magnetic force relies on the applied magnetic gradient field and the magnetic dipole moment of the microrobot. Thus, for a given magnetic dipole, the induced magnetic force only depends on the magnetic gradient that is controlled by the currents flowing

through the electromagnets. The magnetic force equations can be thereby expressed as the follows to highlight the magnetic gradients as the controllable parameters:

$$\mathbf{f}_{\mathrm{m}} = \begin{pmatrix} m_x & m_y & m_z & 0 & 0 \\ 0 & m_x & 0 & m_y & m_z \\ -m_z & 0 & m_x & -m_z & m_y \end{pmatrix} \begin{pmatrix} \dfrac{\partial b_x}{\partial x} \\ \dfrac{\partial b_x}{\partial y} \\ \dfrac{\partial b_x}{\partial z} \\ \dfrac{\partial b_y}{\partial y} \\ \dfrac{\partial b_y}{\partial z} \end{pmatrix} = \mathcal{F}(\mathbf{m})\mathbf{g} \tag{II.32}$$

where $\mathcal{F}(\mathbf{m})$ indicates the matrix form of the dipole moment $\mathbf{m}$ of the microrobot; and the vector field $\mathbf{g}$ includes the five magnetic gradient components.

Similarly, the applied magnetic torque is dependent on the magnetic field when the dipole moment of the microrobot is determined. Using the Eq. (II.23), the magnetic force is represented as:

$$\mathbf{t}_{\mathrm{m}} = \mathrm{Skew}(\mathbf{m})\mathbf{B} = \begin{pmatrix} 0 & -m_z & m_y \\ m_z & 0 & -m_x \\ -m_y & m_x & 0 \end{pmatrix} \begin{pmatrix} b_x \\ b_y \\ b_z \end{pmatrix} \tag{II.33}$$

In this way, the Eq. (II.24) can also be expressed as:

$$\begin{pmatrix} \mathbf{t}_{\mathrm{m}} \\ \mathbf{f}_{\mathrm{m}} \end{pmatrix} = \begin{pmatrix} \mathrm{Skew}(\mathbf{m}) \\ \mathcal{F}(\mathbf{m}) \end{pmatrix} \begin{pmatrix} \mathbf{B} \\ \mathbf{g} \end{pmatrix} \tag{II.34}$$

Considering the current flowing through the n electromagnetic coils of the EMA system has a linearly mapping to the magnetic field (II.25) and gradient (II.26)-(II.28), it follows that the Eq. (II.29) can be then represented as:

$$\begin{pmatrix} \mathbf{t}_{\mathrm{m}} \\ \mathbf{f}_{\mathrm{m}} \end{pmatrix} = \mathcal{A}(\mathbf{m}, \mathbf{p})\mathbf{i} = \begin{pmatrix} \mathcal{A}_t(\mathbf{m}, \mathbf{p}) \\ \mathcal{A}_f(\mathbf{m}, \mathbf{p}) \end{pmatrix} \mathbf{i} = \begin{pmatrix} \mathrm{Skew}(\mathbf{m}) \\ \mathcal{F}(\mathbf{m}) \end{pmatrix} \begin{pmatrix} \mathcal{B}(\mathbf{p}) \\ \mathcal{G}(\mathbf{p}) \end{pmatrix} \mathbf{i} \tag{II.35}$$

where $\mathcal{B}$ is a $3 \times n$ matrix and $\mathcal{G}$ is a $5 \times n$ matrix, that are defined as:

$$\mathbf{g} = \mathcal{G}(\mathbf{p})\mathbf{i}, \text{ with: } \mathcal{G}(\mathbf{p}) = \begin{pmatrix} \dfrac{\partial \mathcal{B}_x}{\partial x} & \dfrac{\partial \mathcal{B}_x}{\partial y} & \dfrac{\partial \mathcal{B}_x}{\partial z} & \dfrac{\partial \mathcal{B}_y}{\partial y} & \dfrac{\partial \mathcal{B}_y}{\partial z} \end{pmatrix}^{\mathsf{T}} \tag{II.36}$$

Besides, both $\mathcal{B}$ and $\mathcal{G}$ are a function of the location $\mathbf{p}$ of the microrobot in the workspace Ω. Through investigating the matrices $\mathcal{F}(\mathbf{m})$ and $\mathrm{Skew}(\mathbf{m})$, the conditioning of magnetic field and its gradient can be analyzed.

Since the orientation of microrobot tends to be aligned on the applied magnetic field, it is more convenient to linearize the system by specifying the desired field directly instead of magnetic torque. Hence, the magnetic field and inducing force can be obtained from:

$$\begin{pmatrix} \mathbf{B} \\ \mathbf{f}_{\mathrm{m}} \end{pmatrix} = \begin{pmatrix} \mathbb{1} & \mathbb{0} \\ \mathbb{0} & \mathcal{F}(\mathbf{m}) \end{pmatrix} \begin{pmatrix} \mathcal{B}(\mathbf{p}) \\ \mathcal{G}(\mathbf{p}) \end{pmatrix} \mathbf{i} = \mathcal{A}_b(\mathbf{m}, \mathbf{p})\ \mathbf{i} \tag{II.37}$$

where $\mathbb{1}$ is an identity matrix, and $\mathbb{0}$ is a zero matrix in an appropriately size.

If the microrobot is made of permanent magnet, magnetic torque is linear with the current. If the microrobot is composed of a soft magnetic material and it does not reach the magnetic saturation, there is a linear relation between the magnetic moment and the magnetic field. Consequently, the magnetic torque becomes quadratic with the current [153]. Thus, the capability of the EMA system, such as DOFs of manipulation of the microrobot, can be evaluated from the Eq. (II.37). Similarly to the Eq. (II.30), the input currents $\mathbf{i}$ can be also here computed using the pseudo-inverse of $\mathcal{A}_b(\mathbf{m}, \mathbf{p})$ matrix when the matrix has full rank.

Furthermore, as the magnetic field and force are decoupled in eq. (II.37), they can be first analyzed separately. As the magnetic field is linear with the current $\mathbf{i}$, the sole $\mathbf{B}$ field control relies on the properties of the matrix $\mathcal{B}(\mathbf{p})$. It can be easily shown that if the rank of $\mathcal{B}(\mathbf{p})$ is equal to the dimension of the workspace $\forall \mathbf{p} \in \Omega$, that leads to a full control of $\mathbf{B}$. In other words, the number of current inputs $\mathbf{i}$ should be equal or more than the dimension of the workspace Ω.

In contrast, the force control requires more advanced investigations that are presented hereafter. For the sake of simplicity, we only consider a unit current when analysis is performed on the magnetic field and the dipole moment direction in the following section pangolin 100.

II.3.2 Magnetic force control

The matrix $\mathcal{F}(\mathbf{m})$ is a 3×5 non-square matrix, and it can be shown that its row rank is full. Thus, $\mathcal{F}(\mathbf{m})$ has a right Moore-Penrose inverse which is expressed by $\mathcal{F}(\mathbf{m})^{\dagger} = \mathcal{F}(\mathbf{m})^{\intercal} \left(\mathcal{F}(\mathbf{m})\mathcal{F}(\mathbf{m})^{\intercal}\right)^{-1}$. From Eq. (II.31), the desired magnetic gradient vectors $\mathbf{g}^{\star}$ are thereby obtained using the right inverse when the magnetic force is required. This leads to:

$$\mathbf{g}^{\star} = \mathcal{F}(\mathbf{m})^{+}\mathbf{f}_{\mathrm{m}}$$

$$\begin{pmatrix} \frac{\partial b_x^{\star}}{\partial x} \\ \frac{\partial b_x^{\star}}{\partial y} \\ \frac{\partial b_x^{\star}}{\partial z} \\ \frac{\partial b_y^{\star}}{\partial y} \\ \frac{\partial b_y^{\star}}{\partial z} \end{pmatrix} = \begin{pmatrix} m_x & 0 & -m_z \\ m_y & m_x & 0 \\ m_z & 0 & m_x \\ 0 & m_y & -m_z \\ 0 & m_z & m_y \end{pmatrix} \left(\begin{pmatrix} m_x & m_y & m_z & 0 & 0 \\ 0 & m_x & 0 & m_y & m_z \\ -m_z & 0 & m_x & -m_z & m_y \end{pmatrix} \begin{pmatrix} m_x & 0 & -m_z \\ m_y & m_x & 0 \\ m_z & 0 & m_x \\ 0 & m_y & -m_z \\ 0 & m_z & m_y \end{pmatrix} \right)^{-1} \mathbf{f}_{\mathrm{m}}$$

$$= \begin{pmatrix} \frac{(m_n)\, m_x}{(m_n)^2 - (m_x m_y)^2} & \frac{-m_x^2 m_y}{(m_n)^2 - (m_x m_y)^2} & \frac{-m_z}{m_x^2 + m_y^2 + 2m_z^2} \\ \frac{m_y^3 + m_y m_z^2}{(m_n)^2 - (m_x m_y)^2} & \frac{m_x^3 + m_x m_z^2}{(m_n)^2 - (m_x m_y)^2} & 0 \\ \frac{(m_n)\, m_z}{(m_n)^2 - (m_x m_y)^2} & \frac{-m_x m_z^2}{(m_n)^2 - (m_x m_y)^2} & \frac{m_x}{m_x^2 + m_y^2 + 2m_z^2} \\ \frac{-m_x m_y^2}{(m_n)^2 - (m_x m_y)^2} & \frac{(m_n)\, m_y}{(m_n)^2 - (m_x m_y)^2} & \frac{-m_z}{m_x^2 + m_y^2 + 2m_z^2} \\ \frac{-m_x m_z^2}{(m_n)^2 - (m_x m_y)^2} & \frac{(m_n)\, m_z}{(m_n)^2 - (m_x m_y)^2} & \frac{m_y}{m_x^2 + m_y^2 + 2m_z^2} \end{pmatrix} \mathbf{f}_{\mathrm{m}} \tag{II.38}$$

with $m_n = m_x^2 + m_y^2 + m_z^2$. As one can see, the matrix $\mathcal{F}(\mathbf{m})$ is a function of the dipole moment $\mathbf{m} = (m_x, m_y, m_z)^\intercal$ of the microrobot. Obviously, the pseudo-inverse matrix $\mathcal{F}(\mathbf{m})^+$ is also affected by the dipole moment of microrobot.

If the magnetic moment $\mathbf{m}$ of the microrobot is fixed (e.g. when a uniform static magnetic field $\mathbf{B}_0$ is applied), only three independent magnetic gradients of $\mathbf{g}$ are required to produce an arbitrary force $\mathbf{f}_{\mathrm{m}}$. However, the all five magnetic gradient components are required for continuous force control if $\mathbf{m}$ is changing. Therefore, there are ten linear relations between magnetic gradients, that are described in the following.

Case #1: linear dependence between $\frac{\partial b_x}{\partial x}$ and $\frac{\partial b_y}{\partial y}$

Let us express this linear dependence through adding a coefficient $\alpha \in \mathbb{R}^*$, that is: $\frac{\partial b_y}{\partial y} = \alpha \frac{\partial b_x}{\partial x}$. The Eq. (II.31) is then written with a unit current input as follows:

$$\begin{aligned} \mathbf{f}_{\mathrm{m}} = \mathcal{F}(\mathbf{m})\mathbf{g} &= \begin{pmatrix} m_x & m_y & m_z & 0 & 0 \\ 0 & m_x & 0 & m_y & m_z \\ -m_z & 0 & m_x & -m_z & m_y \end{pmatrix} \begin{pmatrix} \frac{\partial b_x}{\partial x} \\ \frac{\partial b_x}{\partial y} \\ \frac{\partial b_x}{\partial z} \\ \alpha \cdot \frac{\partial b_x}{\partial x} \\ \frac{\partial b_y}{\partial z} \end{pmatrix} \\ &= \begin{pmatrix} m_x & m_y & m_z & 0 \\ \alpha m_y & m_x & 0 & m_z \\ -m_z - \alpha m_z & 0 & m_x & m_y \end{pmatrix} \begin{pmatrix} \frac{\partial b_x}{\partial x} \\ \frac{\partial b_x}{\partial y} \\ \frac{\partial b_x}{\partial z} \\ \frac{\partial b_y}{\partial z} \end{pmatrix} \end{aligned} \tag{II.39}$$

If the magnetic microrobot is aligned along the z-axis, the magnetic force in z-axis direction is expressed as:

$$f_z = -\left(1+\alpha\right) m_z \frac{\partial b_x}{\partial x} \tag{II.40}$$

Obviously, f_z equals to zero when: $\alpha = -1$, that is for $\dfrac{\partial b_y}{\partial y} = -\dfrac{\partial b_x}{\partial x}$.

Let us now assume that the microrobot has a magnetic dipole moment defined by:

$$\mathbf{m} = \left\{(m, \beta m, 0)^\intercal, (m, 0, \beta m)^\intercal \text{ or } (0, m, \beta m)^\intercal\right\} \tag{II.41}$$

with $\beta \in \mathbb{R}^*$ a coefficient term. Then, these values have to be taken into the Eq. (II.38) to investigate the existence of a solution. The necessary and sufficient condition for a matrix reversibility is that the determinant is not equal to 0. Since the determinant of a matrix is equal to the product of all of their eigenvalues, all eigenvalues must be not equal to 0 in order to enable the existence of the inverse matrix. Thus, the singularly values of the system for the considered linear dependence can be mathematically analyzed by computing whether $\det\left(\mathcal{F}(\mathbf{m})\mathcal{F}(\mathbf{m})^\intercal\right) = 0$. The determinants with regard to the magnetic dipole moments of $\mathbf{m}$ are obtained as:

$$\det\left(m, \beta m, 0\right) = m\left(\alpha^2\beta^6 + \alpha^2\beta^4 + 2\alpha\beta^4 + 2\alpha\beta^2 + \beta^2 + 1\right) \tag{II.42}$$

$$\det\left(m, 0, \beta m\right) = m\left(\alpha^2\beta^6 + \alpha^2\beta^4 + 2\alpha\beta^6 + 4\alpha\beta^4 + 2\alpha\beta^2 + \beta^6 + 3\beta^4 + 3\beta^2 + 1\right) \tag{II.43}$$

$$\det\left(0, m, \beta m\right) = m\left(\alpha^2\beta^6 + 3\alpha^2\beta^4 + 3\alpha^2\beta^2 + \alpha^2 + 2\alpha\beta^6 + 4\alpha\beta^4 + 2\alpha\beta^2 + \beta^6 + \beta^4\right) \tag{II.44}$$

where det represents the determinant operator, such as $\det\left(\mathbf{m}\right)$ is expressed as the determinant of $\left(\mathcal{F}(\mathbf{m})\mathcal{F}(\mathbf{m})^\intercal\right)$ for the given dipole moment.

When the determinant becomes 0, the rank of matrix $\mathcal{F}(\mathbf{m})$ is less than 3 and the inverse matrix does not exist, thereby, the system becomes singular. Thus, the system should avoid the relationship between β and α regarding the three dipole moments, respectively, meets the followings:

$$\beta = \pm\frac{1}{\sqrt{\alpha}} \tag{II.45}$$

$$\beta = \pm\frac{1}{\sqrt{-\alpha - 1}} \tag{II.46}$$

$$\beta = \pm\frac{\sqrt{-\alpha\left(\alpha+1\right)}}{\alpha+1} \tag{II.47}$$

When the above equations are satisfied, one of magnetic force components becomes linear dependent to one of the others. For instance, for a dipole moment $\mathbf{m} = (m, \beta m, 0)^\intercal$, the basic condition is: $\alpha > 0$ and not satisfy Eq. (II.45), and then a singularity can be avoided. The other singular cases are summarized in table II.1.

Case #2: linear dependence between $\frac{\partial b_x}{\partial x}$ and $\frac{\partial b_x}{\partial y}$

Here, it can be easily mathematically verified that the magnetic force exists in any direction regardless of the orientation of the microrobot magnetic moment. Thus, following the same

Table II.1: The singular cases caused by the linear dependent between $\frac{\partial b_x}{\partial x}$ and $\frac{\partial b_y}{\partial y}$

$\mathbf{m}^\intercal$	Relationship between β and α	Condition on α
$(m, \beta m, 0)$	$\beta = \pm\frac{1}{\sqrt{\alpha}}$	$\alpha > 0$
$(m, 0, \beta m)$	$\beta = \pm\frac{1}{\sqrt{-\alpha - 1}}$	$\alpha < -1$
$(0, m, \beta m)$	$\beta = \pm\frac{\sqrt{-\alpha(\alpha+1)}}{\alpha+1}$	$\alpha \neq -1 \wedge \alpha(\alpha+1) \leq 0$

reasoning as in case#1 and setting $\frac{\partial b_x}{\partial y} = \alpha\frac{\partial b_x}{\partial x}$, the Eq. (II.31) can be rewritten as follows:

$$\mathbf{f}_\mathrm{m} = \mathcal{F}(\mathbf{m})\mathbf{g} = \begin{pmatrix} m_x + \alpha m_y & m_z & 0 & 0 \\ \alpha m_x & 0 & m_y & m_z \\ -m_z & m_x & -m_z & m_y \end{pmatrix} \begin{pmatrix} \frac{\partial b_x}{\partial x} \\ \frac{\partial b_x}{\partial z} \\ \frac{\partial b_y}{\partial y} \\ \frac{\partial b_y}{\partial z} \end{pmatrix} = \mathcal{F}_\alpha(\mathbf{m}) \tag{II.48}$$

Then, using the same magnetic moment definition given by Eq. (II.41), the singularities of the following matrices have to be analyzed:

$$\mathcal{F}_\alpha \begin{pmatrix} m \\ \beta m \\ 0 \end{pmatrix} = m \begin{pmatrix} 1+\alpha\beta & 0 & 0 & 0 \\ \alpha & 0 & \beta & 0 \\ 0 & 1 & 0 & \beta \end{pmatrix} \tag{II.49}$$

$$\mathcal{F}_\alpha \begin{pmatrix} m \\ 0 \\ \beta m \end{pmatrix} = m \begin{pmatrix} 1 & \beta & 0 & 0 \\ \alpha & 0 & 0 & \beta \\ -\beta & 1 & -\beta & 0 \end{pmatrix} \tag{II.50}$$

$$\mathcal{F}_\alpha \begin{pmatrix} 0 \\ m \\ \beta m \end{pmatrix} = m \begin{pmatrix} \alpha & \beta & 0 & 0 \\ 0 & 0 & 1 & \beta \\ -\beta & 0 & -\beta & 1 \end{pmatrix} \tag{II.51}$$

The possible singular cases are then summarized in table II.2.

For example, if the linear dependence of magnetic gradients is $\frac{\partial b_x}{\partial y} = \alpha\frac{\partial b_x}{\partial x}$, the singular case will happen in force control when either m_y or m_z equals to zero.

Table II.2: The singular cases caused by the linear dependent between $\frac{\partial b_x}{\partial x}$ and $\frac{\partial b_x}{\partial y}$

$\mathbf{m}^\intercal$	Relationship between β and α	Condition on α
$(m, \beta m, 0)$	$\beta = 0$	No
	$\beta = -\dfrac{1}{\alpha}$	No
$(m, 0, \beta m)$	$\beta = 0$	No
$(0, m, \beta m)$	$\beta = \pm\sqrt{-\frac{\alpha^2}{4} - \frac{\sqrt{-(-\alpha^2+2\alpha+1)(\alpha^2+2\alpha-1)}}{4} - \frac{1}{4}}$	No
	$\beta = \pm\sqrt{\frac{\sqrt{-(-\alpha^2+2\alpha+1)(\alpha^2+2\alpha-1)}}{4} - \frac{\alpha^2}{4} - \frac{1}{4}}$	No

Case #3: linear dependence between $\frac{\partial b_x}{\partial x}$ and $\frac{\partial b_x}{\partial z}$

As previously, the Eq. (II.31) can be rearranged as the follows when the linear dependence relation is $\frac{\partial b_x}{\partial x} = \alpha \frac{\partial b_x}{\partial z}$:

$$\mathbf{f}_\mathrm{m} = \mathcal{F}(\mathbf{m})\mathbf{g} = \begin{pmatrix} m_x + \alpha m_z & m_y & 0 & 0 \\ 0 & m_x & m_y & m_z \\ \alpha m_x - m_z & 0 & -m_z & m_y \end{pmatrix} \begin{pmatrix} \dfrac{\partial b_x}{\partial x} \\ \dfrac{\partial b_x}{\partial y} \\ \dfrac{\partial b_y}{\partial y} \\ \dfrac{\partial b_y}{\partial z} \end{pmatrix} = \mathcal{F}_\alpha(\mathbf{m}) \tag{II.52}$$

And the following matrices are analyzed with respect to three basic dipole moments of magnetic microrobot:

$$\mathcal{F}_\alpha \begin{pmatrix} m \\ \beta m \\ 0 \end{pmatrix} = m \begin{pmatrix} 1 & \beta & 0 & 0 \\ 0 & 1 & \beta & 0 \\ \alpha & 0 & 0 & \beta \end{pmatrix} \tag{II.53}$$

$$\mathcal{F}_\alpha \begin{pmatrix} m \\ 0 \\ \beta m \end{pmatrix} = m \begin{pmatrix} 1+\alpha\beta & 0 & 0 & 0 \\ 0 & 1 & 0 & \beta \\ \alpha - \beta & 0 & -\beta & 0 \end{pmatrix} \tag{II.54}$$

$$\mathcal{F}_\alpha \begin{pmatrix} 0 \\ m \\ \beta m \end{pmatrix} = m \begin{pmatrix} \alpha\beta & 1 & 0 & 0 \\ 0 & 0 & 1 & \beta \\ -\beta & 0 & -\beta & 1 \end{pmatrix} \tag{II.55}$$

The predicted singular cases are then summarized in table II.3.

From the table II.3, in such relationship of magnetic gradients, it is obvious that the force control always exists singularities. For instance, when either m_y or m_z equals to zero, the magnetic force on microrobot can not be fully controlled. The other singular cases are also released in the above table that should be avoided in the further force control.

Table II.3: The singular cases caused by the linear dependent between $\frac{\partial b_x}{\partial x}$ and $\frac{\partial b_x}{\partial z}$

$\mathbf{m}^\intercal$	Relationship between β and α	Condition on α
$(m, \beta m, 0)$	$\beta = 0$	No
	$\beta = \pm\sqrt{-\frac{\sqrt{(\alpha^2+3)(\alpha-1)(\alpha+1)}}{2} - \frac{\alpha^2}{2} - \frac{1}{2}}$	No
	$\beta = \pm\sqrt{\frac{\sqrt{(\alpha^2+3)(\alpha-1)(\alpha+1)}}{2} - \frac{\alpha^2}{2} - \frac{1}{2}}$	No
$(m, 0, \beta m)$	$\beta = 0$	No
	$\beta = -\frac{1}{\alpha}$	No
$(0, m, \beta m)$	$\beta = \pm\sqrt{-\frac{\sqrt{(\alpha^2-2\alpha+2)(\alpha^2+2\alpha+2)}+\alpha^2+2}{2\alpha^2}}$	$\alpha = 0$
	$\beta = \pm\sqrt{-\frac{\alpha^2-\sqrt{(\alpha^2-2\alpha+2)(\alpha^2+2\alpha+2)}+2}{2\alpha^2}}$	$0 \leq \alpha^2 \left(\left(\alpha^2-2\alpha+2\right)\left(\alpha^2+2\alpha+2\right) - \left(\alpha^2+2\right)^2\right)$

Case #4: linear dependence between $\frac{\partial b_x}{\partial x}$ and $\frac{\partial b_y}{\partial z}$

Similarly, if $\frac{\partial b_x}{\partial x} = \alpha\frac{\partial b_y}{\partial z}$, the Eq. (II.31) is here written as:

$$\mathbf{f}_\mathrm{m} = \mathcal{F}(\mathbf{m})\mathbf{g} = \begin{pmatrix} m_x & m_y & m_z & 0 \\ \alpha m_z & m_x & 0 & m_y \\ \alpha m_y - m_z & 0 & m_x & -m_z \end{pmatrix} \begin{pmatrix} \dfrac{\partial b_x}{\partial x} \\ \dfrac{\partial b_x}{\partial y} \\ \dfrac{\partial b_x}{\partial z} \\ \dfrac{\partial b_y}{\partial y} \end{pmatrix} = \mathcal{F}_\alpha(\mathbf{m}) \tag{II.56}$$

and the following matrices to be analyzed:

$$\mathcal{F}_\alpha \begin{pmatrix} m \\ \beta m \\ 0 \end{pmatrix} = m \begin{pmatrix} 1 & \beta & 0 & 0 \\ 0 & 1 & 0 & \beta \\ \alpha\beta & 0 & 1 & 0 \end{pmatrix} \tag{II.57}$$

$$\mathcal{F}_\alpha \begin{pmatrix} m \\ 0 \\ \beta m \end{pmatrix} = m \begin{pmatrix} 1 & 0 & \beta & 0 \\ \alpha\beta & 1 & 0 & 0 \\ -\beta & 0 & 1 & -\beta \end{pmatrix} \tag{II.58}$$

$$\mathcal{F}_\alpha \begin{pmatrix} 0 \\ m \\ \beta m \end{pmatrix} = m \begin{pmatrix} 0 & 1 & \beta & 0 \\ \alpha\beta & 0 & 0 & 1 \\ \alpha-\beta & 0 & 0 & -\beta \end{pmatrix} \tag{II.59}$$

The different singular cases are then summarized in table II.4.

Table II.4: The singular cases caused by the linear dependent between $\frac{\partial b_x}{\partial x}$ and $\frac{\partial b_y}{\partial z}$

$\mathbf{m}^\intercal$	Relationship between β and α	Condition on α
$(m, \beta m, 0)$	No	No
$(m, 0, \beta m)$	No	No
$(0, m, \beta m)$	$\beta = \frac{1 \pm \sqrt{-(2\alpha-1)(2\alpha+1)}}{2\alpha}$	$\alpha \neq 0 \wedge 4\alpha^2 - 1 \leq 0$

Thus, the singular case only exists when the $\frac{\partial b_x}{\partial x}$ and $\frac{\partial b_y}{\partial z}$ are linearly dependent and the dipole moment meets $m_z = \beta m_y$. The other two linear dependencies between the terms of magnetic dipole moment lead to singular-free force control.

Case #5: linear dependence between $\frac{\partial b_x}{\partial y}$ and $\frac{\partial b_x}{\partial z}$

Similarly, for the linear relation of $\frac{\partial b_x}{\partial y}$ and $\frac{\partial b_x}{\partial z}$ the Eq. (II.31) is here written as:

$$\mathbf{f}_\mathrm{m} = \mathcal{F}(\mathbf{m})\mathbf{g} = \begin{pmatrix} m_x & m_y + \alpha m_z & 0 & 0 \\ 0 & m_x & m_y & m_z \\ -m_z & \alpha m_x & -m_z & m_y \end{pmatrix} \begin{pmatrix} \frac{\partial b_x}{\partial x} \\ \frac{\partial b_x}{\partial y} \\ \frac{\partial b_y}{\partial y} \\ \frac{\partial b_y}{\partial z} \end{pmatrix} \tag{II.60}$$

The three corresponding force matrices of $(m, \beta m, 0)$, $(m, 0, \beta m)$ and $(0, m, \beta m)$ as shown in the followings:

$$\mathcal{F}_\alpha \begin{pmatrix} m \\ \beta m \\ 0 \end{pmatrix} = m \begin{pmatrix} 1 & \beta & 0 & 0 \\ 0 & 1 & \beta & 0 \\ 0 & \alpha & 0 & \beta \end{pmatrix} \tag{II.61}$$

$$\mathcal{F}_\alpha \begin{pmatrix} m \\ 0 \\ \beta m \end{pmatrix} = m \begin{pmatrix} 1 & \alpha\beta & 0 & 0 \\ 0 & 1 & 0 & \beta \\ -\beta & \alpha & -\beta & 0 \end{pmatrix} \tag{II.62}$$

$$\mathcal{F}_\alpha \begin{pmatrix} 0 \\ m \\ \beta m \end{pmatrix} = m \begin{pmatrix} 0 & 1 + \alpha\beta & 0 & 0 \\ 0 & 0 & 1 & \beta \\ -\beta & 0 & -\beta & 1 \end{pmatrix} \tag{II.63}$$

The different singular cases are thus summarized in table II.5.

From the Table II.5, it presents that the force control always exists singular cases when the $\frac{\partial b_x}{\partial x}$ and $\frac{\partial b_y}{\partial z}$ is linearly dependent.

Table II.5: The singular cases caused by the linear dependent between $\frac{\partial b_x}{\partial y}$ and $\frac{\partial b_x}{\partial z}$

$\mathbf{m}^\intercal$	Relationship between β and α	Condition on α
$(m, \beta m, 0)$	$\beta = 0$	No
$(m, 0, \beta m)$	$\beta = 0$	No
	$\beta = \pm\sqrt{-\frac{2\alpha^2+\sqrt{-4\alpha^4-4\alpha^2+1}+1}{4\alpha^2}}$	$\frac{2\alpha^2+\sqrt{-4\alpha^4-4\alpha^2+1}+1}{\alpha^2} \leq 0$
	$\beta = \pm\sqrt{-\frac{2\alpha^2-\sqrt{-4\alpha^4-4\alpha^2+1}+1}{4\alpha^2}}$	$\frac{2\alpha^2-\sqrt{-4\alpha^4-4\alpha^2+1}+1}{\alpha^2} \leq 0$
$(0, m, \beta m)$	$\beta = -\frac{1}{\alpha}$	No

Case #6: linear dependence between $\frac{\partial b_x}{\partial y}$ and $\frac{\partial b_y}{\partial y}$

When $\frac{\partial b_x}{\partial y}$ and $\frac{\partial b_y}{\partial y}$ are linearly dependent, the Eq. (II.31) is here written as:

$$\mathbf{f}_\mathrm{m} = \mathcal{F}(\mathbf{m})\mathbf{g} = \begin{pmatrix} m_x & m_y & m_z & 0 \\ 0 & m_x + \alpha m_y & 0 & m_z \\ -m_z & -\alpha m_z & m_x & m_y \end{pmatrix} \begin{pmatrix} \frac{\partial b_x}{\partial x} \\ \frac{\partial b_x}{\partial y} \\ \frac{\partial b_x}{\partial z} \\ \frac{\partial b_y}{\partial z} \end{pmatrix} \tag{II.64}$$

and the following matrices to be analyzed:

$$\mathcal{F}_\alpha \begin{pmatrix} m_x \\ \beta m_x \\ 0 \end{pmatrix} = m_x \begin{pmatrix} 1 & \beta & 0 & 0 \\ 0 & 1+\alpha\beta & 0 & 0 \\ 0 & 0 & 1 & \beta \end{pmatrix} \tag{II.65}$$

$$\mathcal{F}_\alpha \begin{pmatrix} m_x \\ 0 \\ \beta m_x \end{pmatrix} = m_x \begin{pmatrix} 1 & 0 & \beta & 0 \\ 0 & 1 & 0 & \beta \\ -\beta & -\alpha\beta & 1 & 0 \end{pmatrix} \tag{II.66}$$

$$\mathcal{F}_\alpha \begin{pmatrix} 0 \\ m_y \\ \beta m_y \end{pmatrix} = m_y \begin{pmatrix} 0 & 1 & \beta & 0 \\ 0 & \alpha & 0 & \beta \\ -\beta & -\alpha\beta & 0 & 1 \end{pmatrix} \tag{II.67}$$

The possible singular cases are summarized in table II.6.

The computation results indicate that only such linear magnetic dipole moment $(m, 0, \beta m)$ can reach singular-free force control.

Table II.6: The singular cases caused by the linear dependent between $\frac{\partial b_x}{\partial y}$ and $\frac{\partial b_y}{\partial y}$

$\mathbf{m}^\intercal$	Relationship between β and α	Condition on α
$(m, \beta m, 0)$	$\beta = -\frac{1}{\alpha}$	No
$(m, 0, \beta m)$	No	No
$(0, m, \beta m)$	$\beta = 0$	No
	$\beta = \pm\sqrt{-\frac{3\alpha^2-\sqrt{5\alpha^4+2\alpha^2+1}+1}{2\alpha^2+2}}$	$\left(3\alpha^2+1\right)^2 - 5\alpha^4 - 2\alpha^2 - 1 \leq 0$

Case #7: linear dependence between $\frac{\partial b_x}{\partial y}$ and $\frac{\partial b_y}{\partial z}$

Similarly, the Eq. (II.31) can be written when $\frac{\partial b_x}{\partial y} = \alpha\frac{\partial b_y}{\partial z}$:

$$\mathbf{f}_{\mathrm{m}} = \mathcal{F}(\mathbf{m})\mathbf{g} = \begin{pmatrix} m_x & m_y & m_z & 0 \\ 0 & m_x + \alpha m_z & 0 & m_y \\ -m_z & \alpha m_y & m_x & -m_z \end{pmatrix} \begin{pmatrix} \dfrac{\partial b_x}{\partial x} \\ \dfrac{\partial b_x}{\partial y} \\ \dfrac{\partial b_x}{\partial z} \\ \dfrac{\partial b_y}{\partial y} \end{pmatrix} \tag{II.68}$$

The magnetic force matrices are analyzed in dipole moment $(m, \beta m, 0)$, $(m, 0, \beta m)$ and $(0, m, \beta m)$, respectively, as the follows:

$$\mathcal{F}_\alpha \begin{pmatrix} m \\ \beta m \\ 0 \end{pmatrix} = m \begin{pmatrix} 1 & \beta & 0 & 0 \\ 0 & 1 & 0 & \beta \\ 0 & \alpha\beta & 1 & 0 \end{pmatrix} \tag{II.69}$$

$$\mathcal{F}_\alpha \begin{pmatrix} m \\ 0 \\ \beta m \end{pmatrix} = m \begin{pmatrix} 1 & 0 & \beta & 0 \\ 0 & 1+\alpha\beta & 0 & 0 \\ -\beta & 0 & 1 & -\beta \end{pmatrix} \tag{II.70}$$

$$\mathcal{F}_\alpha \begin{pmatrix} 0 \\ m \\ \beta m \end{pmatrix} = m \begin{pmatrix} 0 & 1 & \beta & 0 \\ 0 & \alpha\beta & 0 & 1 \\ -\beta & \alpha & 0 & -\beta \end{pmatrix} \tag{II.71}$$

The different singular cases are thereby summarized in table II.7.

The obtained results show that only the magnetic dipole moment $(m, \beta m, 0)$ can achieve singular-free force control when $\frac{\partial b_x}{\partial y}$ and $\frac{\partial b_y}{\partial z}$ exist linear dependence.

Table II.7: The singular cases caused by the linear dependent between $\frac{\partial b_x}{\partial y}$ and $\frac{\partial b_y}{\partial z}$

$\mathbf{m}^\intercal$	Relationship between β and α	Condition on α
$(m, \beta m, 0)$	No	No
$(m, 0, \beta m)$	$\beta = -\frac{1}{\alpha}$	No
$(0, m, \beta m)$	$\beta = 0$	No
	$\beta = \pm\sqrt{-\frac{\alpha^2+\sqrt{-4\alpha^4-4\alpha^2+1}+1}{4\alpha^2}}$	$\frac{\alpha^2+\sqrt{-4\alpha^4-4\alpha^2+1}+1}{\alpha^2} \leq 0$
	$\beta = \pm\sqrt{-\frac{\alpha^2-\sqrt{-4\alpha^4-4\alpha^2+1}+1}{4\alpha^2}}$	$\frac{2\alpha^2-\sqrt{-4\alpha^4-4\alpha^2+1}+1}{\alpha^2} \leq 0$

Case #8: linear dependence between $\frac{\partial b_x}{\partial z}$ and $\frac{\partial b_y}{\partial y}$

Similarly, the Eq. (II.31) can be rearranged to Eq. (II.72) if $\frac{\partial b_x}{\partial z}$ and $\frac{\partial b_y}{\partial y}$ are linearly dependent.

$$\mathbf{f}_\mathrm{m} = \mathcal{F}(\mathbf{m})\mathbf{g} = \begin{pmatrix} m_x & m_y & m_z & 0 \\ 0 & m_x & \alpha m_y & m_z \\ -m_z & 0 & m_x - \alpha m_z & m_y \end{pmatrix} \begin{pmatrix} \frac{\partial b_x}{\partial x} \\ \frac{\partial b_x}{\partial y} \\ \frac{\partial b_x}{\partial z} \\ \frac{\partial b_y}{\partial z} \end{pmatrix} \tag{II.72}$$

and the following matrices are to be analyzed:

$$\mathcal{F}_\alpha \begin{pmatrix} m \\ \beta m \\ 0 \end{pmatrix} = m \begin{pmatrix} 1 & \beta & 0 & 0 \\ 0 & 1 & \alpha\beta & 0 \\ 0 & 0 & 1 & \beta \end{pmatrix} \tag{II.73}$$

$$\mathcal{F}_\alpha \begin{pmatrix} m \\ 0 \\ \beta m \end{pmatrix} = m \begin{pmatrix} 1 & 0 & \beta & 0 \\ 0 & 1 & 0 & \beta \\ -\beta & 0 & 1-\alpha\beta & 0 \end{pmatrix} \tag{II.74}$$

$$\mathcal{F}_\alpha \begin{pmatrix} 0 \\ m \\ \beta m \end{pmatrix} = m \begin{pmatrix} 0 & 1 & \beta & 0 \\ 0 & 0 & \alpha & \beta \\ -\beta & 0 & -\alpha\beta & 1 \end{pmatrix} \tag{II.75}$$

The different singular cases are then summarized in table II.8.

Since both the dipole moments $(m, \beta m, 0)$ and $(0, m, \beta m)$ can keep the force matrices full rank, force control can be performed with singular-free in such dipole moments. Besides, there is singular case if the dipole moment is $(m, 0, \beta m)$ that should be avoided.

Table II.8: The singular cases caused by the linear dependent between $\frac{\partial b_x}{\partial z}$ and $\frac{\partial b_y}{\partial y}$

$\mathbf{m}^\intercal$	Relationship between β and α	Condition on α
$(m, \beta m, 0)$	No	No
$(m, 0, \beta m)$	$\beta = \frac{\alpha}{2} - \frac{\sqrt{(\alpha-2)(\alpha+2)}}{2}$	$0 \leq \alpha^2 - 4$
	$\beta = \frac{\alpha}{2} + \frac{\sqrt{(\alpha-2)(\alpha+2)}}{2}$	$0 \leq \alpha^2 - 4$
$(0, m, \beta m)$	No	No

Case #9: linear dependence between $\frac{\partial b_x}{\partial y}$ and $\frac{\partial b_y}{\partial z}$

Similarly, when $\frac{\partial b_x}{\partial y}$ and $\frac{\partial b_y}{\partial z}$ are linearly dependent, the Eq. (II.31) is written as:

$$\mathbf{f}_{\mathrm{m}} = \mathcal{F}(\mathbf{m})\mathbf{g} = \begin{pmatrix} m_x & m_y & m_z & 0 \\ 0 & m_x & \alpha m_z & m_y \\ -m_z & 0 & m_x + \alpha m_y & -m_z \end{pmatrix} \begin{pmatrix} \frac{\partial b_x}{\partial x} \\ \frac{\partial b_x}{\partial y} \\ \frac{\partial b_x}{\partial z} \\ \frac{\partial b_y}{\partial y} \end{pmatrix} \tag{II.76}$$

With the three specific dipole moments as represented as Eq. (II.41), the following matrices of magnetic force will be analyzed:

$$\mathcal{F}_\alpha \begin{pmatrix} m \\ \beta m \\ 0 \end{pmatrix} = m \begin{pmatrix} 1 & \beta & 0 & 0 \\ 0 & 1 & 0 & \beta \\ -\beta & 0 & 1+\alpha\beta & 0 \end{pmatrix} \tag{II.77}$$

$$\mathcal{F}_\alpha \begin{pmatrix} m \\ 0 \\ \beta m \end{pmatrix} = m \begin{pmatrix} 1 & 0 & \beta & 0 \\ 0 & 1 & \alpha\beta & 0 \\ -\beta & 0 & 1 & -\beta \end{pmatrix} \tag{II.78}$$

$$\mathcal{F}_\alpha \begin{pmatrix} 0 \\ m \\ \beta m \end{pmatrix} = m \begin{pmatrix} 0 & 1 & \beta & 0 \\ 0 & 0 & \alpha\beta & 1 \\ -\beta & 0 & \alpha & -\beta \end{pmatrix} \tag{II.79}$$

The different singular cases are then summarized in table II.9.

As presented in the Table II.9, the dipole moment in form $(m, \beta m, 0)$ can achieve singular-free force control when $\frac{\partial b_x}{\partial z}$ is linearly dependent with $\frac{\partial b_y}{\partial z}$. The singular cases exist in force control when dipole moment is $(m, o, \beta m)$ or $(0, m, \beta m)$.

Table II.9: The singular cases caused by the linear dependent between $\frac{\partial b_x}{\partial z}$ and $\frac{\partial b_y}{\partial z}$

$\mathbf{m}^\intercal$	Relationship between β and α	Condition on α
$(m, \beta m, 0)$	No	No
$(m, 0, \beta m)$	$\beta = \pm\sqrt{\frac{\sqrt{-(2\alpha-1)(2\alpha+1)}-3}{2\alpha^2+4}}$	$(2\alpha-1)(2\alpha+1) \leq -9$
$(0, m, \beta m)$	$\beta = \pm\sqrt{-\frac{\sqrt{-(2\alpha^2-1)(2\alpha^2+1)}+2\alpha^2+1}{4\alpha^2+2}}$	$\sqrt{-(2\alpha^2-1)(2\alpha^2+1)}+2\alpha^2 \leq -1$
	$\beta = \pm\sqrt{-\frac{2\alpha^2-\sqrt{-(2\alpha^2-1)(2\alpha^2+1)}+1}{4\alpha^2+2}}$	$2\alpha^2-\sqrt{-(2\alpha^2-1)(2\alpha^2+1)} \leq -1$

Case #10: linear dependence between $\frac{\partial b_y}{\partial y}$ and $\frac{\partial b_y}{\partial z}$

Lastly, the Eq. (II.31) can be written as follows when $\frac{\partial b_y}{\partial y}$ and $\frac{\partial b_y}{\partial z}$ are linear dependence:

$$\mathbf{f}_{\mathrm{m}} = \mathcal{F}(\mathbf{m})\mathbf{g} = \begin{pmatrix} m_x & m_y & m_z & 0 \\ 0 & m_x & 0 & m_y + \alpha m_z \\ -m_z & 0 & m_x & \alpha m_y - m_z \end{pmatrix} \begin{pmatrix} \frac{\partial b_x}{\partial x} \\ \frac{\partial b_x}{\partial y} \\ \frac{\partial b_x}{\partial z} \\ \frac{\partial b_y}{\partial y} \end{pmatrix} \tag{II.80}$$

Bringing the dipole moments Eq. (II.41) into the $\mathcal{F}(\mathbf{m})$ and thereby the following matrices are analyzed.

$$\mathcal{F}_\alpha \begin{pmatrix} m \\ \beta m \\ 0 \end{pmatrix} = m \begin{pmatrix} 1 & \beta & 0 & 0 \\ 0 & 1 & 0 & \beta \\ 0 & 0 & 1 & \alpha\beta \end{pmatrix} \tag{II.81}$$

$$\mathcal{F}_\alpha \begin{pmatrix} m \\ 0 \\ \beta m \end{pmatrix} = m \begin{pmatrix} 1 & 0 & \beta & 0 \\ 0 & 1 & 0 & \alpha\beta \\ -\beta & 0 & 1 & -\beta \end{pmatrix} \tag{II.82}$$

$$\mathcal{F}_\alpha \begin{pmatrix} 0 \\ m \\ \beta m \end{pmatrix} = m \begin{pmatrix} 0 & 1 & \beta & 0 \\ 0 & 0 & 0 & 1+\alpha\beta \\ -\beta & 0 & 0 & \alpha-\beta \end{pmatrix} \tag{II.83}$$

The possible singular cases of force control are revealed in table II.10.

The calculation results show that there is always a singularity in this linear relation between $\frac{\partial b_y}{\partial y}$ and $\frac{\partial b_y}{\partial z}$. Therefore, the magnetic dipole moment of microrobot should avoid the orientation shown in table II.10 when the mentioned magnetic gradients meet the linearly dependent relation.

Table II.10: The singular cases caused by the linear dependent between $\frac{\partial b_y}{\partial y}$ and $\frac{\partial b_y}{\partial z}$

$\mathbf{m}^\intercal$	Relationship between β and α	Condition on α
$(m, \beta m, 0)$	$\beta = \pm\sqrt{-\frac{\sqrt{(\alpha^2+3)(\alpha-1)(\alpha+1)}}{2} - \frac{\alpha^2}{2} - \frac{1}{2}}$	$\frac{\alpha^2}{2} + \frac{1}{2} \leq -\frac{\sqrt{(\alpha^2+3)(\alpha-1)(\alpha+1)}}{2}$
	$\beta = \pm\sqrt{\frac{\sqrt{(\alpha^2+3)(\alpha-1)(\alpha+1)}}{2} - \frac{\alpha^2}{2} - \frac{1}{2}}$	$\frac{\alpha^2}{2} + \frac{1}{2} \leq \frac{\sqrt{(\alpha^2+3)(\alpha-1)(\alpha+1)}}{2}$
$(m, 0, \beta m)$	$\beta = \pm\sqrt{-\frac{\alpha^2-\sqrt{(\alpha^2-2\alpha+2)(\alpha^2+2\alpha+2)}+2}{2\alpha^2}}$	$0 \leq \alpha^2 \left(\left(\alpha^2 - 2\alpha + 2\right)\left(\alpha^2 + 2\alpha + 2\right) - \left(\alpha^2 + 2\right)^2\right)$
$(0, m, \beta m)$	$\beta = 0$	No
	$\beta = -\frac{1}{\alpha}$	No

Discussions

The Tables II.1 to II.10 summarize the different conditions to enable a linear relationship between the magnetic gradients terms of $\mathbf{g}$. If these conditions are fulfilled, the matrix $\mathcal{F}(\mathbf{m})$ is not always full rank. Thereby, the magnetic force control becomes singular because the matrix $\mathcal{F}(\mathbf{m})$ is not full rank when any two magnetic gradients exist linear dependence. It means that magnetic force $\mathbf{f}_\mathrm{m}$ cannot be controlled in some orientations and positions where non-full rank happens. To apply an arbitrary force $\mathbf{f}_\mathrm{m}$ on the microrobot in any position $\mathbf{p} \in \Omega$ and orientation requires the all five magnetic gradients, whose terms must be controlled independently.

It is obvious that the magnetic gradient is a variation in the magnetic field $\mathbf{B}$ with respect to position. Thus, when the magnetic gradients are applied on a microrobot for providing propulsion force, it is synchronously placed in a global magnetic field. According to Eq. (II.21), if the magnetic field $\mathbf{B}$ is changing, a magnetic torque $\mathbf{t}_\mathrm{m}$ is simultaneously generated on the microrobot, which will change its magnetic moment orientation and then affects the applied magnetic force. For an EMA system to continuously apply a desired force, it must be capable of controlling the microrobot's orientation, and updating the magnetic gradients faster than the change of dipole-moment direction. Therefore, the control of magnetic field should be considered when applying magnetic gradient to the microrobot.

II.3.3 Combined torque and force control

Torque control can be analyzed directly through the magnetic field properties, as expressed in eq. (II.37). Commonly, the three magnetic fields components are required to generate magnetic torque to align microrobot to any directions in the workspace Ω. As discussed above, the control of the five independent magnetic gradients is the necessary and sufficient condition for a singular-free force control. Hence, the Eq. (II.37) can be used to analyze the combined torque and force control. In addition, from equation Eq. (II.37), the matrix $\mathcal{B}$ and matrix $\mathcal{G}$ are combined as

a 6×8 matrix defined as:

$$\mathbf{C}(\mathbf{m}) = \begin{pmatrix} \mathbb{1} & \mathbb{0} \\ \mathbb{0} & \mathcal{F}(\mathbf{m}) \end{pmatrix} \tag{II.84}$$

The first three columns are the expansion of the identity matrix $\mathbb{1}$, thus there is no singular case. The last five columns are relevant to force control. The above matrix $\mathbf{C}(\mathbf{m})$ can be reduced to $\mathcal{C}(\mathbf{m})$ that is a 6×7 matrix by replacing a linear combination between one of the first three columns and one of the last five columns. The obtained matrix $\mathcal{C}(\mathbf{m})$ describes an EMA system where there is a linear dependence between the magnetic field and its gradient, similarly to Eqns. (II.39), (II.48), (II.52), (II.56), (II.60), (II.64), (II.68), (II.72), (II.76) and (II.80).

Moreover, the all 10 singular cases have been already investigated regarding linearly dependent relations of magnetic gradients. There is always a singular case if any one of such 10 linear dependencies exists. Besides, there are 3 linear dependencies between magnetic fields. As discussed, these 3 linear relations will lead to singular case of field control. Thus, only the linear dependence between the first three columns and last five columns should be considered in the analysis of the matrix $\mathbf{C}$. In fact, there are totally 28 linear dependencies in the matrix $\mathbf{C}(\mathbf{m})$.

Consequently, there are 10 dependent relationships between each magnetic gradients, and 3 linear dependencies between the magnetic fields. Since, there is a total of 28 linear dependencies in the matrix $\mathcal{C}$, thereby, the linear combinations between fields and gradients are 15. These linear relationships are investigated hereafter.

Let us recall that an unrestrained magnetic microrobot will be aligned with the applied field direction for quasi-static manipulations. Specifically, we assume that the direction of magnetic moment changes slower compared to the rotational time of the alignment of the microrobot with the $\mathbf{B}$-field.

Case #A: linear dependencies on $\frac{\partial b_x}{\partial x}$

Let us define the linear dependencies between the magnetic gradient component $\frac{\partial b_x}{\partial x}$ and the magnetic field $\mathbf{B} = (b_x, b_y, b_z)^\intercal$ with the following linear relations: a) $\frac{\partial b_x}{\partial x} = \alpha b_x$, b) $\frac{\partial b_x}{\partial x} = \alpha b_y$, and c) $\frac{\partial b_x}{\partial x} = \alpha b_z$, with $\alpha \in \mathbb{R}^*$ a coefficient. The corresponding matrix $\mathcal{C}(\mathbf{m})$ can be expressed respectively as follows:

$$\mathcal{C}_a = \begin{pmatrix} 1 & 0 & 0 & 0 & 0 & 0 & 0 \\ 0 & 1 & 0 & 0 & 0 & 0 & 0 \\ 0 & 0 & 1 & 0 & 0 & 0 & 0 \\ \alpha m_x & 0 & 0 & m_y & m_z & 0 & 0 \\ 0 & 0 & 0 & m_x & 0 & m_y & m_z \\ -\alpha m_z & 0 & 0 & 0 & m_x & -m_z & m_y \end{pmatrix}, \mathcal{C}_b = \begin{pmatrix} 1 & 0 & 0 & 0 & 0 & 0 & 0 \\ 0 & 1 & 0 & 0 & 0 & 0 & 0 \\ 0 & 0 & 1 & 0 & 0 & 0 & 0 \\ 0 & \alpha m_x & 0 & m_y & m_z & 0 & 0 \\ 0 & 0 & 0 & m_x & 0 & m_y & m_z \\ 0 & -\alpha m_z & 0 & 0 & m_x & -m_z & m_y \end{pmatrix}, \mathcal{C}_c = \begin{pmatrix} 1 & 0 & 0 & 0 & 0 & 0 & 0 \\ 0 & 1 & 0 & 0 & 0 & 0 & 0 \\ 0 & 0 & 1 & 0 & 0 & 0 & 0 \\ 0 & 0 & \alpha m_x & m_y & m_z & 0 & 0 \\ 0 & 0 & 0 & m_x & 0 & m_y & m_z \\ 0 & 0 & -\alpha m_z & 0 & m_x & -m_z & m_y \end{pmatrix} \tag{II.85}$$

When $\frac{\partial b_x}{\partial x}$ and b_x are linearly dependent, it is obvious that the matrix $\mathcal{C}_a$ is not full rank. The magnetic force on the x-direction is directly related to the magnetic field when the dipole moment is $\mathbf{m} = (m_x, 0, 0)^\intercal$. That is the magnitude of magnetic field will be proportional to the magnetic force required in the dependent direction. However, when the force is applied to a direction, the orientation of the microrobot may be affected due to the linear dependence between the generated force and the applied field.

Moreover, there is still an issue on the sign of the force that can not be changed. Anyway, we assume that the magnetic field is used to align the microrobot magnetic moment along the same direction, that is: $m_x = \beta b_x$, with $\beta \in \mathbb{R}^*$ a coefficient. From the above analysis, the

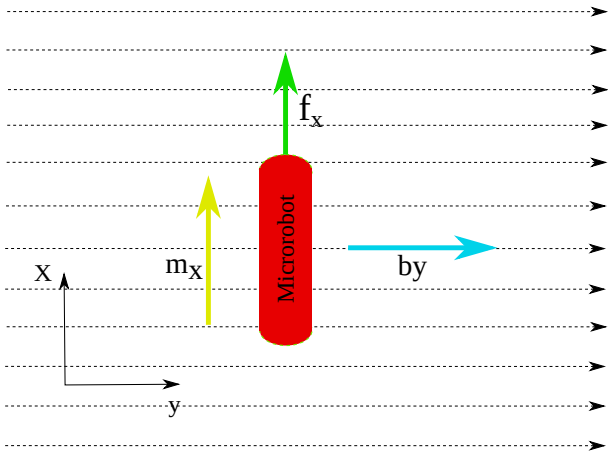

Figure II.5: The illustration of the contradiction of microrobot orientation and magnetic field for generating magnetic force.

x-directed magnetic force is not linearly independent to the magnegtic field, which is expressed as: $f_x = \alpha b_x m_x = \alpha\beta b_x^2$. Hence, the sign of f_x can not be changed because the sign of dipole moment and the sign of field are always the same.

Therefore, such control system requires a nonmagnetic restoring force in the x-direction. If a suitable nonmagnetic restoring force exists, the EMA system with the linear dependence between $\frac{\partial b_x}{\partial x}$ and b_x can be used to control the microrobot in the desired direction and position, thus, at least 7 inputs are required.

Some other linearly dependent relationships between magnetic field and its gradient can cause physical impossibility. For instance, a contradiction exists between the orientation of the microrobot and the direction of magnetic field. Indeed, the orientation of microrobot should be aligned along direction of magnetic field as we assumed.

When $\frac{\partial b_x}{\partial x}$ and b_y are linearly dependent, and if $\mathbf{m} = (m_x, 0, 0)^\intercal$, it is impossible for any EMA system to apply a magnetic force in the x-direction. In this case, the force is expressed by $f_x = \alpha b_y m_x$. Obviously, it is impossible to apply a magnetic force in the x-direction . The reason is that it is not feasible to align the microrobot along the x-axis when the magnetic field is applied in the y-direction. As shown in the Figure II.5, the desired magnetic force requires that the orientation of the microrobot is aligned in x-direction that demands the applied magnetic field is aligned to x-direction. However, the magnetic field is applied to y-direction due to the assumed linear dependence. Hence, the desired magnetic force can not be produced in respect of such dependent relation. Similarly, when $\frac{\partial b_x}{\partial x}$ and b_z are in linear dependence, and dipole moment is $\mathbf{m} = (m_x, 0, 0)^\intercal$, the magnetic force can be expressed as $f_x = \alpha b_z m_x$. This x-direction magnetic force can not be generated due to the constraint that the magnetic field aligns the microrobot to applied direction.

Case #B: linear dependencies on $\frac{\partial b_x}{\partial y}$

Let us consider the linear dependencies of the magnetic gradient component $\frac{\partial b_x}{\partial y}$ with the following linear relations: d) $\frac{\partial b_x}{\partial y} = \alpha b_x$, e) $\frac{\partial b_x}{\partial y} = \alpha b_y$, and f) $\frac{\partial b_x}{\partial y} = \alpha b_z$. The matrix $\mathcal{C}(\mathbf{m})$ is

written respectively into the following matrices:

$$\mathcal{C}_d = \begin{pmatrix} 1 & 0 & 0 & 0 & 0 & 0 & 0 \\ 0 & 1 & 0 & 0 & 0 & 0 & 0 \\ 0 & 0 & 1 & 0 & 0 & 0 & 0 \\ \alpha m_y & 0 & 0 & m_x & m_z & 0 & 0 \\ \alpha m_x & 0 & 0 & 0 & 0 & m_y & m_z \\ 0 & 0 & 0 & -m_z & m_x & -m_z & m_y \end{pmatrix}, \mathcal{C}_e = \begin{pmatrix} 1 & 0 & 0 & 0 & 0 & 0 & 0 \\ 0 & 1 & 0 & 0 & 0 & 0 & 0 \\ 0 & 0 & 1 & 0 & 0 & 0 & 0 \\ 0 & \alpha m_y & 0 & m_x & m_z & 0 & 0 \\ 0 & \alpha m_x & 0 & 0 & 0 & m_y & m_z \\ 0 & 0 & 0 & -m_z & m_x & -m_z & m_y \end{pmatrix}, \mathcal{C}_f = \begin{pmatrix} 1 & 0 & 0 & 0 & 0 & 0 & 0 \\ 0 & 1 & 0 & 0 & 0 & 0 & 0 \\ 0 & 0 & 1 & 0 & 0 & 0 & 0 \\ 0 & 0 & \alpha m_y & m_y & m_z & 0 & 0 \\ 0 & 0 & \alpha m_x & 0 & 0 & m_y & m_z \\ 0 & 0 & 0 & -m_z & m_x & -m_z & m_y \end{pmatrix} \tag{II.86}$$

First, we discuss the impossible situations. In the matrix $\mathcal{C}_d$, the magnetic force $f_x = \alpha b_x m_y$ on the x-axis is physically impossible when the dipole moment is assumed given as $\mathbf{m} = (0, m_y, 0)^\intercal$. Indeed, the orientation of microrobot is rotated to x-direction instead of y-direction when magnetic field is applied to x-direction. Thus, for this configuration, the magnetic force can not be applied in the y-direction. Similarly, for the matrix $\mathcal{C}_e$, the magnetic force in y-direction is physically impossible when dipole moment is assumed as $\mathbf{m} = (m_x, 0, 0)^\intercal$. As shown in its expression $f_y = \alpha b_y m_x$, the applied magnetic field will align microrobot to y-direction instead of x-direction. There are two physical incompatibilities when $\frac{\partial b_x}{\partial y} = \alpha b_z$ as mapped in matrix $\mathcal{C}_f$. The magnetic force in x-direction can not be implemented when microrobot is assumed as $(0, m_y, 0)$. In the same way, the force on y-directions can not be produced with a dipole moment set as $(m_x, 0, 0)$.

Case #C: linear dependencies on $\frac{\partial b_x}{\partial z}$

Let us consider the linear dependencies of the magnetic gradient component $\frac{\partial b_x}{\partial y}$ with the following linear relations: g) $\frac{\partial b_x}{\partial z} = \alpha b_x$, h) $\frac{\partial b_x}{\partial z} = \alpha b_y$, and i) $\frac{\partial b_x}{\partial z} = \alpha b_z$. The matrix $\mathcal{C}$ is rearranged as shown in the follows:

$$\mathcal{C}_g = \begin{pmatrix} 1 & 0 & 0 & 0 & 0 & 0 & 0 \\ 0 & 1 & 0 & 0 & 0 & 0 & 0 \\ 0 & 0 & 1 & 0 & 0 & 0 & 0 \\ \alpha m_z & 0 & 0 & m_x & m_y & 0 & 0 \\ 0 & 0 & 0 & 0 & m_x & m_y & m_z \\ \alpha m_x & 0 & 0 & -m_z & 0 & -m_z & m_y \end{pmatrix}, \mathcal{C}_h = \begin{pmatrix} 1 & 0 & 0 & 0 & 0 & 0 & 0 \\ 0 & 1 & 0 & 0 & 0 & 0 & 0 \\ 0 & 0 & 1 & 0 & 0 & 0 & 0 \\ 0 & \alpha m_z & 0 & m_x & m_y & 0 & 0 \\ 0 & 0 & 0 & 0 & m_x & m_y & m_z \\ 0 & \alpha m_x & 0 & -m_z & 0 & -m_z & m_y \end{pmatrix}, \mathcal{C}_i = \begin{pmatrix} 1 & 0 & 0 & 0 & 0 & 0 & 0 \\ 0 & 1 & 0 & 0 & 0 & 0 & 0 \\ 0 & 0 & 1 & 0 & 0 & 0 & 0 \\ 0 & 0 & \alpha m_z & m_x & m_y & 0 & 0 \\ 0 & 0 & 0 & 0 & m_x & m_y & m_z \\ 0 & 0 & \alpha m_x & -m_z & 0 & -m_z & m_y \end{pmatrix} \tag{II.87}$$

When the dipole moment is assumed as $\mathbf{m} = (m_x, 0, 0)^\intercal$, the magnetic force in z-direction is physically impossible to be generated for the matrices $\mathcal{C}_h$ and $\mathcal{C}_i$. The z-direction forces in $\mathcal{C}_h$ and $\mathcal{C}_i$ are derived as $f_z = \alpha b_y m_x$ and $f_z = \alpha b_z m_x$. Obviously, the orientation of microrobot is not aligned with the direction of the applied $\mathbf{B}$-field. Such physically unachievable cases also occur to matrix $\mathcal{C}_g$ and $\mathcal{C}_h$ when dipole moment is $\mathbf{m} = (0, 0, m_z)^\intercal$. In these cases, the x-component of the magnetic force is derived as: $f_x = \alpha b_x m_z$ and $f_x = \alpha b_y m_z$, respectively, that can not be realizable when the orientation of microrobot is placed in z-direction.

Case #D: linear dependencies on $\frac{\partial b_y}{\partial y}$

Let us consider the linear dependencies of the magnetic gradient component $\frac{\partial b_y}{\partial y}$ with the following linear relations: j) $\frac{\partial b_y}{\partial y} = \alpha b_x$, k) $\frac{\partial b_y}{\partial y} = \alpha b_y$, and l) $\frac{\partial b_y}{\partial y} = \alpha b_z$. The matrix $\mathcal{C}$ can be rearranged as the following matrices for the above linear relations:

$$\mathcal{C}_j = \begin{pmatrix} 1 & 0 & 0 & 0 & 0 & 0 & 0 \\ 0 & 1 & 0 & 0 & 0 & 0 & 0 \\ 0 & 0 & 1 & 0 & 0 & 0 & 0 \\ 0 & 0 & 0 & m_x & m_y & m_z & 0 \\ \alpha m_y & 0 & 0 & 0 & m_x & 0 & m_z \\ -\alpha m_z & 0 & 0 & -m_z & 0 & m_x & m_y \end{pmatrix}, \mathcal{C}_k = \begin{pmatrix} 1 & 0 & 0 & 0 & 0 & 0 & 0 \\ 0 & 1 & 0 & 0 & 0 & 0 & 0 \\ 0 & 0 & 1 & 0 & 0 & 0 & 0 \\ 0 & 0 & 0 & m_x & m_y & m_z & 0 \\ 0 & \alpha m_y & 0 & 0 & m_x & 0 & m_z \\ 0 & -\alpha m_z & 0 & -m_z & 0 & m_x & m_y \end{pmatrix}, \mathcal{C}_l = \begin{pmatrix} 1 & 0 & 0 & 0 & 0 & 0 & 0 \\ 0 & 1 & 0 & 0 & 0 & 0 & 0 \\ 0 & 0 & 1 & 0 & 0 & 0 & 0 \\ 0 & 0 & 0 & m_x & m_y & m_z & 0 \\ 0 & 0 & \alpha m_y & 0 & m_x & 0 & m_z \\ 0 & 0 & -\alpha m_z & -m_z & 0 & m_x & m_y \end{pmatrix} \tag{II.88}$$

When $\frac{\partial b_y}{\partial y}$ is linearly dependent with either αb_x or αb_z, the magnetic force on y-direction is not achieved, because it contradicts the assumption that the magnetic field aligns the microrobot with the applied direction. Assuming that the dipole moment is $\mathbf{m} = (0, m_x, 0)^\intercal$, the expressions of the y-component of the force of matrices $\mathcal{C}_j$ and $\mathcal{C}_l$ are respectively expressed as: $f_y = \alpha b_x m_y$ and $f_y = \alpha b_z m_y$. As mentioned, in the above magnetic expressions, the microrobot is not aligned with the applied magnetic field. Hence, such linear dependencies can not generate a magnetic force in arbitrary direction.

When $\frac{\partial b_y}{\partial y}$ and αb_y are in linear dependence, it is physically possible to generate a magnetic force. However, there are still some issues that need to be investigated. Furthermore, when both $\frac{\partial b_x}{\partial x}$ and αb_x, $\frac{\partial b_y}{\partial y}$ and βb_y are linearly dependent, the matrix $\mathcal{C}$ is rearranged as:

$$\mathcal{C}_{xy} = \begin{pmatrix} 1 & 0 & 0 & 0 & 0 & 0 \\ 0 & 1 & 0 & 0 & 0 & 0 \\ 0 & 0 & 1 & 0 & 0 & 0 \\ \alpha m_x & 0 & 0 & m_y & m_z & 0 \\ 0 & \beta m_y & 0 & m_x & 0 & m_z \\ -\alpha m_z & -\beta m_z & 0 & 0 & m_x & m_y \end{pmatrix} \tag{II.89}$$

It can be shown that the dipole moment $\mathbf{m} = (0, 0, m_z)^\intercal$ precludes the magnetic force generated in z-direction, and the system becomes singular. Otherwise, if the dependence just exists the matrix $\mathcal{C}_a$ or $\mathcal{C}_k$, the EMA system can actuate a microrobot with at least 7 electromagnets to achieve heading and force control when the appropriate nonmagnetic restoring force is provided.

Case #E: linear dependencies on $\frac{\partial b_y}{\partial z}$

Let us consider the linear dependencies of the magnetic gradient component $\frac{\partial b_y}{\partial y}$ with the following linear relations: m) $\frac{\partial b_y}{\partial z} = \alpha b_x$, n) $\frac{\partial b_y}{\partial z} = \alpha b_y$, and p) $\frac{\partial b_y}{\partial z} = \alpha b_z$. The matrix $\mathcal{C}$ can be reduced to the corresponding 6×7 matrices with the above linear dependencies:

$$\mathcal{C}_m = \begin{pmatrix} 1 & 0 & 0 & 0 & 0 & 0 & 0 \\ 0 & 1 & 0 & 0 & 0 & 0 & 0 \\ 0 & 0 & 1 & 0 & 0 & 0 & 0 \\ 0 & 0 & 0 & m_x & m_y & m_z & 0 \\ \alpha m_z & 0 & 0 & 0 & m_x & 0 & m_y \\ \alpha m_y & 0 & 0 & -m_z & 0 & m_x & -m_z \end{pmatrix}, \mathcal{C}_n = \begin{pmatrix} 1 & 0 & 0 & 0 & 0 & 0 & 0 \\ 0 & 1 & 0 & 0 & 0 & 0 & 0 \\ 0 & 0 & 1 & 0 & 0 & 0 & 0 \\ 0 & 0 & 0 & m_x & m_y & m_z & 0 \\ 0 & \alpha m_z & 0 & 0 & m_x & 0 & m_y \\ 0 & \alpha m_y & 0 & -m_z & 0 & m_x & -m_z \end{pmatrix}, \mathcal{C}_p = \begin{pmatrix} 1 & 0 & 0 & 0 & 0 & 0 & 0 \\ 0 & 1 & 0 & 0 & 0 & 0 & 0 \\ 0 & 0 & 1 & 0 & 0 & 0 & 0 \\ 0 & 0 & 0 & m_x & m_y & m_z & 0 \\ 0 & 0 & \alpha m_z & 0 & m_x & 0 & m_y \\ 0 & 0 & \alpha m_y & -m_z & 0 & m_x & -m_z \end{pmatrix} \tag{II.90}$$

There is always a component of the magnetic force that is not physically achievable for the force control in these three matrices $(\mathcal{C}_m, \mathcal{C}_n, \mathcal{C}_p)$. If the dipole moment is given as $\mathbf{m} = (0, m_y, 0)^\intercal$, the magnetic forces in z-direction for matrices $\mathcal{C}_m$ and $\mathcal{C}_p$ are represented as $f_z = \alpha b_x m_y$ and $f_z = \alpha b_z m_y$, respectively. When the dipole moment is assumed to be $(0, 0, m_z)$, the magnetic force in y-direction of matrices $\mathcal{C}_m$ and $\mathcal{C}_n$ are expressed as $f_y = \alpha b_x m_z$ and $f_y = \alpha b_y m_z$, respectively. It is obvious that, in the above situations, the orientation of microrobot is different to the direction of applied magnetic field. In these cases, the microrobot will rotate to be aligned with the direction of the magnetic field instead of maintaining its orientation. Therefore, these magnetic force components can not be realized under real conditions.

Discussions

We can minimize the number of electromagnets of an EMA platform up to provide 5 DOFs control with some appropriate conditions. Actually, there is no torque that can be applied on the microrobot about its dipole moment main axis. Thus, only 2 DOFs torque control can be achieved. From the above analysis, it can be obtained that at least 7 electromagnetic coils are required for 3 DOFs force and 2 DOFs torque control of the microrobot if one of the following

linear relationships exist: $\frac{\partial b_x}{\partial x}$ and αb_x; $\frac{\partial b_y}{\partial y}$ and αb_y; or $\frac{\partial b_x}{\partial x} + \frac{\partial b_y}{\partial y}$ and αb_z (as $\frac{\partial b_x}{\partial x} + \frac{\partial b_y}{\partial y} + \frac{\partial b_z}{\partial z} = 0$). However, reducing the number of coils still causes some problems, that have to be further investigated.

First, the sign and the magnitude of the magnetic field could be affected when the EMA setup applies magnetic force to the microrobot due to the linear dependence between the magnetic field and its gradient. As we have mentioned, the sign of the total force on the microrobot can not be changed if the EMA platform only provides magnetic force without a nonmagnetic restoring force, such as gravity force. In such case, the nonmagnetic force is required to provide an offset and to stabilize the system. Besides, the orientation of the microrobot also becomes unstable if the orientation of its dipole moment and the direction of the magnetic field do not change synchronously. Thus, the dynamics of the EMA system must be fast enough to stabilize the microrobot heading. Nevertheless, the orientation of the microrobot becomes more reactive, which can induce some instabilities in case of strong changes. In addition, when the desired magnetic force is set to zero but the direction of the microrobot has to be rotated, the magnetic gradient is also affected because the magnetic gradient is related to the magnetic field. Hence, it appears clearly that additional electromagnetic coils as additional inputs would allow a more stable and reliable control of the magnetic force and torque.

Basically, a static EMA system requires 8 independent inputs for torque and force control of microrobot with 5 DOFs [149]. There are few ways to reduce the number of coils. First, the specific linear dependence between the magnetic field and its gradient can be used, and an appropriately restoring force is then required in such case. Second, some complementary inputs, that enable direct change in the magnetic field or its gradient, can be added to the system. Last but not least, a simple and efficient solution is to make some electromagnetic coils enable to move, and we thus design a *robotized EMA system*.

II.3.4 Analysis

The minimum required number of electromagnet for a stable magnetic torque and force control of EMA system is investigated in this section. Basically, if a 6 DOFs wrench control has to be designed, the EMA must provide a matrix $\mathcal{A}_b(\mathbf{m}, \mathbf{p})$ (II.37) that has to be full row rank in the workspace Ω. However, in can be easily shown that the matrix $\mathcal{A}_b(\mathbf{m}, \mathbf{p})$ can not realize full rank, as it can be only up-to 5 DOFs. It makes sense that the system can only provide 5 DOFs control including 3 DOFs force control and 2 DOFs torque control. Moreover, referring to Eq. (II.37), 3 magnetic field inputs and 5 magnetic gradient inputs are required to realize such 5 DOFs control without singularity. Hence, the stacked magnetic field and gradient matrix must be full rank, namely the number of input sources should be at least of 8. It does not mean that the configuration must include 8 electromagnets or classical coil pairs because the part of field inputs could be replaced by the electromagnets or coil pairs that are originally responsible for producing gradient inputs. Furthermore, if the number of inputs is less than 8, it is necessary to design the EMA with the admissible singular cases of control in the desired workspace.

Through mathematical analysis, we realize the 8 independent inputs should be considered for the stationary configuration. However, when the configuration is not fixed, the field and gradient distribution can change more flexible, that results in the modification of the orientation or position of coils to be investigated as the additional input parameters. Thereby, the stacked field and gradient matrices become mutative matrices, and the number of electromagnetic coils could be reduced by changing the configuration of coils.

Therefore, the minimum number of the inputs requires at least 6 to independently control

torque and force for the variable configuration instead of 8 inputs for the fixed configuration. The 6 inputs for reconfiguration case are derived because the two gradient inputs can be produced by using the field sources in different time. Once again, the number of inputs can be reduce to 7 when the three linearly dependent relationships exist as we discussed above. The appropriately direct restoring force is required for the such dependence cases. Furthermore, when configuration is variable depending on the requirements of control, as well as existing linear dependencies between field inputs and gradient inputs, the both torque and force control can be achieved by only 5 inputs. In other words, the above torque and force control all can satisfy the 5 DOFs heading and position control. However, the singularity case of the manipulating control in the given workspace should be noted for the less coils configuration. It is obvious that the different number of coils or different configurations show different performances. Normally, the reconfigurable EMA system uses similar control strategy of the inputs to the stationary system with less coils. The reconfigurable coils are able to modify the distribution of field and change the field in some local areas. In addition, the designed EMA system with reconfigurable coils makes its structure more physically simple, in exchange, the analysis of control system becomes complicated.

II.4 Discussions

The untethered microrobot is wirelessly operated by magnetic torque and force that are directly induced by the applied magnetic field and gradient generated through the electromagnetic coils. Thus, the theoretical foundation of electromagnetism is discussed. The magnetic field of electromagnetic coil is derived from a single wire and the magnetic dipole. The magnetic field from any electromagnetic coil can be considered as a magnetic dipole characterized by its magnetic moment $\mathbf{m}_e$, and the point-dipole model is proposed. This model can fit to the distant portion of the on-axis magnetic field data of the equivalent electromagnet. Since the desired workspace is far and on the electromagnet's axis, the point-dipole model remains a suitable approximation of the magnetic field.

When the magnetic dipole moment and the magnetic field are given, the induced magnetic torque and force can be easily obtained by the Maxwell's equations. The induced magnetic field aligns microrobot to a desired direction, and the magnetic force provides the propulsion force to move the microrobot to complete the task. Through the mathematical transformation the equations of torque and force can be rearranged into eq. (II.29) for more convenient investigations of the magnetic actuation. Similarly, for the given magnetic torque and force, the applied current flowing through the electromagnetic coil can be calculated by considering the pseudo-inverse of $\mathcal{A}(\mathbf{m}, \mathbf{p})$ with Eq. (II.30). If the pseudo-inverse value does not exist, it means that the given magnetic torque and force cannot be implemented. Hence, the ranks of equations of torque and force should meet the requirements if the control of torque and force is singular-free. As mentioned above, the rank of force equation is 3 and the rank torque of equation is 2, the microrobot can maximally achieves 3 DOFs translation and 2 DOFs rotation, respectively.

Next, to achieve the 5 DOFs control of microrobot, the minimum number of electromagnets is mathematical analyzed. As discussed, the 3 electromagnets can be used to 3 DOFs force control at a point, but normally all 5 electromagnets are required when the orientation of microrobot is dynamic changed. The number of electromagnets can be reduced to 4, but either a nonmagnetic restoring torque or a nonmagnetic restoring force to stabilize the system. For 2 DOFs torque control, only 3 electromagnets are required because the 3 coils can generate 3D field in workspace. Thus, combined torque and force control requires a minimum of $n = 7$ stationary electromagnets.

Similarly, the 7 electromagnets case also need some additional external conditions. To stabilize the 5 DOFs control of the microrobot, the 8 electromagnets is suggested for the fixed configuration system. Reconfigurable EMA system can achieve similar control authority to stationary system with fewer electromagnets. Only $n = 5$ electromagnets are required for torque and force control. Therefore the mobile electromagnets are more particularly considered in this thesis. Indeed, the field shape in the workspace can be modified by changing the location or orientation of the electromagnets during the motion of the microrobot is performed.

Finally, the environment of the workspace, the type of microrobot and the various magnetic tasks have been introduced in the chapter I. Beside, the required number of electromagnets for different motions control has been studied in this chapter II. On this basis, the relations between the specifications and the number of coils to design an EMA system can be proposed, and are depicted in figure II.6.

Specifically, for the design of a desired EMA system, five main characteristics of an application are required:

1. The dimensions of workspace;
2. The media of the environment;
3. The type of microrobots;
4. The medical tasks;
5. The required motion control.

First of all, the dimension of workspace is determined by the desired biomedical application that can be either 2D or 3D. The media of workspace could be divided into easy-to-operate and non-easy-to-operate for the placed microrobot. Commonly, media with high viscosity or non-Newtonian fluid and flowing status are difficult conditions to manipulate microrobot. In contrast, low viscosity and static environment is easy for operation of microrobot.

Moreover, the type of applied microrobot and its locomotion must be specified. Especially, the helical microrobot or microswimmer could be selected to move in flowing environment and/or high viscosity media since these microrobots can perform drilling motion by the rotating magnetic field. Combining with magnetic force produced by magnetic gradient, such helical microrobot or microswimmer can be also actuated by a strong propulsion force. Besides, the cylindrical, ellipsoidal, spheroidal and irregularly shaped microrobot are choices to the suitable environments. In addition, the type of locomotion of the microrobot should be determined with respect to the given application. As presented in figure II.6, 6 main types of biomedical applications are here considered. But, a distinction is made according to a 2D or 3D workspace that is considered. For 2D workspace, as illustrated in figure II.6a, 4 main types of biomedical applications are considered for 2D workspace: i) surface treatment, ii) marking/sensing, iii) *in vitro* micromanipulation, and iv) controllable structure. Whereas for 3D biomedical operations, the main types of tasks are: i) material removal, ii) marking/sensing, iii) targeted therapy, and iv) controllable structure, as depicted in figure II.6b. For instance, almost all types of microrobot could be used for targeted drug delivery. However, spheroidal microrobot rather than helical microrobot is suitable for marking/sensing application. If helical microrobot is applied for targeted drug delivery, the possible motion of microrobot is required as translation and rotation. If spheroidal microrobot is used for targeted drug delivery, the possible motion could be translation, rotation and punching.

Finally, the number of electromagnetic coils is determined by the specific motions of selected microrobot. For instance, the translational locomotion can be achieved by magnetic force on spheroidal microrobot, and it can also be reached by magnetic torque generated by rotating magnetic field on helical microrobot. Considering a 3D workspace as an example, the reliable locomotion of spheroidal microrobot requires $n = 5$ numbers of electromagnets, while the locomotion of helical microrobot only demands $n = 3$ numbers of electromagnets. Similarly, other necessary information for designing EMA system can also be obtained in the same way following the figure II.6. Therefore, from the above five requirements, the specifications of desired EMA system are obtained.

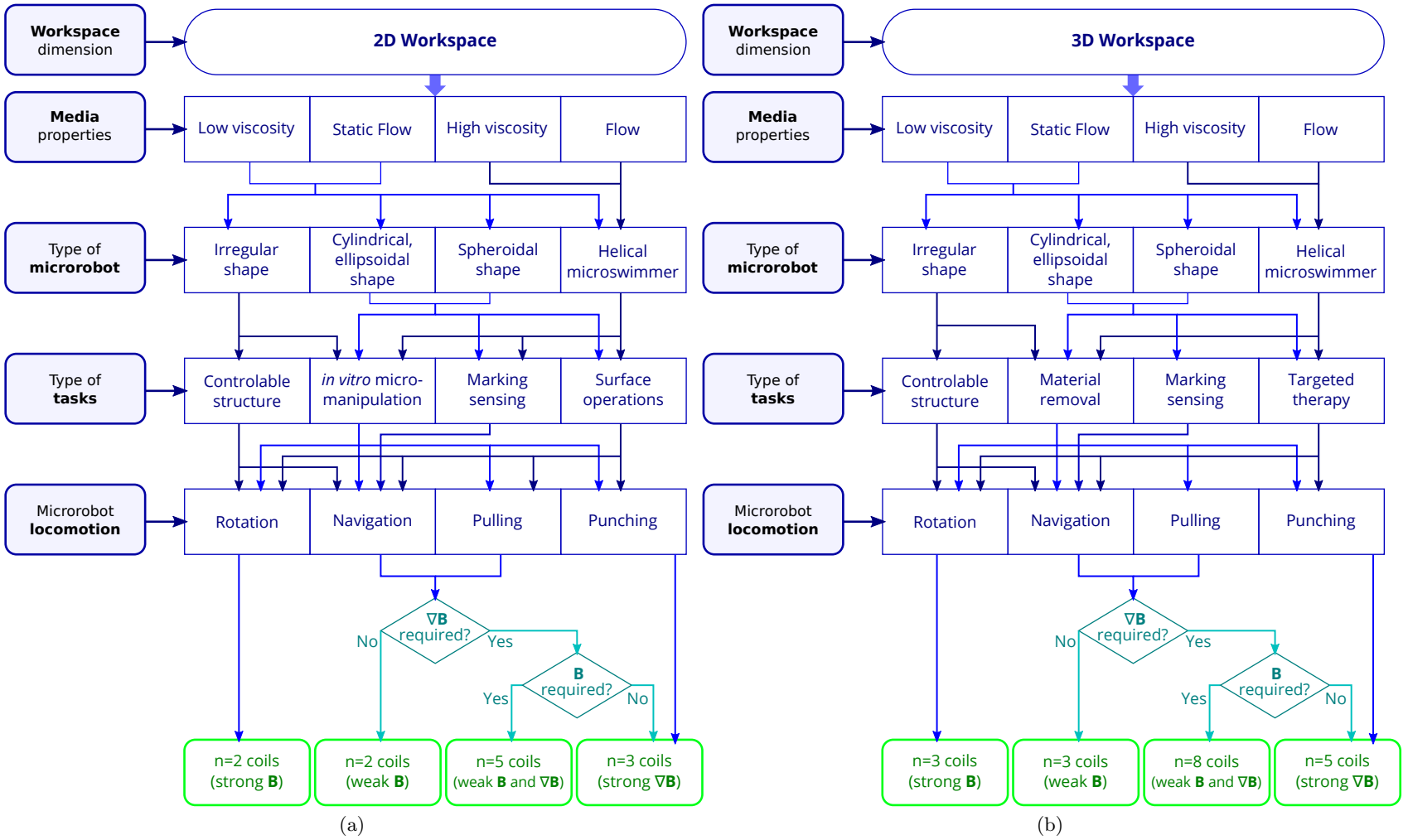

Figure II.6: The diagram of the specifications of EMA system design for (a) 2D and (b) 3D workspaces.

II.5 Conclusion

In the chapter, theoretical foundation of electromagnetism has been studied, especially, the point-dipole model is analyzed for magnetic field simulation. Moreover, the electromagnetic manipulation of the untethered microrobot is investigated where the motion includes translation and rotation actuated by magnetic force and torque, respectively. Furthermore, the required minimum electromagnetic coils for EMA system are estimated mathematically. Indeed, the linear dependencies regarding the applied field and gradient, and their resulting singular cases have been fully investigated. Obtaining the specifications of EMA system, the various arrangements of electromagnetic coils will be studied hereafter. Simulation and optimization of the performance of EMA system are presented in next chapter.

Chapter III

Simulation and Optimization of the Performance of EMA system

Chapter contents

Introduction

In this chapter, the simulations of various EMA systems are realized to analyze their performances. Indeed, when the number of electromagnets is determined, their spatial arrangement can be then studied. As discussed in Chapter II, the magnetic field and its gradient are generated by the electromagnets of the designed EMA system. Thus, the magnetic field characteristics can be investigated according to different configurations. Moreover, various performance metrics for EMA system will be proposed. These indexes are necessary to quantitatively evaluate EMA setup performances and can further be used to compare different configurations of electromagnets. Basically, the average and uniformity indexes are defined to characterize the strength and the homogeneity within the workspace. Besides the magnetic field characteristics, the magnetic actuation capabilities of the EMA platform are also of prime importance. Inspired by robotic mechanisms, kinematic performance indexes, such as the manipulability index and the matrix condition number are proposed by considering the magnetic actuation matrix $\mathcal{A}(\mathbf{m}, \mathbf{p})$ given by Eq. (II.29). Indeed, this matrix $\mathcal{A}(\mathbf{m}, \mathbf{p})$ gives back the microrobot magnetic control efficiency for the considered EMA system. Then, the possible singular cases of the microrobot motion control can be determined from poor value of kinematic performance indexes.

(a) (b) (c)

Figure III.1: Representation of the different basic multi-electromagnet setups: (a) a 3D arrangement of a six-electromagnet system; (b) and (c) present the 3D placed eight-electromagnet system corresponding to the OctoMag [60] and MiniMag [61], respectively.

When the characteristic metrics are defined, the simulation and optimization of various configurations of electromagnets are then conducted with the aim to analyze their effectiveness. However, it seems difficult to consider all possible electromagnets arrangements. Therefore, we have chosen to focus here[1] on 3D organized configurations depicted in figure III.1. Indeed, commonly, EMA setups with a 3D configuration are more useful for a wider range of biomedical applications [43], [49], [50], [58]–[79]. Particularly, configurations such as the well-known OctoMag [60] and MiniMag [61] are investigated. The relevant configuration will be proposed mainly based on the study of the 3D arrangement of electromagnets. Once again, as stated in Chapter II, the stationary configuration of electromagnets still has inadequacy and limitations that cannot remove the existing singularities of motion control. Through the study of various arrangements of electromagnets, it can be shown that the different EMA configurations always have their own advantages and drawbacks at some locations of the workspace. One objective of this PhD thesis is to try to integrate as many advantages as possible in the designed EMA

[1]The flat configuration of EMA systems including 4, 6 and 8 magnets are reported in the chapter A.

system. Therefore, the numerous simulations results and analysis lead us to propose an EMA platform comprising a reconfigurable arrangement of their electromagnets. This solution should be composed of many benefits, such as less singular positions, flexible and dexterous motion control and efficient energy use. With these goals, the modeling, simulations and optimization are performed in the following sections. Finally, let us notice that this Chapter III will focus mainly on the spatial organization of the electromagnets. The appropriate design of the electromagnetic coils system will be addressed in Chapter IV.

III.1 Modeling of multiple electromagnets system

This section comprises the selection of configurable parameters, and the generation of the magnetic field considering the transformation matrix for the modeling of multi-coil system. First, the size of workspace and the strength of generated magnetic field **B** are considered as important design parameters. Thus, the distance between the electromagnet to the workspace center should be optimized to get the good balance with respect to its dimension and the magnetic field strength. Basically, the electromagnets should surround the workspace to provide it a proper magnetic field distribution. Their positions and orientations will then determine the EMA system arrangements. Hence, these organizations are studied through their positioning distances and heading directions with respect to the workspace. When the configuration of electromagnets is given, the magnetic field distribution induced by the EMA platform can be then analyzed. At first glance, for a multi-electromagnet system the global magnetic field can be superposed, and its computation can start with a single electromagnetic field distribution. When an electromagnet lays around the workspace, the magnetic field calculated by Eq. (II.17) is represented in its local frame instead of the workspace frame. The homogeneous transformations are required, and are determined by the arrangement of each electromagnet. Thus, the magnetic field generation in the reference frame is evaluated.

III.1.1 Design parameters for the electromagnets arrangement

Different multi-electromagnet systems have been investigated by researchers for various applications, and especially for the biomedical field [30], [43], [49], [50], [52]–[79]. In this PhD thesis, we aim to propose a framework for the design of an EMA platform that enables invasiveness and safer procedure for biomedical applications, with a particular attention to assisted MIS procedures. The proposed solutions should provide a higher degree of dexterity allowing a magnetic microrobot to navigate efficiently and reliably within a confined volume. Therefore, the basic objective of the envisioned EMA setup must provide:

- the sufficient and adjustable magnetic actuation in any position and direction in the workspace, for any magnetic microrobot's location and orientation;
- a usable 2D workspace (e.g. about few square centimeters) for planar applications, or a 3D workspace (e.g. about few cubic centimeters);
- a proper organization of electromagnets with enough versatility compared with the shape of applied human parts, such as head, limbs, shoulders, and so on.

With the above requirements, the arrangement of electromagnets will be designed. Indeed, on the one hand the magnetic actuation capabilities are related to the magnets source, and on the other hand the volume of the workspace is related to the placement of the electromagnets, hence both of them are affected intrinsically by the configuration of the electromagnets.

Commonly, the sources of magnetic field should be placed as close to the target as possible to achieve stronger field strength. Erni *et al.* [145] show some approximate reference values for how much space the system should provide on the different applications. The small EMA systems with a characteristic length of 50 mm are designed for *in vitro* applications and for small animals. For small human body parts, such as the ears and eyes, the systems should consider a characteristic length of about 100 mm. Whereas for big human parts, such as the knee or abdomen, large systems with a characteristic length of about 400 mm are required. For instance, the OctoMag system is designed for MIS intervention in the human eyes with the means of magnetic microrobot navigating in a viscous fluid media, and a characteristic length of 130 mm enabling a 3D workspace of about 45 mm × 45 mm × 45 mm [60]. Specifically, the microrobot is assumed to move in a low Reynolds number regime ($R_e \ll 1$) exhibiting a non-Newtonian rheological behavior [81]. Thereby, with a fixed size of workspace, the electromagnets could be set slightly away from workspace center. However, if the electromagnetic coil is placed too far away from the working area, the effective control of the corresponding EMA system will decrease significantly due to weak performance of the magnetic source. Thus, the distance between the electromagnet and the center of the workspace should be chosen as a design parameter for studying the various configurations of electromagnets. Basically, it is difficult to induce a strong magnetic field or gradient in deep tissue. Therefore, for the envisioned application, the boundary values of the generated magnetic field and gradient in the workspace should be investigated within various dispositions of electromagnets.

Moreover, the workspace can be studied not only with different sizes, but also in different shapes. The workspace is determined by both the given application and the external related equipment (microscope, light, tools, etc.), and it is shaped through specific arrangement of electromagnets. For example, for either a drug delivery application within a knee, or a medical treatment in the arm part, the electromagnets could be placed on both sides of the member to provide the desired magnetic field. Whereas the electromagnets should be arranged on the front side of the eyeballs for an ophthalmic MIS intervention. Therefore, the organization of the magnets will be also a design parameter that will be investigated in this chapter. Based on the considered arrangement information, combined with the magnetic field distribution, the feasible configuration of the electromagnets will be analyzed.

III.1.2 Magnetic field generated in the workspace

In Chapter II, we have set out that 3 magnetic fields and 5 magnetic gradients inputs are required to achieve up to 5 DOFs control of microrobot without singularity. At least $n = 8$ magnets for a stationary arrangement are required, or $n = 6$ for the reconfigurable case. Among possible magnetic sources, permanent magnets exhibit an advantageous volume to field-strength ratio. However, the induced magnetic fields are difficult to be accurately adjusted, and cannot be switched off [55]. Next, though the air-filled electromagnet exhibit a smaller magnetic field per volume, a soft-magnetic core can be used to increase the induced magnetic field. Contrarily to systems consisting of air-core electromagnets (e.g. Helmoltz or Maxwell coils), core-filled electromagnets exhibit a nonlinear and coupled behavior. However, electromagnets with cores made of soft-magnetic materials (such as unalloyed iron, iron alloys based on silicon or aluminum.)

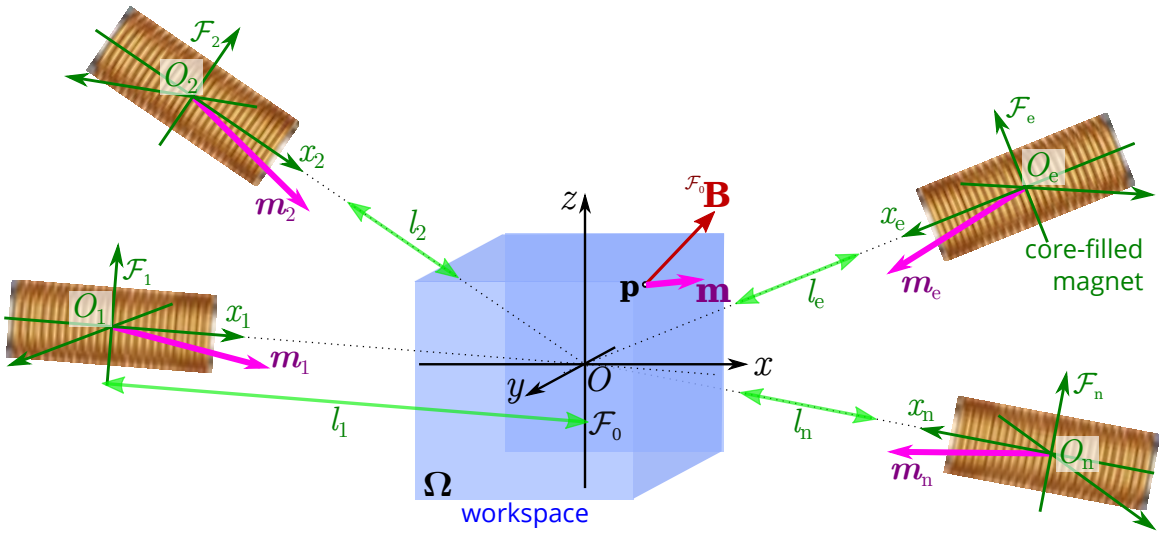

Figure III.2: Schematic representation of a multiple electromagnets system inducing a magnetic flux $\mathbf{B}(\mathbf{p})$ within the workspace Ω (blue square box). The length l_e represents the distance between the coil center O_e to the workspace center O.

impose only a minor constraint on modeling and control [60]. For these reasons, we have chosen to focus on core-filled electromagnets in this work.

Let us to consider a set of n electromagnets that creates a magnetic field ${}^{\mathcal{F}_0}\mathbf{B}(\mathbf{p})$ at any point $\mathbf{p}$ in the workspace Ω, as illustrated in figure III.2. This overall magnetic field is assumed to be the sum of the contributions of all individual electromagnets. Recall that when the current input i_e flows through the coils e, the corresponding magnetic field can be expressed as: $\mathbf{B}_e(\mathbf{p}) = \widetilde{\mathbf{B}}_e(\mathbf{p})i_e$. A key step is thus to compute this magnetic field produced by the electromagnets e. Several models, based either on numerical or analytical approaches, have been proposed in the literature. Numerical models are commonly based on maps of the magnetic field obtained either from FEM or from experimental measurement of the field $\mathbf{B}_e$. Those numerical method allows a good accuracy, but at the cost of an important calculation time. Analytical methods are often based on dipole approximation which offers a better computation time, or even on elliptical integrals [154]–[156]. Hybrid approaches, using a map of the magnetic field obtained from FEM and a fitting of an analytical model can be also considered, such as in [60]. The choice of the method commonly leads to make the best trade-off between speed and accuracy. As in this PhD thesis, numerous simulations are realized, we assume that the magnetic field $\mathbf{B}_e(\mathbf{p})$ induced by the electromagnet e can be approximated by the *magnetic point-dipole model* given by Eq. (II.17) and presented in section II.1.3. Specifically, the point-dipole model expresses the magnetic field ${}^{\mathcal{F}_e}\mathbf{B}_e(\mathbf{p})$ of the coils e with respect to its own frame $\mathcal{F}_e(O_e : x_e, y_e, z_e)$, as shown in figure III.2, and can be written as:

$$ {}^{\mathcal{F}_e}\mathbf{B}_e(\mathbf{p}) = \frac{\mu_0}{4\pi|\mathbf{p}|^3}\left(\frac{3\,(\mathbf{m}_e \cdot \mathbf{p})}{|\mathbf{p}|^2} - \mathbf{m}_e\right) \tag{III.1} $$

where $\mathbf{m}_e$ is the equivalent magnetic dipole moment related to the magnet source e for a unit current input. Indeed, for the sake of clarity and simplicity, we assume that each electromagnet e can be approximated by its analogous dipole moment $\mathbf{m}_e$. The corresponding design of the electromagnetic coil will be addressed later.

The magnetic field ${}^{\mathcal{F}_e}\mathbf{B}_e(\mathbf{p})$ can be then expressed in the reference frame $\mathcal{F}_0(O:x,y,z)$ linked to the workspace center using the homogeneous transformation:

$$ {}^{\mathcal{F}_0}\mathbf{B}_e(\mathbf{p}) = {}^{\mathcal{F}_0}\mathbf{T}_{\mathcal{F}_e} \times {}^{\mathcal{F}_e}\mathbf{B}_e(\mathbf{p}) \tag{III.2} $$

where the homogeneous transformation matrix is basically defined as:

$$ {}^{\mathcal{F}_0}\mathbf{T}_{\mathcal{F}_e} = \left(\begin{array}{c|c} {}^{\mathcal{F}_0}\mathbf{R}_{\mathcal{F}_e} & {}^{\mathcal{F}_0}\mathbf{t}_{\mathcal{F}_e} \\ \hline \mathbf{0} & 1 \end{array} \right) \tag{III.3} $$

where ${}^{\mathcal{F}_0}\mathbf{R}_{\mathcal{F}_e}$ and ${}^{\mathcal{F}_0}\mathbf{t}_{\mathcal{F}_e}$ denote the rotation and translation matrices with respect to the reference frame $\mathcal{F}_0$, respectively.

The overall magnetic field distribution in the workspace produced by a set of n electromagnetic coils can be thus superposed, that is:

$$ \begin{aligned} {}^{\mathcal{F}_0}\mathbf{B}(\mathbf{p}) = \sum_{e=1}^{n} {}^{\mathcal{F}_0}\mathbf{B}_e(\mathbf{p}) &= \sum_{e=1}^{n} {}^{\mathcal{F}_0}\tilde{\mathbf{B}}_e(\mathbf{p}) i_e = {}^{\mathcal{F}_0}\mathcal{B}(\mathbf{p})\mathbf{i} \\ &= \begin{pmatrix} {}^{\mathcal{F}_0}\tilde{\mathbf{B}}_1(\mathbf{p}) & \dots & {}^{\mathcal{F}_0}\tilde{\mathbf{B}}_n(\mathbf{p}) \end{pmatrix} \mathbf{i} \end{aligned} \tag{III.4} $$

with the input currents $\mathbf{i} = (i_1, i_2, \dots, i_n)^\mathsf{T}$.

It can be easily shown that the total magnetic field ${}^{\mathcal{F}_0}\mathbf{B}(\mathbf{p})$ in the workspace can be changed not only thanks to the currents $\mathbf{i}$, but also by varying the position and/or orientation of electromagnets. If the electromagnet is dynamically moved following a control strategy, a similar current-control approach can be designed.

III.2 Performance metrics for EMA system

As stated, though the required number of electromagnets is fixed, numerous arrangements can be obtained through setting their positions and orientations. For instance, Kummer *et al.* [60] have proposed the OctoMag platform with a hemispheric organization of 8 stationary coils. Similarly, the MiniMag system occupies a hemisphere with a tilted arrangement [58], [61]. In contrast, Diller *et al.* [73] have developed a compact EMA system where the electromagnets are surrounding the workspace. Figure III.3 illustrates these three examples of arrangements.

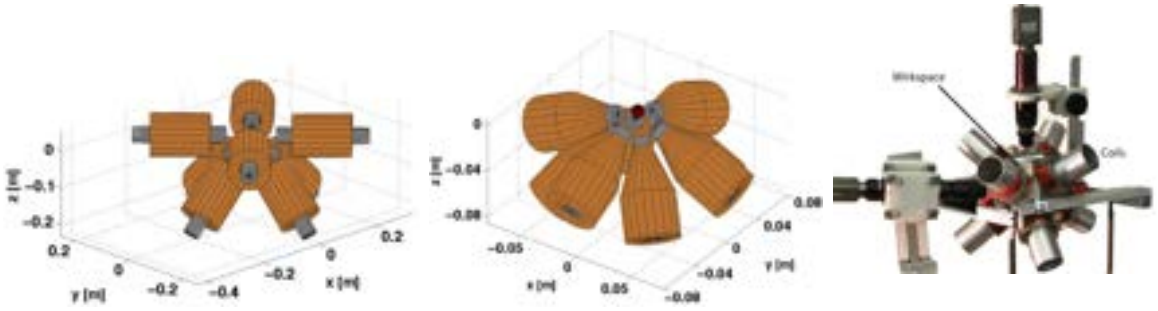

(OctoMag) (MiniMag) (Diller et al. platform)

Figure III.3: Examples of 8 coils arrangement (adapted from [58] and [73]).

To be able to compare such various electromagnetic coils dispositions, it is necessary to define some metrics to get some quantitative assessments of their effectiveness. The basic idea is to set a *score* to a given EMA configuration to allow an effective comparative analysis. Indeed, with respect to the applications objectives, different indexes can be defined and considered.

III.2.1 Magnetic field Indexes

First, the strength and homogeneity of either the magnetic field or its gradient in the workspace are the most significant metrics for medical applications. As example, a strong magnetic field strength leads to powerful torque $\mathbf{t}_\mathrm{m}$ enabling reliable swimming of the helical microrobot. In the meantime, it should be homogeneous along the workspace to simplify the control strategy. Furthermore, the EMA system needs to avoid unexpected magnetic force when varying the orientation of microrobot along with the magnetic field. Similarly, a strong magnetic gradient provides an effective propulsion force $\mathbf{f}_\mathrm{m}$, and its uniformity implies a homogeneous net force on microrobots. To this aim, various indexes can be used from statistical analysis of the fields distributions, such as its maximum, mean, root mean square (RMS), standard deviation (STD), etc. To evaluate the quality of a magnetic field or its gradient, we have chosen to consider mainly the average and the uniformity indexes introduced hereafter.

Average index

In [56], the authors propose to characterize the strength of a sampled vector field φ by its average (i.e. the arithmetic mean) basically defined as:

$$\langle \varphi \rangle = \frac{1}{N} \sum_{\mathbf{p} \in \Omega}^{N} \varphi(\mathbf{p}) \tag{III.5}$$

with N the number of samples, and $\mathbf{p}$ the sampling location in the workspace Ω. This arithmetic mean value reflects the *strength* of a global vector field φ. It can be utilized to quantify the average of the magnitudes of a magnetic field or its gradient from the corresponding samples, and then to evaluate the strength of the torque or force in the workspace.

Uniformity index

The isotropy index measures and yields an intuitive value for the difference between each considered vector of a vector field φ distribution. To evaluate the isotropy, various indexes can be considered, such as the basic minimum-to-maximum ratio, or the coefficient of variation. For a vector field φ, the *uniformity index* γ is usually considered, which is defined as:

$$\gamma(\varphi) = 1 - \frac{1}{2N \langle \varphi \rangle} \sum_{\mathbf{p} \in \Omega}^{N} |\varphi(\mathbf{p}) - \langle \varphi \rangle| \qquad \text{(in \%)} \tag{III.6}$$

where the isotropy index γ should be commonly bounded between 0% and 100%. Then, a uniformity index close to 100% indicates that every sample of the field φ is almost identical.

III.2.2 Magnetic Actuation Indexes

In the other hand, the EMA system has to actuate a magnetic microrobot in the workspace. Hence, the ability to perform or not certain motion at any location and direction is of prime importance. Basically, if there exists some singularities, some motions cannot be achieved, and the DOFs of the microrobot is reduced. For an EMA system, this analysis can be performed through the examination of its magnetic actuation matrix $\mathcal{A}(\mathbf{m}, \mathbf{p})$. As described in Eq. (II.29), $\mathcal{A}(\mathbf{m}, \mathbf{p})$ allows mapping the input currents $\mathbf{i}$ to the magnetic torque and force that are applied to a microrobot possessing a magnetic moment $\mathbf{m}$ at the location $\mathbf{p} \in \Omega$. Hence, the actuation matrix $\mathcal{A}(\mathbf{m}, \mathbf{p})$ can be seen as a *Jacobian matrix*. Commonly, the Jacobian matrix of a system is used to characterize the control efficiency. Here, the columns of the actuation matrix $\mathcal{A}(\mathbf{m}, \mathbf{p})$ represents the wrench on the magnetic microrobot. As long as $\mathcal{A}(\mathbf{m}, \mathbf{p})$ is singularity-free or merely well-conditioned, the direct mapping will exist and full wrench control of the microrobot can be achieved in the workspace. Thus, the structure of $\mathcal{A}(\mathbf{m}, \mathbf{p})$ has to be analyzed to determine the "wrench-kinematic" performance of the EMA system. Therefore, the magnetic actuation matrix provides a similar information as a classic Jacobian matrix in robotics.

There are numerous studies on the kinematic performance indexes of robotic mechanisms [157]–[160]. Most of proposed metrics were derived from the definition of *manipulability index*, introduced by Yoshikawa [158].

Manipulability index

From classic robotic kinematics, measuring the manipulability is a well-known technique for determining the ability to maneuver in workspace. Specifically, manipulability describes the degree to which a robot can freely apply forces and torques in arbitrary directions, and quantifies the ability to perform an action quickly and skillfully [158]. To do so, the manipulability index is defined as a quality measure describing the distance to singular configurations. The approach is based on analyzing the *manipulability ellipsoid* that is spanned by the singular vectors of the Jacobian. Similarly, we investigate the mapping efficiency between the current input $\mathbf{i}$ to the torque and force with this standard manipulability ellipsoid. Figure III.4 illustrates the manipulability ellipsoid, here in 2D, where the minor axis σ_2 represents the direction with the worse kinematic capacity, whereas the major axis σ_1 gives the easiest direction of force/torque transmission. Specifically, from the manipulability ellipsoid, the product of the ellipsoid's axes leads to the manipulability index which gives a measure of the maneuverability of the EMA system, and it is defined as [158]:

$$w(\mathcal{A}) = \sqrt{\det(\mathcal{A}\mathcal{A}^{\intercal})} \tag{III.7}$$

Commonly, the manipulability ellipsoids can be computed from singular value decomposition (SVD) factorization. Let the SVD of a matrix $\mathcal{A}$ be:

$$\mathcal{A} = \mathbf{U}\Sigma\mathbf{V}^{\intercal} \tag{III.8}$$

where the $\mathbf{U}$ and $\mathbf{V}$ are orthogonal matrices, with $\mathbf{U}$ a 6×6 unitary matrix and $\mathbf{V}$ a $n \times n$

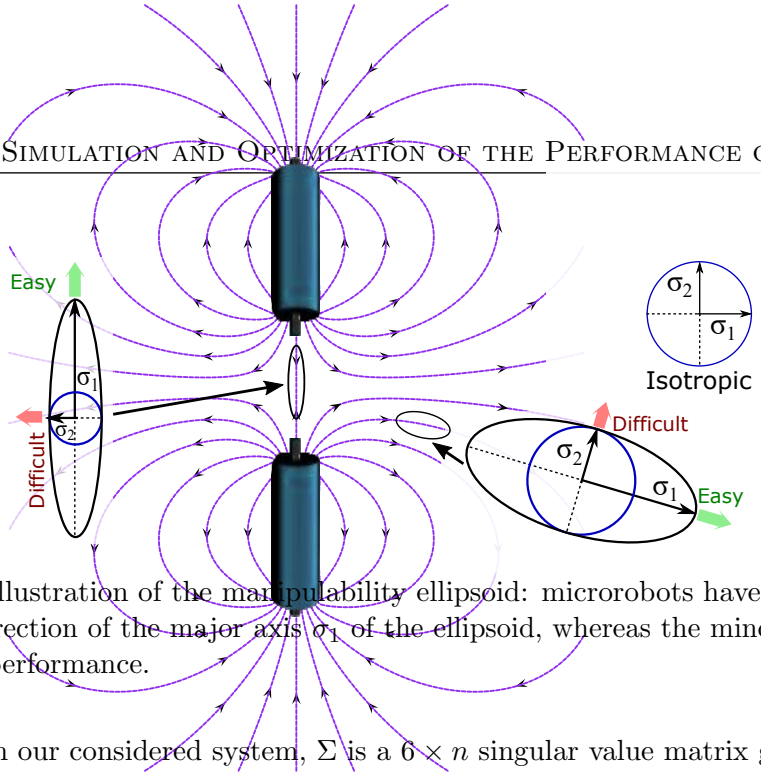

Figure III.4: 2D illustration of the manipulability ellipsoid: microrobots have better kinematic capacity in the direction of the major axis σ_1 of the ellipsoid, whereas the minor axis σ_2 induces worse kinematic performance.

unitary matrix. In our considered system, Σ is a $6 \times n$ singular value matrix given as follows:

$$\Sigma = \begin{pmatrix} \sigma_1 & 0 & 0 & 0 & 0 & 0 & 0 & \cdots & 0 \\ 0 & \sigma_2 & 0 & 0 & 0 & 0 & 0 & \cdots & 0 \\ 0 & 0 & \sigma_3 & 0 & 0 & 0 & 0 & \cdots & 0 \\ 0 & 0 & 0 & \sigma_4 & 0 & 0 & 0 & \cdots & 0 \\ 0 & 0 & 0 & 0 & \sigma_5 & 0 & 0 & \cdots & 0 \\ 0 & 0 & 0 & 0 & 0 & \sigma_6 & 0 & \cdots & 0 \end{pmatrix} \tag{III.9}$$

where $\sigma_1 \geq \sigma_2 \geq \ldots \geq \sigma_6 \geq 0$ are the singular values of $\mathcal{A}$. The singular values are significant indexes for the evaluation of system and that can be considered as a scalar gain by which each input is multiplied to produce the corresponding output.

Since the singular values give information about the quality of the workspace [158], the product of all singular values can be used to analyze the control capability of points or configurations in certain directions. Thereby, the measure of manipulability index w can be expressed as the product of the singular values:

$$w(\mathcal{A}) = \prod_{e=1}^{n} \sigma_e \tag{III.10}$$

It can be noticed that w is proportional to the volume of the manipulability ellipsoid. Generally, a larger measure of w indicates a better conditioning of the actuation matrix $\mathcal{A}(\mathbf{m}, \mathbf{p})$, that means an effective control of the microrobot. Hence, the manipulability index w measures the "distance" from singularities, that represents the capability of the EMA system to control efficiently the magnetic microrobot.

Finally, as the above manipulability index Eq. (III.7) depends on the scale or units, the normalized manipulability can be preferred:

$$w_n = \frac{w(\mathcal{A}(\mathbf{m}, \mathbf{p}))}{\max\limits_{\mathbf{p} \in \Omega} w(\mathcal{A}(\mathbf{m}, \mathbf{p}))} \tag{III.11}$$

Condition number

Another way to characterize the manipulability ellipsoid is to measure its isotropy. This is commonly achieved by computing the condition number of a matrix, which is defined as:

$$\kappa(\mathcal{A}) = \|\mathcal{A}\| \|\mathcal{A}^{\dagger}\| \in [1; +\infty) \tag{III.12}$$

where $\mathcal{A}^{\dagger}$ is the Moore-Penrose pseudo-inverse of $\mathcal{A}$, and $\|.\|$ denotes the Euclidean (or Frobenius) norm defined as:

$$\|\mathcal{A}\| = \sqrt{\mathrm{tr}\left(\mathcal{A}\mathbf{W}\mathcal{A}^{\intercal}\right)} \tag{III.13}$$

with $\mathbf{W}$ a weighting matrix, and especially, $\mathbf{W} = \mathbb{I}$ for the Euclidean norm.

To evaluate the control accuracy and isotropy of system, the inverse of the condition number of a matrix, also termed as *isotropic index*, was introduced by Salisbury and Craig [157], and is defined as:

$$1/\kappa = \frac{\sigma_{\min}}{\sigma_{\max}} = \frac{\sigma_6}{\sigma_1} \in [0;1] \tag{III.14}$$

The isotropic index indicates how well the microrobot can move in all directions, and characterizes in some sense the *dexterity* of the microrobot [160]. Therefore, when $1/\kappa\left(\mathcal{A}(\mathbf{m},\mathbf{p})\right)$ is close to 1, its manipulability ellipsoid is more close to be a sphere, which means the EMA system has more capacity to transmit the same force or torque in all directions (see also figure III.4).

III.2.3 Discussions

As discussed previously in Chapter II, any considered EMA system can enable the motion control of magnetic microrobots to only 5-DOFs. Actually, no torque $\mathbf{t}_{\mathrm{m}}$ can be produced on the microrobot dipole main axis. Therefore, to evaluate the performance indexes related to the torque $\mathbf{t}_{\mathrm{m}}$, the corresponding null singular value should be removed. Similarly, the same reasoning is applied for the other cases when some DOFs are lost.

Secondly, let us notice that the previous indexes are only local metrics for a dedicated location $\mathbf{p} \in \Omega$. To evaluate the system efficiency over the workspace Ω, many global performance indexes have been proposed [159], [160]. Classically, to define such global performance indexes, the integral of a local performance index ξ over a domain $\mathcal{W}$ is considered given by Eq. (III.15) or its sampled expression Eq. (III.16):

$$\Gamma_{\xi}(\mathcal{A}) = \frac{\int_{\mathcal{W}} \xi(\mathcal{A}) d\mathcal{W}}{\int_{\mathcal{W}} d\mathcal{W}} \tag{III.15}$$

$$\Gamma_{\xi}(\mathcal{A}) = \frac{1}{N} \sum_{x \in \mathcal{W}}^{N} \xi(\mathcal{A}, x) \tag{III.16}$$

When the domain is the workspace, that is $\mathcal{W} = \Omega \subset \mathbb{R}^3$ and $x = \mathbf{p}$, and for $\xi = w_n$, $\Gamma_{w_n}(\mathcal{A})$ leads to the *global manipulability index*. Similarly, for $\xi = 1/\kappa$, $\Gamma_{1/\kappa}(\mathcal{A})$ denotes the *global isotropic index*, also termed as the *global conditioning index* [159], [160].

Likewise, we can evaluate the performance indexes for any direction of the magnetic moment $\mathbf{m}$ by considering the 3D rotation group as domain, leading to: $\mathcal{W} = \mathrm{SO}(3)$. In the following, to express the orientation of the magnetic moment, we will consider the spherical coordinate representation, as shown in figure III.5. Obviously, when both location $\mathbf{p} \in \Omega$ of the microrobot and the orientation of its magnetic moment $\mathbf{m}$ are considered, the domain is defined accordingly, that is $\mathcal{W} = \Omega \times \mathrm{SO}(3)$.

In this PhD thesis, the global performance metrics consisting of the average index (III.5), the uniformity index (III.6), the normalized manipulability index (III.11), and the (inverse) condition number (III.14) for EMA systems are proposed. The considered configuration of electromagnets is estimated in relation with these proposed performance metrics. Thereby, the

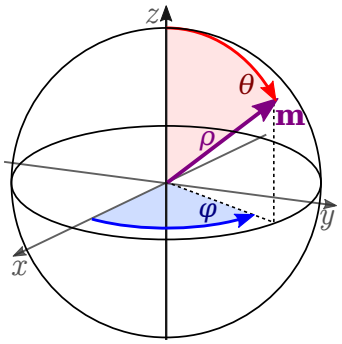

Figure III.5: Spherical coordinates (ρ, θ, φ) with ρ the radial distance, θ the polar angle, and φ azimuthal angle.

various configurations can be quantitatively evaluated for their magnetic field distribution and actuation efficiency.

III.3 Simulation and Evaluation of 3D stationary EMA system

The configuration of the EMA system should be designed in regard with the considered application and objectives. Especially, the arrangement of electromagnets must be adapted to the application geometry. In general, most EMA configurations can be divided into 2D (e.g. flat configurations) and 3D organized electromagnets. The 2D arrangement with $n = 4$, 6 and 8 coils are presented in the chapter A. The 3D configuration with $n = 6$ and 8 coils illustrated in figure III.1 are further investigated in the following. Specifically, the various performance indexes of the induced magnetic field, its gradient and actuation matrix $\mathcal{A}(\mathbf{m}, \mathbf{p})$ will be analyzed for each considered configuration.

To this aim, numerous simulations have been realized using the magnetic point-dipole model Eq. (III.1) to calculate the magnetic fields ${}^{\mathcal{F}_e}\mathbf{B}_e(\mathbf{p})$ generated by the different electromagnetic coils[2], which are then projected in the reference frame $\mathcal{F}_0$ with Eq. (III.2). In the simulations, each coil is computed with the same unit current leading to a magnetic moment magnitude of: $\|\mathbf{m}_e\| = 8.178\,\mathrm{A\,m^2}$, comparable to the data from the OctoMag setup [60]. To be consistent, a workspace of at least $\Omega = 45\,\mathrm{mm} \times 45\,\mathrm{mm} \times 45\,\mathrm{mm}$ is considered throughout the simulations. The microrobot is modeled from its magnetic moment $\mathbf{m} = (1, \theta, \varphi)$, with a unit magnitude; but its orientation may vary and would be expressed with the spherical coordinate representation, with azimuth angles $\varphi \in [0; 360°)$ and polar angles $\theta \in [0; 180°]$, as depicted in figure III.5.

III.3.1 3D organized six-electromagnet EMA system

The considered 3D six-coil EMA system is shown in figure III.1a. It consists of three pairs of opposing electromagnets aligned along the x, y and z-axis. For the sake of simplicity, we consider that each coil has the same distance $l_1 = l_2 = l_3 = l_4 = d_w$ between their center O_e to the center O of the workspace (see also figure III.2). Thus, the $n = 6$ identical magnets are arranged in an

[2]In this Chapter III, the electromagnetic coils are approximated solely through their point-dipole magnetic moment $\mathbf{m}_e$. Neither their geometry, nor their materials are considered here. These aspects would be taken into account and further investigated in Chapter IV.

axisymmetric way around the center O of the workspace. From this structure, it is reasonable to assume that the magnetic field $\mathbf{B}$ will become more symmetrical in the three xyz-directions.

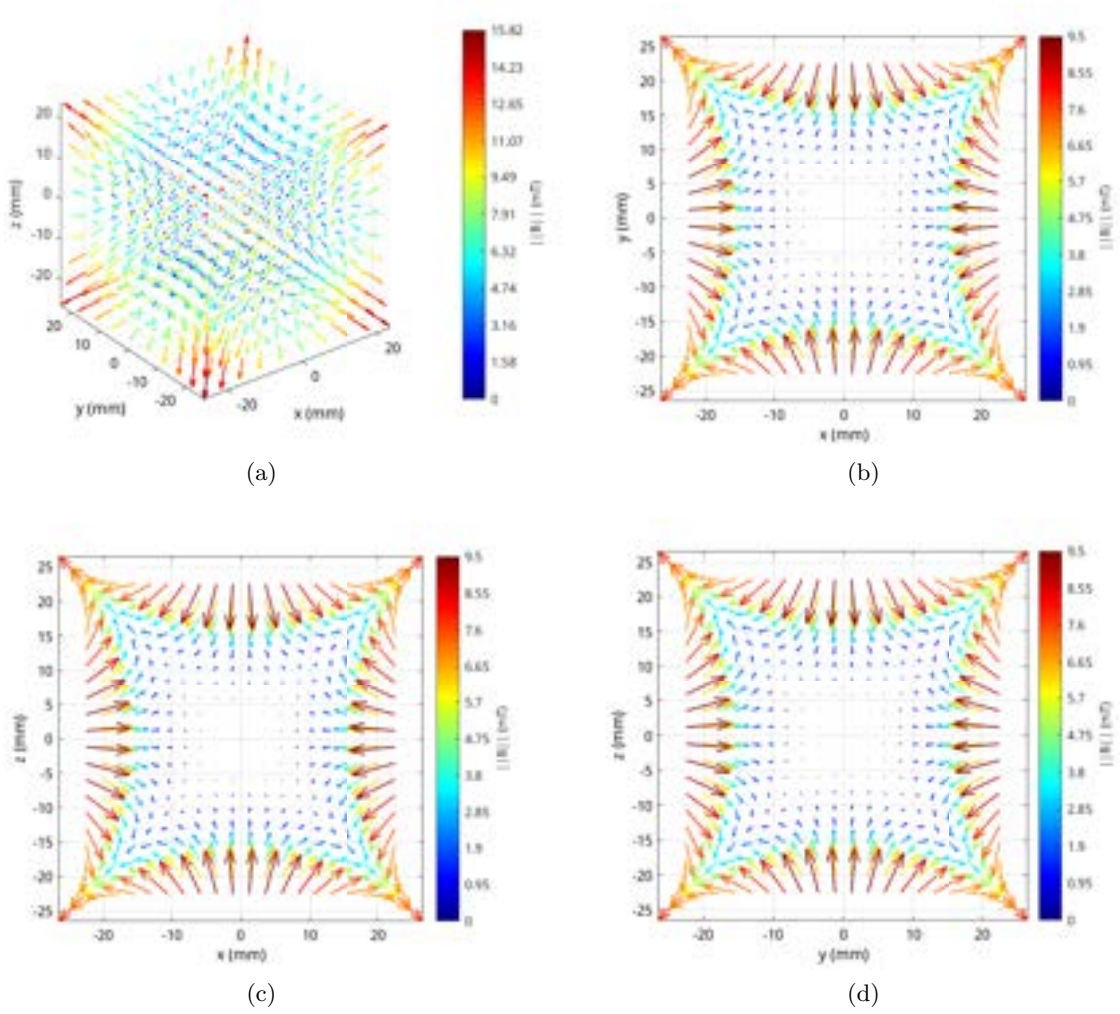

Figure III.6: The magnetic field $\mathbf{B}$ generated by the 3D organized six-coil EMA system with $d_w = 65\,\text{mm}$: (a) a 3D view, (b) the xy-plane, (c) the xz-plane and (d) the yz-plane. The colorbar indicates the magnetic field magnitude.

First, the magnetic field $\mathbf{B} = (b_x, b_y, b_z)$ generated by the 3D six-coil EMA system is analyzed and shown in figure III.6. Figure III.6a depicts the vector distributions of the magnetic field produced in the 3D workspace of $\Omega = 45\,\text{mm} \times 45\,\text{mm} \times 45\,\text{mm}$, with a woking distance set to $d_w = 65\,\text{mm}$. These results of the distribution of the magnetic field in the xy, xz and yz-plane confirm our assumption that the magnetic field behaves identically in the three planes. Figure III.7 presents the magnetic field magnitude $\|\mathbf{B}\|$ in the xy-plane for lengths of $d_w = 60\,\text{mm}$, $70\,\text{mm}$ and $80\,\text{mm}$. As expected, the distribution of the induced magnetic field strength decreases as the length d_w increases. Comparing these results from the flat six-coil arrangement in figure A.4 in Section A.1, it appears that the magnetic field magnitude is significantly reduced with the 3D organized configuration, whereas its uniformity seems improved. For instance, when the working

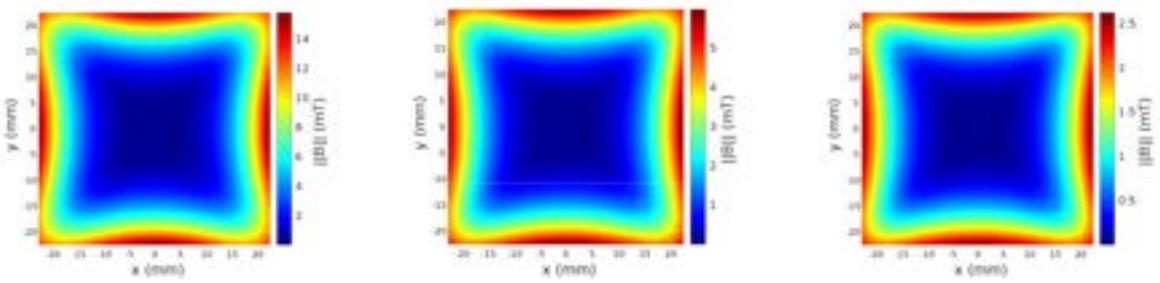

(a) (b) (c)

Figure III.7: The magnetic field magnitude $\|\mathbf{B}\|$ in the xy-plane for lengths of (a) $d_w = 60\,\text{mm}$, (b) $d_w = 70\,\text{mm}$ and (c) $d_w = 80\,\text{mm}$.

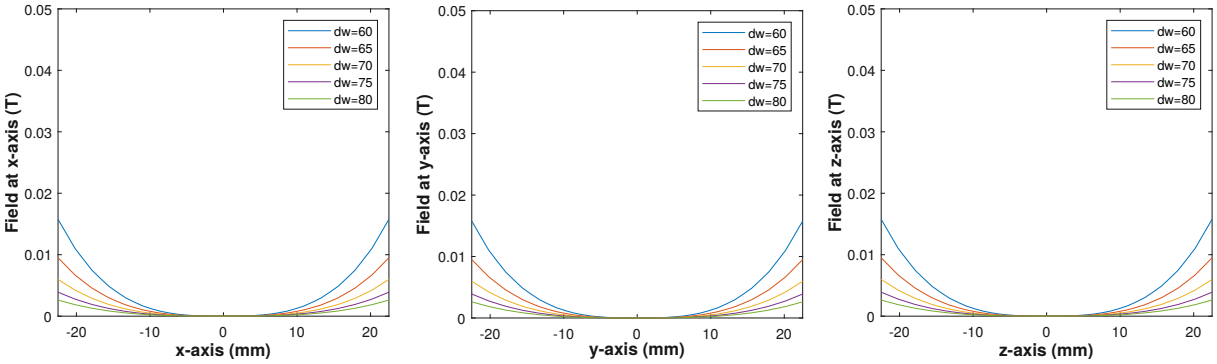

(a) (b) (c)

Figure III.8: Magnetic field magnitude $\|\mathbf{B}\|$ along (a) the x-axis, (b) the y-axis, and (c) the z-axis, for d_w ranging from 60 mm to 80 mm.

distance is set to $d_w = 60\,\text{mm}$, the maximum magnetic intensity decreases from 39.18 mT with the flat six-coil arrangement to 22.28 mT with the 3D configuration, however, its uniformity increases.

Next, figure III.8 depicts the evolution of the magnetic field strength $\|\mathbf{B}\|$ along the x, y and z axes. These results show that the magnetic field behaves equally in x and y- axis and is also similar to z-axis, that is $\|\mathbf{B}\|$ becomes weaker as the electromagnets move away from the workspace center O. It can be shown that the average of the strength of magnetic field is significantly reduced compared to the previous flat six-electromagnet EMA system in figure A.5 in Section A.1. As one can see in figure III.9, as the distance d_w increases, the average value $\langle\|\mathbf{B}\|\rangle$ of the magnetic field intensity decreases within the workspace. In particular, the components of the magnetic field have a mean value $\langle b_x\rangle$, $\langle b_y\rangle$ and $\langle b_z\rangle$ close to zero, meaning a complete symmetry of the field distribution around each axis. Furthermore, the uniformity index $\gamma(\|\mathbf{B}\|)$ slightly decreases from 47.8% to 51.1%. Interestingly, the uniformity metrics of all component of the magnetic field $\mathbf{B} = (b_x, b_y, b_z)$ are here equal, suggesting a complete isotropy between the different axes.

As the 3D six-coil arrangement is axissymetric, the magnetic field is axisymmetric around each axis, and consequently, its spatial gradient becomes axisymmetric as well. The statistical

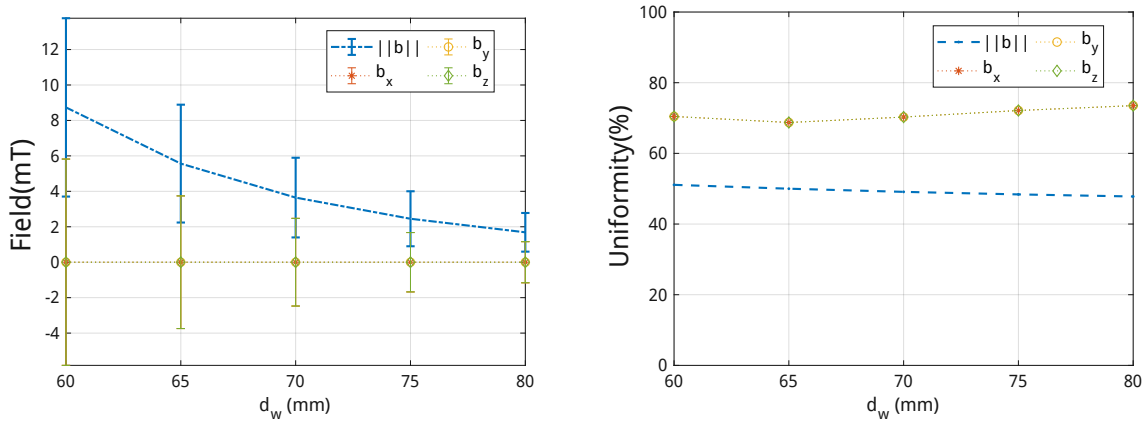

(a) (b)

Figure III.9: Magnetic field metrics: (a) error-bar showing the average and STD values; and (b) the uniformity index γ.

data of the magnetic field gradient are represented in figure III.10. It is obvious in figure III.10a that the mean values of the magnetic field gradients are very low with a value close to zero. Moreover, the uniformities γ of the magnetic field gradients components set $\left\{\frac{\partial b_x}{\partial x}, \frac{\partial b_y}{\partial y}, \frac{\partial b_z}{\partial z}\right\}$ and $\left\{\frac{\partial b_y}{\partial x}, \frac{\partial b_x}{\partial z}, \frac{\partial b_y}{\partial z}\right\}$ behave similarly with a slight decrease with longer length d_w, as reported in figure III.10b. Once again, these simulations results suggest a complete isotropy between the different planes.

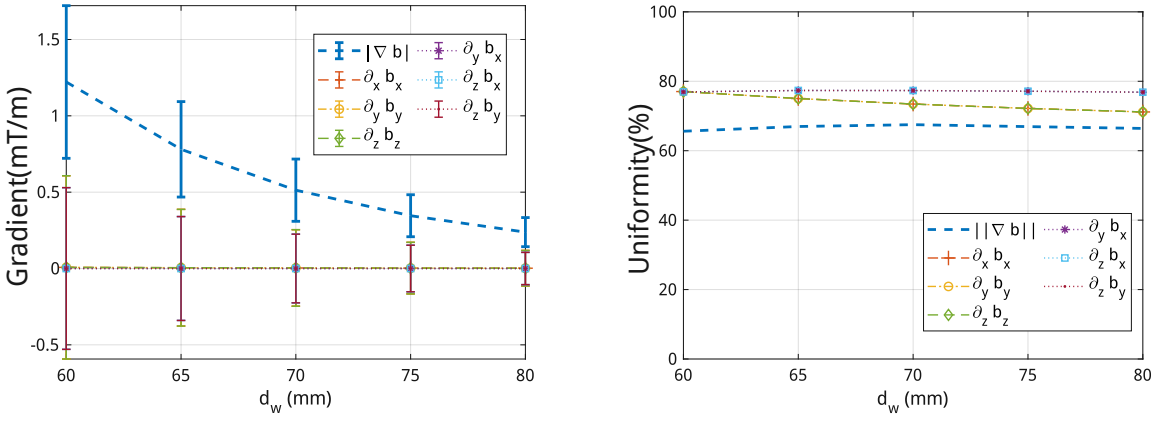

(a) (b)

Figure III.10: Magnetic field gradient metrics: (a) the mean and STD values; and (b) the uniformity index γ. $\partial_y b_x$ denotes $\frac{\partial b_x}{\partial y}$ and other symbols are similar.

Figures III.11 and III.12 illustrates the performance indexes of the actuation matrices of the force $\mathcal{A}_{\mathbf{f}_m}(\mathbf{p}, \mathbf{m})$ and of the torque $\mathcal{A}_{\mathbf{t}_m}(\mathbf{p}, \mathbf{m})$, respectively. As example, figures III.11a, III.11d, III.12a and III.12d show the performance indexes in the workspace (i.e. $\mathbf{p} \in \Omega$), when

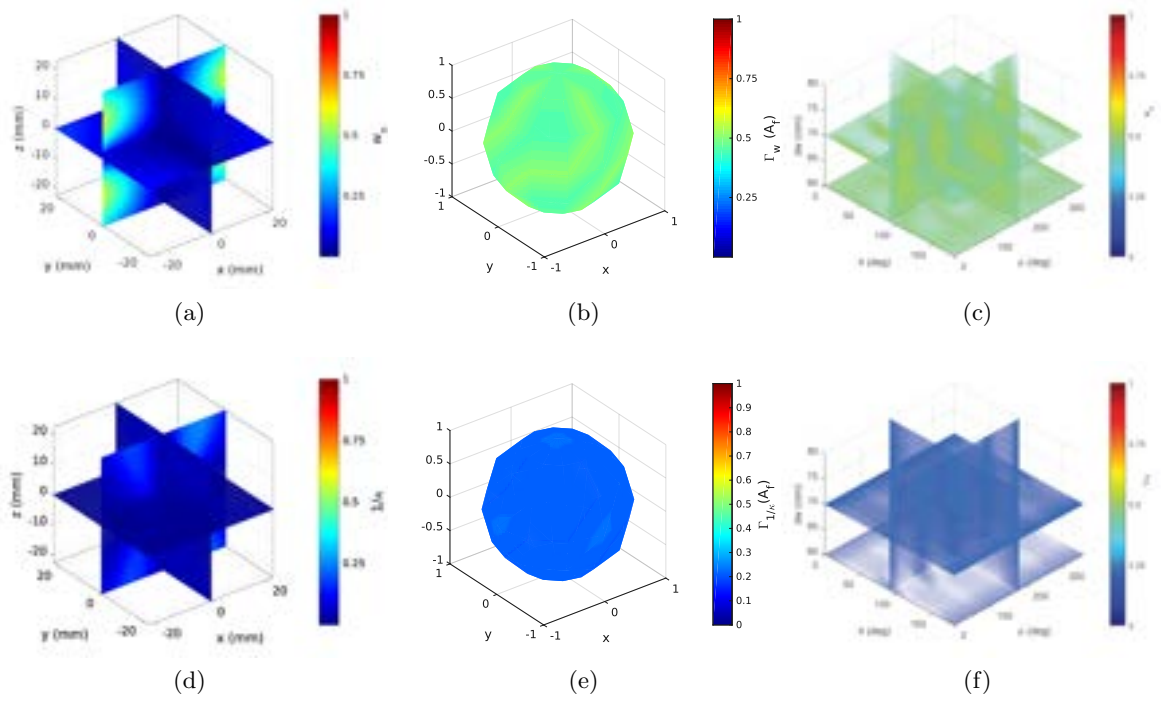

Figure III.11: Performance metrics of the force actuation matrix $\mathcal{A}_{\mathbf{f}_\mathrm{m}}$: (a) the manipulability w_n and (d) conditioning number $1/\kappa$ indexes in the workspace Ω when the magnetic moment $\mathbf{m}$ of the microrobot is aligned along the x-direction; (b) the global manipulability index $\Gamma_{w_n}(\mathcal{A}_{\mathbf{f}_\mathrm{m}})$ and (e) the global conditioning index $\Gamma_{1/\kappa}(\mathcal{A}_{\mathbf{f}_\mathrm{m}})$ for the sampled orientation of $\mathbf{m}$; and similarly (c) $\Gamma_{w_n}(\mathcal{A}_{\mathbf{f}_\mathrm{m}})$ and (f) $\Gamma_{1/\kappa}(\mathcal{A}_{\mathbf{f}_\mathrm{m}})$ as function of the working distance d_w.

the magnetic moment $\mathbf{m}$ of the microrobot is aligned along the x-axis and a working distance set to $d_w = 65\,\mathrm{mm}$. It appears clearly that the manipulabity index w_n and conditioning number $1/\kappa$ are axisymmetric. Next, figures III.11b and III.12b depict the global manipulability index of the force $\Gamma_{w_n}(\mathcal{A}_{\mathbf{f}_\mathrm{m}})$ and of the torque $\Gamma_{w_n}(\mathcal{A}_{\mathbf{t}_\mathrm{m}})$ for the sampled orientations (azimuth angles $\varphi \in [0; 360°)$ and polar angles $\theta \in [0; 180°]$) of the magnetic dipole moment $\mathbf{m}$ in the workspace and with $d_w = 65\,\mathrm{mm}$. In the same way, figures III.11e and III.12e report the global conditioning index of the force $\Gamma_{1/\kappa}(\mathcal{A}_{\mathbf{f}_\mathrm{m}})$ and of the torque $\Gamma_{1/\kappa}(\mathcal{A}_{\mathbf{t}_\mathrm{m}})$. These results show that the global performance indexes behave almost identically in all $\mathbf{m}$ direction. The global manipulability index $\Gamma_{w_n}(\mathcal{A}_{\mathbf{f}_\mathrm{m}})$ and $\Gamma_{w_n}(\mathcal{A}_{\mathbf{t}_\mathrm{m}})$, and the global conditioning index $\Gamma_{1/\kappa}(\mathcal{A}_{\mathbf{f}_\mathrm{m}})$ and $\Gamma_{1/\kappa}(\mathcal{A}_{\mathbf{t}_\mathrm{m}})$ as function of the distance d_w is illustrated in figures III.11c, III.11f, III.12c and III.12f. These performance indexes are increasing with longer distance d_w. The mean values of these global performance indexes are illustrated in figure III.13. As shown in figure III.13a, the long length d_w leads to a higher normalized manipulability index for the torque control, while w_n of the force control is reduced. With the result in figure III.13b, it appears that the dexterity indexes of both the force and torque are increasing with the long working distance d_w. However, $1/\kappa$ index is much more significant for the torque $\mathbf{t}_\mathrm{m}$ than the force $\mathbf{f}_\mathrm{m}$. Hence, with the 3D six-coil EMA system, it is easier to perform magnetic torque control than magnetic force control on microrobot.

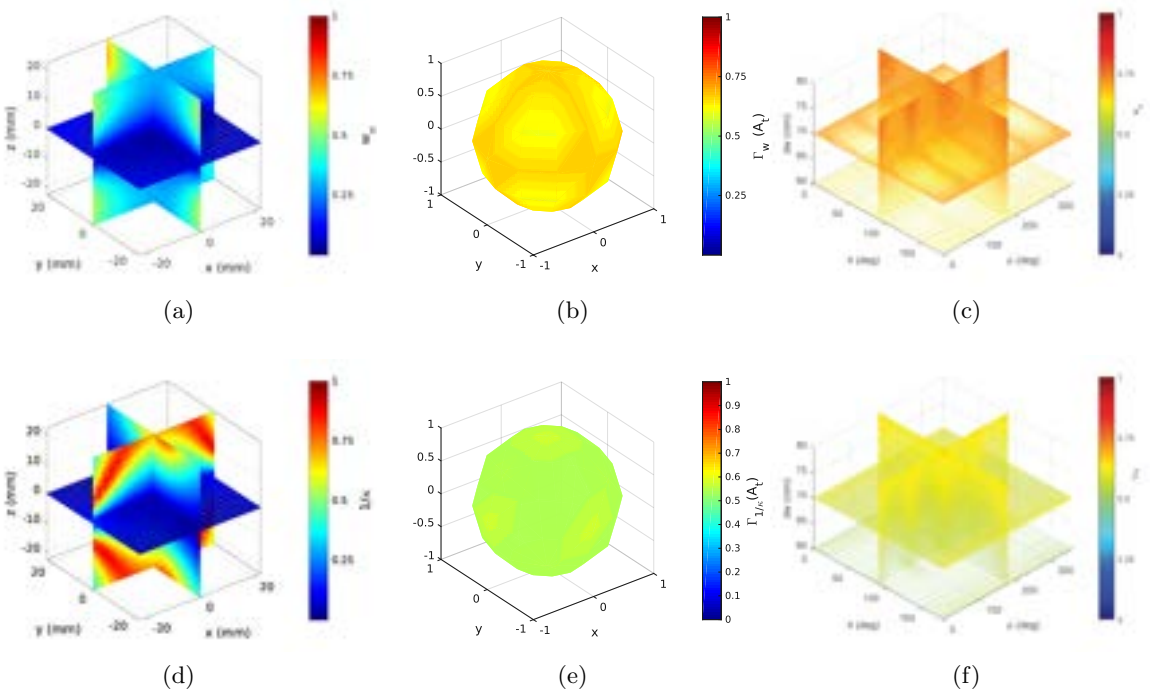

Figure III.12: Performance metrics of the torque actuation matrix $\mathcal{A}_{\mathbf{t}_\mathrm{m}}$: (a) the manipulability w_n and (d) conditioning number $1/\kappa$ indexes in Ω when $\mathbf{m}$ is aligned along the x-direction; (b) $\Gamma_{w_n}(\mathcal{A}_{\mathbf{t}_\mathrm{m}})$ and (e) $\Gamma_{1/\kappa}(\mathcal{A}_{\mathbf{t}_\mathrm{m}})$ for the sampled orientation of $\mathbf{m}$; and (c) $\Gamma_{w_n}(\mathcal{A}_{\mathbf{t}_\mathrm{m}})$ and (f) $\Gamma_{1/\kappa}(\mathcal{A}_{\mathbf{t}_\mathrm{m}})$ as function of d_w.

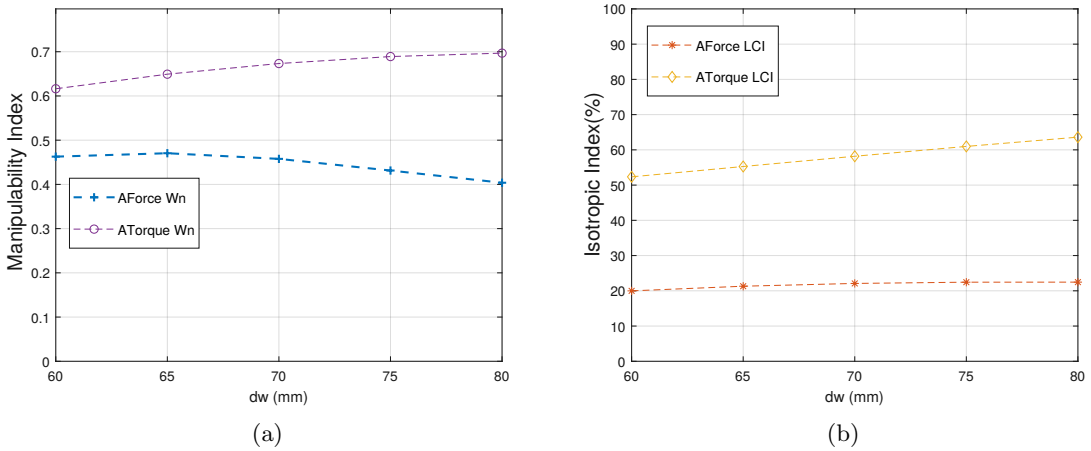

Figure III.13: Mean of the global performance indexes: (a) manipulability and (b) uniformity of the force $\mathcal{A}_{\mathbf{f}_\mathrm{m}}$ and torque $\mathcal{A}_{\mathbf{t}_\mathrm{m}}$ actuation matrices for different distance d_w.

III.3.2 OctoMag EMA system

The well-known OctoMag system is a platform already designed and developed at the ETH Zurich [60]. Its structure is a set of $n = 8$ electromagnets, as illustrated in figure III.14. It is firstly developed for ophthalmic MIS procedure in the retinal veins. Here, the eight electromagnets of the OctoMag setup have been divided into two sets of four coils referred as the upper and lower sets, equally spaced and organized around the z-axis. The lower set comprises four magnets in the xy-plane like the flat four-coils shown in **??**, that is rotated of 45° with respect to the x-axis, as illustrated in figure III.14b. The remaining upper set is tilted from the xy-plane by angle of 45°, as represented in figure III.14c. In our study, the influence of the distance d_w between the workspace center O and each electromagnet regarding the performance of OctoMag system is investigated. In particular, when this length is set to $d_w = 65\,\text{mm}$, it corresponds exactly to the OctoMag platform [60].

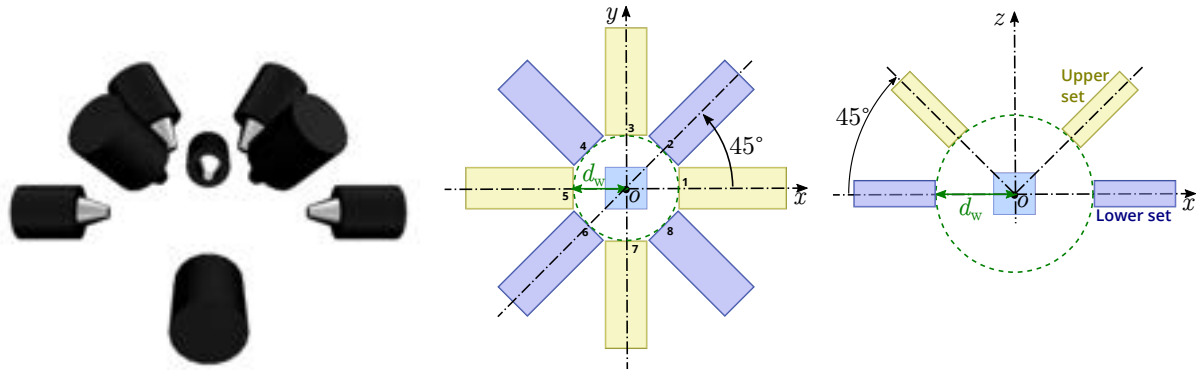

Figure III.14: OctoMag-like EMA system arrangement: (a) 3D view of the EMA setup; (b) top view of the xy-plane and (c) side view of the xz-plane.

As presented in figure III.15, the magnetic field $\mathbf{B}$ distribution is mainly oriented along the z-axis direction. As the OctoMag setup shares the same arrangement of electromagnets in the xy-plane with the flat four-coil configuration, the vector field in the xy-plane are similar (cf. **??**). The directions of the magnetic field vectors mainly along the z-axis are basically due to the upper set of electromagnets. Figure III.16 shows the magnetic field magnitude $\|\mathbf{B}\|$ in the xy-plane for working distance of $d_w = 60\,\text{mm}$, 70 mm and 80 mm respectively. Comparing these results from the flat eight-coil arrangement in figure A.12, the magnetic field distribution looks much less like a radial field in OctoMag system. While, as previously stated, the magnetic field $\mathbf{B}$ becomes stronger for the shorter distance d_w. However, if a magnetic microrobot moves outward from the center of xy-plane, the longer distance d_w can make magnetic field more homogeneous in each direction. This means that OctoMag system is able to actuate microrobot to any direction with less interference in long distance d_w. Secondly, the intensity of magnetic field for OctoMag setup is slightly weakened than the flat eight-coil configuration. For instance, when the working distance is set to $d_w = 65\,\text{mm}$, the maximum magnetic intensity decreases from 36.99 mT with the 2D configuration to 35.86 mT with the OctoMag platform.

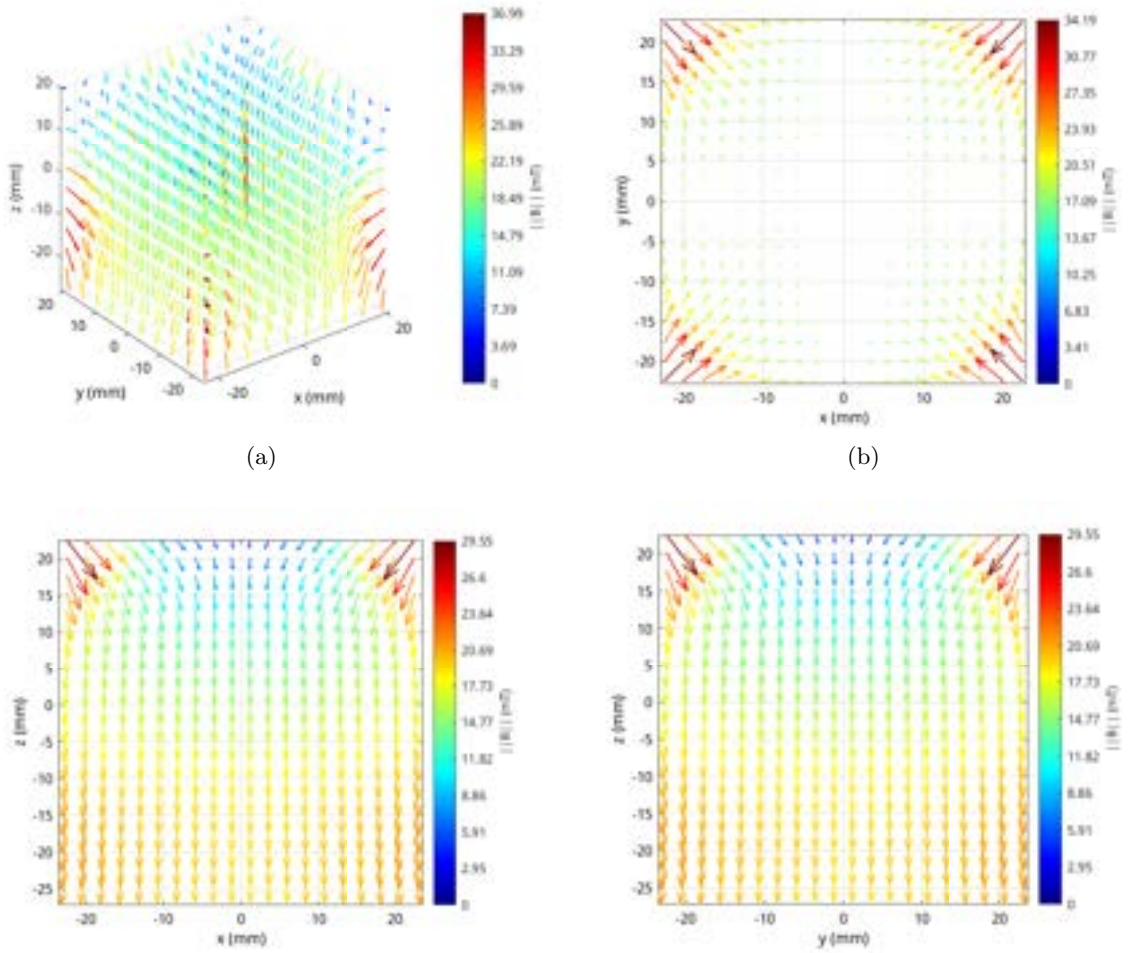

(a) (b)

(c) (d)

Figure III.15: The magnetic field $\mathbf{B}$ generated by OctoMag-like EMA system with $d_w = 65\,\text{mm}$: (a) a 3D view, (b) the xy-plane, (c) the xz-plane and (d) the yz-plane. The colorbar indicates the magnetic field magnitude.

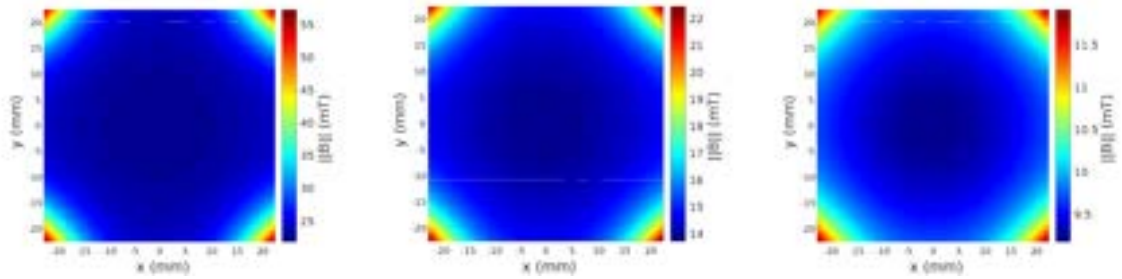

(a) (b) (c)

Figure III.16: The magnetic field magnitude $\|\mathbf{B}\|$ in the xy-plane for lengths of (a) $d_w = 60\,\text{mm}$, (b) $d_w = 70\,\text{mm}$, and (c) $d_w = 80\,\text{mm}$.

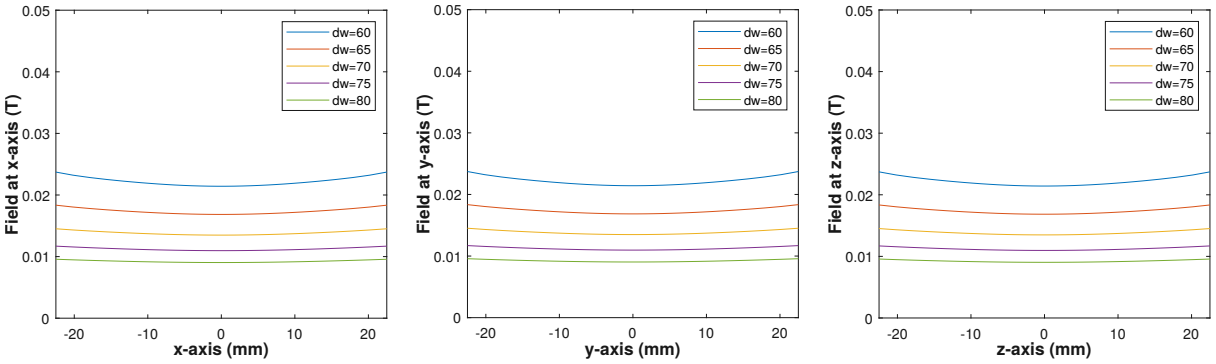

(a) (b) (c)

Figure III.17: Magnetic field magnitude $\|\mathbf{B}\|$ along (a) the x-axis, (b) the y-axis, and (c) the z-axis, for lengths of $d_w = 50\,\text{mm}$, $60\,\text{mm}$, $65\,\text{mm}$, $70\,\text{mm}$, $75\,\text{mm}$, and $80\,\text{mm}$.

Figure III.17 presents the magnetic field intensity along x, y and z-axis. It appears that the magnetic field strength does not change significantly along x and y-axis. In addition, the magnetic field becomes stronger in the deeper locations of workspace. Hence, the magnetic field becomes more uniform in the xy-plane with respect to this configuration, moreover, the stronger magnetic field can be provided in the deep workspace. The magnetic field metrics are shown in figure III.18. It appears that the average value $\langle\|\mathbf{B}\|\rangle$ of the magnetic field magnitude is equivalent to the flat eight-coil arrangement, but, its STD value is here improved. Nevertheless, compared to the previous configurations, only the average values $\langle b_x\rangle$ and $\langle b_x\rangle$ herein remain close to zero. Furthermore, the uniformity index $\gamma(\|\mathbf{B}\|)$ is more important and is increasing with the length d_w. Therefore, OctoMag-like arrangement is a promising solution to efficiently actuate a magnetic microrobot in a 3D workspace.

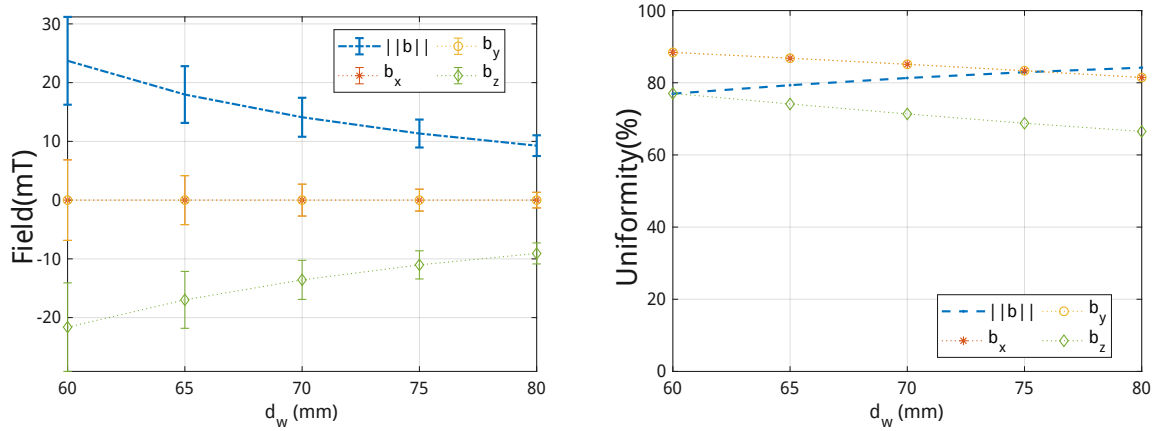

(a) (b)

Figure III.18: Magnetic field metrics over the workspace Ω for d_w ranging from 60 mm to 80 mm: (a) error-bar showing the average and STD values; and (b) the uniformity index γ.

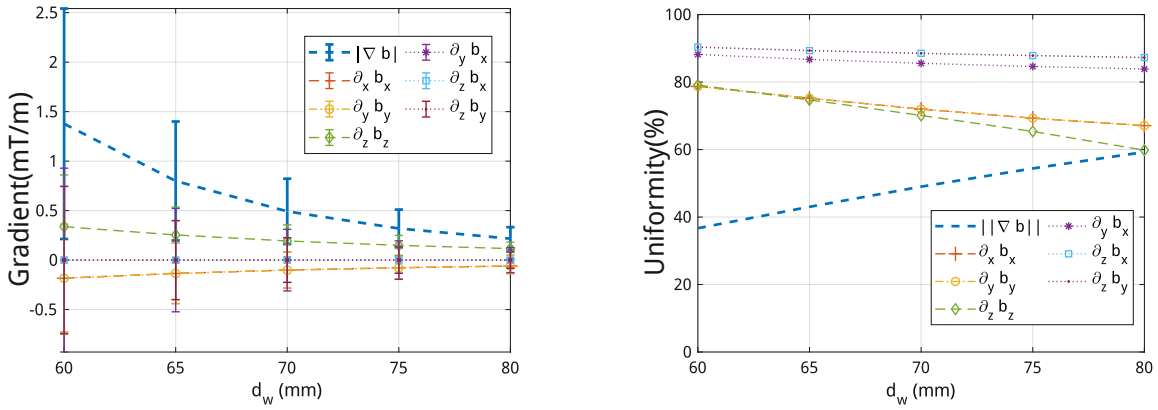

(a) (b)

Figure III.19: Magnetic field gradient metrics for distance d_w ranging from 60 mm to 80 mm: (a) the mean and STD values; and (b) the uniformity index γ.

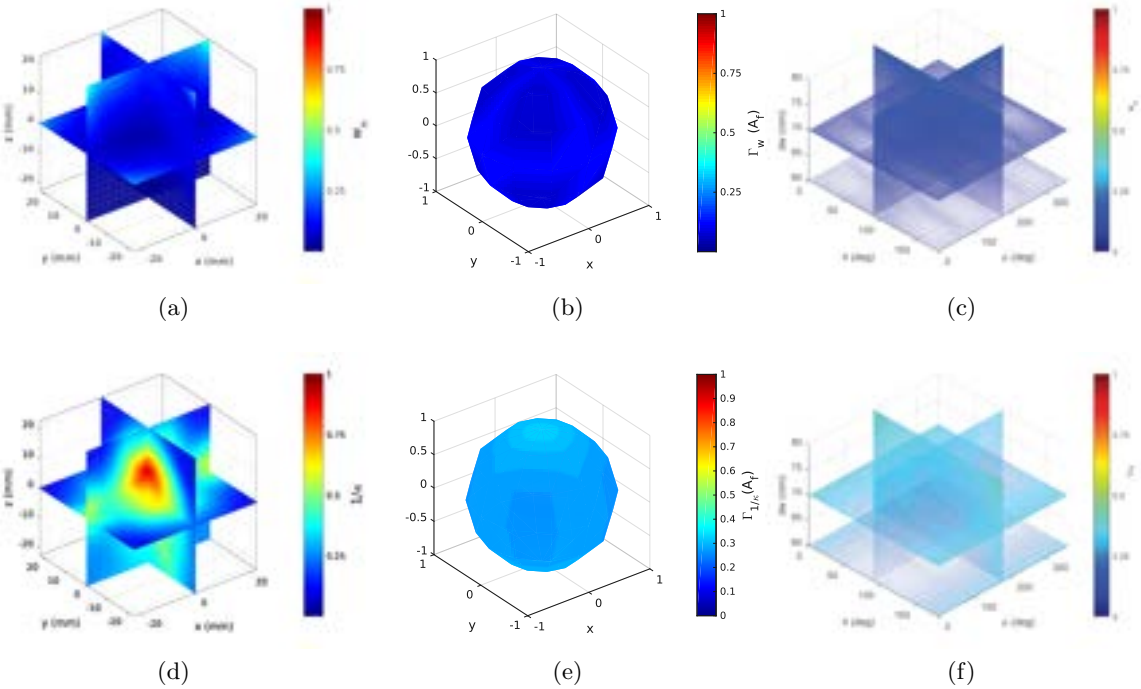

(a) (b) (c)

(d) (e) (f)

Figure III.20: Performance metrics of the force actuation matrix $\mathcal{A}_{\mathbf{f}_\mathrm{m}}$: (a) the manipulability w_n and (d) conditioning number $1/\kappa$ indexes for $\mathbf{p} \in \Omega$ when $\mathbf{m}$ is aligned along the x-direction; (b) $\Gamma_{w_n}(\mathcal{A}_{\mathbf{f}_\mathrm{m}})$ and (e) $\Gamma_{1/\kappa}(\mathcal{A}_{\mathbf{f}_\mathrm{m}})$ for the sampled orientation of $\mathbf{m}$; and (c) $\Gamma_{w_n}(\mathcal{A}_{\mathbf{f}_\mathrm{m}})$ and (f) $\Gamma_{1/\kappa}(\mathcal{A}_{\mathbf{f}_\mathrm{m}})$ as function of d_w.

The metrics of the magnetic field gradient are illustrated in figure III.19. The average of magnetic field gradient behaves equivalently to flat eight-electromagnet configuration (see also figure A.15). However, as the magnetic field becomes more uniform, its gradient is obviously lower.

Next, it appears that the uniformity of the magnetic gradient induce is decreasing significantly with d_w, especially, for the component $\frac{\partial b_y}{\partial y}$ and $\frac{\partial b_z}{\partial z}$.

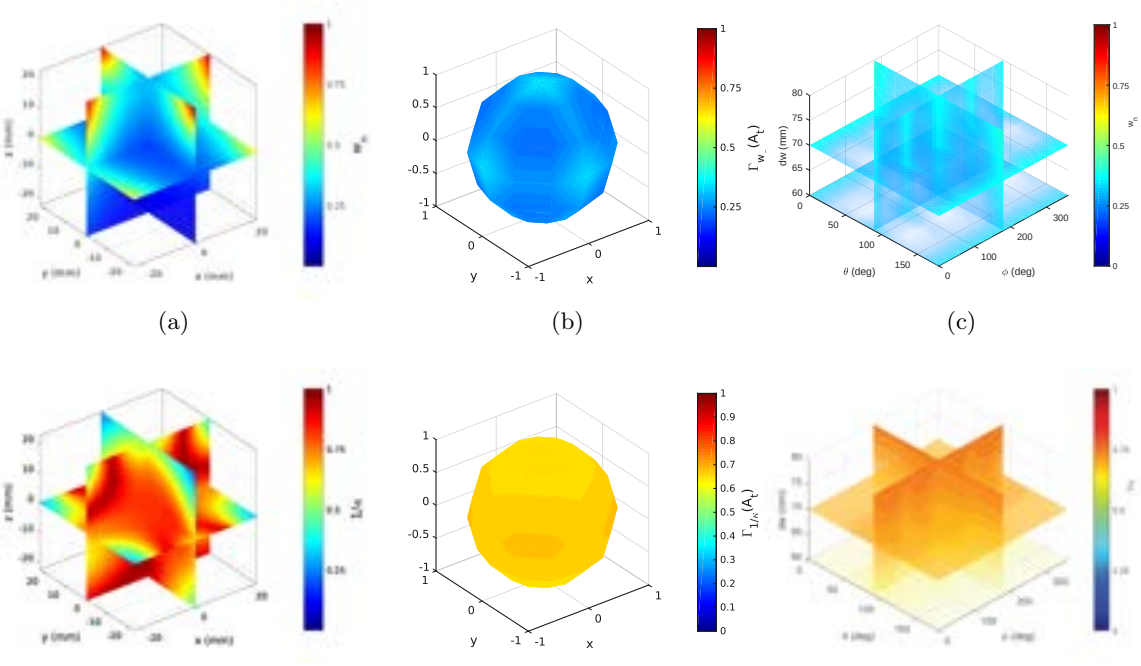

Figure III.21: Performance metrics of the torque actuation matrix $\mathcal{A}_{\mathbf{t}_\mathrm{m}}$: (a) the manipulability w_n and (d) conditioning number $1/\kappa$ indexes in $\mathbf{p} \in \Omega$ when $\mathbf{m}$ is aligned along the x-direction; (b) $\Gamma_{w_n}(\mathcal{A}_{\mathbf{t}_\mathrm{m}})$ and (e) $\Gamma_{1/\kappa}(\mathcal{A}_{\mathbf{t}_\mathrm{m}})$ for the sampled orientation of $\mathbf{m}$; and (c) $\Gamma_{w_n}(\mathcal{A}_{\mathbf{t}_\mathrm{m}})$ and (f) $\Gamma_{1/\kappa}(\mathcal{A}_{\mathbf{t}_\mathrm{m}})$ as function of d_w.

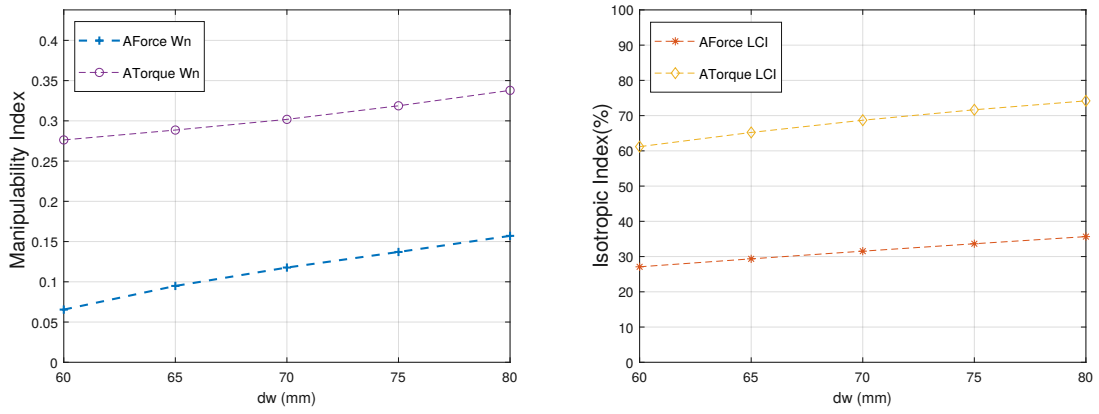

Figure III.22: Mean of the global performance indexes (a) manipulability and (b) uniformity of the force $\mathcal{A}_{\mathbf{f}_\mathrm{m}}$ and torque $\mathcal{A}_{\mathbf{t}_\mathrm{m}}$ actuation matrices for different distances d_w.

The performance metrics of the force and torque actuation matrices in the workspace for the sampled orientations of dipole moment $\mathbf{m}$ are presented in figures III.20 and III.21, respectively. The manipulabilities w_n of the force and torque have better performance when the orientation of the microrobot magnetic moment $\mathbf{m}$ is in the xy-plane ($\theta = 90°$) and along z-axis ($\theta = 0°$). The conditioning indexes $1/\kappa$ of force and torque reach a high value when the dipole moment $\mathbf{m}$ is aligned along the z-axis. From these results, it can be seen that these global performance indexes increase when the distance d_w is increasing. The simulation results of the average global performance indexes are represented in figure III.22. In the OctoMag configuration, the performance metrics are all increasing with d_w for the both force and torque control. Nevertheless, they remain lower than the flat eight-coils arrangement.

III.3.3 MiniMag EMA system

As OctoMag, the MiniMag system is a platform designed and developed at the ETH Zurich [61]. Similarly, the eight electromagnets of the MiniMag system have been divided into upper and lower sets, and organized around the z-axis, as illustrated in figure III.23. The OctoMag system was designed to optimize the manipulability of the magnetic field $\mathbf{B}$, whereas the MiniMag setup has been designed to restrict the locations of the electromagnets to a single hemisphere. This is accomplished by shifting all the $n = 8$ electromagnets from the xy plane. Hence, the four lower set of MiniMag is rotated to 26° from the xy-plane, and the upper set is fixed to 47.5°, as shown in figure III.23c. It can be seen from the structure of MiniMag system, the volume occupied by the coils is reduced thanks to a more compact electromagnet arrangement. In the following, the influence of the distance d_w on the magnetic field distribution and its actuation efficiency is analyzed through several simulations of MiniMag arrangement.

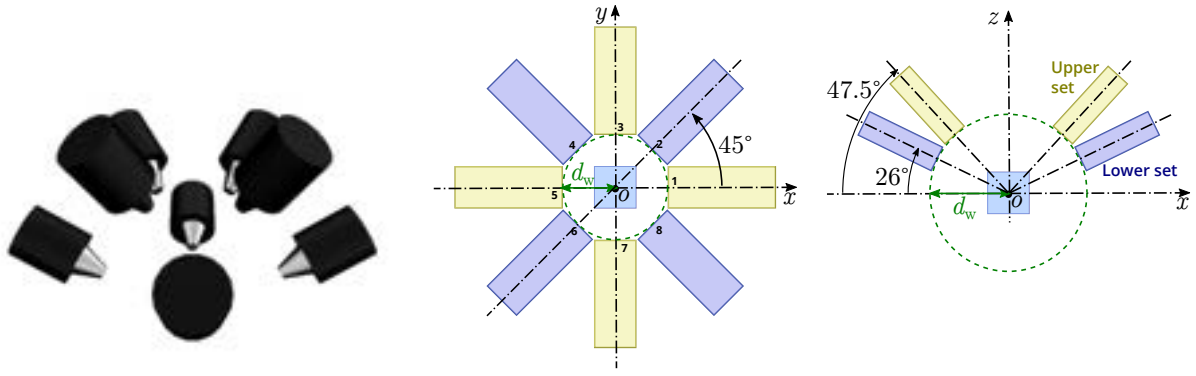

(a) (b) (c)

Figure III.23: MiniMag-like EMA system arrangement: (a) 3D view of the EMA setup; (b) top view of the xy-plane and (c) side view of the xz-plane.

Figure III.24 presents the magnetic field $\mathbf{B}$ distribution generated by MiniMag configuration, where the vectors are mainly applied downward along the z-axis. Here again, the significant orientation along the z-axis is basically due to the shifting of the electromagnets above the xy-plane. Likewise, the distribution of $\mathbf{B}$ in the xy-plane is similar to the flat eight-coil configuration, as in figure A.11. However, the radial directions of the magnetic field are opposite in these two compared systems. Indeed, the magnetic field in xy-plane can be understood as obtaining a

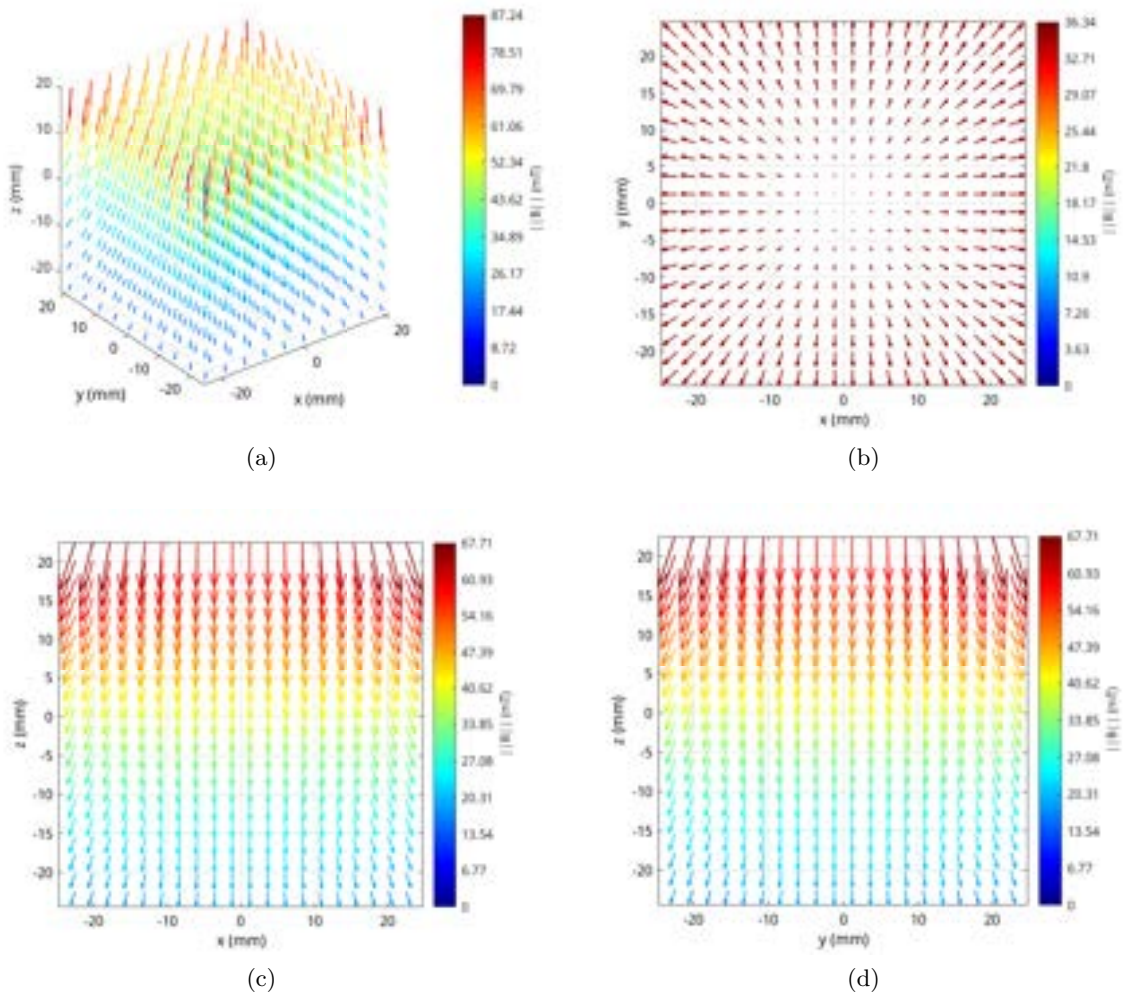

Figure III.24: The magnetic field $\mathbf{B}$ generated by MiniMag-like EMA system with $d_w = 65\,\text{mm}$: (a) a 3D view, (b) the xy-plane, (c) the xz-plane and (d) the yz-plane. The colorbar indicates the magnetic field magnitude.

specified superposition from each independent coil. Thus, the detected positions referred to their coils are different because the angles of the coils relative to the common axis are different. Therefore, the difference in overlap referred to coils leads to different directions of the induced magnetic field. Next, Figure III.25 shows the strength of magnetic field in the xy-plane for different lengths d_w. As previously analyzed, the intensity $\|\mathbf{B}\|$ in xy-plane still decreases with the longer distance d_w. However, the maximum magnetic field magnitude induced with MiniMag configuration is stronger than the one generated by either the flat eight-coil or OctoMag arrangements. For example, with $d_w = 60\,\text{mm}$ the maximum magnitude is $\max \|\mathbf{B}\| = 165.31\,\text{mT}$ for the MiniMag setup, compared to a maximum value of $58.10\,\text{mT}$ and $59.47\,\text{mT}$ regarding the flat eight-coil and OctoMag configuration, respectively.

Figure III.26 shows the evolution of the magnetic field strength along x, y and z-axis. As for the MiniMag configuration, the magnitude $\|\mathbf{B}\|$ remains almost unchanged along x and y-axis.

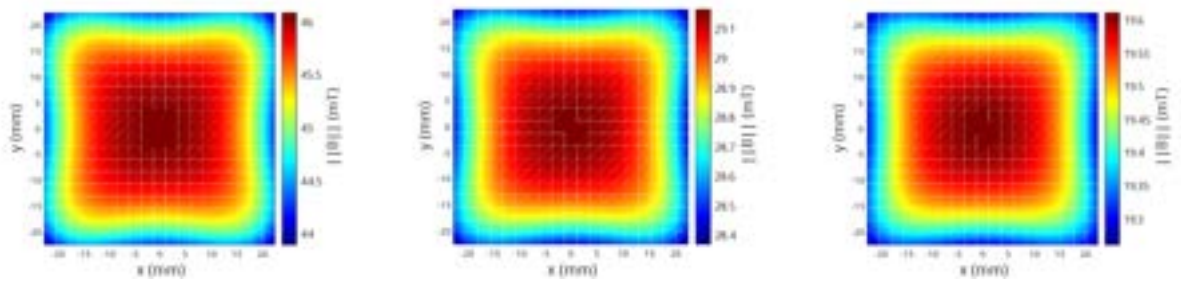

(a) (b) (c)

Figure III.25: The magnetic field magnitude $\|\mathbf{B}\|$ in the xy-plane for lengths of (a) $d_w = 60\,\text{mm}$, (b) $d_w = 70\,\text{mm}$ and (c) $d_w = 80\,\text{mm}$.

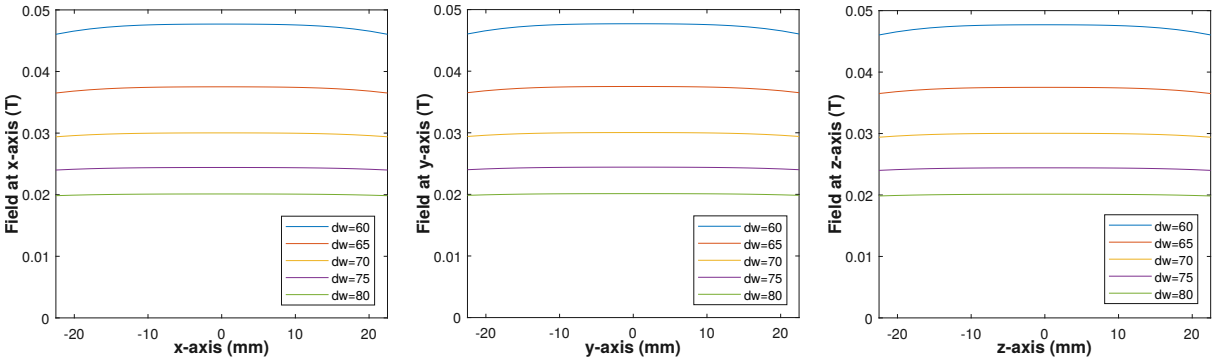

(a) (b) (c)

Figure III.26: Magnetic field magnitude $\|\mathbf{B}\|$ along (a) the x-axis, (b) the y-axis, and (c) the z-axis.

Especially, the magnetic field induced from MiniMag setup seems the most uniform along x and y-axis comparing to other discussed configurations. In contrast to OctoMag configuration, figure III.26c represents that the magnetic field strength is increased when the location is close to magnet in the upper of workspace of MiniMag configuration. Figure III.27 depicts the mean value of the overall magnetic field. The average $\langle\|\mathbf{B}\|\rangle$ is almost identical to the OctoMag and the flat eight-coil arrangements. MiniMag platform is able to generate stronger magnetic field in the desired workspace Ω. Secondly, as OctoMag setup, only the average values $\langle b_x\rangle$ and $\langle b_x\rangle$ remain close to zero. Nevertheless, the magnetic field uniformity herein appears lower than the OctoMag system. It can be explained by the fact that the magnetic field along the z-axis evolves more rapidly.

The metrics of the magnetic field gradient generated by a MiniMag setup is shown in figure III.28. It has been shown that short distance d_w allows achieving stronger magnetic field gradient as presented in figure III.28a; while the uniformity index of the magnetic gradient requires longer distance as illustrated in figure III.28b. Also, these results demonstrate that the MiniMag configuration provides most important magnetic field gradient metrics than the others considered EMA arrangements.

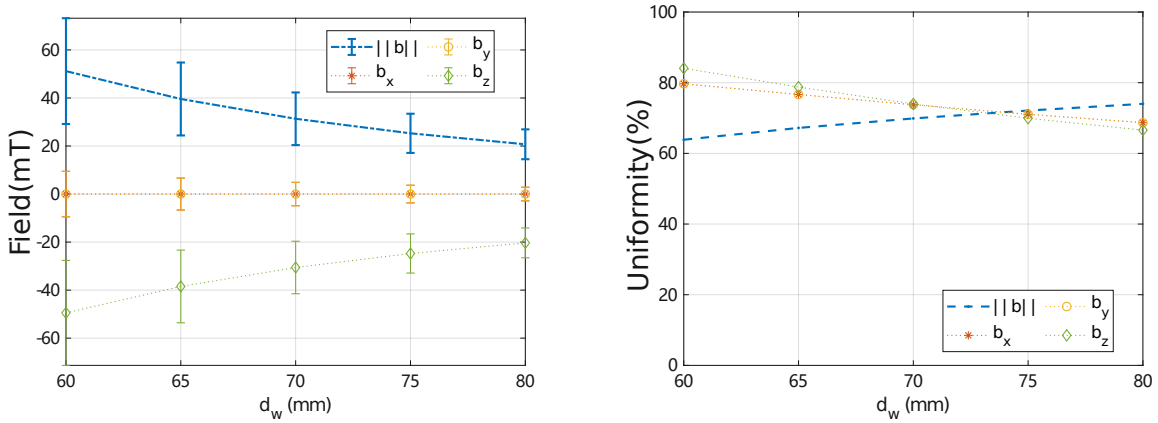

(a) (b)

Figure III.27: Magnetic field metrics over the workspace Ω: (a) error-bar showing the average and STD values; and (b) the uniformity index γ.

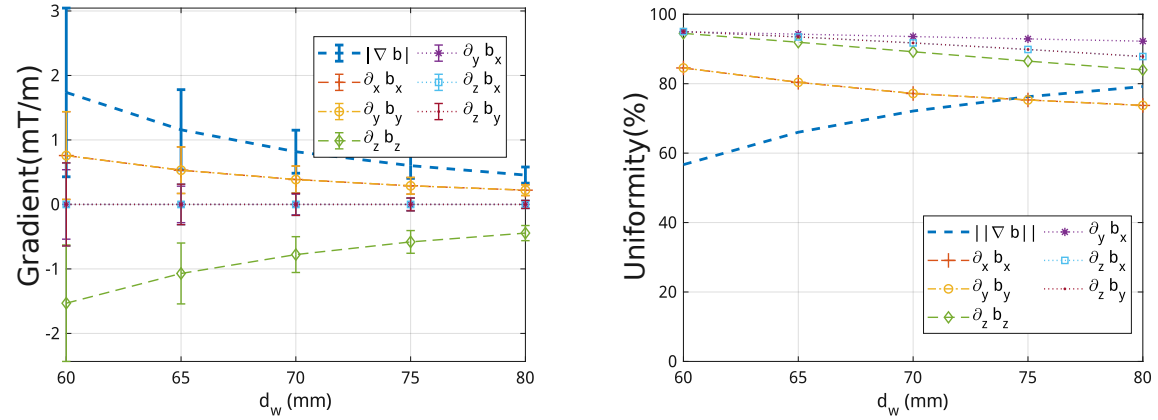

(a) (b)

Figure III.28: Magnetic field gradient metrics: (a) the mean and STD values; and (b) the uniformity index γ.

Finally, the performance metrics are analyzed through actuation matrices (II.29) with the magnetic moment $\mathbf{m}$ of arbitrary microrobot in any location of the workspace. Figure III.29 presents the simulation results of performance indexes for the sampled orientation of $\mathbf{m}$. The normalized manipulability index of magnetic force $\mathbf{f}_\mathrm{m}$ becomes efficient when the orientation of magnetic moment is pointing on the xy-plane ($\theta = 90°$) as illustrated in figure III.29a. Whereas w_n of magnetic torque $\mathbf{t}_\mathrm{m}$ is higher when $\mathbf{m}$ is aligned to along z-axis ($\theta = 0°$) as represented in figure III.29c. From figures III.29b and III.29d, it can be observed that the dexterity indexes $1/\kappa$ of both magnetic force and torque are more uniform when the orientation of microrobot is pointing to z-axis. Moreover, the effect of distance d_w is investigated, and the results demonstrate that the performance indexes are obviously increasing with the longer distance d_w. The influence of the working distance d_w on the performance indexes is illustrated in figure III.30. Basically,

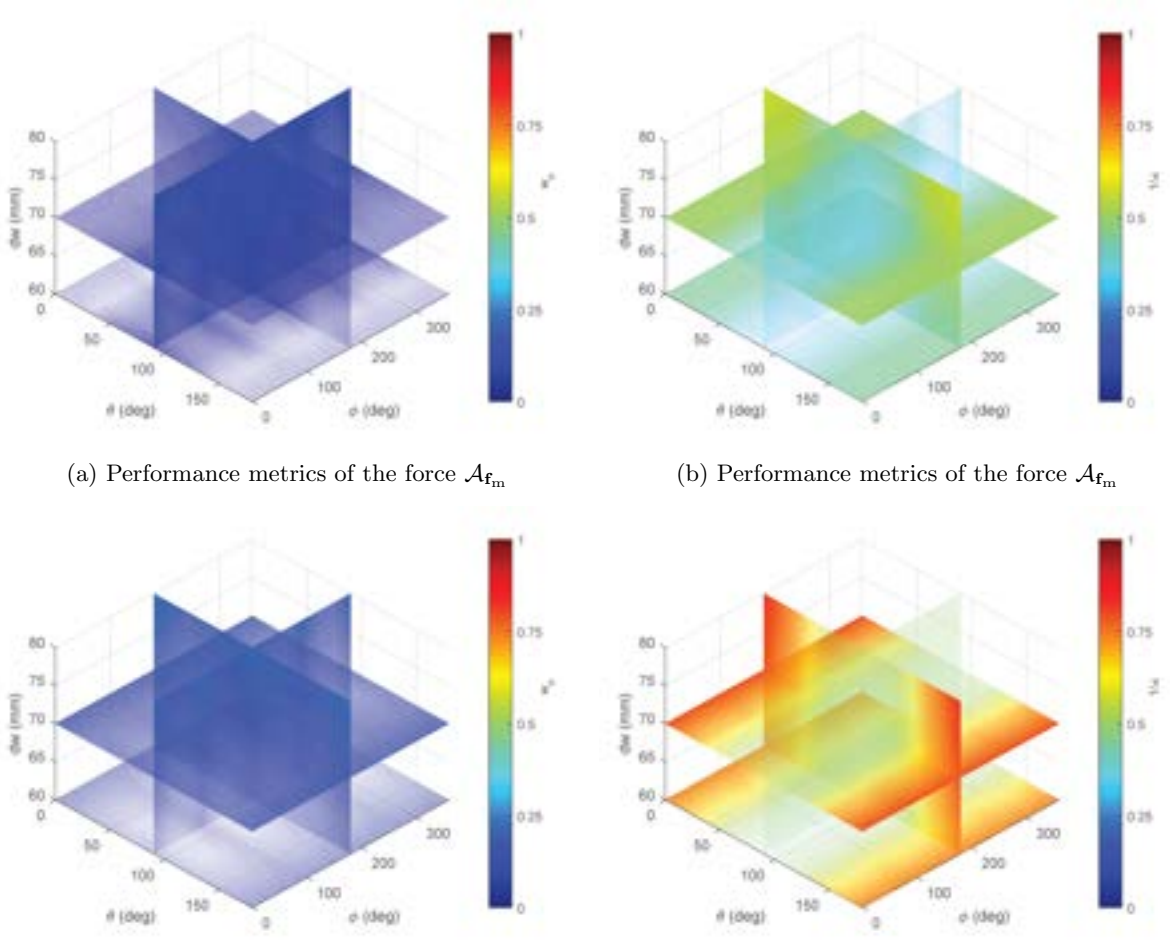

(a) Performance metrics of the force $\mathcal{A}_{\mathbf{f}_\mathrm{m}}$

(b) Performance metrics of the force $\mathcal{A}_{\mathbf{f}_\mathrm{m}}$

(c) Performance metrics of the torque $\mathcal{A}_{\mathbf{t}_\mathrm{m}}$

(d) Performance metrics of the torque $\mathcal{A}_{\mathbf{t}_\mathrm{m}}$

Figure III.29: Performance metrics of the force (a)-(b) and torque (c)-(d) actuation matrices in the workspace for averaged magnetic moment orientations: (a)-(c) show the normalized manipulability index w_n; and (b)-(d) show the dexterity index $1/\kappa$.

the longer distance d_w provides more efficient control for both $\mathbf{f}_\mathrm{m}$ and $\mathbf{t}_\mathrm{m}$, since their normalized manipulability and dexterity indexes are growing with the distance d_w. Furthermore, the control of the magnetic torque is easier than the magnetic force because w_n and $1/\kappa$ indexes of $\mathbf{t}_\mathrm{m}$ remain better than the indexes of $\mathbf{f}_\mathrm{m}$ in the all mentioned configurations.

III.3.4 Discussions

Different arrangements of EMA system have been investigated from numerous simulations, and different metrics have been calculated to evaluate their performances. To sum up, the RMS values and uniformity index γ of the magnetic field are synthesized in table III.1, and in table III.2 for its gradient. Obviously, EMA setup with $n = 8$ coils produce stronger magnetic field and gradient than configuration with fewer magnets. Furthermore, as presented in section III.3.3, MiniMag arrangement with shifted coils generates the strongest and the most uniform magnetic

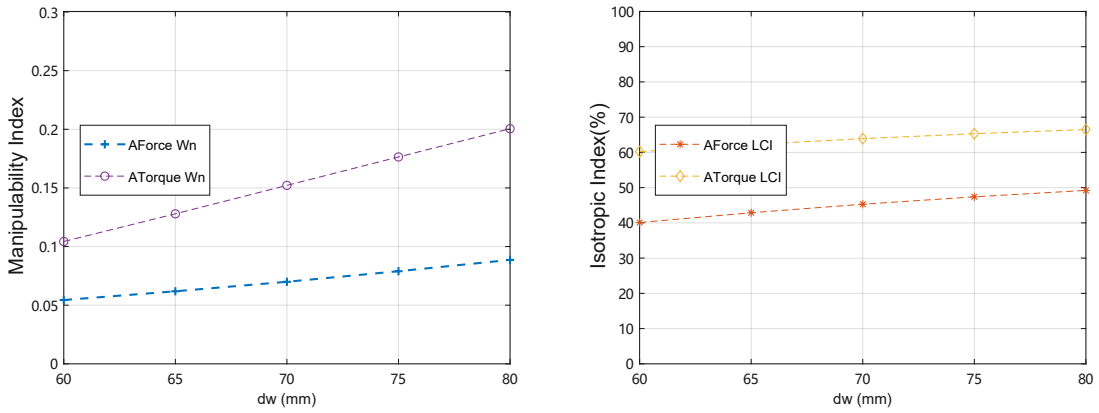

(a) (b)

Figure III.30: Mean of the global performance indexes (a) manipulability and (b) uniformity of the force $\mathcal{A}_{\mathbf{f}_\mathrm{m}}$ and torque $\mathcal{A}_{\mathbf{t}_\mathrm{m}}$ actuation matrices for different distances d_w.

field, specially in xy-plane. From these results, it seems promising to further investigate the impact of changing the shifting angles of EMA system with $n = 8$ coils.

Table III.1: Metrics of the magnetic field strength: its RMS (mT) and uniformity γ metric (%)

	Distance d_w (mm)				
EMA System	60	65	70	75	80
Flat four-coil	13.13 (71.18)	9.39 (70.97)	6.91 (70.82)	5.21 (70.81)	4.00 (70.88)
Flat six-coil	20.55 (72.55)	14.69 (72.96)	10.80 (73.03)	8.13 (72.96)	6.24 (72.85)
Flat eight-coil	27.41 (73.05)	19.59 (73.26)	14.41 (73.23)	10.85 (73.09)	8.33 (72.92)
3D six-coil	10.08 (51.09)	6.48 (50.00)	4.28 (49.11)	2.90 (48.39)	2.01 (47.80)
OctoMag	24.86 (76.97)	18.61 (79.32)	14.49 (81.32)	11.58 (82.92)	9.44 (84.19)
MiniMag	55.73 (63.86)	42.40 (67.20)	33.21 (69.89)	26.57 (72.12)	21.63 (74.02)

Indeed, as discussed in Chapter II, the number n of electromagnets is strongly related to the envisioned biomedical application. Especially, the definition of n number depends on the required DOFs to efficiently control the medical magnetic microrobot. In particular, for singular-free 5 DOFs control, it appears that a stationary EMA system requires at least 7 current inputs, and then $n = 7$ electromagnets. However, the use of $n = 8$ coils allows improving the magnetic actuation stability. The following section will address the optimization of the EMA configuration for singular-free 5 DOFs control using $n = 8$ electromagnets.

Table III.2: Metrics of the magnetic field gradient strength: its RMS (mT/m) and uniformity γ metric (%)

	Distance d_w (mm)				
EMA System	60	65	70	75	80
Flat four-coil	1.18 (59.89)	0.78 (64.58)	0.54 (68.95)	0.38 (72.99)	0.28 (76.78)
Flat six-coil	1.48 (64.27)	0.97 (70.66)	0.68 (75.34)	0.50 (78.69)	0.38 (81.21)
Flat eight-coil	1.87 (66.49)	1.27 (71.77)	0.91 (75.60)	0.67 (78.66)	0.51 (81.20)
3D six-coil	1.32 (65.61)	0.84 (66.97)	0.55 (67.50)	0.37 (66.94)	0.26 (66.42)
OctoMag	1.80 (36.68)	1.00 (43.02)	0.59 (49.00)	0.37 (54.40)	0.25 (59.26)
MiniMag	2.17 (56.69)	1.31 (66.02)	0.88 (72.13)	0.63 (76.26)	0.47 (79.18)

III.4 Optimal configuration of EMA setup for 5-DOFs control

Commonly, long distance d_w from the workspace center O to the electromagnet leads globally to a slight more uniform magnetic field and gradient, in addition, the effective control of magnetic microrobot is improved. Nevertheless, stronger magnetic field and gradient require a short length d_w. Thus, a compromise should be made with respect to the biomedical applications specifications. Indeed, the value of d_w will affect the size of the workspace: a great length enables larger workspace dimension. This geometric relation will be further analyzed in Chapter IV. In the following, we have chosen to set the working distance to $d_w = 65\,\text{mm}$, that is similar to the OctoMag EMA setup [60]. For consistency, once again, a workspace of $\Omega = 45\,\text{mm} \times 45\,\text{mm} \times 45\,\text{mm}$ is considered throughout the simulations.

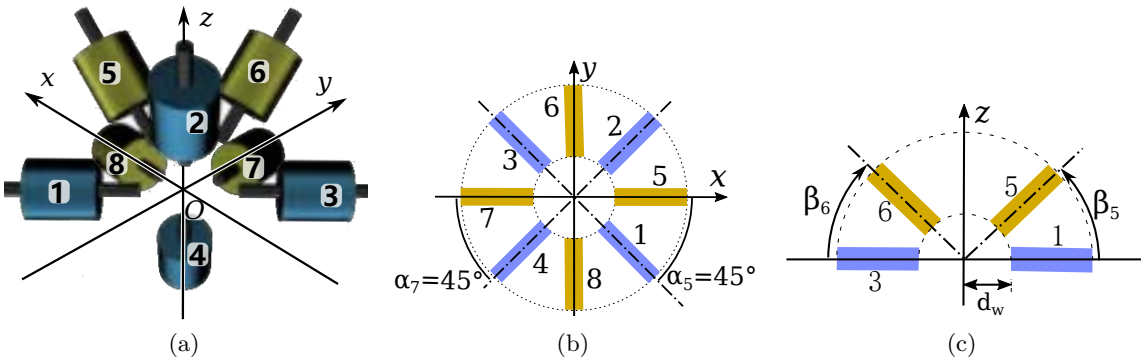

(a) (b) (c)

Figure III.31: Representation of the basis reconfigurable EMA system for 5 DOFs magnetic actuation: (a) 3D view of the electromagnetic coils arrangement; (b) the 2D top view, and (c) side view.

When the workspace size of the EMA system is determined, the orientation of electromagnetic could be further studied. As mentioned, $n = 8$ electromagnets are chosen here to enable reliable 5 DOFs magnetic actuation. For the sake of simplicity, in the following, the different electromagnetic coils of the EMA platform are divided in two sets: i) four stationary electromagnets: $e = 1..4$;

and ii) four mobile coils: $e = 5..8$, as illustrated in figure III.31. These two sets are arranged around a common axis of rotation with an azimuth angle $\alpha_e = 45°$ ($e = 1..8$, as in figure III.31b), and are pointing to the common center O of the workspace. The mobile sets are able to rotate their polar angle $\beta_e \in [0; 90°)$ ($e = 5..8$). Two cases are considered for the stationary coils set where the polar β_e ($e = 1..4$) is fixed to:

case #1: $\beta_e = 0°$ (as in figure III.31c), that is equivalent to the OctoMag [60] configuration;

case #2: $\beta_e = 26°$, that is close to the MiniMag [61] arrangement.

Hence, the considered reconfigurable EMA platform can shift from one to another of these configurations by changing the orientation of the polar angle β_e of their two sets of electromagnets.

In the following sections, the influence of the mobile angle β_e on the magnetic field and gradient performance indexes, and on the magnetic actuation indexes are investigated. As previously stated, each electromagnet is computed with a point dipole moment magnitude of: $\|\mathbf{m}_e\| = 8.178\,\mathrm{A\,m^2}$, and the microrobot is modeled from its magnetic moment $\mathbf{m} = (1, \theta, \varphi)$, with a unit magnitude, azimuth $\varphi \in [0; 360°)$ and polar angles $\theta \in [0; 180°]$. Let us recall that the possible collision of the coils is not taken into account in this study.

III.4.1 Case #1: reconfigurable OctoMag-like setup

This section investigates EMA platform similar to the OctoMag system, already introduced in section III.3.2. Specifically, the mobile set of coils is able to rotate with the same angle $\beta = \beta_e \in [0; 90°)$ ($e = 5..8$, as in figure III.31c). To analyze the performance of such reconfigurable EMA setup, different simulations are conducted, and their results are presented hereafter.

First, the magnetic field performance indexes are analyzed and shown in figure III.32, for different moving angles $\beta \in [0; 90°)$. As previously analyzed, the performance indexes are axisymmetric around the z-axis, and the magnetic field and gradient behave similarly between the x and y components. In particular, the average values $\langle b_x \rangle$ and $\langle b_x \rangle$ of $\mathbf{B}$, and $\left\langle \frac{\partial b_x}{\partial y} \right\rangle$, $\left\langle \frac{\partial b_x}{\partial z} \right\rangle$ and $\left\langle \frac{\partial b_y}{\partial z} \right\rangle$ of $\nabla \mathbf{B}$ are close to zero. Moreover, from these results, two distinguishing behaviors appear: i) for low angle $\beta \lesssim 45°$, the magnetic field gradient is the strongest and more uniform; whereas ii) for higher value of β, the magnetic field becomes stronger and more uniform. Thus, the reconfigurable OctoMag-like platform exhibits a versatility to manipulate either the magnetic field or its gradient, which is only driven by simply regulating the orientation β_e of some electromagnets.

To analyze the performance indexes of the actuation matrix $\mathcal{A}(\mathbf{p}, \mathbf{m})$ given by (II.29), once again the magnetic moment $\mathbf{m}$ of an arbitrary microrobot for sampled location $\mathbf{p} \in \Omega$ is defined. Thus, a unit-strength dipole moment with different orientations expressed in spherical coordinates with azimuth angles $\varphi \in [0; 360°)$ and polar angles $\theta \in [0; 180°]$ is simulated to evaluate the global actuation performances (III.15). Figure III.33 shows these global performance indexes for the sampled orientations of the magnetic moment $\mathbf{m}$ with different moving β angles. From these simulation results, it appears that if $\mathbf{m}$ is parallel to the xy-plane (ie. $\theta = 90°$), the global performance indexes of the torque $\mathbf{t}_\mathrm{m}$ are low, whereas the force $\mathbf{f}_\mathrm{m}$ is low when $\mathbf{m}$ is aligned along the z-axis ($\theta = 0° \mod 180°$). To further investigate these results, table III.3 reports the maximal and minimal values of the global performance indexes, and the corresponding angles for the sampled orientations of a unit-strength magnetic moment. It can be shown that to improve

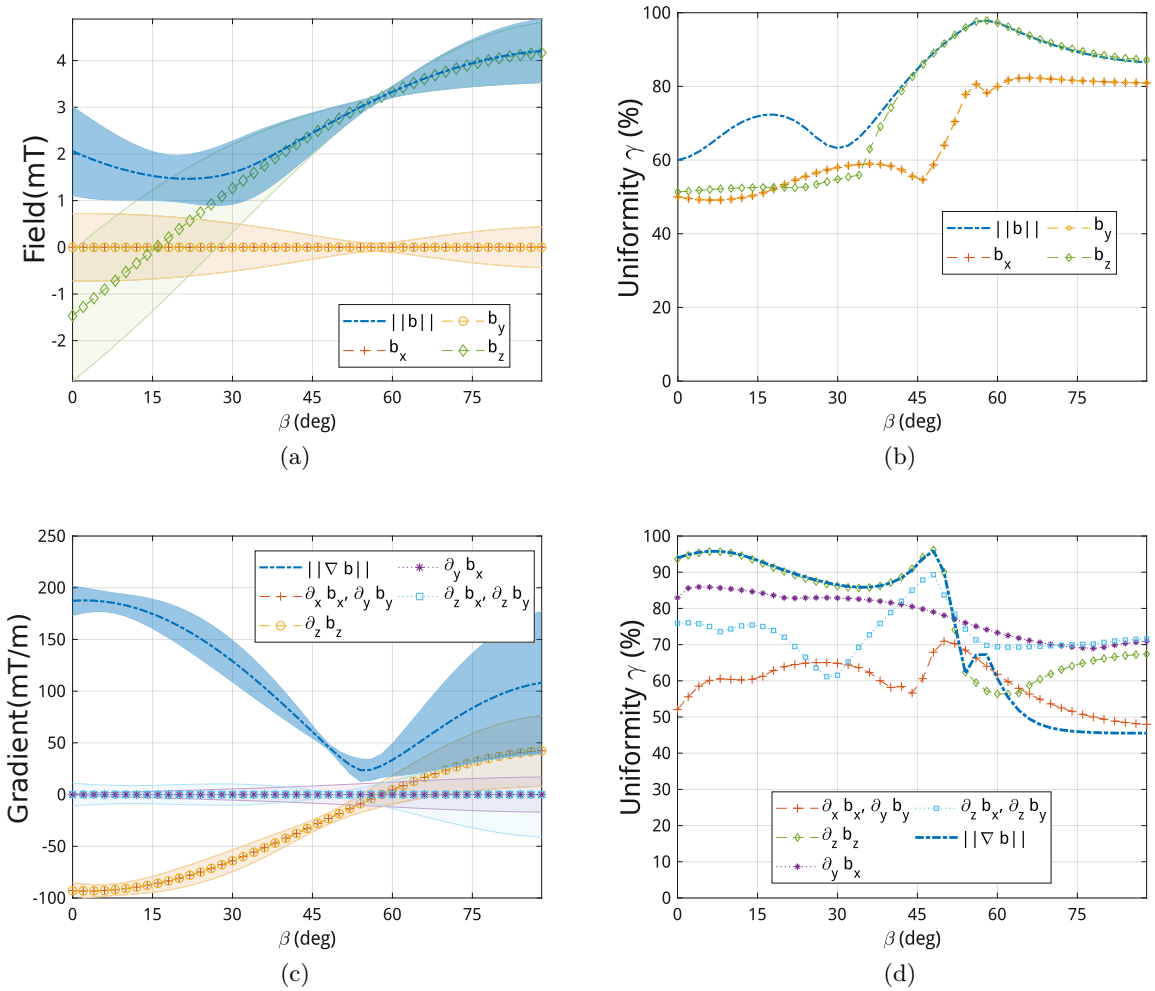

Figure III.32: Performance metrics of (a)-(b) the magnetic field and (c)-(d) its gradient of reconfigurable OctoMag-like setup when the mobile coils set is rotating with $\beta \in [0; 90°)$. The markers and envelopes (a)-(c) refer to the mean and standard deviation (STD) of the fields.

the perfromacnes of magnetic actuation, firstly, $\mathbf{m}$ should be globally aligned along the z-axis. Secondly, the moving angle must be set to $\beta = 32°$ in order to maximize the dexterity index $1/\kappa$ of the force, whereas a value around $\beta = 68°$ is required for the torque. In contrast, the normalized manipulability of the force and torque needs a low value below $\beta \leq 22°$ for improvement.

Table III.3: Minimum and Maximum values of the global actuation performance indexes.

	min	$(\varphi, \theta, \beta)_{\min}$	max	$(\varphi, \theta, \beta)_{\max}$
$\Gamma_{w_n}(\mathcal{A}_{\mathbf{f}_m})$	0.241	$(0, 0, 89)$	0.772	$(0, 0, 22)$
$\Gamma_{1/\kappa}(\mathcal{A}_{\mathbf{f}_m})$	0.133	$(180, 180, 89)$	0.739	$(0, 0, 32)$
$\Gamma_{w_n}(\mathcal{A}_{\mathbf{t}_m})$	0.446	$(90, 90, 0)$	0.889	$(0, 0, 0)$
$\Gamma_{1/\kappa}(\mathcal{A}_{\mathbf{t}_m})$	0.227	$(210, 90, 0)$	0.973	$(0, 0, 68)$

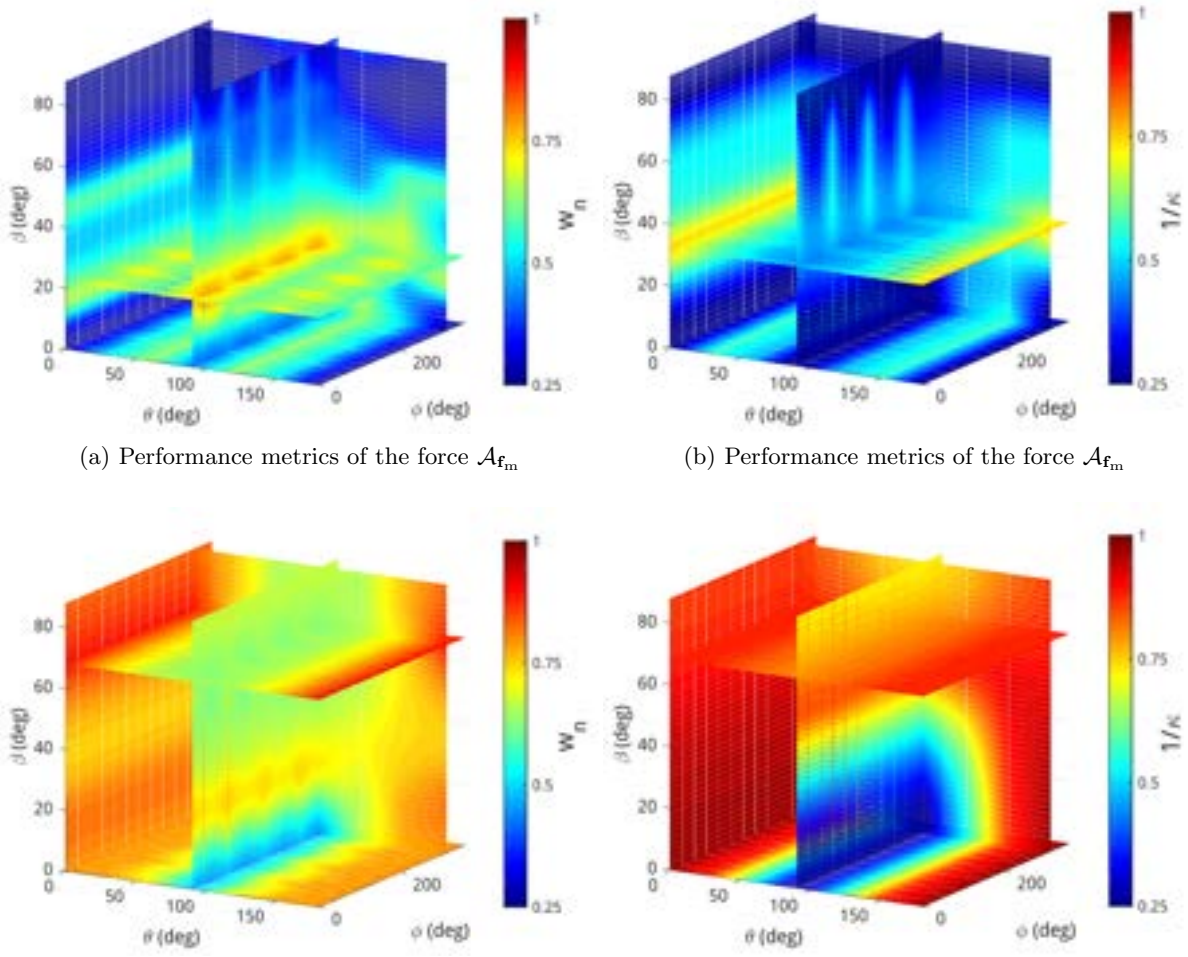

(a) Performance metrics of the force $\mathcal{A}_{\mathbf{f}_\mathrm{m}}$

(b) Performance metrics of the force $\mathcal{A}_{\mathbf{f}_\mathrm{m}}$

(c) Performance metrics of the torque $\mathcal{A}_{\mathbf{t}_\mathrm{m}}$

(d) Performance metrics of the torque $\mathcal{A}_{\mathbf{t}_\mathrm{m}}$

Figure III.33: Actuation performance indexes of the (a)-(b) force and (c)-(d) torque actuation matrices for the sampled orientations of the magnetic moment of the microrobot: (a)-(c) the global normalized manipulability index Γ_{w_n}; and (b)-(d) the global conditioning index $\Gamma_{1/\kappa}$.

To exhibit the influence of the moving angle β on the magnetic actuation performance, figure III.34 depicts the mean and uniformity metrics of the global performance indexes Γ_{w_n} and $\Gamma_{1/\kappa}$. The analysis of the force and torque global performance indexes reveals that it is more efficient to control $\mathbf{f}_\mathrm{m}$ with low angle, whereas $\mathbf{t}_\mathrm{m}$ requires a higher β, especially to increase its uniformity. These simulation results demonstrate that rotating the moving angle β could make the EMA platform more flexible to control efficiently either the force or the torque.

Finally, the impact of the moving angle β on the workspace size has been also investigated. Since the indexes are axisymmetric around the z-axis, the analysis is reported only along this direction. In particular, to evaluate the tissue penetration, the locations behind the workspace Ω could be considered. The different performance metrics are shown in figure III.35. The results in figures III.35a and III.35c show that high angle β leads to strong magnetic field and reliable torque dexterity. Specifically, a high angle $\beta \gtrsim 50°$ allows the increasing of the magnetic field strength

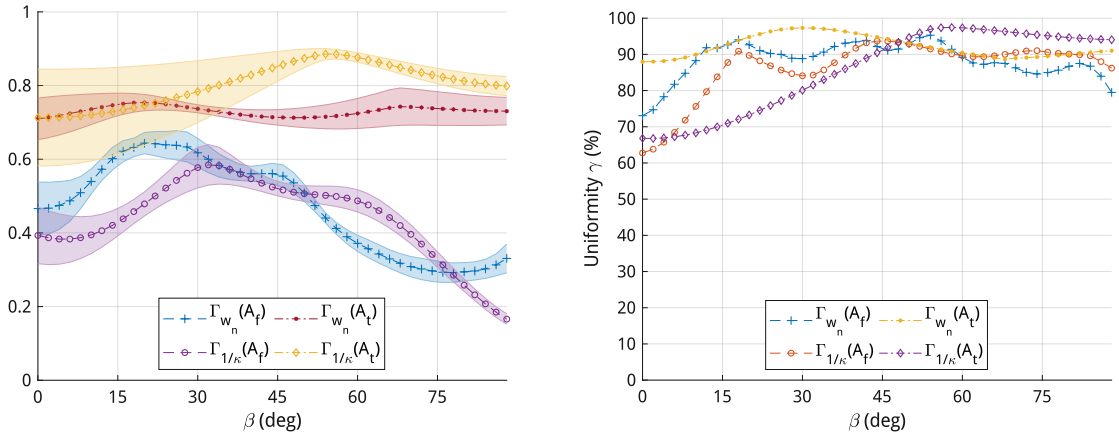

(a) (b)

Figure III.34: Statistical data of the global performance indexes of the force and torque actuation matrices for $\beta \in [0; 90°)$: (a) the mean and STD, and (b) the uniformity γ metrics.

$\|\mathbf{B}\|$ with a good uniformity (see also Figure III.32a), and the large value of the conditioning number $1/\kappa$ indicates that a reconfigurable EMA system is able to transmit a torque $\mathbf{t}_\mathrm{m}$ along any directions more efficient. However, to enable sufficient force $\mathbf{f}_\mathrm{m}$ in deep locations together with a good manipulability index w_n, a low angle $\beta \lesssim 30°$ is required. Therefore, these results exhibit that to design a versatile EMA system with both effective force and torque control, it is necessary to be able to vary the moving angle β_e of some coils. Such design objective seems a promising way to achieve optimal control of $\mathbf{f}_\mathrm{m}$ and $\mathbf{t}_\mathrm{m}$.

III.4.2 Case #2: reconfigurable MiniMag-like setup

The second case correspond to EMA platform similar to the MiniMag system, already introduced in section III.3.3. Specifically, the mobile set of coils is able here to rotate with the same angle $\beta = \beta_e \in [0; 90°)$ ($e = 5..8$, as shown in figure III.31c), while the stationary set of coils is fixed to $\beta_e = 26°$ ($e = 1..4$).

Figure III.36 shows the performance metrics of the magnetic field and its gradient with a moving angle $\beta \in [0; 90°)$. Similarly, the high moving angle value $\beta \gtrsim 45°$ provides stronger and more uniform magnetic field $\mathbf{B}$. Especially, the reconfigurable MiniMag-like setup induces a larger magnetic field strength along the z-axis than the OctoMag-like one (cf. figure III.32). However, the magnetic field gradient requires a low moving angle β to be stronger and more uniform. In particular, it can be seen in figure III.36d that their uniformity metrics γ are decreasing for $\beta < 26°$, and increasing again for $\beta > 56°$. In such case #2, it appears that it is more convenient to use high angles around $\beta \approx 50°$–$60°$ to get a suitable uniform magnetic field and gradient.

The performance indexes of the actuation matrix $\mathcal{A}(\mathbf{p}, \mathbf{m})$ are evaluated for different moving β angles, and reported in figure III.37. From these simulation results, it appears that if $\mathbf{m}$ is parallel to the xy-plane (ie. $\theta = 90°$), the global conditioning indexes $\Gamma_{1/\kappa}$ of both the force and torque are low, whereas the global normalized manipulability indexes Γ_{w_n} are advantageous. Moreover, when $\mathbf{m}$ is aligned along the z-axis ($\theta = 0° \mod 180°$), a good Γ_{w_n} is obtained and

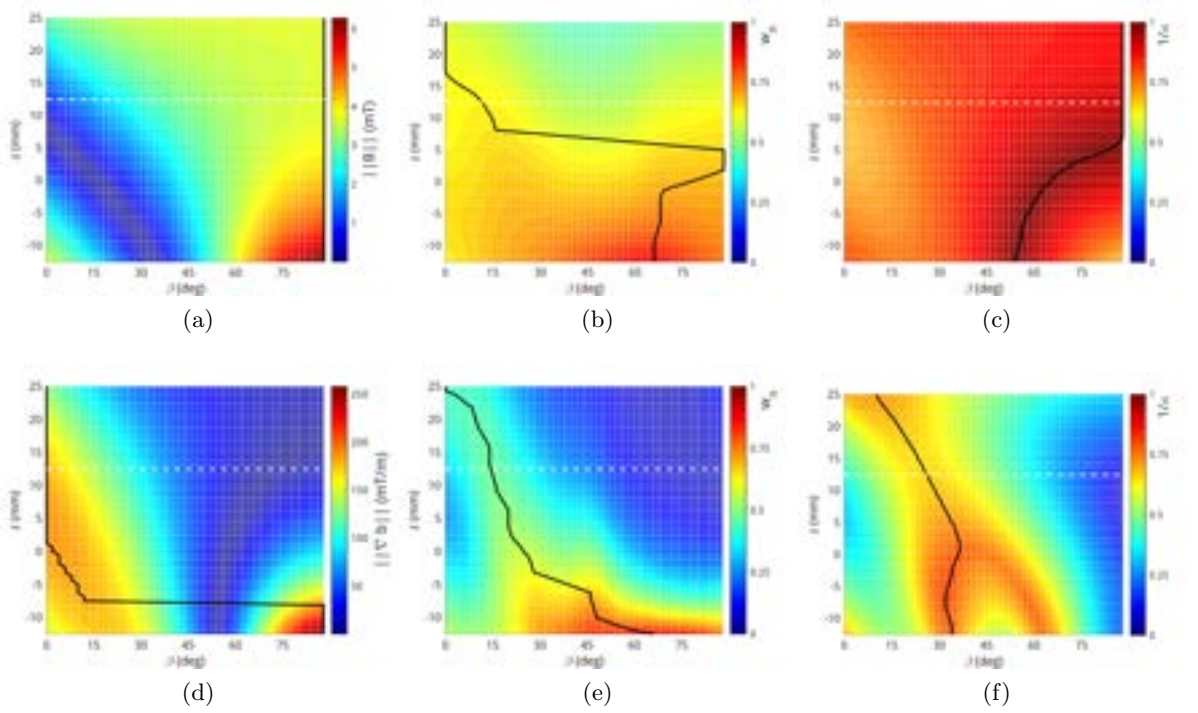

Figure III.35: Performance indexes along the z-axis of (a) the magnetic field and (d) its gradient magnitude; (b)-(c) the torque and (e)-(f) the force actuation matrices: (e)-(b) the normalized manipulability index w_n; and (f)-(c) the dexterity index $1/\kappa$. The black line represents the maximum value of the performance indexes.

$\Gamma_{1/\kappa}$ has the greatest value. Next, the moving angle β should have a low value to enable the good global performance indexes Γ_{w_n} of the torque and the force, while their $\Gamma_{1/\kappa}$ require a value around $\beta = 60°$. These trends are more clearly revealed in figure III.38 that shows the magnetic actuation performance indexes statistical data and uniformity γ.

Here again, the influence of $\beta \in [0; 90°)$ along the z-axis has been evaluated and is reported in figure III.39. Figure III.39a shows that high angle β leads to strong magnetic field strength $\|\mathbf{B}\|$. However, to maximize the other performance indexes, the moving angle should be adjusted with respect to the z-depth position of the magnetic moment $\mathbf{m}$ of the microrobot. For instance, figure III.39f shows that there are two angle routes to provide a force with a good dexterity: one with $\beta \lesssim 35°$ and the second with $\beta \gtrsim 65°$. Basically, for deep location, a low angle β enables a reliable manipulability w_n and conditioning number $1/\kappa$ metrics of both the force and torque. Therefore, changing the mobile angles β_e of electromagnets can obviously improve the versatility of the considered EMA system.

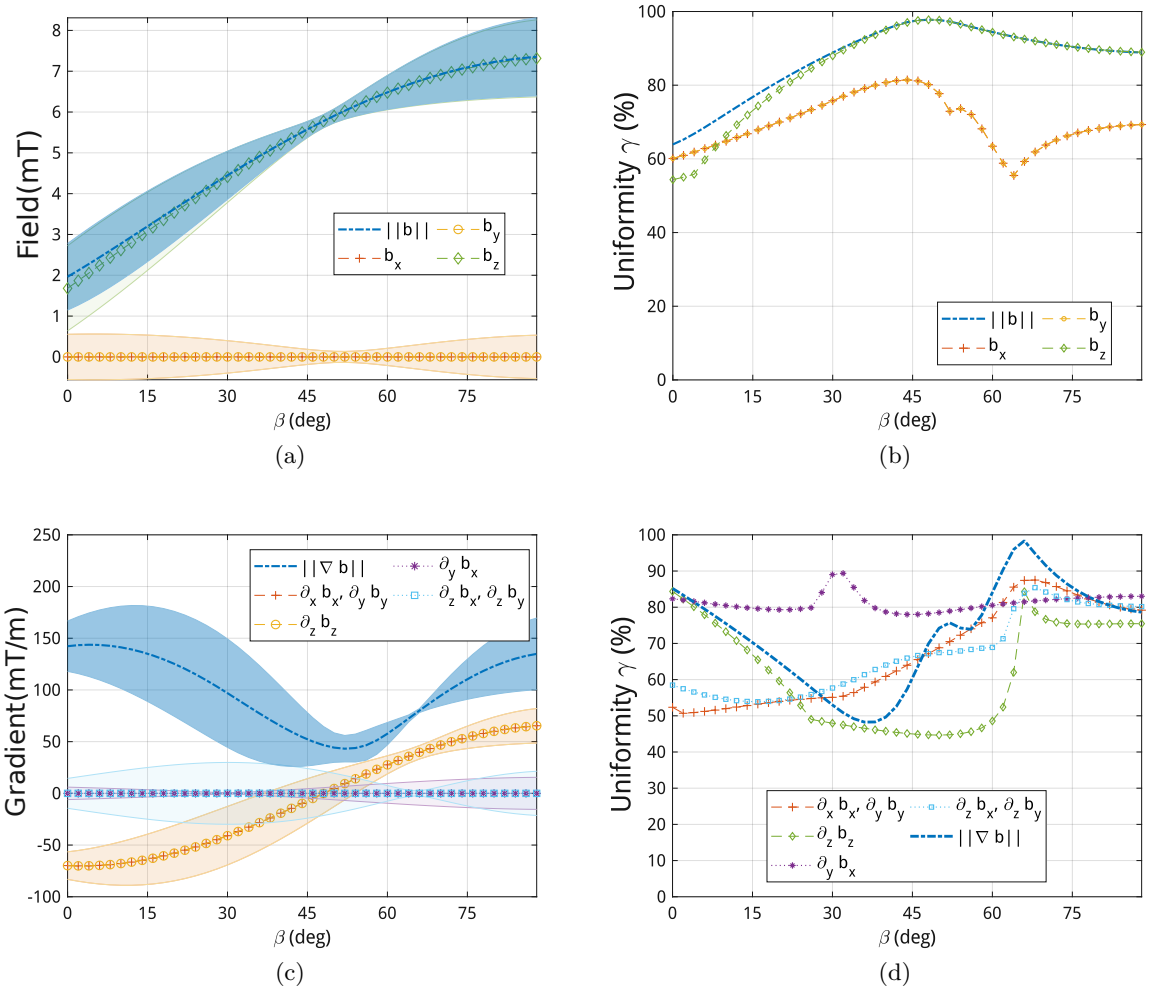

Figure III.36: Performance metrics of (a)-(b) the magnetic field and (c)-(d) its gradient of reconfigurable MiniMag-like setup when the mobile coils set is rotating with $\beta \in [0; 90°)$. The markers and envelopes (a)-(c) refer to the mean and standard deviation (STD) of the fields.

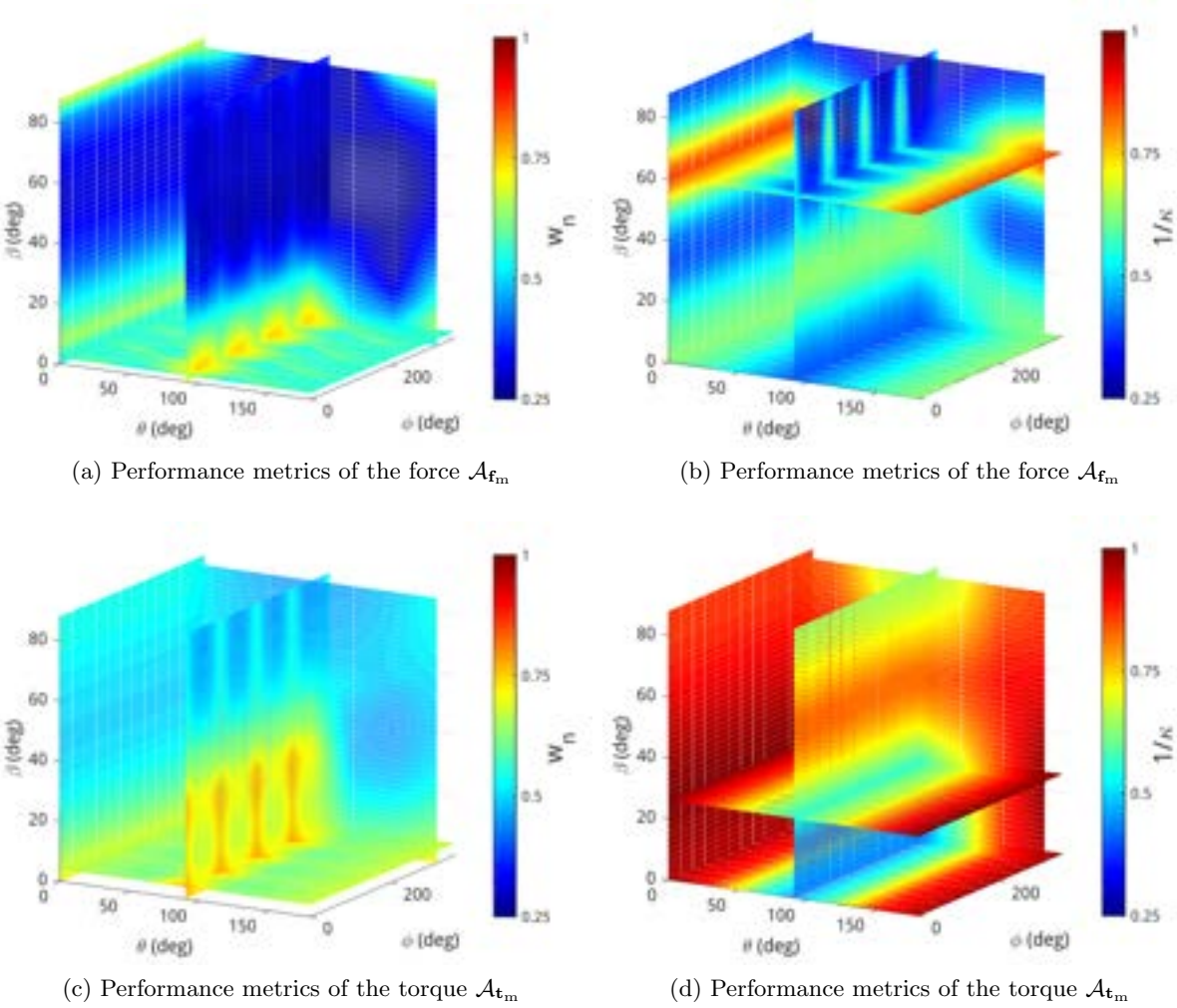

(a) Performance metrics of the force $\mathcal{A}_{\mathbf{f}_\mathrm{m}}$

(b) Performance metrics of the force $\mathcal{A}_{\mathbf{f}_\mathrm{m}}$

(c) Performance metrics of the torque $\mathcal{A}_{\mathbf{t}_\mathrm{m}}$

(d) Performance metrics of the torque $\mathcal{A}_{\mathbf{t}_\mathrm{m}}$

Figure III.37: Actuation performance indexes of the (a)-(b) force and (c)-(d) torque actuation matrices for the sampled orientations of the magnetic moment of the microrobot: (a)-(c) the global normalized manipulability index Γ_{w_n}; and (b)-(d) the global conditioning index $\Gamma_{1/\kappa}$.

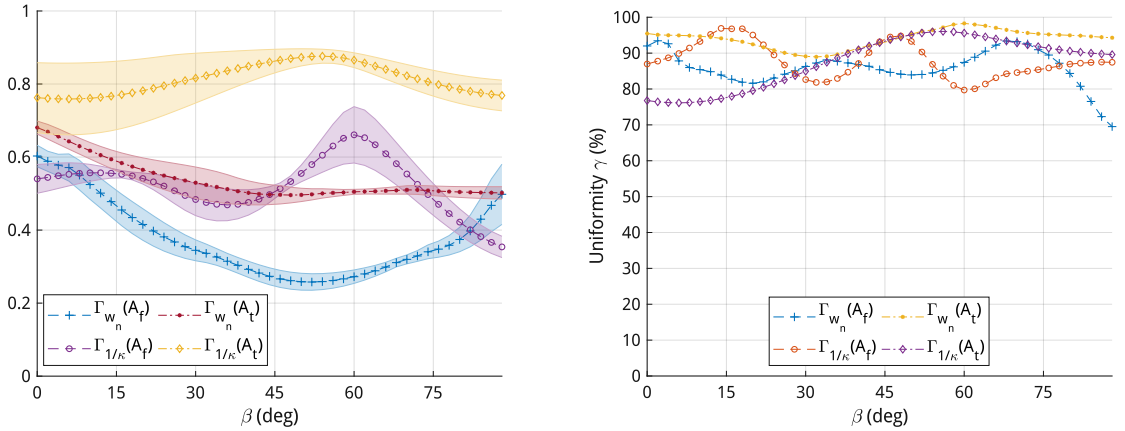

(a) (b)

Figure III.38: Statistical data of the global performance indexes of the force and torque actuation matrices for $\beta \in [0; 90°)$: (a) the mean and STD, and (b) the uniformity γ metrics.

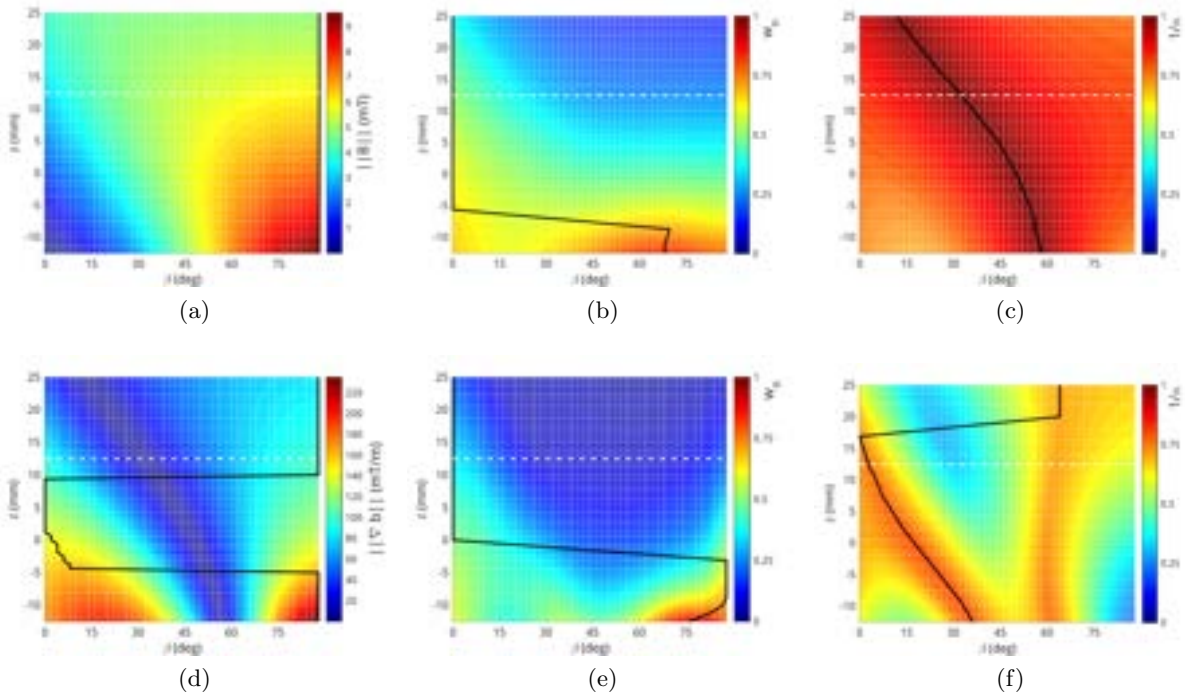

(a) (b) (c)

(d) (e) (f)

Figure III.39: Performance indexes along the z-axis of (a) the magnetic field and (d) its gradient magnitude; (b)-(c) torque and (e)-(f) the force actuation matrices: (e)-(b) the normalized manipulability index w_n; and (f)-(c) the dexterity index $1/\kappa$. The black line represents the maximum value of the performance indexes.

III.4.3 Discussions

Based on the numerous simulations, it appears that MiniMag-like arrangement provides the greatest magnetic field and gradient, besides, the most effective actuation performance can also be performed among the various considered configurations. However, the magnetic field distribution uniformity index γ of MiniMag-like arrangement is less interesting than OctoMag-like arrangement, implying some difficulties to derive the control strategy. Therefore, the choice of the basic EMA configuration should be motivated based on the applications objectives and the design specifications.

In the other hand, the investigation of the moving angle β shows that different performances can be achieved according to its value. Basically, lower values of β promote the magnetic field gradients, and thus the force $\mathbf{f}_{\mathrm{m}}$, while higher values enhance the magnetic fields and the torque $\mathbf{t}_{\mathrm{m}}$. Therefore, an adaptive EMA system composed of $n = 8$ electromagnets based on either a OctoMag-like or MiniMag-like reconfigurable platform seems a promising solution to enable the design of EMA platform for singular-free control of an untethered magnetic microrobot with 5 DOFs.

Furthermore, this section has focused on a reconfigurable EMA system by allowing a set of electromagnets to rotate with the same angle β. Obviously, the mobile electromagnets can clearly rotate with different angles β_e, which would improve the flexibility of the designed EMA system. Some simulation results concerning this aspect are presented in the Chapter A. Moreover, the former OctoMag and MiniMag EMA platforms have been optimized by the authors to achieve sufficient force generation capability within the entire workspace [60], [61]. In addition, the reconfigurable EMA system has been considered and evaluated with the same unit-current flowing into each electromagnet, which achieves a Maxwell-like configuration. It is also possible to use an Helmholtz-like configuration and different input currents.

Besides, the electromagnetic coils can be changed not only around the pitch axis (transverse axis), but also around the yaw axis (vertical axis). Véron *et al.* [161] demonstrate a magnetic parallel kinematic manipulator that controls the position and the orientation of the three electromagnets around the their yaw axes respectively in the horizontal plane. Similarly, the linear superposition principle is applied to the computation of the overall magnetic field, and the point-dipole model is used by the authors in this system. However, such rotational mode could cause some errors. Let us recall that the point-dipole model only can fit to the distant portion of the on-axis magnetic field data of the equivalent electromagnet and valid for location $\mathbf{p}$ along the electromagnet's axis. It should be noted that the applied workspace is shifted from the common center when the coils are rotated according to [161]. Hence, the point-dipole model can not perfectly fit the magnetic field within the real-time workspace once positions are not located along the vicinity of coil's axis. For such case, the numerical method such as using FEM model is required for magnetic field computation. However, there is a tough problem about the calculation. The computation time of numerical methods is much important than point-dipole model approximation.

Finally, the reconfigurable EMA system with moving angle β requires fewer current inputs flowing through the electromagnets for force and torque control, that then largely prevents significant Joule heating. Especially, the reconfigurable EMA setup allows decreasing the minimum number of electromagnets from $n = 8$ for the stationary case to $n = 6$ for mobile case for independently controlling torque and force [60]. The moving EMA system composed of less fewer permanent magnets/electromagnets has also been built and investigated where the few

DOFs are provided or the system is prone to singularities [54], [130], [131], [161]. However, in such case, the mapping between the input angles β_e and the outputs (ie. the force and torque or the magnetic field and its gradient) is nonlinear. Moving the angles β_e can change both the shape and magnitude of the magnetic field, which leads to the inconstancy of mapping matrices $\mathcal{B}(\mathbf{p})$ and $\mathcal{G}_{x,y,z}(\mathbf{p})$. This aspect should be considered for the control of the magnetic field and gradient.

III.5 Design analysis

Different arrangements of electromagnetic coils can produce various magnetic field distributions. The flat multi-electromagnet EMA systems are used for 2D manipulation. The flat four-coil system consists of two pairs of opposing electromagnets arranged orthogonally at 90°. Other systems with 6 or 8 electromagnets have been evaluated as shown in chapter A. The flat six-coil is arranged in a plane with angle 60° between each other. Similarly, the flat eight-coil is arranged in a plane with angle 45° to each other. For the 3D control of microrobot, the 3D configurations have been studied. The 3D six-coil EMA system composed of three pairs of opposing electromagnets and the eight-coil EMA system consists of eight independently placed electromagnets have been simulated. The OctoMag and MiniMag configurations both are eight-coil EMA system. For the OctoMag, four electromagnets are placed in one plane at 90°, other four electromagnets are offset by 45° and tilted down by 45° as shown in figure III.1b. For the MiniMag, each coil is offset by 45° from horizontal view, where the orientation angle of the four coils are 64° and the other four coils are rotated at 42.5° from the vertical direction as illustrated in figure III.1c. It seems the main difference is on the relation between different system geometries. However, the performances of the field and gradient are actually needed to be distinguished. Each considered EMA system has been simulated and analyzed. Based on these results, optimal configuration can be determined for the suitable application.

Obviously, the investigated EMA systems all can be reconfigurable where either the distance d_w or mobile angle β is adjusted. If either the strong magnetic field or gradient is required in 2D plane, $n = 2$ and 3 coils are necessary, respectively. The flat-four EMA system with short distance d_w can be applied for the control with redundancy as presented in chapter A. Commonly, if 2D applications require only a weak magnetic field with its gradient, a minimum of $n = 5$ electromagnets is essential. Thus, the flat-six or flat-eight EMA systems set to long distance d_w can be used to improve the field distribution and the control redundancy.

Similarly, the 3D EMA systems are also formulated with different distances d_w to achieve the desired performances. Especially, the efficiency of OctoMag-like and MiniMag-like systems has been further investigated with respect to the mobile angle β. When a strong magnetic field and gradient are of prime importance for the application, d_w has to be set to a short distance. Moreover, to enhance the magnetic field $\mathbf{B}$, the moving angle β has to be set to an high value. In contrast, to enable a proper magnetic field gradient $\nabla \mathbf{B}$, different specific values of β can be considered. Conversely, the long distance d_w leads to a more uniform magnetic field and gradient, higher manipulability of torque and force, and higher dexterity of torque and force. Moreover, these performance's improvements can also be realized by implementing the corresponding mobile angles β to superimpose their advantages with d_w.

From these various results, different system performances can be obtained, depending on the

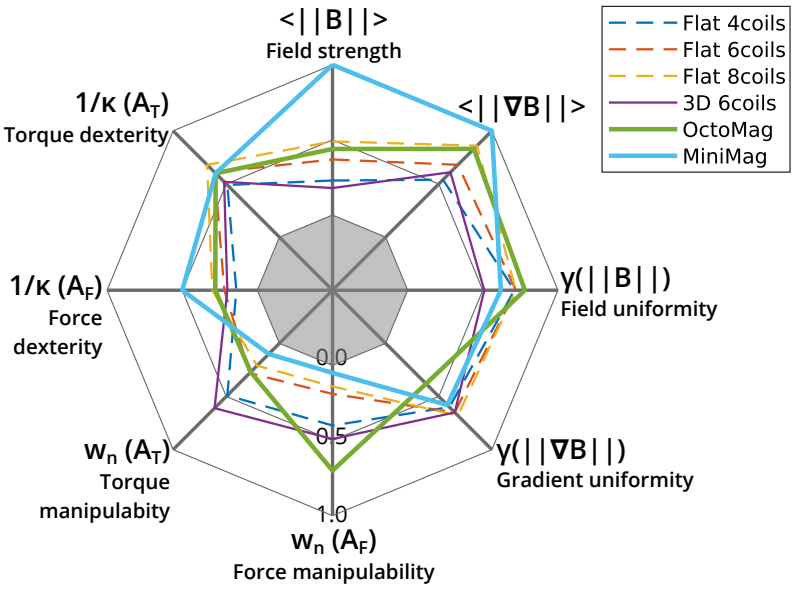

(a)

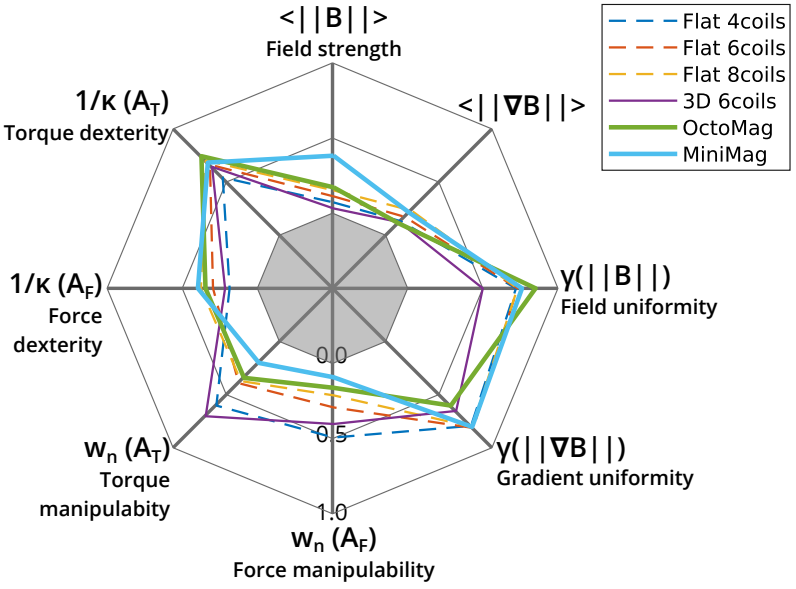

(b)

Figure III.40: The optimal performances for each EMA system design for (a) short and (a) long distance d_w.

given design parameters. All these capabilities are summarized in the chart[3] given in figures III.40 and III.41. In figure III.40, it is observed that the more electromagnets lead to the stronger magnetic field strength $\langle \|\mathbf{B}\| \rangle$. However, the uniformity of field does not change significant by applying more coils. If the magnetic gradient is prioritized for control, MiniMag, OctoMag and flat eight-coil configurations are set to short working distance d_w. Meanwhile, MiniMag, flat

[3]For the sake of consistency between the different results, the magnetic field strength and gradient are here normalized.

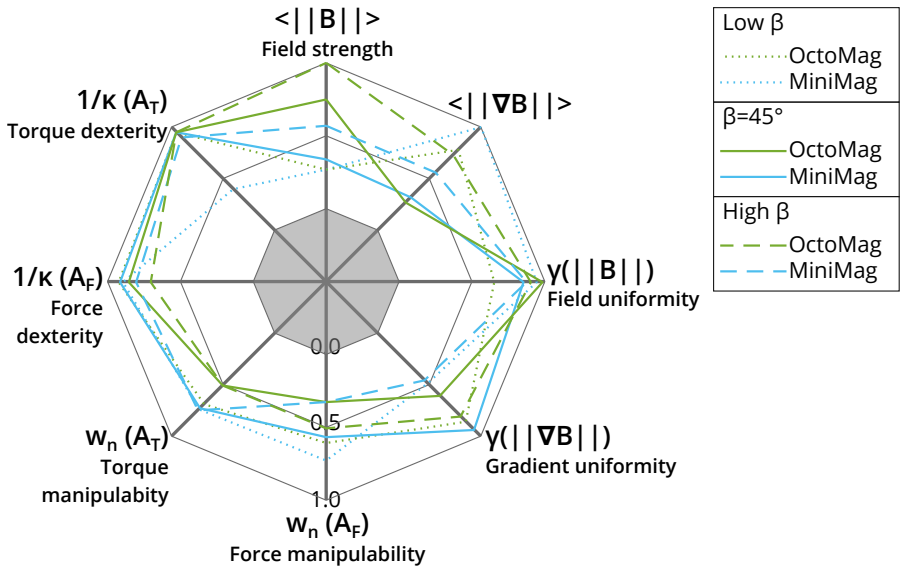

Figure III.41: The optimal performances for the OctoMag-like and MiniMag-like designs regrading the mobile angle β value.

eight-coil and 3D six-coil configurations are proposed for long distance d_w. Considering the uniformity of magnetic field and gradient, MiniMag system has the capability of generating both uniform field and gradient. OctoMag system can produce more uniform magnetic field as well, while its weakness lies in the uniformity of magnetic gradient. Besides, the flat configurations are also able to provide uniform magnetic gradient. The 3D six-coil and flat four-coil configurations carry the benefit of the good manipulability of torque. Especially in long distance d_w, flat four-coil arrangement has significant capability of producing better manipulability of force than other configurations. With short distance d_w, OctoMag system can be used to provide good manipulability of the force. Whereas, the great dexterity of force is produced by using MiniMag system since the eight coils with such configuration could lead to more dexterous force control. Such improved phenomenon also occurs in the term of the dexterity of torque through applying more coils.

The mobile angle β is hereafter further investigated with figure III.41. It can be observed that the magnetic field generated by MiniMag-like arrangement becomes much more strong than OctoMag-like configuration when the β is set to a high angle value. Conversely, the lower mobile angle allows OctoMag-like system to produce a stronger and more uniform magnetic gradient $\nabla \mathbf{B}$. Comparing Figure III.41, MiniMag-like configuration commonly presents better performance of force and torque control. When β is set to around 45°, MiniMag-like configuration has the significant capability to provide more manipulabilities of force and torque. When β is rotated to higher angle, OctoMag-like systems is able to achieve high manipulability of torque control, whereas MiniMag is good at controlling force. Therefore, for the desired application and required system performance, the optimal configuration or the design inspiration could be obtained from it.

III.6 Conclusion

The arrangement of multi-electromagnet has been analyzed in this chapter. The performance evaluation of the reconfigurable EMA system is thereby investigated. Several simulations were proceeded, and performance metrics of the actuated system were analyzed under the different distances and orientations of electromagnets. Results show that the reconfigurable platform of electromagnets enables a variety of local magnetic field distribution. The evaluations of the force, torque, manipulability and the dexterity indexes demonstrate that the reconfigurable system provides more flexibility. Overall, the shorter distance d_w can be used to generate the strong magnetic field and gradient, while their uniformities require longer distance d_w. Moreover, the low angle β leads to the more efficient magnetic force control. But the magnetic torque becomes less controllable as it requires an higher angle β. Thus, the reconfigurable EMA system is resourceful to perform various tasks by enabling the control of the distance d_w and angle β. These would help to develop more advanced navigation control strategy of biomedical magnetic microrobot for different micromanipulation tasks. In particular, it can be used for improving the convenience of minimally invasive operation. The next chapter will be addressed in building a reconfigurable platform for instance ophthalmic MIS.

Chapter IV

Design and implementation of OctoRob

Chapter contents

Introduction

Biomedical magnetic microrobots provide a promising alternative approach for many clinical procedures. To this aim, a reliable and effective EMA setup should be designed with respect to the medical applications objectives. In chapters II and III, the magnetic source generation, the minimum number of electromagnets for EMA system and the optimal configuration of electromagnets have been fully studied for different common applications. In this chapter, we will focus on the design of a novel EMA platform using the proposed method. As the envisioned requirements of the considered applications, the design parameters and objectives should be specified accordingly. As previously presented, we have chosen to focus on the study and analysis of a reconfigurable EMA system, namely a *robotic EMA platform*. For a concrete instance, we have particularly considered an *ophthalmic MIS* procedure using the medical magnetic microrobot.

Certainly, the use of the intraocular medical microrobot could allow less invasive and safer interventions in the eye. To date, many retinal procedures have been limited by human performance and perception. Indeed, the manipulation of retinal membranes is very delicate, and safe interaction requires forces at best of the order of what the surgeon can feel. The use of microrobots will mitigate traction on the retina with potentiality to circumvent the necessity to perform a vitrectomy of retina. It can be navigated in the eye cavity and then perform ophthalmic MIS tasks (such as material removal, drug delivery, punctures), that thus has the great potential to revolutionize the eye therapy and improve the patient care and recovery. Specifically, biomedical microrobot can be injected in the retina through a small incision, and controlled by manipulating the applied magnetic field and its gradient basically induced from the external EMA platform, as represented in figure IV.1. The corresponding EMA system should be designed accordingly to manipulate the untethered microrobot with full dexterity. In particular, the biomedical microrobot would be actuated to perform its tasks in vitreous humor (VH) that is not easy to evolve due to its high viscous environment. It means that, for completing the medical tasks, the microrobot should be able to evolve in the 3D workspace of the eyeball. Thereby, the heading of the microrobot needs to be controlled, and magnetic pulling would be required to perform the therapeutic tasks (puncture, peeling, etc.). The corresponding magnetic force $\mathbf{f}_{\mathrm{m}}$ and torque $\mathbf{t}_{\mathrm{m}}$ must be enough powerful to overcome the mostly gel-like medium, while allowing a reliable and safe interaction with the retina. Therefore, the generation of the proper magnetic field and gradient distribution from the applied EMA setup is important issue that must be investigated with regard to the specific biomedical application.

This chapter is devoted to the study of the design of appropriate magnetic microrobotic platform to provide more effective magnetic field and gradient on microrobot for performing the given medical tasks, that is an ophthalmic MIS intervention. To this aim, this chapter is organized as follows: Ophthalmology and ophthalmic surgery are discussed and the requirements of the considered application are thereby obtained. The overall concept of the designed EMA system is represented according to the given specifications. In addition, the operations of intraocular microrobot are investigated on the precise order of magnitude. When the requirements of application have been fully studied, the OctoRob platform is going to be designed. The electromagnetic coil is firstly investigated including magnetic core and optimal dimensions of electromagnet, moreover, the designed coil is evaluated and implemented. Furthermore, the design of the robotic arm is performed. The kinematic mechanism is then analyzed. Finally, the designed prototype is built from the obtained specifications, and the necessary evaluation of OctoRob is performed.

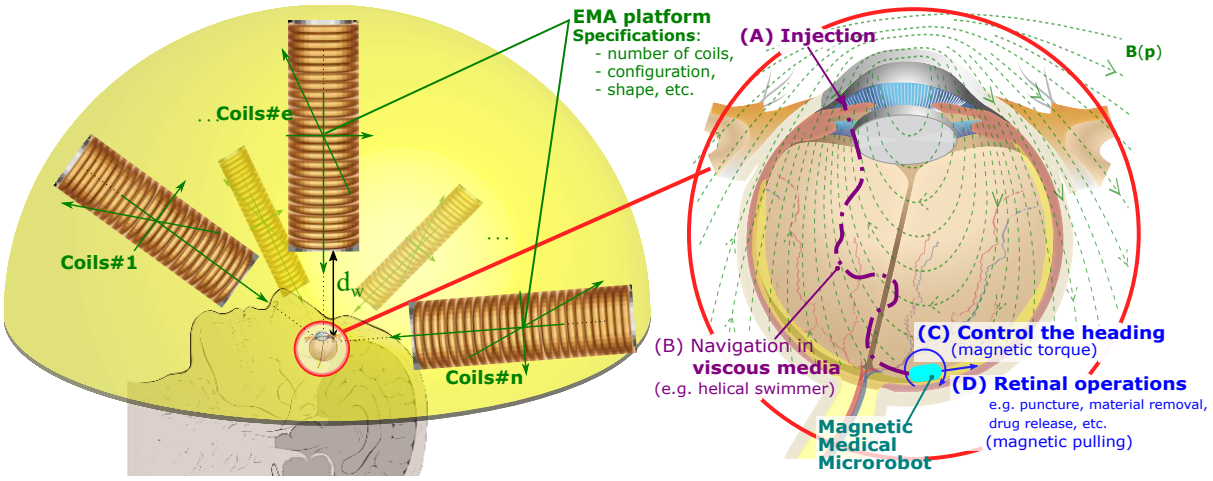

Figure IV.1: Illustration of the ophthalmic microrobotic MIS system: (left) the EMA platform that should respect the geometry of the human head, that is arranged in the yellow hemisphere; (right) the ophthalmic microrobotic MIS procedure where biomedical mirorobot is injected by surgeon and controlled by the EMA setup; the generated magnetic field and gradient induce the magnetic torque and pulling force to the medical microrobot for the different steps of the operations.

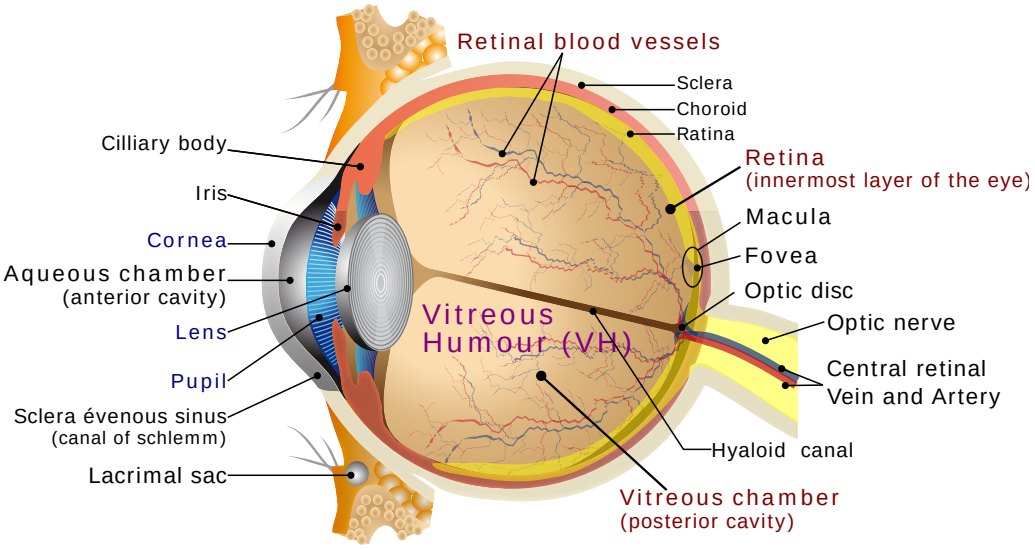

Figure IV.2: Schematic representation of the Human eye.

IV.1 Ophthalmology and ophthalmic surgery

Ophthalmology is the branch of medicine that is concerned with the eye and its diseases. There exists a number of textbooks with in-depth analysis of the eye such as the work by Snell and Lemp [162]. Similarly, there are numerous conditions of the eye that all require their specific forms of treatments. In particular, the discipline of vitreoretinal surgery includes basically all operations related to the vitreous and to the delicate retina (see also figure IV.2), whose health is essential for a good vision. Such ophthalmic procedures have great potential to be performed

involving less invasiveness through medical intraocular magnetic microrobots. Retinal surgery requires extremely precise movements and small tool/tissue interaction forces. Otherwise, there is a potential risk of permanent damage (i.e. permanent vision loss) through even small surgeon error.

For instance, one particularly difficult procedure is the retinal vein cannulation to alleviate its occlusion. Such retinal occlusion is among the most common causes of vision loss around the world, with a prevalence of 1.6% for adults aged 49 years or older [163]. Various treatment methods for this pathology have been proposed. For instance, intravitreal thrombolysis[1] with tissue plasminogen activator injection is the most promising treatment [164]. To do so, thrombolytic enzyme (i.e. clot-busting) has to be injected into the tiny occluded vein (diameter of about 100 µm).

Another challenging procedure is the peeling of epiretinal membranes (also called macular pucker). This disease of the eye makes a change in the vitreous humor (VH) leading to distortions of the vision, and its contraction can lead to severe vision impairment. The formation of such scar tissue on the retina can have a variety of reasons like age, trauma, idiopathic cause, etc. In order to remove such membrane, surgeon can peel it off with a micro-forceps. All these retinal procedures involve accurate positioning and force sensing that are at or beyond the sensation and control ability of most surgeons [165]–[167]. For instance, Gupta *et al.* [165] determined that only approximately 20% of contact events between the surgical tool and the retinal tissue during retinal microsurgery can be felt by the practitioner. This implies that a majority of retinal surgery is probably performed without haptic feedback and the surgeon relies on visual tissue interaction only. This lack of haptic feedback could adversely affect surgical outcome, as prior studies have shown that using only visual feedback increases the duration of manual manipulation tasks and reduces accuracy. Roughly 75% of all forces measured during retinal microsurgery were found to be less than 7.5 mN [165]. Although the forces in the study of Jagtap and Riviere [166] are somewhat higher, there is still substantial evidence that the forces involved during retinal surgery are at or beyond the limits of human perception.

In addition to its complexity, conventional vitreoretinal surgery is an invasive process. During the intervention different tools are placed in the patient's eye, such as an irrigation line to maintain constant pressure, a light source to improve the visibility, and the required surgical instrument to perform the desired task [168]. Furthermore, most procedures that are performed on the retina require a preliminary *vitrectomy* to be able to target the actual disease site. Secondly, the traction induced on the VH by the surgeon's tool is transferred to the retina, and it can cause retinal detachment or retinal tears (see figure IV.2). Hence, the vitrectomy could reduce significantly such impairment. Indeed, vitrectomy is the partial or complete removal of the VH from the patient's eye. In the case of non-resolving vitreous opacity, a vitrectomy is the sole solution. Nevertheless, performing a vitrectomy is an arduous procedure that requires extreme care. Moreover, the performance is hampered because it is difficult to determine the VH that needs to be removed. Additionally, there is a high risk of complications after the procedure.

Due to the difficulty of accessing to the delicate retina during the MIS procedures, vitreoretinal surgery could be rendered less invasive and safer through the use of intraocular magnetic microrobots. In comparison to larger tools, the small size of such therapeutic agents will mitigate traction on the retina with the potential to completely circumvent the necessity to perform a vitrectomy to access the retina. With the goal of enabling less invasiveness and safer retinal

[1] Thrombolysis, also called fibrinolytic therapy, is the breakdown of blood clots formed in blood vessels.

operations, as well as providing an increased level of dexterity desired by clinicians, the designed EMA platform is considered for the magnetic micromanipulation of a fully untethered and dexterous microrobotic device inside the volume of a human eye. Thereby, the requirements of magnetic micromanipulation will be investigated in the following sections.

IV.1.1 Ophthalmic microrobotic MIS

Even the most skilled surgeons have involuntary physiological tremors, which causes most ophthalmic surgeries at the peak of human capabilities [165]–[167]. To improve the surgeon's performance, different robotics technologies have been involved [60], [169]–[172]. Although most of these current robotic solutions improve the quality of ophthalmic surgery, the invasiveness of the procedure is not fully reduced. The use of untethered magnetic microrobot is a promising alternative to enhance the overall ophthalmic MIS operations.

As introduced in chapter I, there is a wide variety of solutions and techniques to magnetically actuate a medical microrobot. The choice of the proper magnetic microrobotic system should be defined with respect to the biomedical application, here an ophthalmic MIS procedure. The envisioned microrobotic MIS system for eye intervention is shown in figure IV.1. First, magnetic microrobot is injected by the operator through a tiny incision to potentially circumvent the necessity of performing a vitrectomy. The biomedical microrobot consists of magnetic material and can be controlled through the applied magnetic field and gradient generated by an external EMA setup. Next, the magnetic microrobot is actuated to navigate in the VH that fills the space between the lens and the retina (see also figure IV.2). Its workspace is basically filled by a transparent gel-like steady medium with a non-Newtonian rheological property [173]–[175]. In details, the VH is composed of about $\sim 99\%$ water with the addition of $\sim 0.9\%$ salts, and $\sim 0.1\%$ of a network of collagen[2] fibrils and hyaluronan[3] that all form a scaffolding [175]. The collagen concentration in VH is around $40\,\mu g/cm^3$ to $120\,\mu g/cm^3$, and collagen type II is the most abundant type in the eye. This presence of collagen leads to a gelatinous consistency, and thus the VH has a viscosity 2-4 times greater than of water ($\rho_{\text{water}} = 1\,\text{mPa}\,\text{s}$). To perform the specified medical tasks, the microrobot must be capable of moving efficiently and reliably in the 3D workspace of the eyeball. Typically, microrobot is manipulated in fluids at the low-Reynolds-number regime (e.g. $R_e \ll 1$), where viscous drag significantly dominates over inertia [87]. In such physiological condition, helical microswimmer is known to be one of the most efficient propulsion mechanism [44], [100], [113]–[115], [119] (see also section I.2.2.2).

On the other hand, the microrobot is positioned and oriented on the targeted site and then performs the specified ophthalmic tasks, such as targeted therapy and/or material removal (peeling, puncture, drug delivery, etc.). For instance, to perform a lamina puncture for the treatment of retinal vein occlusion, the biomedical microrobot must navigate to the desired location and be rotated to a given heading to punch successfully the considered tissue. To realize a targeted drug delivery, the microrobot also needs to navigate to a specific region in order to control the release kinetics of the drug and modulate the concentration at the therapeutic window. To do so, the overall motion of the magnetic microrobot in the 3D workspace of the eyeball is simply summarized as its 3 translations and 2 rotations, that is with 5 DOFs. The motion of microrobot can be controlled by either the applied magnetic field or gradient. Basically,

[2]Collagen is the main structural protein in the extracellular matrix in the various connective tissues in the body.

[3]Hyaluronic acid (HA) is an anionic glycosaminoglycan (an animo sugar) that is a major component of synovial tissues and fluid.

the magnetic field produces the magnetic torque $\mathbf{t}_\mathrm{m}$ in order to rotate the microrobot heading, perform a corkscrew swim, or a drilling operation. The magnetic gradient is commonly used to generate a pulling force $\mathbf{f}_\mathrm{m}$ to propel the microrobot or to perform a robotic task (puncture, peeling, etc.).

Finally, as shown in figure IV.1, the external EMA platform should be conveniently placed in front of the head with a suitable distance with respect to the eye. Then, the corresponding magnetic field and gradient have to be effectively applied within the 3D workspace of the eyeball. Especially, the control of the magnetic actuation should precisely and reliably meet the requirements of the ophthalmic MIS procedure. The next section sets out the specifications for the design of such EMA platform regarding ophthalmic MIS operation.

IV.1.2 Intraocular MIS operations requirements

First, the geometric constraints of the eyeball should be considered. As reported by Bekerman *et al.* [176], the size of a human adult eye is about 21 mm to 27 mm, without significant difference between gender and age groups. Hence, the diameter of the considered workspace should be at least 27 mm. However, some extra spaces should be reserved for other eye tissues and the movement of eyeballs. Similarly, the workspace Ω should be defined in respect of the working distance d_w between the workspace center O and the electromagnet, as reported in figure IV.3. From the analysis carried in section III.3, d_w should be sufficiently small to enable strong magnetic field. Based on these results and requirements, the workspace is defined as a cube of volume of $\Omega = 45\,\mathrm{mm} \times 45\,\mathrm{mm} \times 45\,\mathrm{mm}$ with a working distance $d_w = 65\,\mathrm{mm}$.

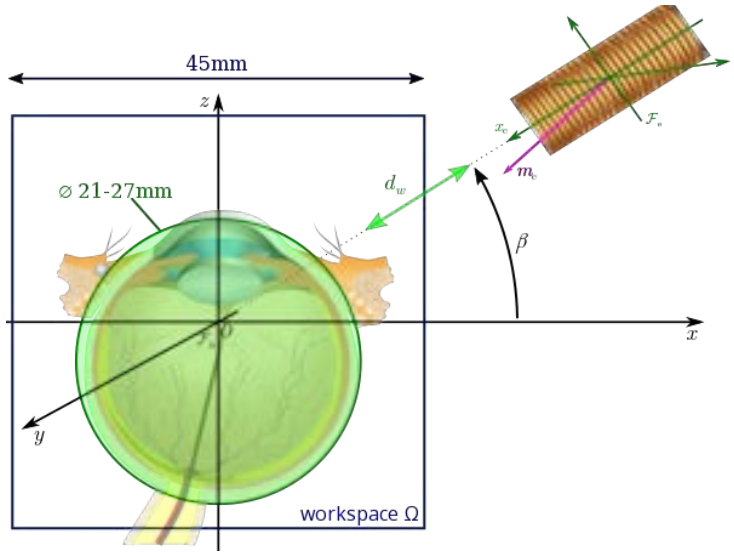

Figure IV.3: Representation of the workspace with respect to the eye geometry.

In the considered intraocular application, the microrobot will be actuated in the VH to perform the biomedical tasks. Basically, the VH is a complex transparent biofluid that exhibits non-Newtonian rheological properties. The VH contains no blood vessels and very few cells that are composed mostly of phagocytes. Commonly, two different phases is distinguished in VH: i) a liquid phase near the center of the eyeball, and ii) a gelatinous phase near the edges due to the presence of the network of collagen fibrils and hyaluronic acid [173]–[175]. Specifically, Bonfiglio

et al. [173], [174] report that the kinematic viscosity can be considered from $5 \times 10^{-6}\,\mathrm{m}^2/\mathrm{s}$ to $8 \times 10^{-4}\,\mathrm{m}^2/\mathrm{s}$. While the density is around $1.0053\,\mathrm{g/m}^3$ to $1.0089\,\mathrm{g/m}^3$. VH liquid phase has a surface tension of 47.8 mN/m, that behaves like a typical viscoelastic gel, presenting an elastic region and followed by a delayed elastic region [175]. Therefore, the physiological properties of the medium are changing significantly, and the EMA platform should adapt the magnetic field and gradient distribution accordingly.

As reported by Amblard *et al.* [177], a force between 0.1 pN to 1 pN is enough for moving a micro-object through a moderately dense actin filament network. If the microrobot is made of SPIO material with a magnetization of 50 emu/g with an equivalent diameter of about $L \sim 2\,\mu\mathrm{m}$, at least a magnetic field magnitude of about 200 mT and a magnetic gradient strength of 0.1 mT/m are required. Let us recall, that the necessary field intensity decreases or increases following a cubic power of the characteristic length (L^3) of the magnetic material of the microrobot. Also, for some operation, such as human retinal vessel puncture, stronger magnetic forces are required. For instance, Dogangil *et al.* [89] report some experimental results on the required magnetic force for puncture tasks with an upper bound around 10 mN. Their results are in agreement with medical data given by Gupta *et al.* [165] where it is reported that most puncture forces during vitreoretinal surgery should be below 12.5 mN. Moreover, smaller and sharper microneedles tip will reduce the required puncture forces [178]. Therefore, for microrobot of size of few $L \sim 100\,\mu\mathrm{m}$, the required magnetic field strength could be assumed to be at least about $\|\mathbf{B}\| = 15\,\mathrm{mT}$, and the magnetic gradient strength at least on the order of 100 mT/m. To summarize, the required amount of magnetic field and gradient may vary according to the different tasks that has to be achieved by the medical microrobot, such as navigating in different VH phase, and performing the specified ophthalmic interventions (e.g. peeling, punctures).

Considering these biomedical specifications, the designed EMA platform has to provide the necessary magnetic field and gradient for producing magnetic torque $\mathbf{t}_\mathrm{m}$ and force $\mathbf{f}_\mathrm{m}$. As shown in chapters II and III, the generated magnetic field and gradient distribution are affected by many parameters, including the number of electromagnets or their arrangement, also by their shape and material properties. Secondly, to allow a reliable and efficient ophthalmic MIS intervention, the characteristic of these fields must be able to adapt the task in progress. Thereby, the *reconfigurable EMA setup* fulfilling the application objectives will be designed in detail by the following section.

IV.2 OctoRob platform design

The effective design of the EMA setup must best meet the requirements for the considered application objectives. Since the main components of the system are the electromagnetic coils, it is necessary to determine their number, arrangement, material properties, geometry and size.

With the suitable electromagnets, the first issue is to chose the configuration arrangement of the electromagnets around the human head. Indeed, the chosen configuration must yield the human head geometry allowing the eyeball as workspace (see figures IV.1 and IV.3). Commonly, the minimum size of the workspace is restricted by the dimension of the coils, which is also related to the shortest distance d_w. Obviously the larger electromagnetic coil leads to a more powerful magnetic source, but it will make the coils more crowded surrounding of the workspace. Furthermore, the larger coils generally require longer distance d_w. Thus, the maximum diameter of electromagnets can be obtained through their most compact geometric arrangement considering

a working distance with a value of $d_w = 65\,\text{mm}$. In addition, from the previous investigation, at least $n = 8$ electromagnets sources are necessary to achieve 3D magnetic manipulation in the human eyeball. Therefore, either the OctoMag-like or the MiniMag-like configuration seems to be a proper arrangement solution to fulfill the EMA design specifications. Besides, the realized EMA sytem (called OctRob) should be adaptable and adjustable in real-time with respect to the microrobotic task. The distance (d_w) and orientation (β) of each electromagnet are important parameters to be adjusted. Specifically, as reported in chapter III, the adaptation of the moving angle β of a mobile coil set makes it possible to favor either the magnetic field or its gradient. That is why a kinematic mechanism should be devised in order to adapt in real-time the orientation of each movable electromagnet.

The reconfigurable electromagnet system is realized by the use of robotic arms, where the spatial transformation matrices are applied. Since the mobile angle β at the end-effector of the robotic arm is the sole parameter, only the kinematic rotation is utilized to achieve dynamic analysis. Thereby, the simulations of the realized robotic EMA system will be further investigated for performance estimation. These different aspects are presented in the following sections.

IV.2.1 Electromagnetic coil design

To design the magnetic sources of OctoRob, core-filled electromagnet has been selected. The core-filled electromagnet is able to generate a stronger magnetic field than the air-filled electromagnet since the magnetic core can concentrate the magnetic field. Basically, the magnetic material, the shape, the geometry of the core are the key design parameters of the electromagnet.

IV.2.1.1 Magnetic core

To enhance the magnetic strength, a core is added within the coil to confine and guide the magnetic field. However, the presence of a magnetic core involves some non-linearity and coupling between the electromagnets in the magnetic field distribution. Furthermore, different loss effects occur when the flowing current is varying in the coils, such as winding, eddy currents and hysteresis losses. Therefore, the choice of its material is an important issue. Basically, soft-ferromagnetic material should be chosen [146]. Indeed, to select an efficient magnetic core material, its permeability, saturation magnetization ($\mathbf{M}_{sat}$, A/m) and coercivity ($\mathbf{H}_c$, A/m) are the main relevant characteristics (see figure IV.4). The higher permeability and saturation magnetization are preferred for flux confinement and focusing. Whereas, a low coercivity is important for high-frequency applications and to reduce the core losses. Table IV.1 reports properties of some common soft-magnetic materials. Moreover, some additional constraints should be also considered in the choice of the core material. For instance, to deal with mechatronic constraints, its weight may come an essential issue. Obviously, the cost of the material is also a significant factor in the final choice.

Once the magnetic core material is chosen, the shape of its tip may be estimated. Commonly, flat-faced, rounded and sharp-faced magnetic cores have been investigated by researchers [147], [181]. In particular, if the tip of the magnetic core is not flat but pointed or round, the magnetic field is nonuniform and severely distorted. In contrast, the use of sharp-faced allows the generation of higher magnetic field and a larger field gradient near electromagnet. For instance, the effect of core tip geometry on magnetic field projection is evaluated by Kummer [147] with the FEM analysis reported in figure IV.5. From these results, it appears that the more soft-magnetic material is packed up to the very edge of the coil, the more induced magnetic field will be emitted,

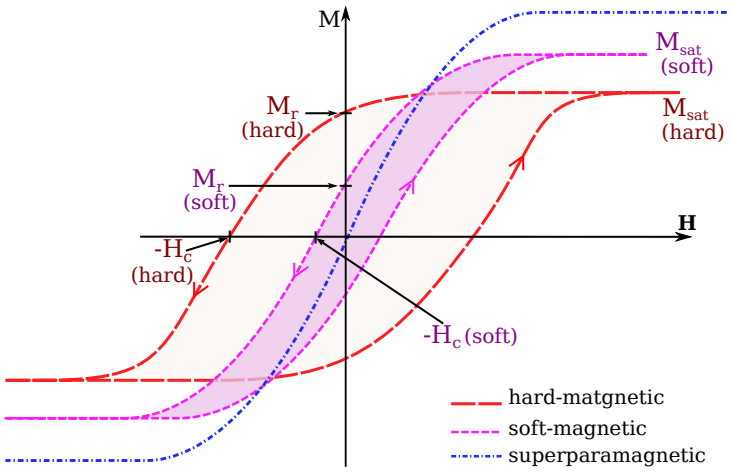

Figure IV.4: Typical hysteresis curve for ferromagnetic materials. The intercepts $\mathbf{H}_c$ and $\mathbf{M}_r$ are the intrinsic coercivity and magnetization remanence.

Table IV.1: Typical properties of some soft-magnetic materials. (adapted from [147], [179], [180])

Material	Saturation (A/m)	Remanence (T)	Coercivity (A/m)	Relative permeability (μ_r)	Density (kg/m^3)
Cobalt (Co)	2.4×10^6	0.5	795.7	250	890
Iron (Fe)	3.1×10^6	1.3	79.5	5000	7874
Nickel (Ni)	5.1×10^5	0.4	55.7	600	8908
Low carbon steel[a]	1.7×10^6	0.9	397	1560	7850
FeCo alloy[b]	1.8×10^6	1.6	100	7000	8120
FeNi alloy[c]	1.2×10^6	1.1	2.8	190 000	8200

[a]properties for C35 standard carbon steel with 0.35% C, 0.15% Si, 0.5% Mn, and 0.015% S
[b]properties for Vacoflux®50, from Vacuumschmelze Gmbh, that is composed of 49% Fe, 49% Co, 2% V
[c]properties for Supra50, from Aperam S.A., a Mu-metal that is composed of 51.9% Fe, 47.5% Ni, 0.5% Mn, 0.1% Si

and will generate a stronger magnetic field. For our application objective with a working distance of $d_w = 65\,\text{mm}$, flat-faced tip (or equivalent cylindrical tip) can make electromagnet to generate the strongest and the most uniform magnetic field in a workspace of $\Omega = 45\,\text{mm} \times 45\,\text{mm} \times 45\,\text{mm}$. However, the flat-faced tip could cause more crowded space when the $n = 8$ electromagnetic coils are arranged together around the workspace. Especially, it is clear that the induced magnetic field will be enhanced when magnetic core increases its volume. Thereby, with sufficient space for the electromagnet to move, the core-filled electromagnet can be enlarged to increase the induced magnetic field strength. The electromagnet dimensions is discussed hereafter.

IV.2.1.2 Optimal electromagnets sizing

Suitable electromagnet dimension is important for generating the necessary magnetic field and gradient in a limited workspace Ω. The requirement for magnetic manipulation in the compatible intraocular procedure leads to a working distance of about $d_w = 65\,\text{mm}$. As mentioned in figure IV.6, the different coils of the EMA platform are divided in two sets: i) four stationary

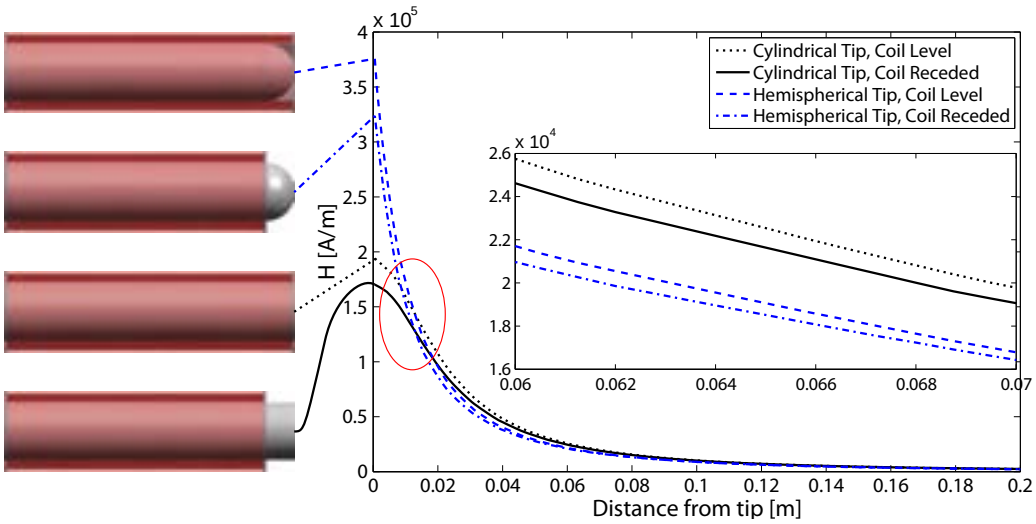

Fig. 3.7: *Magnetic field strength along the symmetry axis of different electromagnets. Two pairs of cores, with hemispherical and flat tips respectively, were used with coils that cover the entire length of the core or leave the last core-radius-long piece of core freestanding. It can be seen that an electromagnet with a cylindrical, flat tip core that is completely surrounded by the coil will have a magnetic field that projects the farthest.*

Figure 3.7: Magnetic field strength along the main axis of electromagnets with different tip-shapes: hemispherical shape tip or flat shape tip in two different length coils (from [147]).

electromagnets: $e = i = 1..4$, and ii) four mobile coils: $e = j = 5..8$. These two sets are arranged around a common z-axis with an azimuth angle $\alpha_e = 45°$ ($e = 1..8$), and are pointing to the common center O of the octahedron that the $n = 8$ electromagnets are identical with a cylindrical geometry and an external radius[4] r. They are initially considered placed to get the maximum value $r_{\max}$ of their dimension. Specifically, the largest $r_{\max}$ is obtained when all coils are closely contacted with their neighboring. In our case, any mobile coils are in contact with all its adjacent coils (either a mobile or stationary ones). However, the stationary coil set is in contact only with the neighboring mobile coils, but not with the other (stationary) coils. For instance, the stationary coil $i = 1$ touch the $j_1 = 5$ and $j_2 = 8$ ones; whereas the mobile coil 5 is in contact with 2, 6, 1 and 8.

3.5.3 Electromagnet Dimensions

To determine the dimensions of the electromagnets, different considerations needed to be accounted for. All considerations that led to the final geometry of the electromagnets will be presented here.

Spatial considerations

Recall that the open space surrounding the center of the setup was chosen to be a sphere with a 130 mm diameter. This information together with the knowledge of the optimal pose of the electromagnets determined in Section 3.4 can be used to find the maximum allowable tip diameter of the electromagnets. The working distance of any electromagnet in the setup, upper or lower, to the center of the setup is $w = 63$ mm. Figure 3.8a shows a bottom view and a side view where three electromagnets were removed. In this picture one can clearly recognize that there is a densest packing of electromagnets for a given working distance and system geometry. At this critical value the electromagnets start to contact one another. Thus the radius r_{magn} of the face of an electromagnet is r_{max}, and the maximum diameter $d_e = 2r_{max}$ of each electromagnet is $d_e = 2r_{max} = 26$ mm.

Figure IV.6 represents the geometric view of the $n = 8$ electromagnetic coils, where the cyan lines denote the distance $d_1 = OO_e$ from the tip center O_e of the electromagnet e to the workspace center O; the yellow lines represent its external radius r; and the green lines indicate the distance between the core center O_e to the adjacent contacting electromagnets. First, due to the axisymmetric arrangement, the distance $d_{i_1 i_2} = O_{i_1}O_{i_2}$ between two neighboring stationary coils i_1 and i_2 are identical in the same way all distances $d_{j_1 j_2} = O_{j_1}O_{j_2}$ between two adjacent moving coils j_1 and j_2 are equal. Next, each electromagnet has a cylindrical face of radius r. It can be shown that it is tangent to the sphere of radius d_e and they are in the same plane for the two contacting coils, and that OO_e and any connecting line at right angles (90°), as represented in figures IV.6b, IV.6c and IV.7. As all coils share the same radius r and working distance d_w, for stationary coils $i_1 = 1..4$ and their adjacent mobile coils $j = 5..8$, the distances $d_{ij} = O_iO_j$ all have the same length. Thus, a mobile coil $j = 5..8$ and its two adjacent stationary coils i_1 and i_2 form an isosceles triangle $O_{i_1}O_jO_{i_2}$, and in the same way $O_{j_1}O_iO_{j_2}$ also form an isosceles triangle. Following the same reasoning, it can be seen that all angles[6] $\theta_{j_1 j_2}$ between two adjacent

Using the relationship of the angle between two vectors $\mathbf{a}$ and $\mathbf{b}$ and their dot product

$$\mathbf{a} \cdot \mathbf{b} = |\mathbf{a}| \cdot |\mathbf{b}| cos(\alpha) \ , \tag{3.5.1}$$

[4] The external radius encompass the core, the coil winding, and eventually the cooling part.

[5] O_iO_j: possible cases are O_1O_5, O_2O_5, O_2O_6, O_3O_6, O_3O_7, O_4O_7, O_4O_8, and O_1O_8.

[6] $\theta_{j_1 j_2}$: possible cases are θ_{56}, θ_{67}, θ_{78} and θ_{85}.

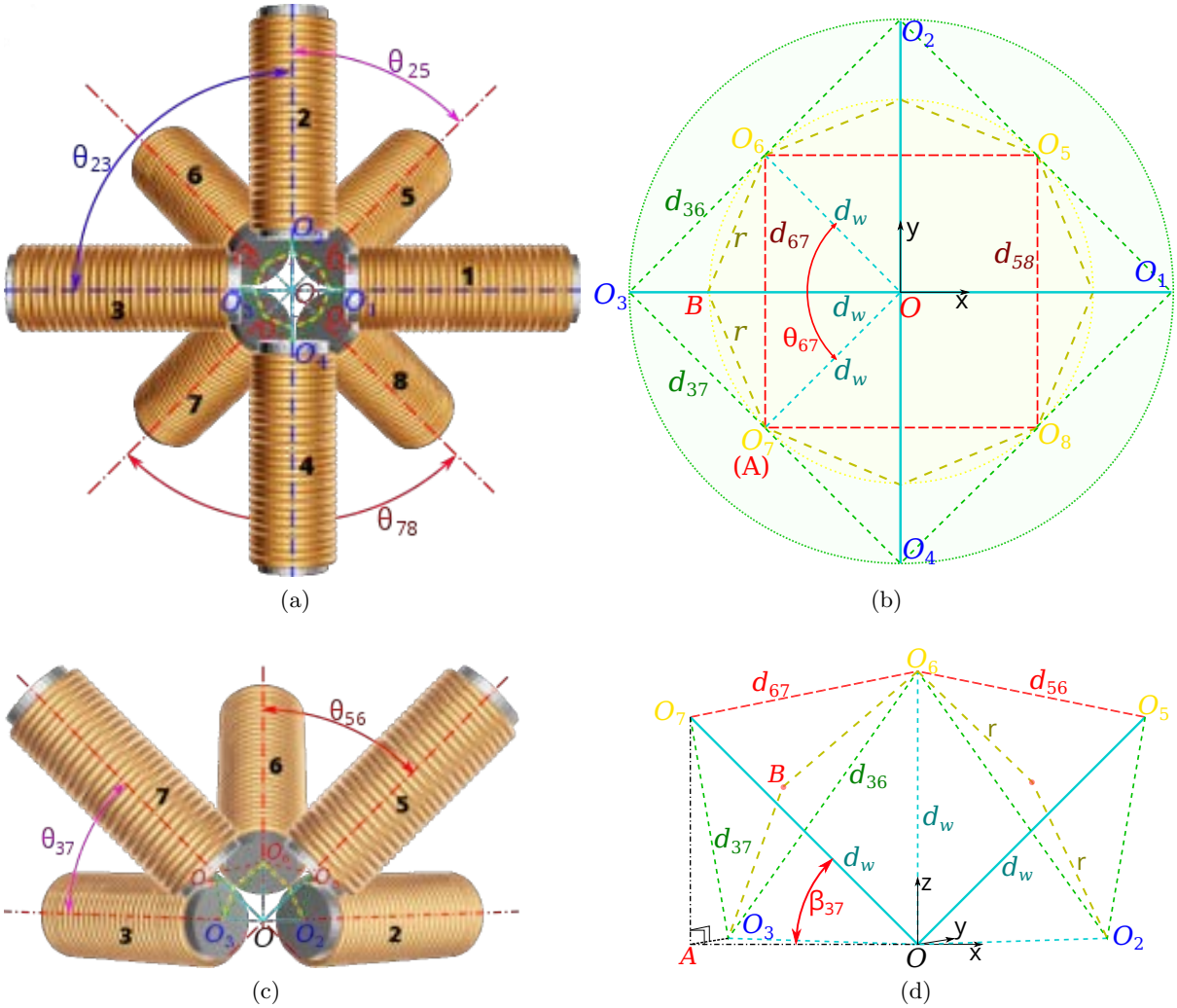

Figure IV.6: Representation of the geometric arrangement of the 3D $n = 8$ electromagnetic coils: (a) top views; (c) side views where three electromagnetic coils are removed to show clearly internal space; (b) and (d) show the geometry between the electromagnets center O_e. The plain lines depict the in-plane lengths, whereas dashed lines represent the out-of-plane one.

mobile coils j_1 and j_2 are identical; and similarly, every angle[7] θ_{ij} between a mobile coil j and a neighboring stationary coil i has the same value, respectively.

To determine the maximum value $r_{\max}$ for every angle β_i and β_j, let us define the projection P_e of the center O_e of the electromagnet e in the xy-plane, as represented in figure IV.7a. As one can see, each angle θ_{ij} is defined as:

$$\theta_{ij} = 2 \arcsin\left(\frac{d_{ij}}{2d_w}\right) \tag{IV.1}$$

[7] θ_{ij}: possible cases are θ_{15}, θ_{25}, θ_{26}, θ_{36}, θ_{37}, θ_{47}, θ_{48} and θ_{18}.

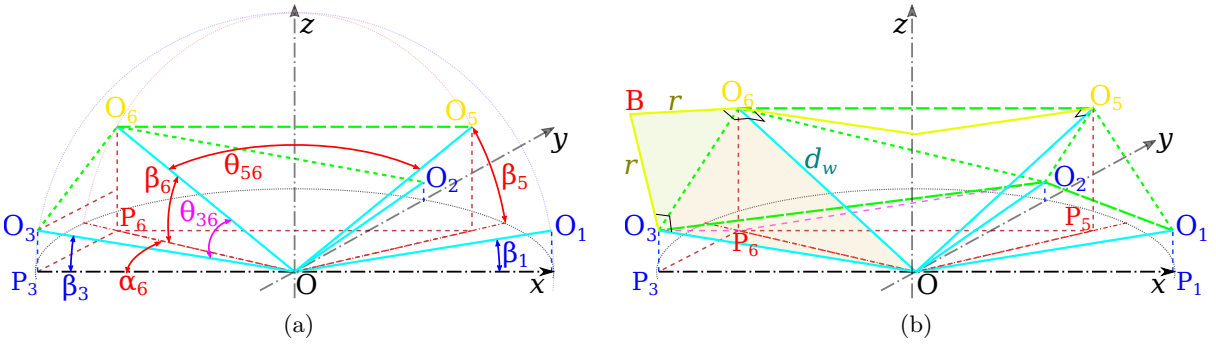

(a) (b)

Figure IV.7: Representation of (a) the angles and (b) lengths definitions.

with the length $d_{ij} = O_iO_j = \sqrt{P_iP_j^2 + (O_jP_j - O_iP_i)^2}$, where

$$P_iP_j = \sqrt{OP_i^2 + OP_j^2 - 2(OP_i)(OP_j)\cos\alpha_j} \quad (\text{here } \alpha_j = 45°) \tag{IV.2}$$

$$O_iP_i = d_w \sin\beta_i \tag{IV.3}$$

$$O_jP_j = d_w \sin\beta_j \tag{IV.4}$$

$$OP_i = d_w \cos\beta_i \tag{IV.5}$$

$$OP_j = d_w \cos\beta_j \tag{IV.6}$$

Similarly, the angle between two adjacent mobile coils j_1 and j_2 is derived as:

$$\theta_{j_1j_2} = 2\arcsin\left(\frac{d_{j_1j_2}}{2d_w}\right) \tag{IV.7}$$

where $d_{j_1j_2} = O_{j_1}O_{j_2} = \sqrt{OP_{j_1}^2 + OP_{j_2}^2}$. If all mobile coils j have the same moving angle β_j, then we obtain: $d_{j_1j_2} = \sqrt{2}d_w\cos\beta_j$ from (IV.6).

When a stationary coil i touches a mobile coil j, their radii must be:

$$r_{ij} = \frac{d_{ij}}{2\cos(\theta_{ij}/2)} = \frac{d_{ij}}{2\sqrt{1-\left(\frac{d_{ij}}{2d_w}\right)^2}} \tag{IV.8}$$

and when a mobile coil j_1 is in contact with a mobile coil j_2, their radii are defined as:

$$r_{j_1j_2} = \frac{d_{j_1j_2}}{2\cos(\theta_{j_1j_2}/2)} = \frac{d_{j_1j_2}}{2\sqrt{1-\left(\frac{d_{j_1j_2}}{2d_w}\right)^2}} \tag{IV.9}$$

Since all radii are equal, we get: $r_{\max} = r_{ij} = r_{j_1j_2}$. Hence, it can be shown that the maximal admissible radii are obtained when

$$2 - \sqrt{2}\cos(\beta_i)\cos(\beta_j) - 2\sin(\beta_i)\sin(\beta_j) = 2\cos(\beta_j)^2 \tag{IV.10}$$

Figure IV.8 shows the evolution of the admissible radius $r_{\max}$ and of mobile angle β_j when the contact constraints are satisfied. For instance, when the OctoMag configuration is considered,

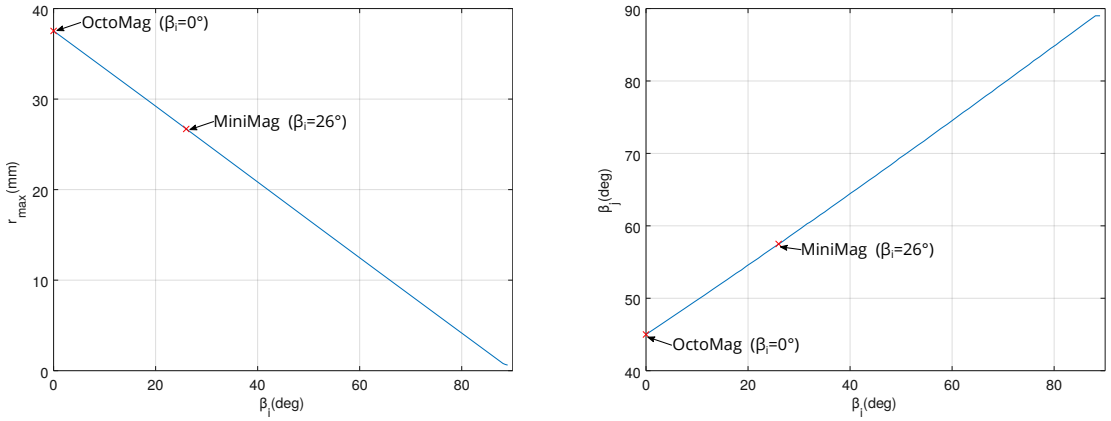

(a) (b)

Figure IV.8: Evolution of (a) admissible radius $r_{\max}$ and (b) the mobile angle β_j when the contact constraints are satisfied.

$\beta_i = 0$ for the stationary coil set leads to $\beta_j = 45°$ for the moving coil set (or the upper set equivalently). Obviously, $d_{ij} = d_{j_1 j_2} = d_w$ can be computed from the above equations that brings the maximum coil dimension. Thus, when the d_w is set to $65mm$, the radius of $r_{\max} = 37.5278\,\text{mm}$ can be derived.

IV.2.1.3 Coil implementation

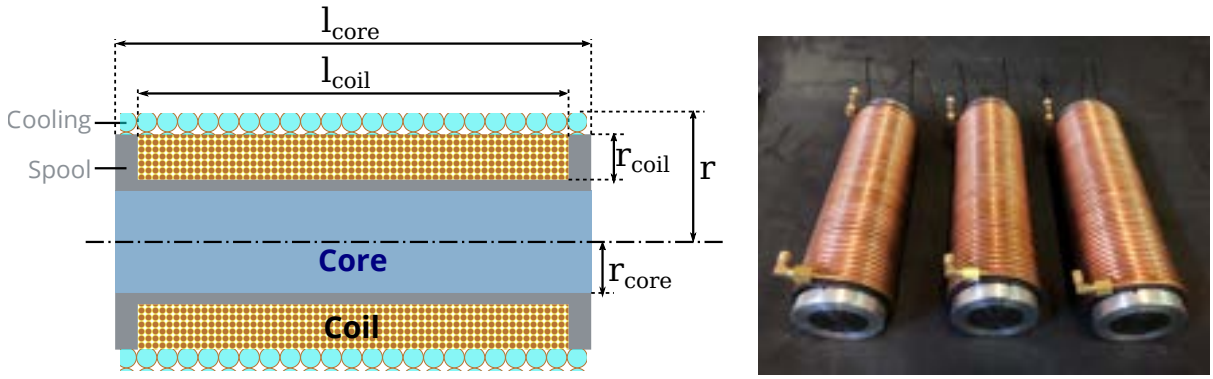

(a) (b)

Figure IV.9: (a) illustrates the electromagnet shape, with its core, coil winding and its cooling part. The spool part allows containing the winding and to separate it from the core. (b) presents the implemented electromagnet prototype.

As specified, a cylindrical electromagnetic coil depicted in figure IV.9a is considered in this study. In such case, the magnetic performance can be approximated using the solenoid model. Indeed, the magnetic field strength at the ends of a infinite solenoid corresponding to an

electromagnet e is given by [148] through applying the Ampère's law (II.1):

$$\|\mathbf{B}_e\| = \mu \frac{i_e N}{2l} \tag{IV.11}$$

with i_e the electric current, l the length of the solenoid, and N the number of turns of the coil winding.

To maximize the magnetic field strength, two parts of the electromagnet can be optimized: i) the core and its permeability performance μ; and ii) the coil winding. To do so, when the maximum allowable electromagnet size $r_{\max}$ with respect to the spatial arrangement is obtained, its remaining dimensions could be determined easily. Kummer [147] has proposed a electromagnet design that takes into consideration further constraints. Specifically, they have shown that the proper length to radius ratio of the core should be at least $l_{core}/r_{core} \geq 8$ to fit properly the above solenoid characteristics. From their results, it appears that a core with a radius of about $r_{core} \approx 20\,\text{mm}$ and then a length $l_{core} = 10 r_{core}$ enable reliable magnetic field performance.

Next, the coil thickness should be determined. From the infinite solenoid (IV.11), the best magnetic performance is achieved when the number of turns N is maximized. However, the winding of coil is limited by the current density that would cause safety problem. Basically, from transformer design, without cooling, it is shown that the current density should not exceed $\mathbf{J}_{\max} = 3\,\text{A/mm}^2$. Nevertheless, to enable strong magnetic field, the current i_e must be high enough. Therefore, the parameter of $\mathbf{J}_{\max} = 3\,\text{A/mm}^2$ normally requires the wire made of a larger cross-section of conductor that will thus limit the number of turns N. In order to increase i_e together with a great N in a limited room, a cooling system will be mandatory. Different strategies can be envisioned for the cooling part, such as using fan, radiator vent, or water/coolant system. Classically, using a circulating coolant is the most effective technology to cool a system.

From these considerations, we have chosen the following design parameters to implement each electromagnet. The core is composed of low carbon steel (C35, ThyssenKrupp AG, France) with $r_{core} = 21\,\text{mm}$ and $l_{core} = 240\,\text{mm}$. An aluminum[8] (Aluminum EN AW-2017a-en 573-3, ThyssenKrupp AG, France) spool is added to separate the core and the coil, and to keep the winding in the given space. This spool has an inner length of $l_{coil} = 210\,\text{mm}$ and a thickness of 1 mm. The coil is composed of winding of 6 layers of copper[9] wire (Enameled copper wire, cl 200 degrees, diameter 1.60mm, grade 2. APX, France) of size of 1.6 mm, leading to a thickness of 9.6 mm and a number of turns $N = 787$. Finally, a cooling unit is built around the coil winding. The cooling system consists of a circulating coolant liquid flowing through a copper tube with a diameter of 4 mm. All these elements lead to an electromagnet with a overall size of $r = 35.6\,\text{mm}$, and electromagnet prototype has been realized shown in figure IV.9b.

IV.2.1.4 Coil performance evaluation

The methodology used in the thesis is based on the assumption that the point-dipole model given by Eq. (III.1) approximate properly the magnetic field distribution. The assumption is validated in this section.

FEM modeling using ANSYS® Maxwell[10] software has been performed. Hence, the specified electromagnetic coils have been modeled and simulated through finite element analysis (Finite Element Analysis (FEA)). Figure IV.10 shows some simulation results where a current of 1 A/turn

[8] Aluminum is a paramagnetic material that is essentially unaffected by the magnetic fields.
[9] Copper is a diamagnetic material, and thus is repelled by the magnetic field.
[10] `https://www.ansys.com/products/electronics/ansys-maxwell`

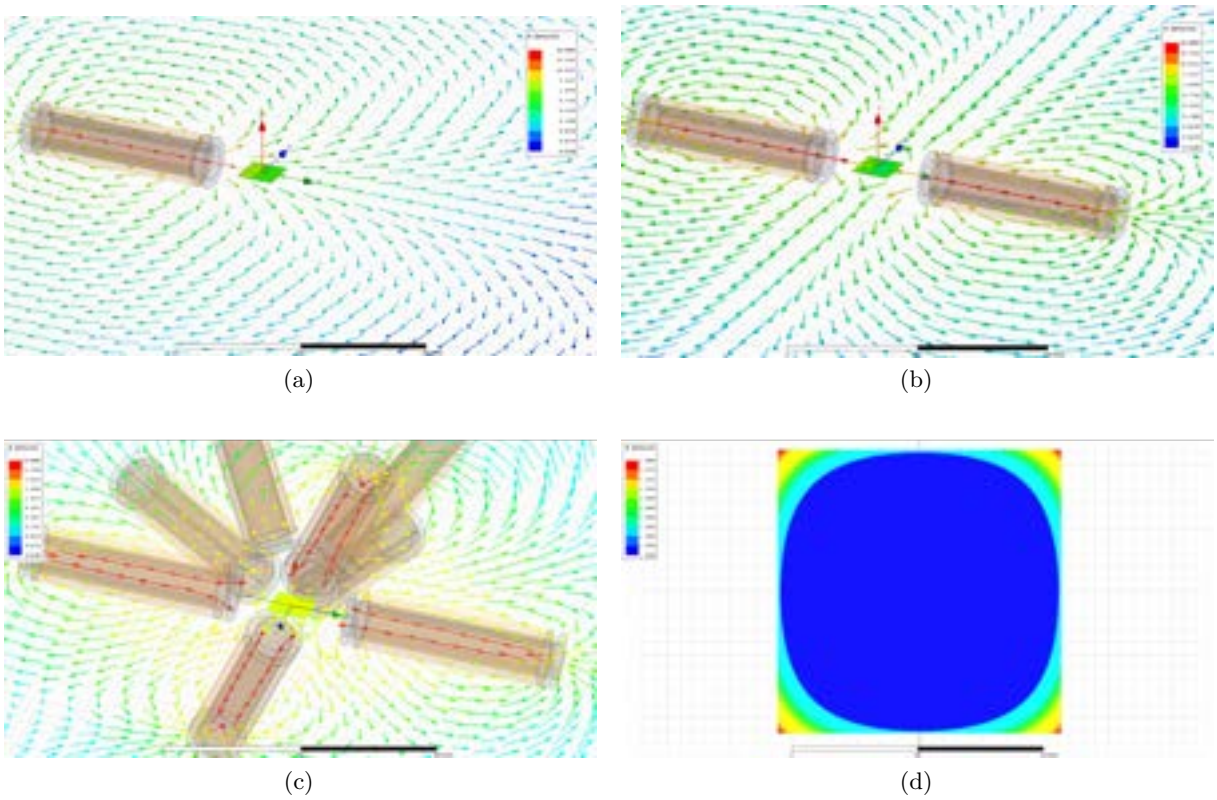

(a) (b)

(c) (d)

Figure IV.10: Magnetic field distribution using FEM: (a) a single and (b) a dual electromagnets systems; and (c)-(d) the $n = 8$ electromagnets arrangement with $\beta_i = 0°$ and $\beta_j = 45°$. (d) shows the magnetic field magnitude within the workspace.

is flowing in each electromagnet. Figures IV.10a and IV.10b illustrate the magnetic field $\mathbf{B}$ where the workspace is surrounded by a single and a pair of electromagnet(s), respectively. Likewise, figures IV.10c and IV.10d present the magnetic field distribution of the retained $n = 8$ electromagnets configuration where the stationary coil set has an angle $\beta_i = 0$ and the mobile coil set has an angle $\beta_j = 45°$. As one can see, the results in figure IV.10d are similar to those presented in III.15b where the point-dipole model is used to evaluate the magnetic field. To confirm this assessment, figure IV.11 shows the comparison between the FEM results and the point-dipole results along the x-axis. Especially, figure IV.11b reports the relative error of the magnetic field magnitude within the workspace. It appears that the point-dipole model is a convenient method to approximate the magnetic field distribution with a relative error less than $|3.5|\%$.

IV.2.2 Design of the robotic arm

When the parameters of the electromagnets of the reconfigurable EMA system have been determined, the arrangement of the $n = 8$ electromagnets is hereafter further discussed. As mentioned in chapter III, to induce powerful magnetic field and gradient in the workspace, the hemispherical configuration (such as either OctoMag-like or MiniMag-like arrangement) is a good solution. The above motivations lead to the reconfigurable OctoRob platform which makes it

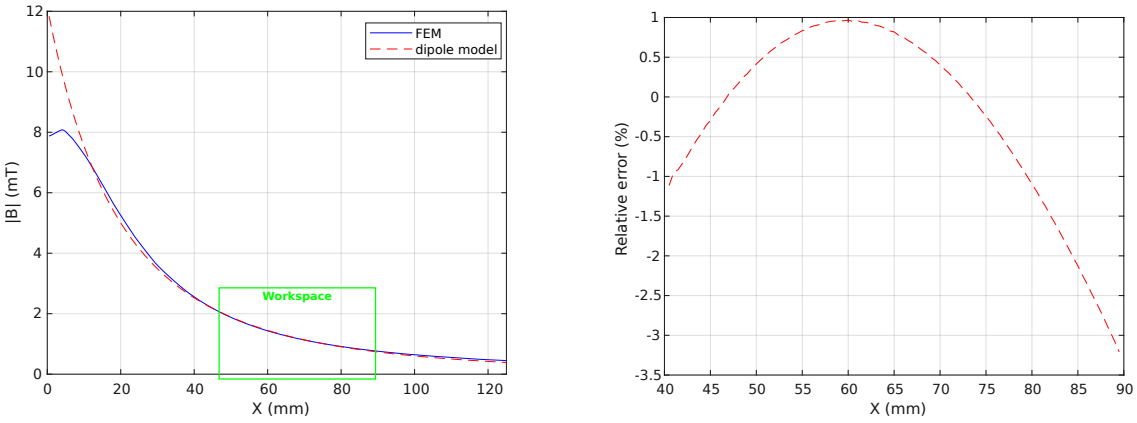

(a) (b)

Figure IV.11: Comparison simulation results between FEM and point-dipole model along the x-axis: (a) the magnetic field magnitude where the green box delimit the range of workspace, and (b) the relative error within the workspace.

possible to sometimes favor the magnetic field regarding the torque, or sometimes the magnetic field gradient in respect of the pulling force. To achieve this, we propose the design of a robotic arm mechanism for controlled electromagnet orientation in the following.

IV.2.2.1 Robotic arm mechanism description

The OctoRob platform must be capable of moving the mobile coil set, that is their polar angles β_j should be changed dynamically. This can be simply achieved by placing it at the end-effector of a robotic arm, as illustrated in figure IV.12. A basic solution for actuating the robotic arm is to use simple DC motors. However, attention must be paid to its placement to limit magnetic field interference and prevent electromagnetic compatibility (Electromagnetic Compatibility (EMC)) issue. Based on these considerations, and as only 1 DOF is required, we have chosen to use a well known four-bar linkage mechanism. Certainly, four-bar linkage architecture has been extensively used in machinery for centuries, and is commonly encountered in robotics manipulation. Specifically, the four-bar linkage architecture allows reliable 1 DOF motion feature, higher energy efficiency, good rigidity, less link inertia and compact drive systems.

Figure IV.12b depicts the kinematic chain of the designed four-bar linkage with the links L_1-L_4, the joints θ_1-θ_4, and the point H located in the end-effector. Specifically, L_1 is the crank, L_2 the coupler and L_3 the rocker. In addition, the frame L_4 is decomposed in four parts: L_{4a}, L_{4b}, L_{4c} and L_{4g}. Each link or part L_i has a length r_i. In particular, the lengths $DE = r_2$, and $CH' = r_{3a}$ can be easily adjusted manually to modify the kinematics of the electromagnet. The lengths $GA = r_{4a}$ and $AB = r_{4b}$ could be also modified to handle smaller or bigger electromagnetic coils if it is necessary. Once fixed and calibrated, the links geometry of the OctoRob platform cannot vary, and would lead to the simplified kinematics chain shown in figure IV.12c. Table IV.2 presents some calibrated parameters of the robotic arm. With the proposed specifications, the robotic arms are realized and attached with electromagnets, DC motors, and angle calibrators, as represented in figure IV.12d

Next, a motor actuates the joint θ_1, that rotates the following links L_2-L_3 and the other

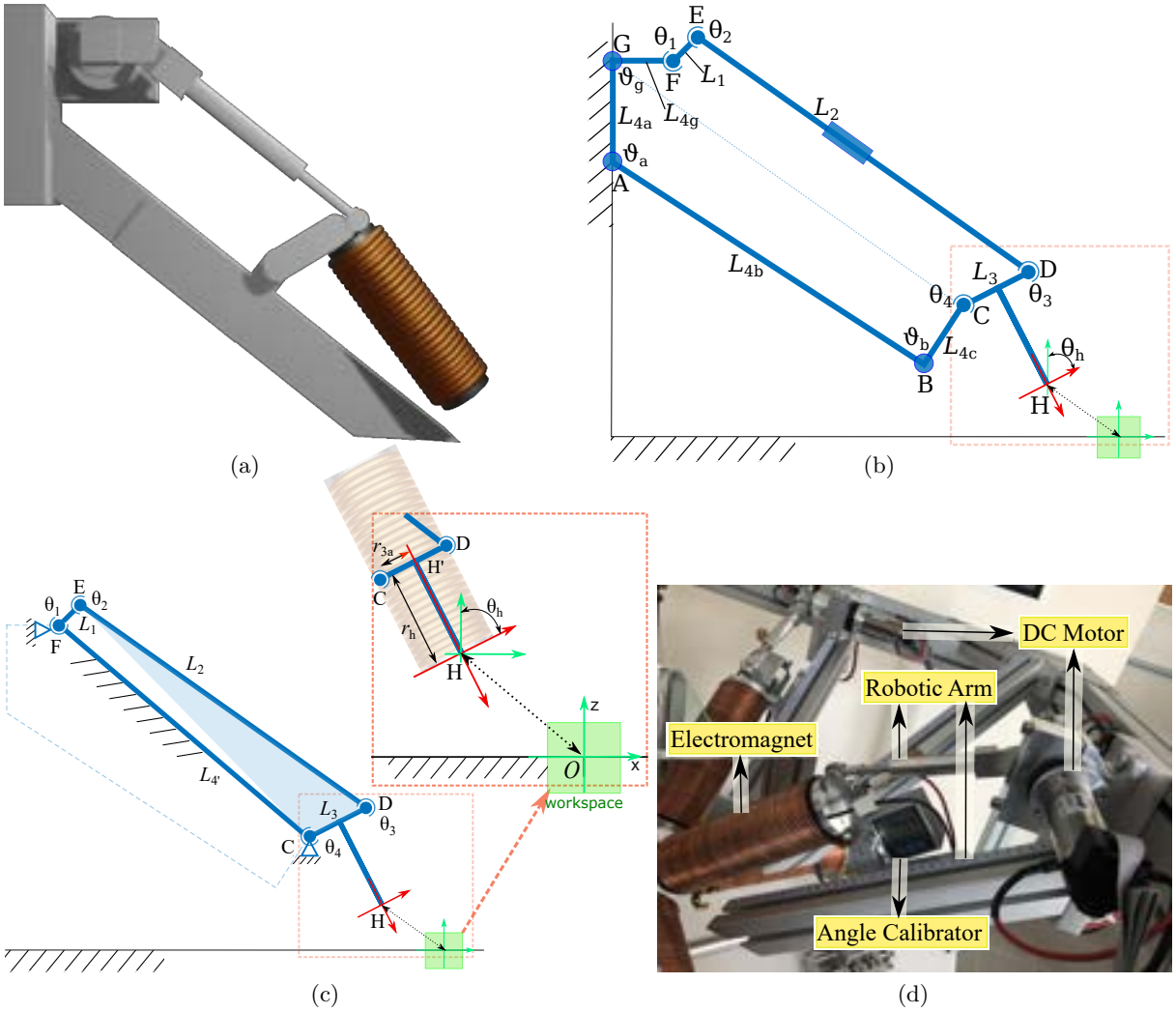

Figure IV.12: Representation of the robotic arm: (a) CAD illustration of the concept, (b)-(c) show the kinematics chain with the four links L_1-L_4 and joints θ_1-θ_4, and (d) represents the realized 1-DOF robotic arm.

joints θ_2-θ_4. Then, the electromagnet fixed to the link L_3 is able to rotate with θ_h. Its orientation and position can be calculated through the analysis of kinematic rotation presented in the next section. Indeed, from the input angle θ_1, the output angle θ_h at the end-effector H is computed by the use of transformation matrices.

IV.2.2.2 Kinematic Analysis

As mentioned in section III.1.2, the magnetic field ${}^{\mathcal{F}_0}\mathbf{B}(\mathbf{p})$ can be expressed in the reference frame $\mathcal{F}_0$ linked to the workspace center by using the homogeneous transformation as in eq. (III.2). Similarly, the input angle θ_1 is transferred to the output angle θ_h through applying transformation matrices, especially the rotation matrix for the proposed robotic arm. For more details of analysis of its definition of transformation, please see chapter C.

Table IV.2: Parameters of the robotic arm†: (a) the simplified four-bar mechanism as in (c); and (b) the detail of the components of the link L_4.

(a)

Link	L_1	L_2	L_3	L_4
r_i (mm)	33	444	75	372
θ_i	θ_1	θ_2	θ_3	θ_3

(b)

Part	L_{4a}	L_{4b}	L_{4c}	L_{4g}
r_i (mm)	100	365	68	60
ϑ_i	123°	90°	-	90°

†The robotic arm is made of aluminum material.

With the transformation matrix, the desired position and orientation of electromagnet are computed hereafter. The position of the point G is fixed, and we assume that its location is known with respect to the reference frame $\mathcal{F}_0$ as ${}^{\mathcal{F}_0}G = (x_g, y_g, z_g, 1)^\intercal$ in homogeneous coordinates. Next, when the $L_{4a} - L_{4c}$ are set to a given values, the position $C = (x_c, y_c, z_c, 1)^\intercal$ of the joint θ_4 is fixed and can be determined in $\mathcal{F}_0$ as:

$$ {}^{\mathcal{F}_0}C = \mathrm{Rot}_y(\vartheta_b)\,\mathrm{Trans}_z(r_{4c})\,\mathrm{Trans}_x(r_{4b})\,\mathrm{Trans}_z(-r_{4a})\,{}^{\mathcal{F}_0}G \tag{IV.12} $$

where $\mathrm{Rot}_y(\vartheta_b)$ denotes the pure rotation operation along the y-axis with angle ϑ_b, and $\mathrm{Trans}_z(r_{4c})$ indicates a pure translation along the z-axis with the displacement r_{4c}. Similarly, we apply the same methodology for the other transformation operations.

The location of $E = (x_e, y_e, z_e, 1)^\intercal$ of the joint θ_2 can be expressed in $\mathcal{F}_0$ as follows:

$$ {}^{\mathcal{F}_0}E = \mathrm{Rot}_y(\theta_1)\,\mathrm{Trans}_z(r_1)\,\mathrm{Trans}_x(r_{4d})\,{}^{\mathcal{F}_0}G \tag{IV.13} $$

As the lengths $CD = r_3$ and $DE = r_2$ are fixed, the geometrical figure CDE forms a triangle whose sides are fixed. Its angle θ_3 can be easily obtained by using the law of cosines in Euclidean geometry.

Through the transformation operations, the position of the end-effector ${}^{\mathcal{F}_0}H$, together with the point ${}^{\mathcal{F}_0}H'$ can be determined by:

$$ {}^{\mathcal{F}_0}H' = \mathrm{Rot}_y(\theta_3)\,\mathrm{Rot}_y(\vartheta_b)\,\mathrm{Trans}_z(r_3)\,\mathrm{Trans}_z(r_{4c})\,\mathrm{Trans}_x(r_{4b})\,\mathrm{Trans}_z(-r_{4a})\,{}^{\mathcal{F}_0}G \tag{IV.14} $$

$$ \begin{aligned} {}^{\mathcal{F}_0}H = {} & \mathrm{Rot}_y(\pi/2)\,\mathrm{Rot}_y(\theta_3)\,\mathrm{Rot}_y(\vartheta_b)\,\mathrm{Trans}_z(r_h)\,\mathrm{Trans}_z(r_3)\,\mathrm{Trans}_z(r_{4c})\,\mathrm{Trans}_x(r_{4b}) \\ & \times \mathrm{Trans}_z(-r_{4a})\,{}^{\mathcal{F}_0}G \end{aligned} \tag{IV.15} $$

The orientation θ_h of the end-effector can be then determined by the obtained θ_3 since the surface of electromagnet is parallel to L_3:

$$ \theta_h = \theta_3 \tag{IV.16} $$

Therefore, both position and orientation parameters of the end-effector can be computed.

IV.2.3 Implementation of the OctoRob prototype

Analogous to a traditional kinematic manipulator, a magnetic manipulator has also a reachable workspace, that is, a set of achievable magnetic field and gradient combinations. From the design specifications, we proposed the OctoRob platform design illustrated in figure IV.13a. It is composed of eight robotic arms: four mobile robotic arms to control the mobile electromagnets orientation

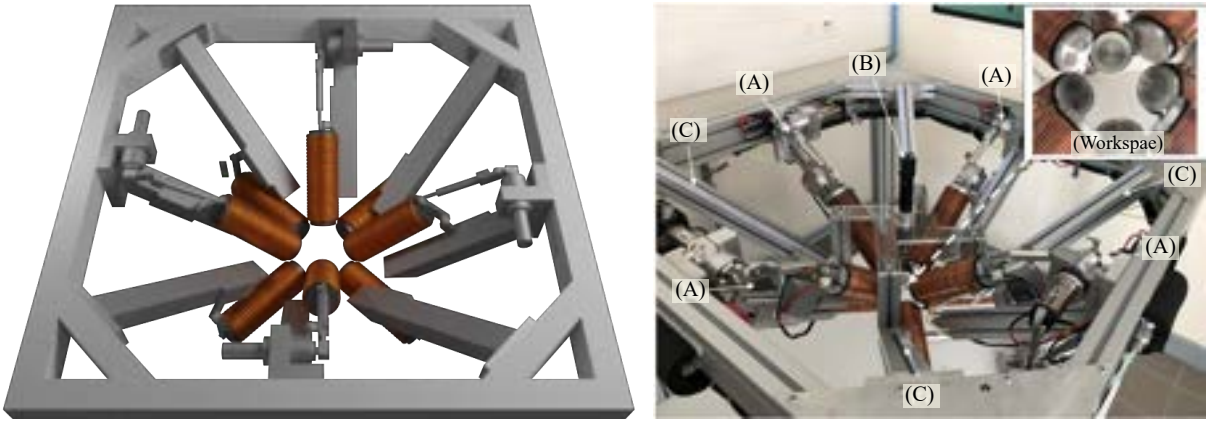

(a) (b)

Figure IV.13: OctoRob design. (a) CAD representation of the EMA platform and (b) experimental prototype: (A) 1-DOD mobile robotic arms; (B) optical microscope with a CCD camera; (C) stationary robotic arms.

and four stationary robotic arms supporting the fixed electromagnets. The electromagnetic micromanipulation platform (OctoRob) developed at the Laboratoire PRISME is represented in figure IV.13b.

During the design process, we were particularly careful with the machine stiffness because of the long stationary and mobile robotic arms which have direct consequences on micromanipulation accuracy of the microrobotic tool. To deal with these constraints, the eight arms are rigidly fixed to the frame reference structure to avoid mechanical vibrations to be transmitted to the end-effectors. Furthermore, mechanical deformations of robotic arms linked to external forces have been mechanically reinforced. When the robotic platform has been assembled, the eight robotic arms axes are calibrated in order to ensure that a unique point O is settled at the center of the workspace. The calibration process is based on a laser pointing system where eight laser spots are pointing towards the same focusing point O with few micrometer accuracy. The geometrical design rules have been respected during the design stage in order to have a semi-hemispherical workspace of $45mm \times 45mm \times 45mm$. As shown in the inset of figure IV.13b, the limits of semi-hemispherical workspace are prone of any collisions : 1) the optical microscope has a direct access to the workspace to provide a top-view of the eyeball, 2) the magnetic coils do not contact each other, and 3) the orientation of the mobile coils are limited by mechanical stops. Figure IV.14 shows closed-views of the OctoRob prototype. In the current configuration, the stationary coils have their polar angles fixed to $\beta_i = 0$ as the OctoMag setup. If necessary, these polar angles can be modified to other configurations, for instance, the MiniMag configuration.

Figure IV.15 shows the overall system architecture of the OctoRob magnetic manipulation platform. The system architecture is divided in power, driving, cooling and sensing units. The current for the eight electromagnetic coils is sourced through custom-designed switched amplifiers with a maximum current of 15A per channel and controlled through two data acquisition (DAQ) card (NI PCI-6229, NI) with 12-bit resolution. The current flowing through each channel is controlled through PID controllers (Epos2 50/2 Maxon) within a range of 0 to 15A (i1-to-8). However, heat dissipation poses the limit to the maximum achievable magnetic field generated by each electromagnet. A common solution consists in using copper tubes in which a coolant flows

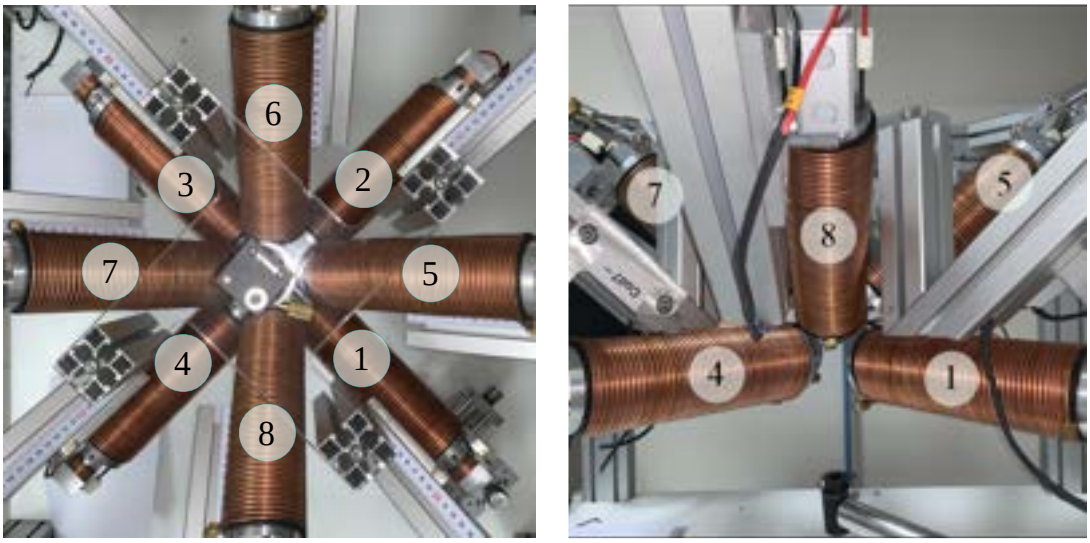

(a) (b)

Figure IV.14: Photograph of the (a) top-view and (b) sideview of OctoRob prototype.

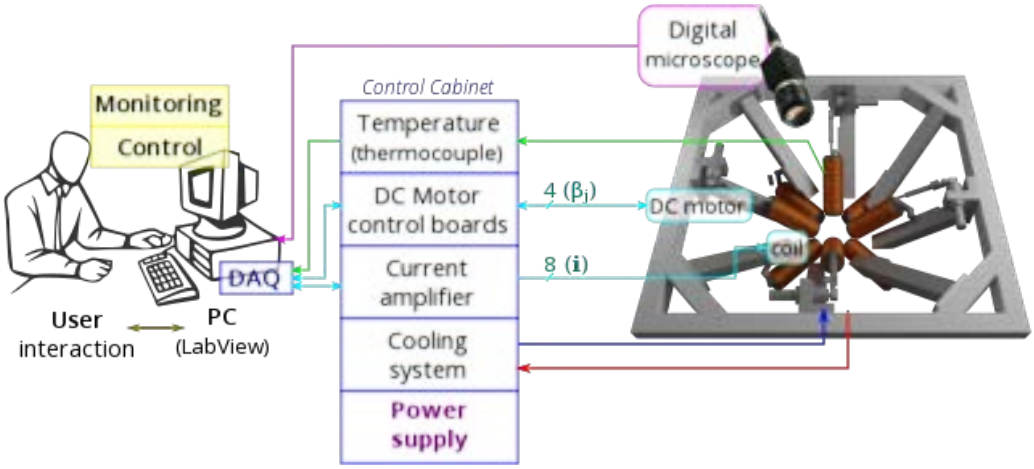

Figure IV.15: Synoptic of OctoRob platform architecture.

around the coil windings. We developed a custom cooling system capable of circulating a coolant through the copper tubing wrapped around each coil. The system comprises a liquid storage tank for placing an external insulation cooling liquid in a freezer refrigerator, an electromagnetic coil cooling pipeline which an internal insulation cooling liquid flows through, and a liquid driving pumps for driving the internal insulation cooling liquid to flow along the electromagnetic coil cooling pipeline. The custom-made cooling system is shown In figure IV.16. The temperature of coil windings is monitored through temperature thermocouple sensors ($-40°$ up to $+100°C$ Radial lead, UK) integrated at the center of the coil between the spool and the winding.

The four mobile robotic arms are motorized by DC motors (MDP DCX32L, France) with optical encoders for position measurement. The orientation of the electromagnets (β_{1-4}) is performed through position controllers (Epos2 50/5 Maxon, France). A stationary camera

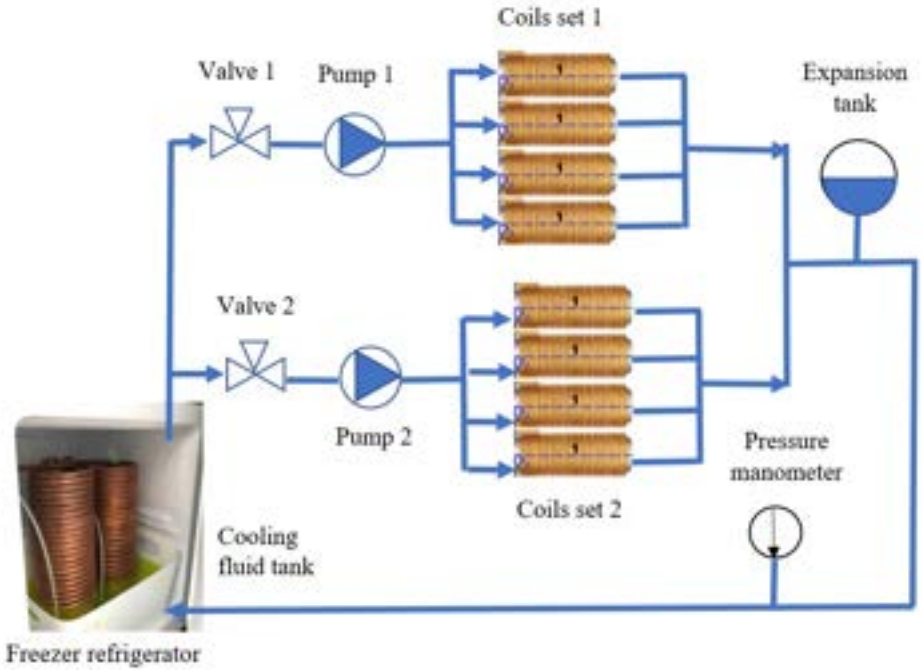

Figure IV.16: Cooling system for temperature control of electromagnets.

assembly provide visual feedback from the top view of the workspace. The vision system is composed of an optical microscope from Infinity Photo-Optical Company fitted with a 20x zoom lens (M Plan APO SL 100X, Edmund Optics, USA) and connected to a digital CMOS Firewire camera delivering images and real-time video to a PC. The working distance of 90 mm with a limited depth-of-field of few tens of mm to image microrobots and a frame size of 640 × 480 pixels. Since the interior of the human eye is externally observable by optical microscopy, computer vision algorithms have been developed for intraocular localization using OpenCV library. The entire system is controlled through LabView® software[11] environment connected to Matlab® software[12] by a single computer with an Intel® Core 4 Quad CPU 3.0 GHz.

IV.3 Evaluation of OctoRob

The configuration of the OctoRob system should be designed in regard to the considered application, that is an ophthalmic MIS procedure. To evaluate its performance, further simulations and characterization are carried out. Following the investigation presented in chapter III, the performance indexes are investigated in the following sections.

IV.3.1 Magnetic field and gradient of the built platform

The built robotic EMA system consists of eight electromagnets. Each electromagnet e generates a magnetic field $b_e\,(p, i_e)$ independently. For the sake of simplicity, a unit-current is considered to flow through the eight electromagnetic coils. Since the magnetic fields induced from multiple

[11] http://www.ni.com/labview/
[12] http://fr.mathworks.com

electromagnets can be linearly superimposed, we compute the global magnetic field $b(p, i)$ for the eight coils system after analyzing each magnetic field respectively. As confirmed above, the magnetic field can be calculated using transformation matrix and point-dipole model.

As represented in figure IV.14, the four stationary electromagnets ($e = 1, 2, 3, 4$) are considered on the common xy-plane, and behave similarly to a Maxwell coils pairs. The left four mobile electromagnets ($e = 5, 6, 7, 8$) are actuated by robotic arms as designed in the proposed reconfigurable EMA system. Different cases are investigated hereafter.

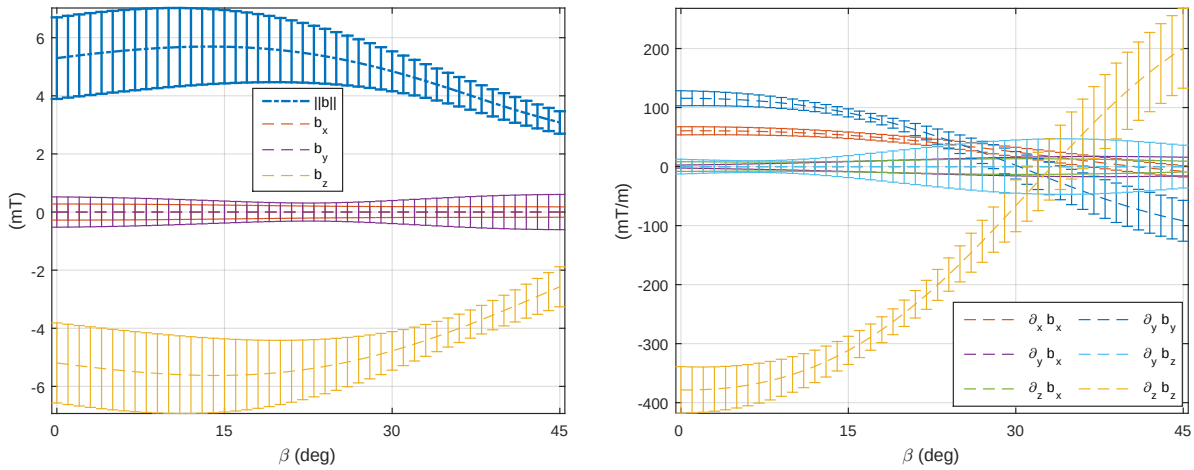

(a) (b)

Figure IV.17: The average value of the (a) magnetic fields and (b) its magnetic gradients with four moving electromagnets rotating with angle $\beta \in [0°, 45°]$. The error bar shows the standard deviation of the value.

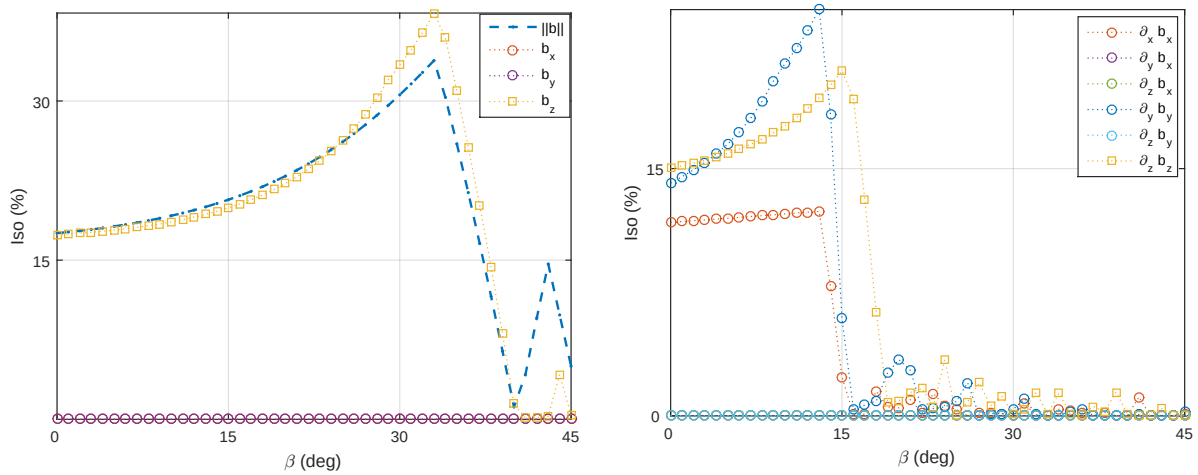

(a) (b)

Figure IV.18: The uniformity of (a) magnetic fields and (b) its magnetic gradients with four moving electromagnets rotating with angle $\beta \in [0°, 45°]$.

1) The four mobile coils rotation: We first consider that the four mobile electromagnets ($e = 5, 6, 7, 8$) are operated in the same way that each mobile coil is rotating together with the same angle β. On this basis, the optimal angle β are investigated to perform different manipulation tasks with magnetic pulling and steering of a magnetized microrobot.

Figure IV.17a and IV.17b show the evaluation of the average and uniformity of the magnetic field and its gradient for the rotating angle $\beta \in [0°, 45°]$. From these simulation results, two distinguishing behaviors appear: i) magnetic field becomes more significant and uniform for mobile angle around $\beta = 33°$; whereas ii) a strong and uniform magnetic gradient appears at $\beta = 14°$. These results also exhibit the versatility to promote the control of either the magnetic field or its gradient by simply adjusting the orientation of some electromagnets thanks to a robotized EMA platform.

2) A single mobile coil rotation: We now investigate the influence of having a single electromagnet ($e = 5$) allowed to rotate, whereas the other mobile coils ($e = 6, 7, 8$) are fixed. The four stationary electromagnets ($e = 1, 2, 3, 4$) remain unchanged in the xy-plane.

As mentioned, for $\beta = 33°$, the magnetic field is more efficient. Thus, at first the mobile coils are fixed to 33°, and only one coil is rotating. Figure IV.19a and IV.19b describe the average strength and the uniformity of the magnetic field in the workspace. Although the magnetic field strength does not change significantly with the rotating angle, a more uniform magnetic field appears at around 35°.

Secondly, the magnetic gradient field is more efficient when $\beta = 14°$, and only one coil is rotating. Figure IV.20a and IV.20b illustrate the average strength and their uniformity of the magnetic gradients within the workspace. The figure IV.20a reveals the magnetic gradient become stronger when the mobile angle is below 20°. Moreover, to get more uniform magnetic gradients, it requires to rotate the single coil in the range of 5° to 25°. Thus, the mobile angles $\beta \in [5°, 20°]$ can be used for more effective force control on magnetized microrobots.

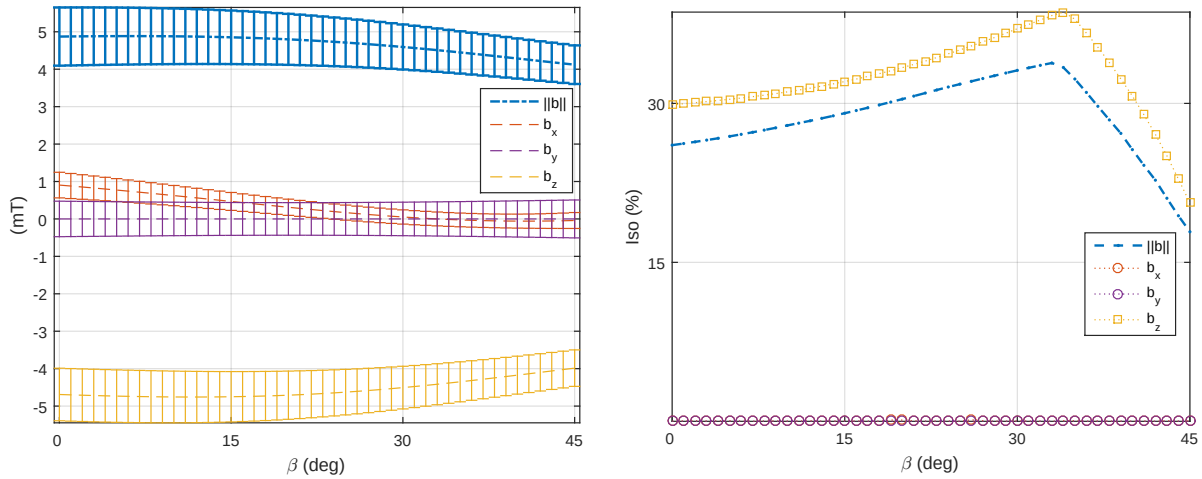

(a) (b)

Figure IV.19: One mobile electromagnet (coil 5) is rotating and the others are set to $\beta = 33°$: (a) the average and (b) the uniformity of the magnetic field.

3) A dual mobile coils rotation: Commonly, electromagnetic coils are used by pair. Hence, a pair of mobile coils that are opposite each other (see coil 5 and coil 7 in figure IV.14) are here

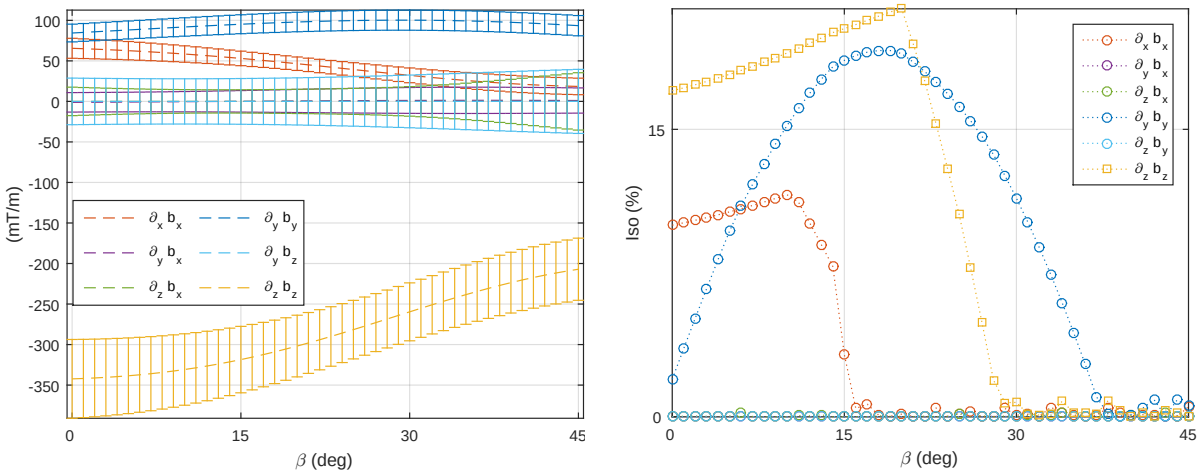

(a) (b)

Figure IV.20: One mobile electromagnet (coil 5) is rotating and others are fixed to $\beta = 14°$: (a) the average and (b) the uniformoty of magnetic gradients.

allowed to rotate with the same angle $\beta \in [0°, 45°]$, while the other mobile coils remain stationary. In such case, the performance of medical EMA system can be adapted by one pair of robotic arms.

As previously described, the unchanged mobile coils ($e = 5, 7$) are firstly fixed to 33° to favor the magnetic field. Figure IV.21 reports the performance metrics of the magnetic field, when only a pair of opposite electromagnets is rotating. Next, the fixed mobile coils ($e = 6, 8$) are set to 14° to favor the magnetic gradient. Figure IV.22 illustrates the corresponding performance indices of the magnetic gradient. As we can see, the influence of the mobile electromagnet pair is quite similar to the result of one single mobile electromagnet.

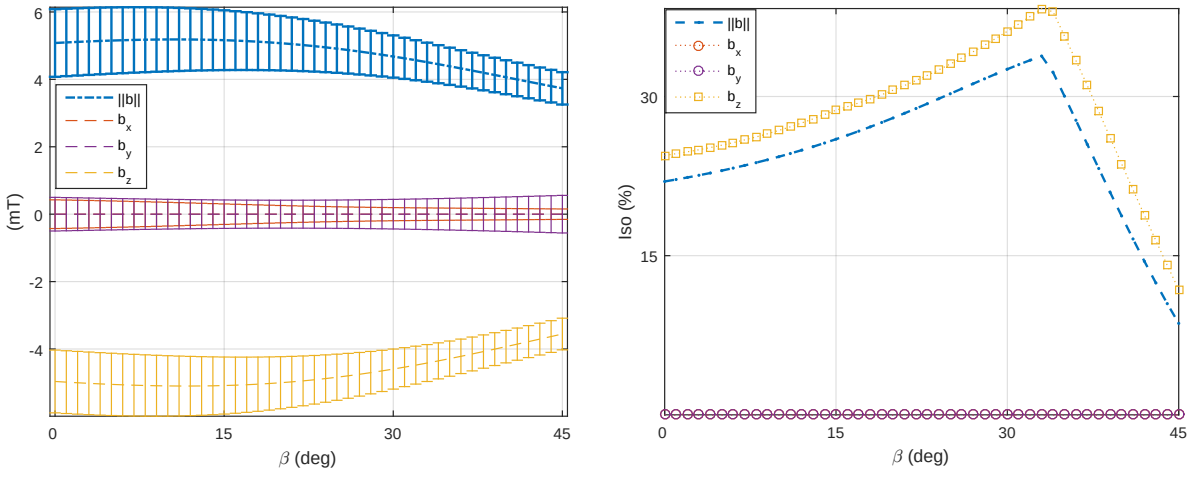

(a) (b)

Figure IV.21: Two mobile electromagnets (dual coils 5 and 7) are rotating and the other coils set to $\beta = 33°$:(a) the average and (b) the uniformity of the magnetic field.

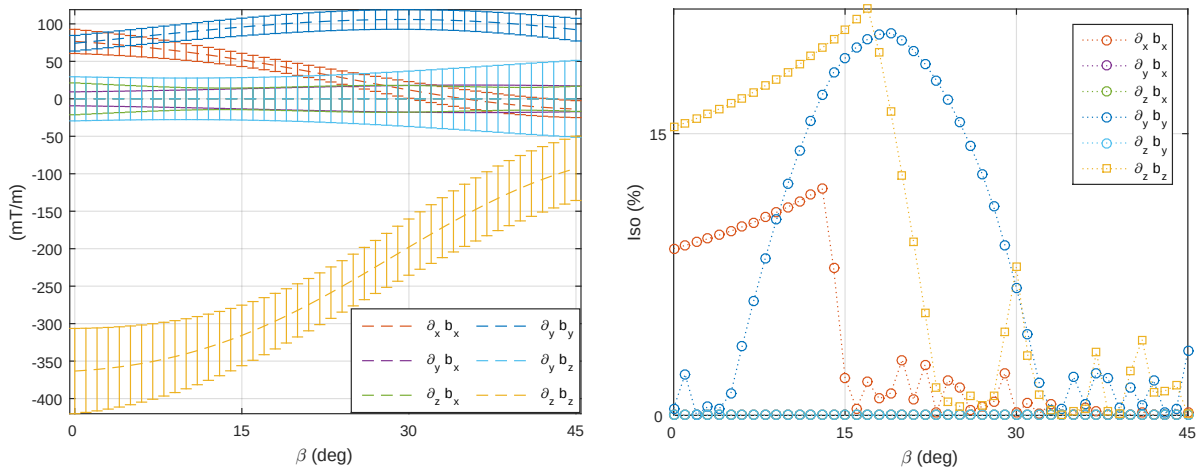

(a) (b)

Figure IV.22: Two mobile electromagnets (dual coils 5 and 7) are rotating and the other coils set to $\beta = 14°$:(a) the average and (b) the uniformity of the magnetic gradient.

IV.3.2 Discussions

The built OctoRob system provides 5 DOFs to biomedical magnetized microrobots including 3 DOFs for force control and 2 DOFs for the heading control. Magnetic torque can be generated by the magnetic field, while the magnetic gradient induce magnetic force. Thus, for the heading control of the biomedical microrobots, the magnetic field should be prioritized; whereas force control can be enhanced by optimizing the magnetic gradient.

In the case of four mobile electromagnets moving in the same time, different mobile angles show diverse magnetic field distributions. These simulation results indicate that the high angle β, especially at around $\beta = 33°$, is most suitable to generate a strong and uniform magnetic field. A most strong and uniform magnetic gradient can be only achieved at angles blow $\beta < 20°$. In the other word, the more efficient force control and torque control require different range of input angle produced by the designed robotic arm.

Furthermore, as we can see the three considered cases provide results that are similar, leading to two interesting aspects. First, we can roughly choose the most simple strategy, for instance, only a sole electromagnet is moving by a robotic arm. However, to achieve precise and efficient trajectory tracking or significant force or torque, more mobile electromagnets should be considered. Secondly, the similarity also suggests that the moving coils do not need to be accurately controlled at the same angle.

IV.4 Conclusion

This chapter presents the investigation of the built robotized OctoRob system for intraocular therapy with the untethered biomedical magnetic microrobots. The developed EMA system is divided into two set: four fixed electromagnets and four robotized electromagnets. Different moving cases of the mobile electromagnets have been simulated and verified. Simulation results show that the robotic arm for electromagnets enables a variety of magnetic field distributions.

Since the magnetic fields induce the torque, and the force is generated by magnetic gradients, this study also demonstrates that the designed robotized OctoRob system provides more mode to effective force and torque control on the biomedical microrobots. Through the evaluations of three case, the results exhibit the interest of properly control the robotic arm. Low angle leads to stronger and more uniform magnetic gradient distribution, whereas most uniform magnetic field is produced near high mobile angle β. Therefore, the developed platform will provide more versatility, maneuverability and flexibility to the magnetic manipulation of biomedical microrobots, which would assist surgeons in difficult retinal MIS procedures. In the future, experiments will be studied on our built platform, and the performances of designed robotized OctoRob system will be experimentally investigated.

Conclusion

This research aims at developing a robotic magnetic actuation system to assist clinicians for various minimally invasive procedures. The design objective is to efficiently control and manipulate the untethered biomedical microrobot for the desired surgical tasks by the generated magnetic field and gradient. The EMA system with proper specifications and configuration can produce magnetic field and gradient in an effectively way, that induces magnetic torque and force used for object control. Mass simulations have been completed for estimating characterization of the proposed configurations. As an application of intraocular MIS, the capabilities of the designed platform were thoroughly investigated by theoretical analysis and evaluated by the mathematical simulations. This conclusion will present a summary of the contributions of the thesis. Moreover, experimental validation and potential perspective of the proposed EMA system have been incorporated in the future work.

Contributions

The different EMA configurations vary their capabilities, thus, the study on configuration for various medical applications could be interesting. Commonly, the EMA systems could be composed of permanent magnets or electromagnets. Considering the adaptability and safety of magnetic control system, electromagnets filled with high performance, soft-magnetic cores are selected in the thesis.

Many EMA systems composed of classic electromagnetic coils, such as Helmholtz coils, Maxwell coils, uniform and gradient saddle coils, have been reported. Through the analysis of various proposed EMA systems, their performances and basic provided functions are clearer. It helps us to comprehend how to design EMA system regarding the considered application. In order to expand the workspace for matching MIS requirement, the spatial structure of platform should be extended to adapt the targeted area, and relevant input current should be increased for providing sufficient actuation energy.

First of all, we sorted out the main performances of EMA platforms in chapter I into the following items: 1) strength and uniformity of magnetic field, 2) strength and uniformity of magnetic gradient, 3) manipulability and dexterity of magnetic force, 4) manipulability and dexterity of magnetic torque. These system performances can be customized based on the following specifications of the medical application: 1) type of tasks, 2) size of workspace, 3) property of media, 4) type of the applied microrobot, 5) locomotion of microrobot, etc,.

Moreover, the design of EMA platform, such as the design of electromagnet, the number of

electromagnets, the arrangement of electromagnets, is determined through the required system performances. Hence, secondly, the estimation of electromagnet number has been studied with respect to different control methods for microrobots. The basic number of stationary electromagnetic coils is evaluated and obtained as 3, 5 and 8 with regard to torque control, force control and combination control of torque and force, respectively.

Furthermore, with the certain number of electromagnets, their organizations are investigated in chapter II. For 2D workspace, performances of flat four-coil, flat six-coil and flat eight-coil configurations are simulated with varying distance d_w. Such estimations have been done for 3D workspace including 3D six-coil, OctoMag and MiniMag systems as well. Especially, the effect of either distance d_w or mobile angle β_e has been studied regarding OctoMag-like and MiniMag-like configurations by utilizing the defined metrics. Obviously, the each specific application, the system performance can be characterized and optimized to the best configuration for providing sufficient electromagnetic actuation. If we go deep into the different tasks to be performed, the configuration of EMA system can be further optimized for each step. The configuration evidently has to adapt its parameters dynamically for different required tasks. Therefore, the reconfigurable system is proposed for the precise control of whole manipulation process.

In chapter III, the eight-coil platform in hemisphere-arranged is investigated, where the both distance d_w and angle β_e could be adjusted for the required operations/applications. Simulation results present that reconfigurable platform enables the different system performances making the wireless control more precise and flexible. Finally in chapter IV, the implementation of reconfigurable system has been completed in our laboratory The built EMA system named OctoRob is consisting of eight electromagnets filled with magnetic cores. The four of eight electromagnets are controlled through four identical robotic arms. The structure of robot arm is well designed to provide the desired orientation and position of movable electromagnet. The type of electromagnet is also investigated and determined in order to generate sufficient magnetic source. With the definite workspace, the relations between the original placement of electromagnets and the electromagnet dimensions are geometrically analyzed. The main structure of OctoRob prototype is completely finalized after the implementation of cooling system. Other external appliances, such as microscope, current amplifiers, power supplies, are also equipped for necessary control.

In the end of thesis, we simulated magnetic field and gradient of OctoRob system since the calibration would be firstly performed regarding magnetic field. Obviously, magnetic gradient, magnetic torque and force all can be derived from magnetic field. The simulation results represent three moving cases of electromagnets confirming that our system enables a variety of magnetic field distributions easily. Hence, the developed system would become resourceful and provide more versatility and flexibility to the magnetic manipulation of medical microrobots, which could assist surgeons in the precise retinal MIS. Therefore, using design methodology as we demonstrated for performant electromagnetic micromanipulation platforms, the various EMA system could be optimized and improved concerning the specific medical application.

Future work

This dissertation presents a promising design methodology of EMA system for effective controlling the untethered microrobot in respect of required singular-free DOF. The designed EMA system is able to adapt the desired MIS helping surgeons for improving manipulability and dexterity, meanwhile, that avoids side effects of operation for patient. Huge amounts of simulations have

been done, however, the built EMA system yet needs to be experimentally validated.

1) Calibration of OctoRob should be performed. As we analyzed in chapter IV, the point dipole model is perfectly fit the finite element model for describing magnetic field and its gradient. Next, a single-point magnetic field calibration will be performed to compare the actual magnetic field being measured to the predicted maps by utilizing the point dipole model. The calibration is used to correct imperfections in the magnetic cores, the coil winding, and the alignment of the electromagnets. The angular and distance errors are then obtained for compensation.

2) Magnetic actuation comprising of magnetic torque and force will be tested on small magnetic object. The motion of rotation and translation will be validated through trajectory tracking test with closed-loop control. The performance of designed EMA system should be thoroughly investigated with respect to different trajectories as well as for a variety of object orientations.

3) In vitro and in vivo experiments are on the schedule after the preliminary experimental validation is accomplished. To move a further step towards a real surgical instrument that can be commercialized, the cell test, animal test and clinical test must be on the plan. The actuation capabilities should be further investigated in real application. Considering the intraocular microrobots to OctoRob system, we must still select for which vitreoretinal procedures an untethered microrobot is appropriate. Microrobots can be applied for remote sensing applications, as well as for targeted delivery of small quantities of concentrated drug. As a particular application, OctoRob system could be used for the targeted drug delivery by injecting and puncturing drug-coated microrobot to retinal veins, and then control its motion for targeted treatment.

Appendices

Appendix A

Analysis of the Performance of 2D EMA arrangements

Introduction

In chapter III, the simulation of various EMA systems are realized to analyze their performances. As a complement, this appendix investigates the flat configurations of EMA systems including $n = 6$ and 8 electromagnets, as illustrated in figures A.1a and A.1b. These 2D arrangements are considered as they offer a first basis commonly studied by researchers. Indeed, planar EMA setups can provide interesting solutions for either any simple biomedical application where the task remains almost in the plane as *in vitro* cell micromanipulation [51], [182], [183] or microfluidic lab-on-chip cell sorting [184], [185]. Moreover, from these simple 2D configurations, advanced 3D spatial arrangement can be further extrapolated.

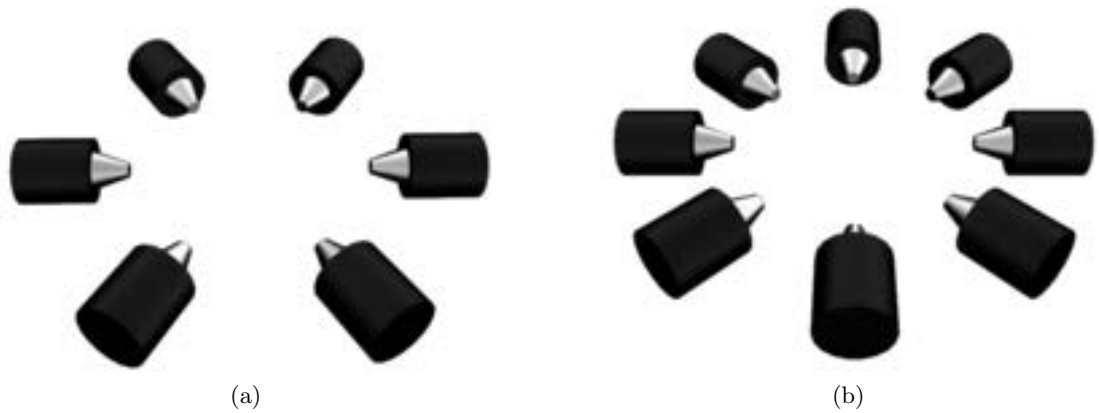

(a) (b)

Figure A.1: Representation of the different basic multi-electromagnets setups: (a) flat six-electromagnet system; (b) flat eight-electromagnet system, respectively.

A.1 Flat six-electromagnet configuration

Figure A.2 shows the considered six-electromagnetic coils configuration. The $n = 6$ identical magnets are arranged in an axisymmetric way in the xy-plane around the workspace center O as illustrated in figure A.2b. More precisely, each electromagnet is placed at the same distance $l_1 = \ldots = l_6 = d_w$ to the center O, and the 6 coils are separated with an offset angle of 60° to each other. The magnetic field distribution investigations of such six-electromagnet EMA system are analyzed through different simulations in the following.

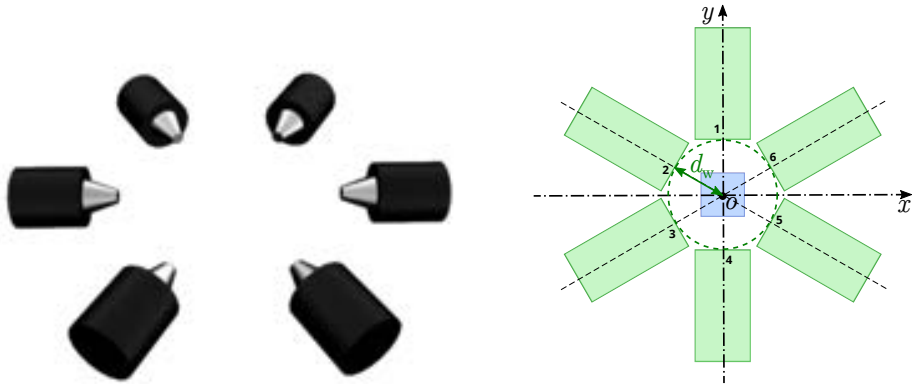

(a) (b)

Figure A.2: Flat six-electromagnet arrangement: (a) 3D view of the EMA setup; and (b) 2D view of the xy-plane. The blue square depicts the workspace Ω.

As shown in figure A.3, the magnetic fields $\mathbf{B} = (b_x, b_y, b_z)$ generated by the flat six-coil EMA system are analyzed. Figure A.3a depicts the vector distributions of the magnetic field produced in the 3D workspace of $\Omega = 45\,\text{mm} \times 45\,\text{mm} \times 45\,\text{mm}$, with $d_w = 65\,\text{mm}$. These simulation results show that strong magnetic fields exist near the border of the workspace. As one can see, the magnetic fields are not uniform within the Ω. In addition, the magnetic field in the xy-plane not only becomes stronger with the increase of the coil number, but also decreases with the shorter distance d_w. Indeed, figure A.4 shows the magnetic field magnitude $\|\mathbf{B}\|$ in the xy-plane for lengths $d_w = 60\,\text{mm}$, 70 mm and 80 mm. Specifically, as this distance d_w increase, the maximum value of the magnetic field intensity $\|\mathbf{B}\|$ within the workspace decreases from 39.18 mT to 10.97 mT.

Figure A.5 reveals the changes in the magnetic field magnitude along the x, y, and z-axis with respect to the working distance d_w. Obviously, the strength of magnetic field is significantly enhanced compared to the flat four-electromagnet EMA system that we actually also simulated. For instance, as presented in figure A.6, when d_w is set to 70 mm, the mean value $\langle\|\mathbf{B}\|\rangle$ of the magnetic field becomes 10.1 mT instead of an average value of 6.4 mT with the four-electromagnets case. The magnetic field distribution is axisymetric as the mean values $\langle b_x\rangle$, $\langle b_y\rangle$ and $\langle b_z\rangle$ are close to zero. Furthermore, the uniformity index $\gamma(\|\mathbf{B}\|)$ remains unchanged with a value around 72.8%. It also appears that the uniformity $\gamma(b_y)$ of the y component of $\mathbf{B}$ is greater than the other b_x and b_z components. This aspect is motivated by the choice of aligning a coil pair along the y-axis, as shown in figure A.2b.

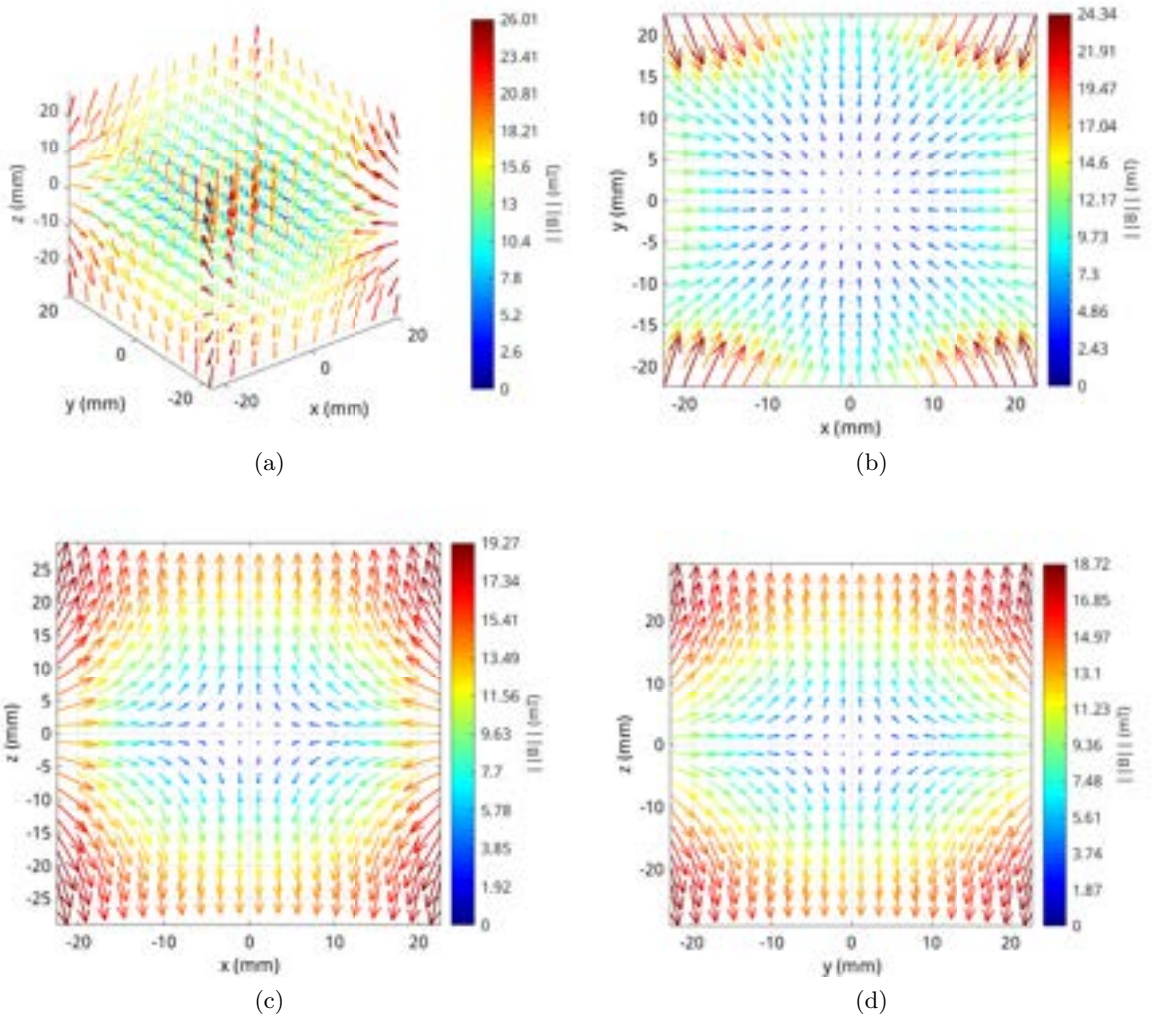

Figure A.3: The magnetic field $\mathbf{B}$ generated by the flat six-coil system with $d_w = 65\,\text{mm}$: (a) a 3D view, (b) the xy-plane, (c) the xz-plane and (d) the yz-plane. The colorbar indicates the magnetic field magnitude.

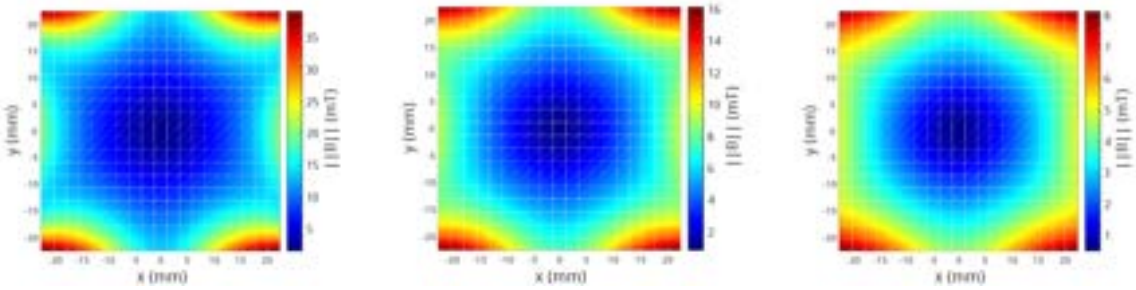

Figure A.4: The magnetic field magnitude $\|\mathbf{B}\|$ in the xy-plane for lengths of (a) $d_w = 60\,\text{mm}$, (b) $d_w = 70\,\text{mm}$ and (c) $d_w = 80\,\text{mm}$.

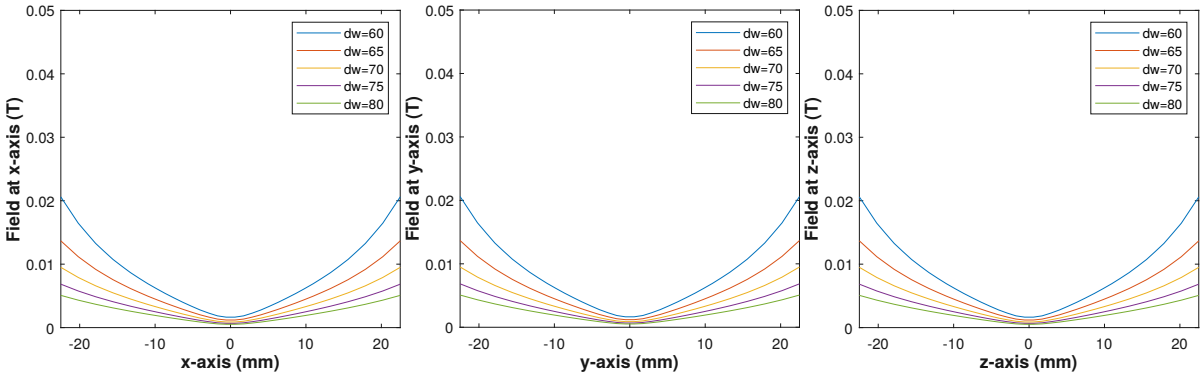

(a) (b) (c)

Figure A.5: Magnetic field magnitude along (a) the x-axis, (b) the y-axis, and (c) the z-axis.

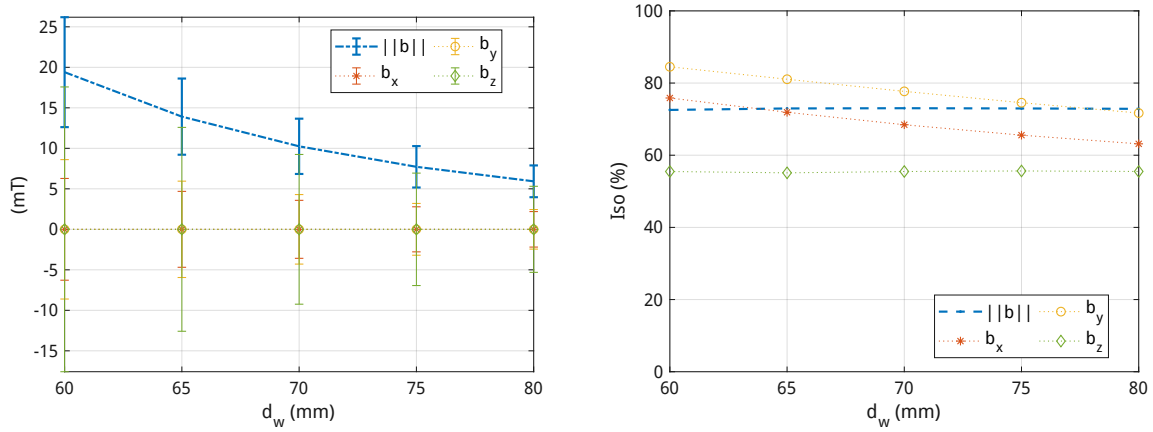

(a) (b)

Figure A.6: Magnetic field metrics over the workspace Ω for d_w ranging from 60 mm to 80 mm: (a) error-bar showing the average and STD values; and (b) the uniformity index γ.

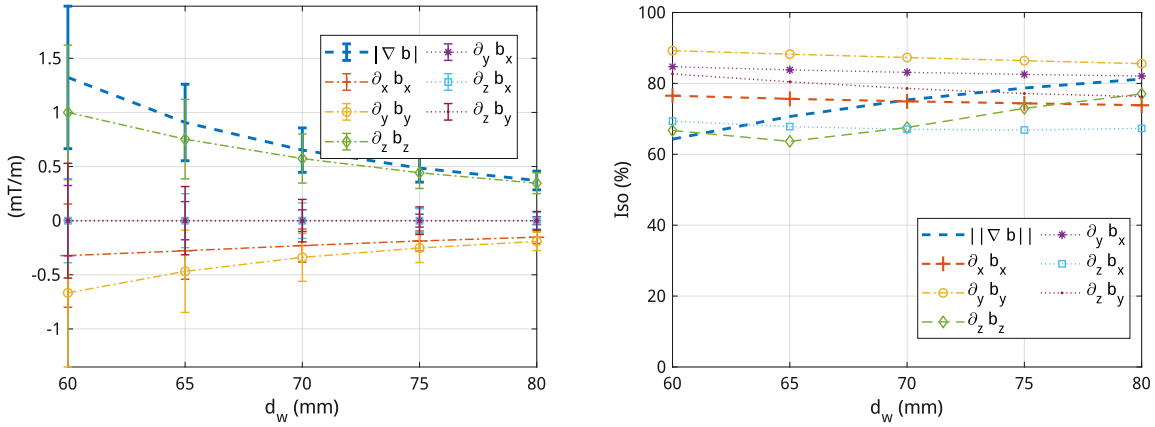

(a) (b)

Figure A.7: Magnetic field gradient metrics for distance d_w ranging from 60 mm to 80 mm: (a) the mean and STD values; and (b) the uniformity index γ.

Here again, the magnetic field is axisymmetric around the z-axis, and for its spatial gradient as well. Figure A.7 shows the magnetic field gradient metric where the magnetic field gradient strength decreases with the long distance d_w. On the contrary, the uniformity index increases with the distance d_w. Thus, the six-coil configuration with a short distance d_w can provide stronger magnetic propulsion force $\mathbf{f}_\mathrm{m}$, however, in the meanwhile, the motion of the microrobot would become more difficult to control as the uniformity index is decreasing. Indeed, the magnetic field and its gradient induce the magnetic torque and force, respectively. After the analysis of magnetic field and its gradient, the global performance of the magnetic actuation has also been investigated.

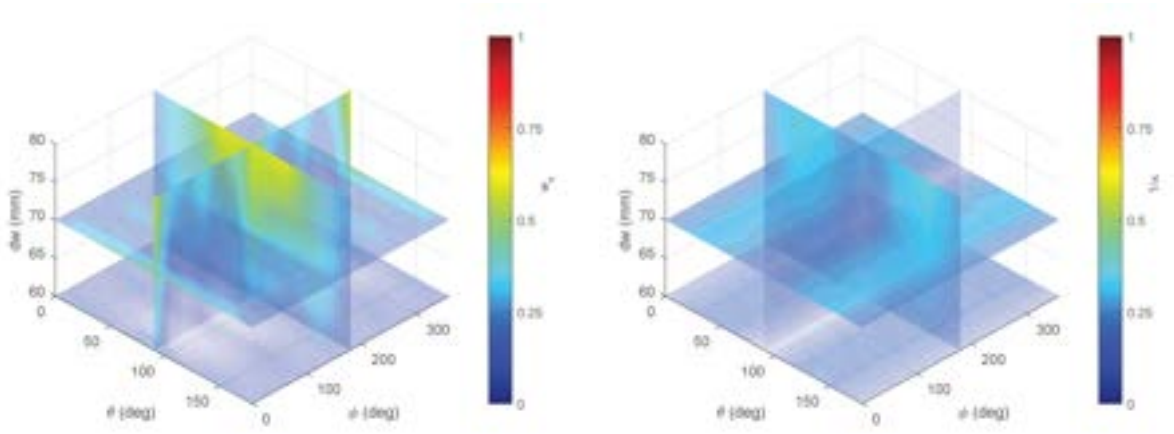

(a) Performance metrics of the force $\mathcal{A}_{\mathbf{f}_\mathrm{m}}$

(b) Performance metrics of the force $\mathcal{A}_{\mathbf{f}_\mathrm{m}}$

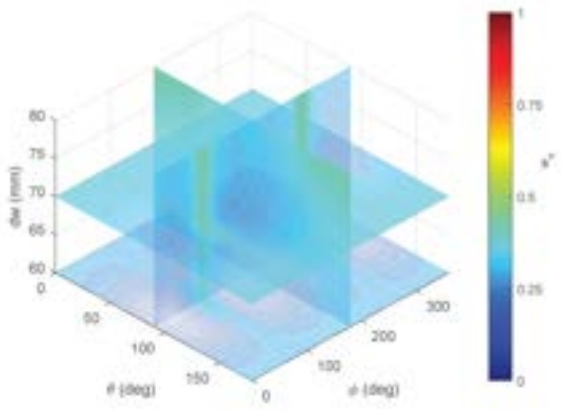

(c) Performance metrics of the torque $\mathcal{A}_{\mathbf{t}_\mathrm{m}}$

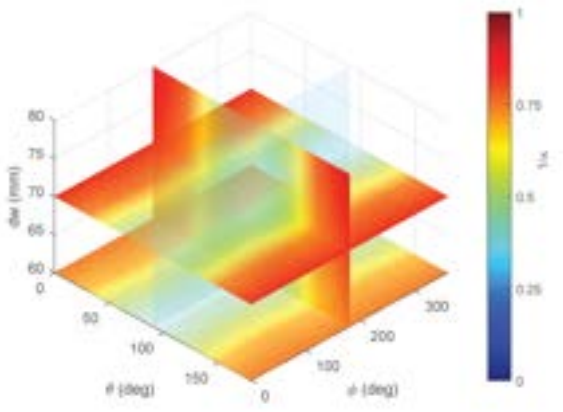

(d) Performance metrics of the torque $\mathcal{A}_{\mathbf{t}_\mathrm{m}}$

Figure A.8: 3D representation of the performance metrics of the force (a)-(b) and torque (c)-(d) actuation matrices in the workspace for averaged magnetic moment orientations: (a)-(c) show the normalized manipulability index w_n; and (b)-(d) show the dexterity index $1/\kappa$.

Figure A.8 shows the performance indexes of the actuation matrix $\mathcal{A}(\mathbf{p}, \mathbf{m})$ with different distances d_w. The actuation matrix is computed for an arbitrary microrobot positioned to the sampled location $\mathbf{p} \in \Omega$, and possessing a unit-strength magnetic moment $\mathbf{m}$ with varying orientation expressed with the azimuth angles $\varphi \in [0; 360°)$ and polar angles $\theta \in [0; 180°]$. Once

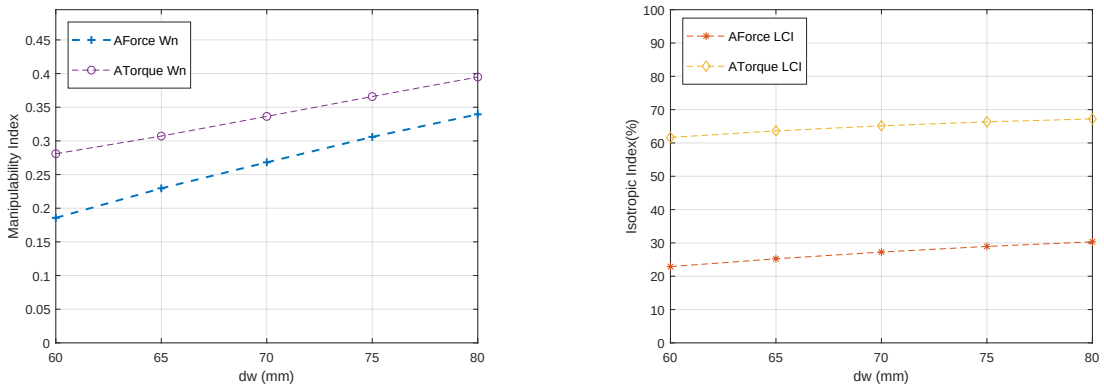

(a) (b)

Figure A.9: Mean of the global performance indexes (a) manipulability and (b) uniformity of the force $\mathcal{A}_{\mathbf{f}_\mathrm{m}}$ and torque $\mathcal{A}_{\mathbf{t}_\mathrm{m}}$ actuation matrices for different distance d_w.

again, the performance indexes of the force $\mathbf{f}_\mathrm{m}$ and torque $\mathbf{t}_\mathrm{m}$ are symmetrical about the xy-plane ($\theta = 90°$), and the values are increasing with the distance d_w. Similarly, as represented in figure A.9, the long length d_w brings higher manipulability of the force and torque. Moreover, the good conditioning indexes $1/\kappa$ of the $\mathbf{f}_\mathrm{m}$ and $\mathbf{t}_\mathrm{m}$ occur mainly for long distance, even though the effect of distance is not significant. The analysis of the actuation performance indexes between the force $\mathbf{f}_\mathrm{m}$ and torque $\mathbf{t}_\mathrm{m}$ from figure A.8 and figure A.9 reveals that $\mathbf{t}_\mathrm{m}$ seems easier to control than $\mathbf{f}_\mathrm{m}$.

A.2 Flat eight-electromagnet configuration

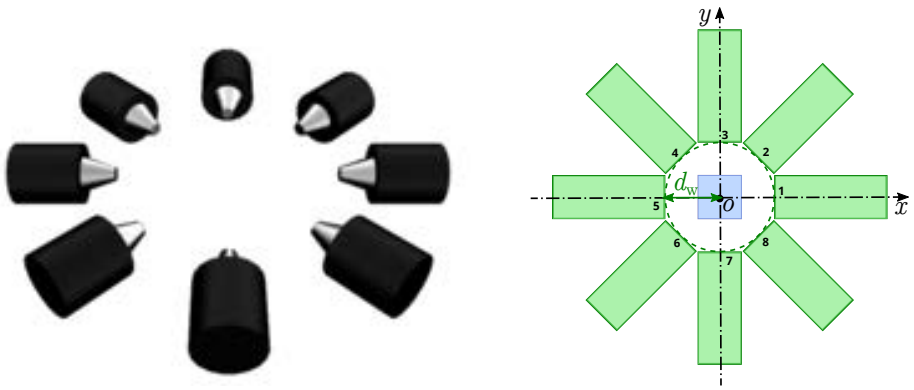

(a) (b)

Figure A.10: Flat eight-electromagnet system: (a) 3D view of the EMA setup; and (b) 2D view of the xy-plane. The blue square depicts the workspace Ω.

As the magnetic field will achieve a more uniform distribution when more coils are placed in 2D plane, the flat eight-coil configuration illustrated in figure A.10 has been investigated.

The considered $n = 8$ coils are organized in axisymmetric fashion around the center of the workspace O in the xy-plane. The $n = 8$ identical electromagnets are placed at the same distance $l_1 = \ldots = l_8 = d_w$ to the center of the workspace, and are separated to each other with an offset angle of 45°. Let us recall that as $n > 6$, the eight-electromagnet EMA setup leads to a "redundant" system. The magnetic field metrics of the eight-electromagnet EMA system are analyzed through several simulations in the following.

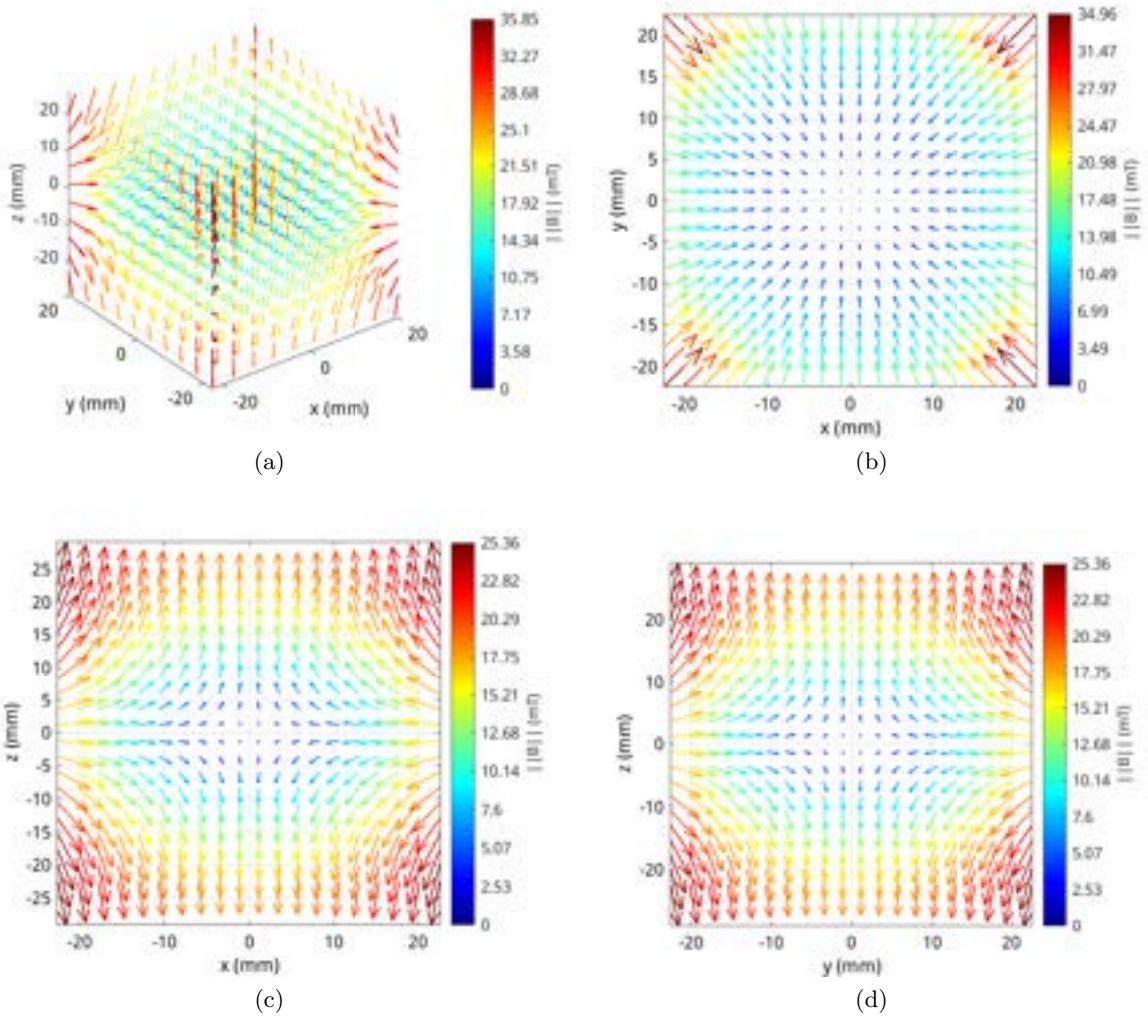

Figure A.11: The magnetic field $\mathbf{B}$ generated by the flat eight-coils system with $d_w = 65\,\text{mm}$: (a) a 3D view, (b) the xy-plane, (c) the xz-plane and (d) the yz-plane. The colorbar indicates the magnetic field magnitude.

The induced magnetic field $\mathbf{B}$ in the desired 3D workspace is shown in figure A.11. From these simulation results, we observe that the magnetic field tends to be a radial field in xy-plane. By comparing the field distribution to the six-coil system, as in figure A.3, such behavior can be easily understood. The distribution of magnetic field strength $\|\mathbf{B}\|$ shows more clearly this aspect, as depicted in figure A.12. It can be noticed that the magnetic field tends to be an increasingly radial field in xy-plane as the distance d_w increases. However, when d_w increases, the simulations

indicate that the strength of magnetic field is significantly weakened, while the magnetic field becomes more uniform within the area where the estimated locations are equidistant from the center.

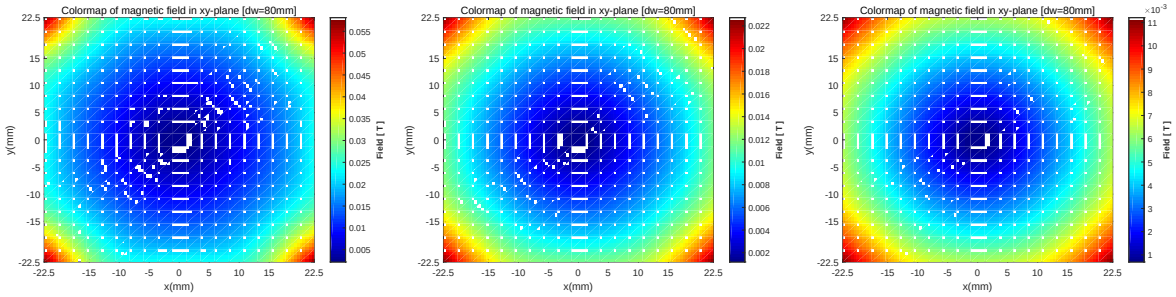

(a) (b) (c)

Figure A.12: The magnetic field magnitude $\|\mathbf{B}\|$ in the xy-plane for lengths of (a) $d_w = 60\,\text{mm}$, (b) $d_w = 70\,\text{mm}$ and (c) $d_w = 80\,\text{mm}$.

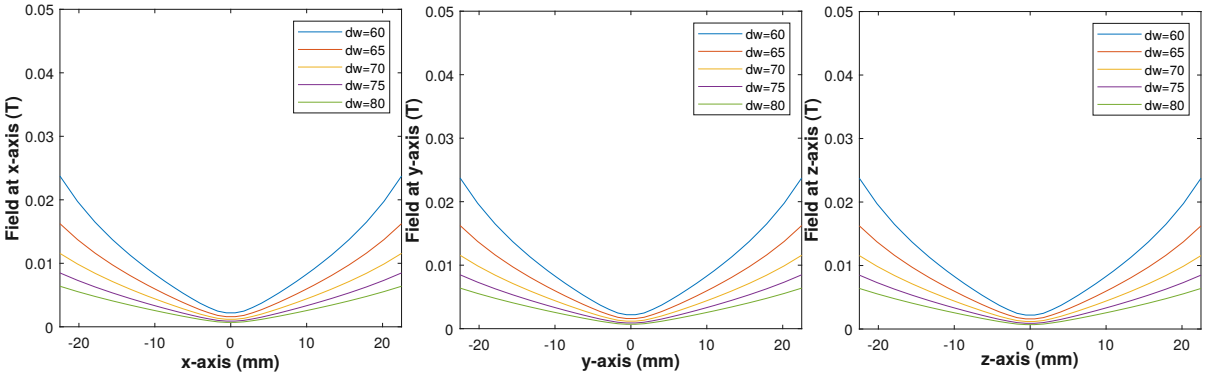

(a) (b) (c)

Figure A.13: Magnetic field magnitude $\|\mathbf{B}\|$ along (a) the x-axis, (b) the y-axis, and (c) the z-axis, for lengths of d_w ranging from 50 mm to 80 mm.

Figure A.13 reveals that the magnetic field magnitude $\|\mathbf{B}\|$ behaves similarly along the x, y and z-axis. In addition, the strength of the magnetic field is also enhanced, and its variation is more consistent from the center outward. The mean and the STD values of the magnetic field intensity for sampled position $\mathbf{p} \in \Omega$ have also been investigated, and are shown in figure A.14. As previously stated, the strength $\|\mathbf{B}\|$ can be improved by arranging the $n = 8$ coils more close to the workspace. Indeed, as d_w increases, the average value of the magnetic field magnitude decreases, while its uniformity index $\gamma(\|\mathbf{B}\|)$ remains unchanged around 73.1%.

The magnetic field is axisymmetric around the z-axis as observed, and correspondingly, its spatial gradient as well. Figure A.15 shows the statistical data and uniformity index γ of the magnetic field gradient for different distances d_w. It can be seen that the short distance d_w should be used to generate stronger magnetic gradient. In particular, $\frac{\partial b_z}{\partial z}$ is the strongest component of the magnetic field gradient, and the $\frac{\partial b_x}{\partial x}$ and $\frac{\partial b_y}{\partial y}$ are superposed. Moreover, the average values

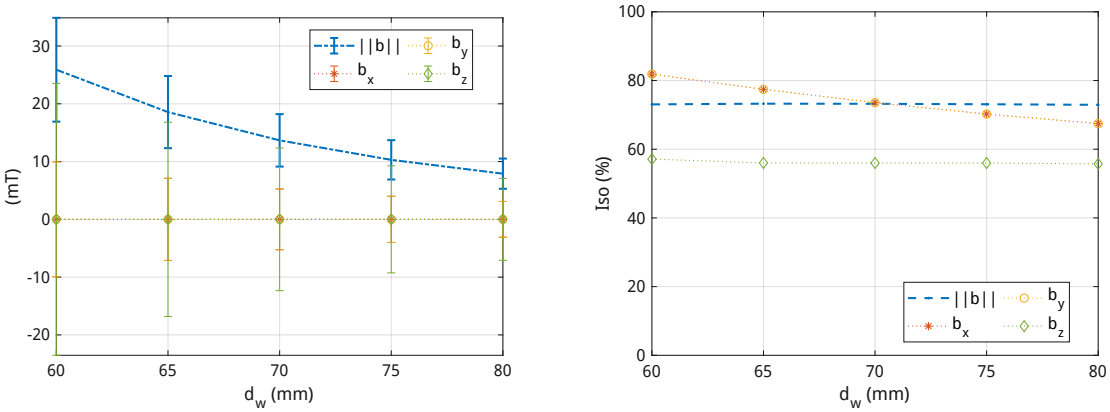

(a) (b)

Figure A.14: Magnetic field metrics over the workspace Ω for d_w ranging from 60 mm to 80 mm. (a) error-bar showing the average and STD values; and (b) the uniformity index γ

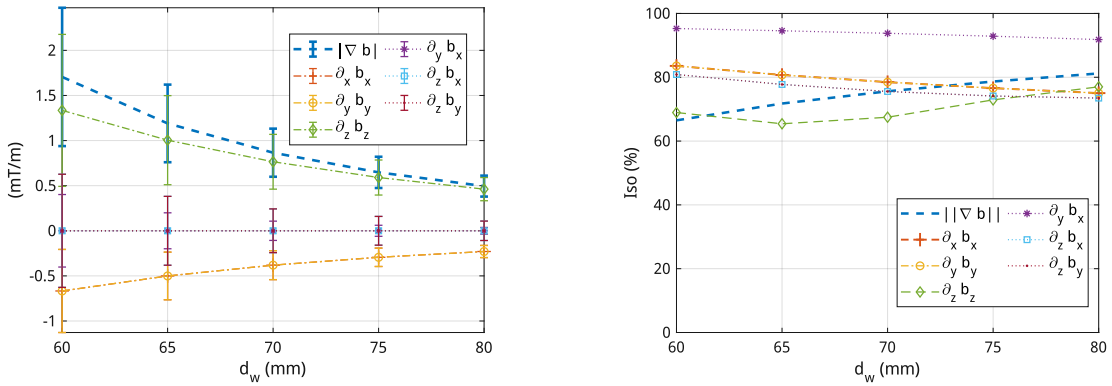

(a) (b)

Figure A.15: Magnetic field gradient metrics for distance d_w ranging from 60 mm to 80 mm: (a) the mean and STD values; and (b) the uniformity index γ.

of the components $\frac{\partial b_x}{\partial y}$, $\frac{\partial b_x}{\partial z}$ and $\frac{\partial b_y}{\partial z}$ are close to zero. The uniformity metrics of $\frac{\partial b_x}{\partial x}$ and $\frac{\partial b_y}{\partial y}$ respond equivalently and slightly decrease with d_w.

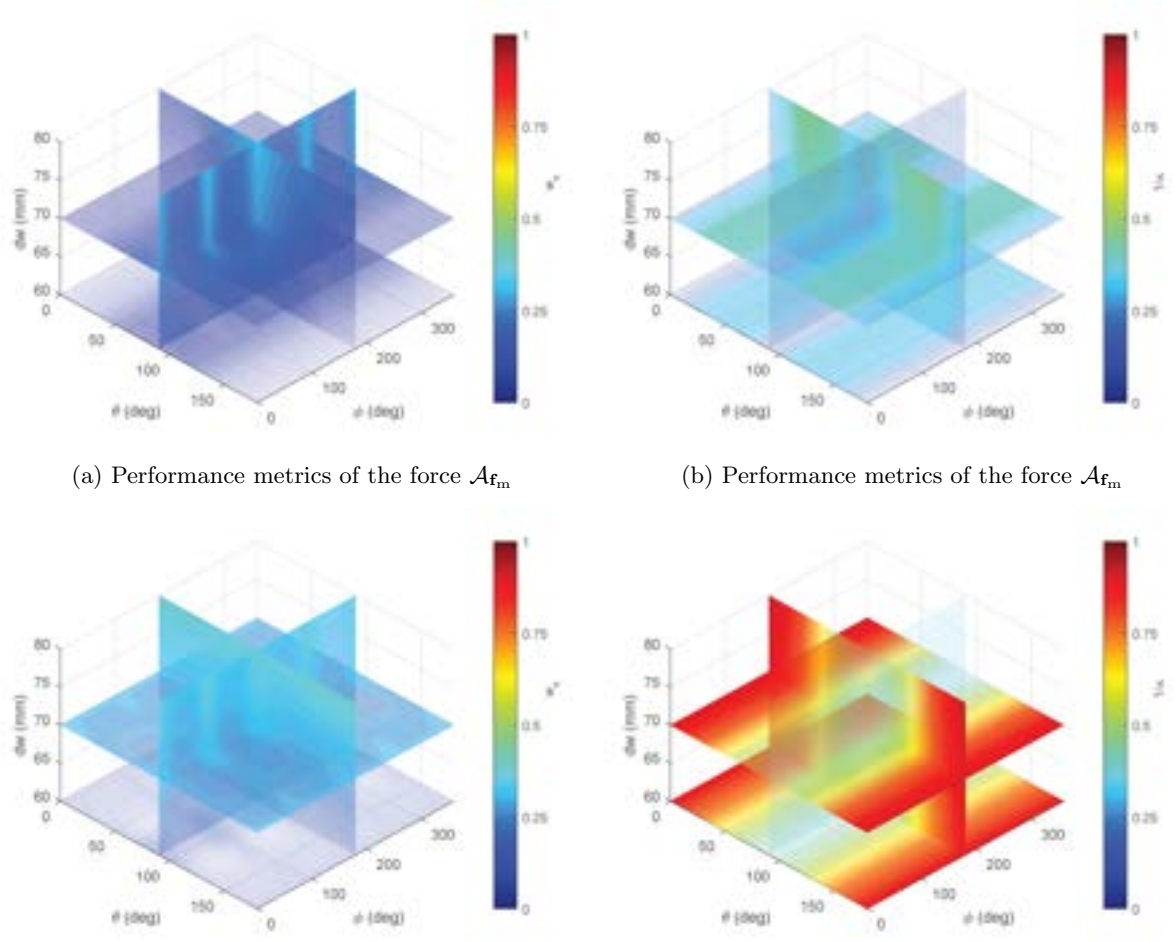

(a) Performance metrics of the force $\mathcal{A}_{\mathbf{f}_\mathrm{m}}$

(b) Performance metrics of the force $\mathcal{A}_{\mathbf{f}_\mathrm{m}}$

(c) Performance metrics of the torque $\mathcal{A}_{\mathbf{t}_\mathrm{m}}$

(d) Performance metrics of the torque $\mathcal{A}_{\mathbf{t}_\mathrm{m}}$

Figure A.16: 3D representation of the performance metrics of the force (a)-(b) and torque (c)-(d) actuation matrices in the workspace for averaged magnetic moment orientations: (a)-(c) show the normalized manipulability index w_n; and (b)-(d) show the dexterity index $1/\kappa$.

The global performance indexes comprising the normalized manipulability and matrix condition number $1/\kappa$ of the actuation matrix $\mathcal{A}(\mathbf{p}, \mathbf{m})$ are presented in figure A.16 to analyze the influence of the length d_w. The all orientations of a unit-strength magnetic moment of arbitrary microrobot are considered for the evaluation of the performance indexes. The simulation results indicate that the global performances become weaker when $\mathbf{m}$ its polar angle is pointing to $\theta = 90°$. Furthermore, the manipulability and conditioning indexes increase obviously with respect to the increasing distance d_w. As shown in figure A.17, the global matrix of condition index $1/\kappa$ does not change significantly with distance d_w, whereas the manipulability index is increasing obviously with the longer distance. Hence, the efficient control with high manipulability should select the long distance d_w between electromagnets and workspace center in this flat eight-coil

configuration. Besides, the overall magnetic torque $\mathbf{t}_{\mathrm{m}}$ can be performed more effectively than the magnetic force $\mathbf{f}_{\mathrm{m}}$, as represented in figures A.16 and A.17.

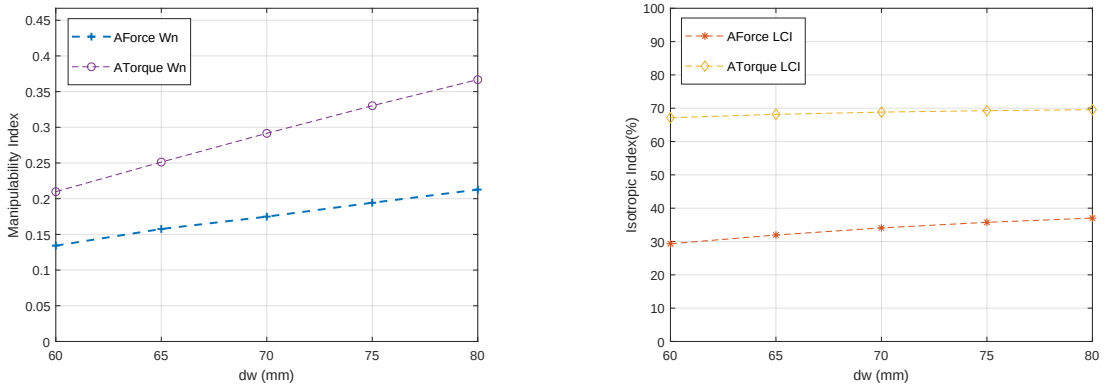

(a) (b)

Figure A.17: Mean of the global performance indexes (a) manipulability and (b) uniformity of the force $\mathcal{A}_{\mathbf{f}_{\mathrm{m}}}$ and torque $\mathcal{A}_{\mathbf{t}_{\mathrm{m}}}$ actuation matrices for different distance d_w.

A.3 Discussions

The simulation results of the different EMA configurations above show that the increase in the number n of electromagnets leads to a proportional increase of magnetic field $\mathbf{B}$ and its gradient $\nabla\mathbf{B}$ over the workspace. Basically, increasing the number of electromagnets (e.g. $n > 6$) leads to a better actuation matrix $\mathcal{A}(\mathbf{m}, \mathbf{p})$ at the origin of an homogeneous isotropic workspace with lower current value [73], [74]. We noticed also that the number of singularity is reduced. In such cases, the EMA system is said "redundant" for the tasks.

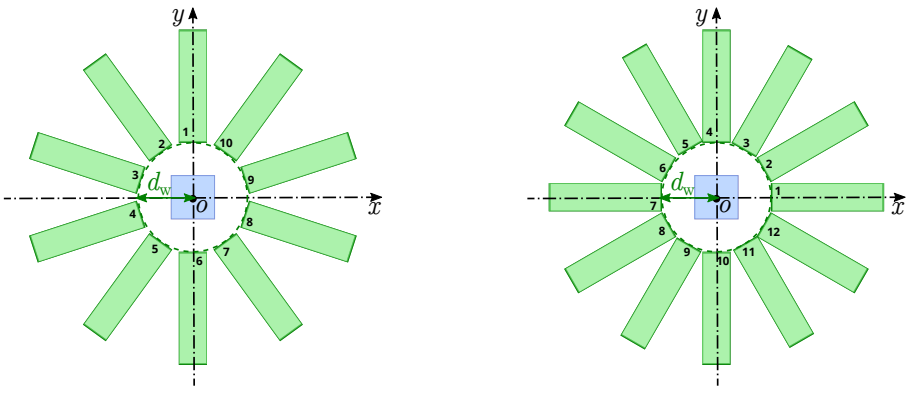

(a) (b)

Figure A.18: Representations of the flat redundant EMA setup: (a) the flat ten-coil and (b) the flat twelve-coil system.

To assess this aspect, we should further investigate the changes in the magnetic field distribu-

tion when the number of coils are more than $n > 8$. Hence, the flat ten-coil and flat twelve-coil configurations have been also simulated. These two configurations are illustrated in figure A.18. In both cases, identical magnets are placed in an axisymmetric way in the xy-plane around the center O of the workspace. Assuming the working distance is set to $d_w = 75\,\text{mm}$, the magnetic fields magnitude in the differently configured systems are investigated.

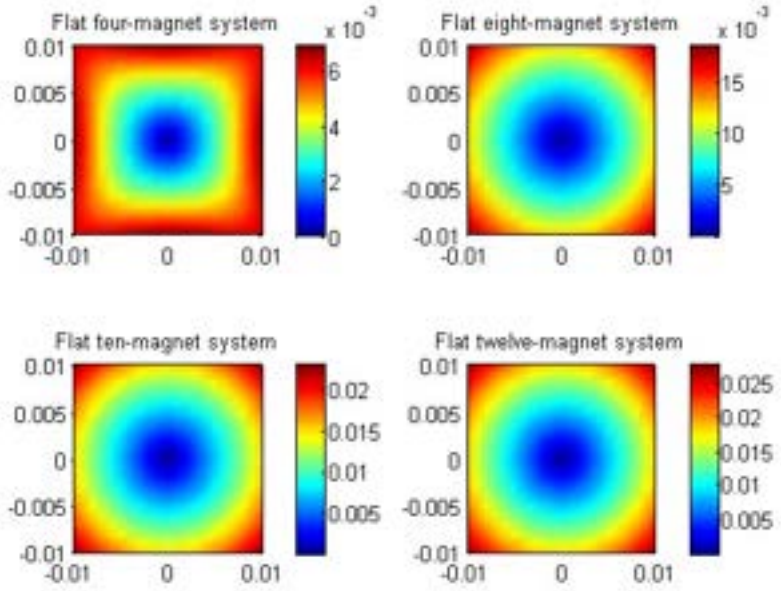

Figure A.19: The simulation results of the magnetic field magnitude $\|\mathbf{B}\|$ (T) produced by differently configured systems.

The simulation results for a set of EMA systems that includes the flat four-coil, flat eight-coil, flat ten-coil and flat twelve-coil systems are illustrated in figure A.19. These results illustrate that a greater number of magnets can truly lead to stronger magnetic field strength. Also, the magnetic field changes more linearly with the distance from the center of the workspace toward the boundary when more coils are applied. When the number of magnets is set to $n \geq 8$, although the distribution of the magnetic field tends to be a more uniform radial field in the workspace, too many redundant electromagnets lead to a more spatially constrained platform with more energy consumption. Therefore, unless increasing the magnetic field strength is an important criterion for the application, there is little interest in considering more than $n > 8$ magnets.

Appendix B

Analysis of the Performance of EMA arrangements

The other reconfigurable cases are investigated based on 8 electromagnets EMA system as well. The original arrangement of 8 electromagnets for EMA system as illustrated in Fig.B.1. The 8 electromagnets are arranged around a common axis of rotation with horizontal angle $\alpha_e = 45°$ ($e = 1..8$, as in Fig.B.1b), and are pointing at the common center O of the workspace with a given distance $d = 65mm$. However, the vertical angle β of electromagnets depends on configurations. For instance, OctoMag system requires: $\beta_e = 0°$ ($e = 1..4$) and $\beta_e = 45°$ ($e = 5..8$) as shown in Fig.B.1c. Therefore, we divide the electromagnets of the EMA actuation into different sets for analysis: stationary sets and mobile sets. Moreover, the static sets are still classified into stationary fixed sets and flexible fixed sets. Although the following investigated configurations are based on the OctoMag-like arrangement, the method of improving performances is also valid to other EMA systems, such as the MiniMag configuration, actually, the simulations of other systems have also been done and compared.

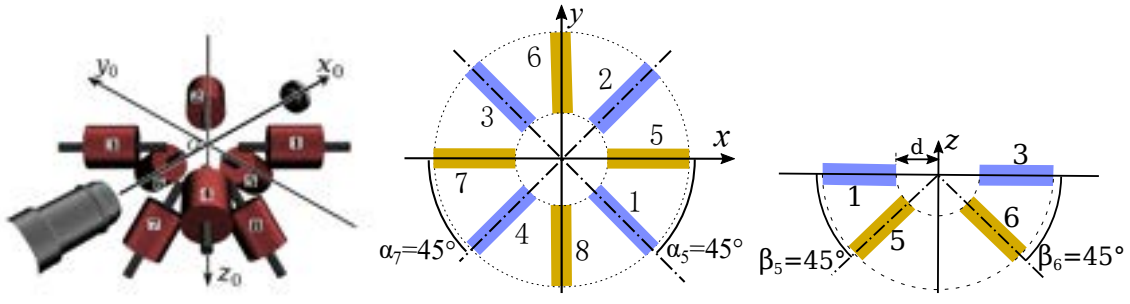

(a) (b) (c)

Figure B.1: Representation of eight-electromagnet system: (a) illustration of the concept, (b) and (c) show top view and side view of EMA system, respectively.

Table B.1: The OctoMag-like configuration(Mobile coil 5).

	Angle	Coil 1	Coil 2	Coil 3	Coil 4	Coil 5	Coil 6	Coil 7	Coil 8
Case 1	α	45°	45°	45°	45°	0°	90°	0°	90°
	β	0°	0°	0°	0°	$[0; 90°)$	0°	0°	0°
Case 2	α	45°	45°	45°	45°	0°	90°	0°	90°
	β	0°	0°	0°	0°	$[0; 90°)$	10°	10°	10°
Case 3	α	45°	45°	45°	45°	0°	90°	0°	90°
	β	0°	0°	0°	0°	$[0; 90°)$	20°	20°	20°
Case 4	α	45°	45°	45°	45°	0°	90°	0°	90°
	β	0°	0°	0°	0°	$[0; 90°)$	30°	30°	30°
Case 5	α	45°	45°	45°	45°	0°	90°	0°	90°
	β	0°	0°	0°	0°	$[0; 90°)$	40°	40°	40°
Case 6	α	45°	45°	45°	45°	0°	90°	0°	90°
	β	0°	0°	0°	0°	$[0; 90°)$	50°	50°	50°
Case 7	α	45°	45°	45°	45°	0°	90°	0°	90°
	β	0°	0°	0°	0°	$[0; 90°)$	60°	60°	60°
Case 8	α	45°	45°	45°	45°	0°	90°	0°	90°
	β	0°	0°	0°	0°	$[0; 90°)$	70°	70°	70°
Case 9	α	45°	45°	45°	45°	0°	90°	0°	90°
	β	0°	0°	0°	0°	$[0; 90°)$	80°	80°	80°

α refers to the azimuth angles (see also Fig.B.1b)

B.1 The OctoMag-like configuration(Mobile coil 5)

We firstly consider OctoMag-like configuration. The electromagnet coils $e = 1..4$ are set as stationary fixed sets. $\beta_e = 0°$ $(e = 1..4)$. The electromagnet coils $e = 6..8$ are set as flexible fixed sets. The flexible fixed angle(β_e, $e = 6..8$) increases from 0° to 80° in steps of 10°. And the electromagnet coil $e = 5$ is set as mobile set, that is able to rotate its angle $\beta_5 \in [0; 90°)$. Thus we will analyze the performance of this configuration in the following cases shown in Table.B.1.

Magnetic fields generated from the 8 electromagnets can be linearly superimposed in the workspace. For example, in the case 1, the flexible fixed sets are rotated at $\beta_e = 0°$ $(e = 6..8)$, and the coil 5 is rotating. Since the indexes are axisymmetric around the z-axis, the analysis is depicted only along this direction. Moreover, the abscissa indicates mobile angles of coil 5. The results of other cases are presented in a similar way.

The performance metrics of magnetic field with all cases are shown in Fig.B.2. When flexible fixed coils are set to low angles and mobile coils are rotating to low angle, the magnetic fields are mainly generated in workspace below, and the magnetic field strength decreases as the angle of the moving coil increases in z-axis direction. Due to the limited number of moving coils, the magnetic field distribution is mainly controlled by a fixed coil. Therefore, magnetic field along z-axis becomes stronger when the flexible fixed coils rotate to high angle.

Also, the manipulability indexes of force and torque present similar characteristic as shown in Fig.B.3. The high flexible fixed angle $\beta_e \gtrsim 45°$ $(e = 6..8)$ leads to stronger manipulability in the upper part of workspace benefiting for actuating microrobots.

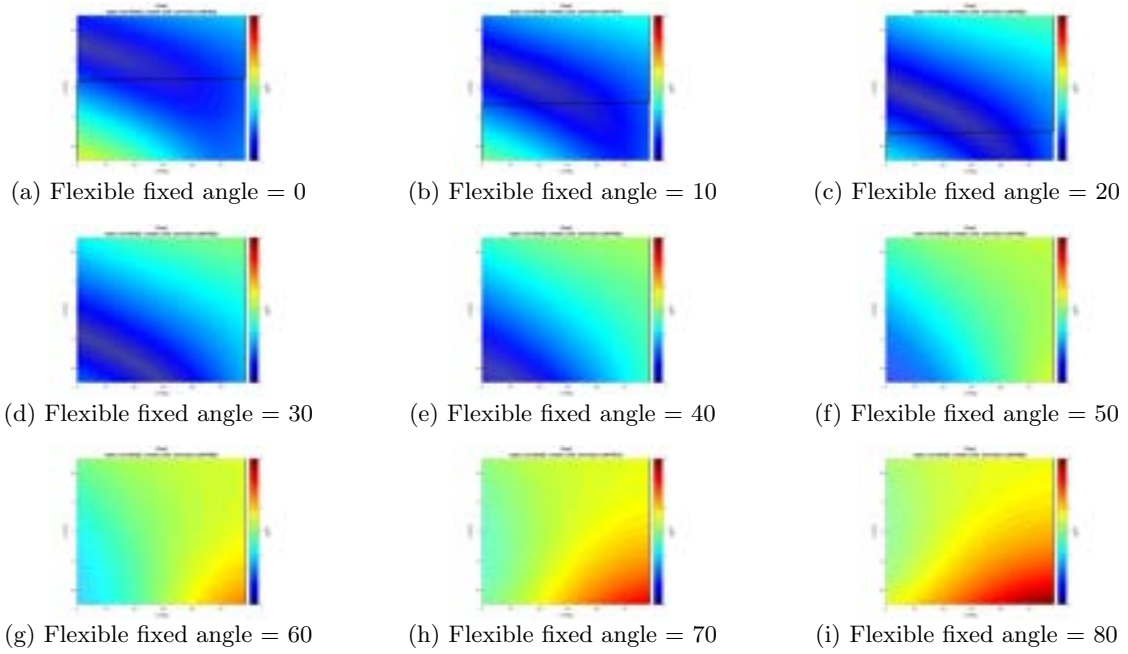

(a) Flexible fixed angle = 0 (b) Flexible fixed angle = 10 (c) Flexible fixed angle = 20

(d) Flexible fixed angle = 30 (e) Flexible fixed angle = 40 (f) Flexible fixed angle = 50

(g) Flexible fixed angle = 60 (h) Flexible fixed angle = 70 (i) Flexible fixed angle = 80

Figure B.2: Mobile coil 5 for OctoMag-like configuration

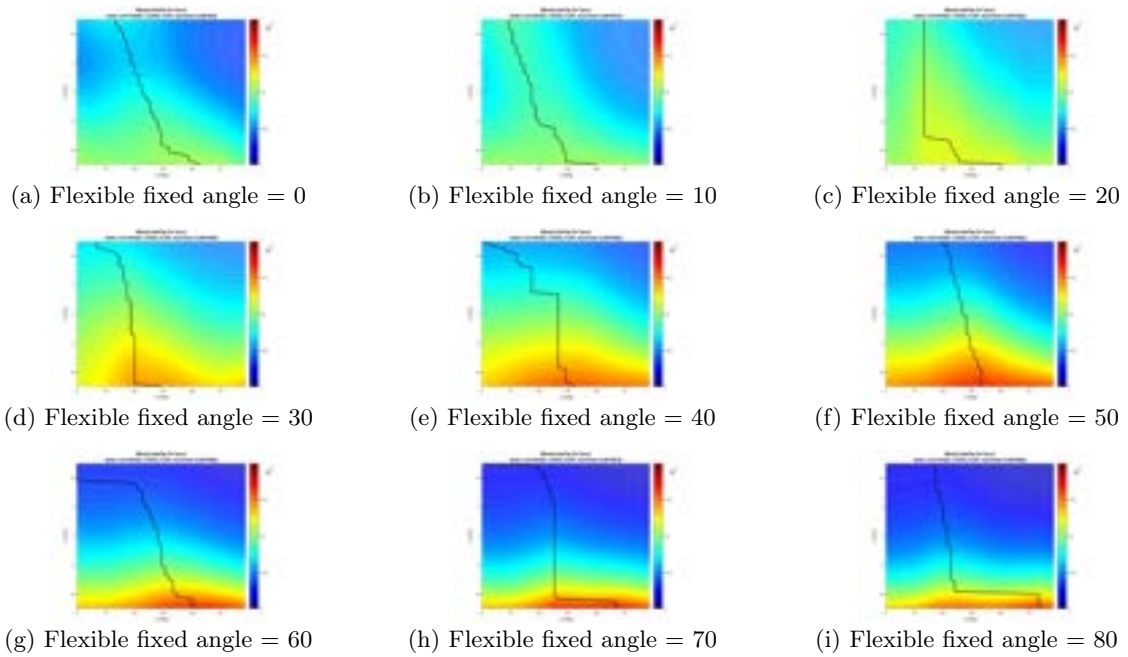

(a) Flexible fixed angle = 0 (b) Flexible fixed angle = 10 (c) Flexible fixed angle = 20

(d) Flexible fixed angle = 30 (e) Flexible fixed angle = 40 (f) Flexible fixed angle = 50

(g) Flexible fixed angle = 60 (h) Flexible fixed angle = 70 (i) Flexible fixed angle = 80

Figure B.3: (Force Manipulability) Mobile coil 5 for OctoMag-like configuration

B.2 The OctoMag-like configuration(Mobile coils 5 and 6)

Obviously if we adjust the number of mobile coils, the system performance will be changed. When the coils 1-4 are fixed as $\beta_e = 0°$ ($e = 1..4$) and the adjacent coils pair (coil 5 and coil

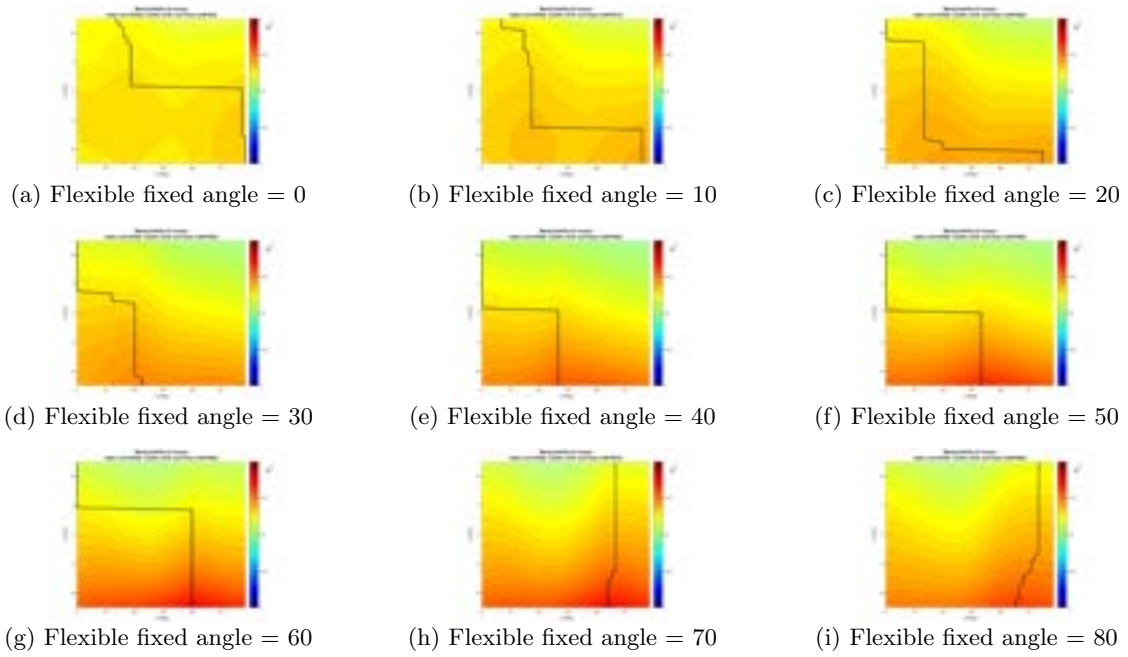

(a) Flexible fixed angle = 0 (b) Flexible fixed angle = 10 (c) Flexible fixed angle = 20

(d) Flexible fixed angle = 30 (e) Flexible fixed angle = 40 (f) Flexible fixed angle = 50

(g) Flexible fixed angle = 60 (h) Flexible fixed angle = 70 (i) Flexible fixed angle = 80

Figure B.4: (Torque Manipulability) Mobile coil 5 for OctoMag-like configuration

6) is set as mobile coils. At the same time the coil 7 and coil 8 are rotated in 0°,10°...70°,80° respectively corresponding to different cases as shown in Table.B.2. Similarly, the simulation results indicate the low mobile angles provide stronger magnetic field shown in B.5, and the influence of the mobile coil on the magnetic field distributions increases as the number of mobile coils increase. Moreover, the high flexible fixed angles make good manipulability distribute in the upper part of workspace(see Fig.B.6 and Fig.B.7).

B.3 The OctoMag-like configuration(Mobile coils 5 and 7)

When opposite coil pair (coil 5 and coil 7) is set as mobile coils, we have also investigated the influence of system performance. In this configuration, the coils 1-4 are fixed as $\beta_e = 0°$ ($e = 1..4$), and the another opposite coils pair (coil 6 and coil 8) is rotated to different cases as flexible fixed sets shown in Table.B.3. Once again the simulation results prove that the magnetic field will be stronger when mobile coils are rotated at low angle (see Fig.B.8). The manipulability of force is significantly improved in this configuration when the flexible fixed angle is around 50°, especially in the upper part of workspace. Also, the manipulability of torque can be increased by rotating mobile sets or flexible fixed set to the high angle.

B.4 The OctoMag-like configuration(Mobile coils 5, 6 and 7)

Similarly, when coil set (coil 5, coil 6 and coil 7) is set as mobile coils, the system performances are evaluated. In such mobile configuration, the coil 1-4 are fixed as $\beta_e = 0°$ ($e = 1..4$), and the last coil (coil 8) is rotated to different cases as flexible fixed set shown in Table.B.3. Once again

Table B.2: The OctoMag-like configuration(Mobile coils 5 and 6).

	Angle	Coil 1	Coil 2	Coil 3	Coil 4	Coil 5	Coil 6	Coil 7	Coil 8
Case 1	α	45°	45°	45°	45°	0°	90°	0°	90°
	β	0°	0°	0°	0°	$[0; 90°)$	$[0; 90°)$	0°	0°
Case 2	α	45°	45°	45°	45°	0°	90°	0°	90°
	β	0°	0°	0°	0°	$[0; 90°)$	$[0; 90°)$	10°	10°
Case 3	α	45°	45°	45°	45°	0°	90°	0°	90°
	β	0°	0°	0°	0°	$[0; 90°)$	$[0; 90°)$	20°	20°
Case 4	α	45°	45°	45°	45°	0°	90°	0°	90°
	β	0°	0°	0°	0°	$[0; 90°)$	$[0; 90°)$	30°	30°
Case 5	α	45°	45°	45°	45°	0°	90°	0°	90°
	β	0°	0°	0°	0°	$[0; 90°)$	$[0; 90°)$	40°	40°
Case 6	α	45°	45°	45°	45°	0°	90°	0°	90°
	β	0°	0°	0°	0°	$[0; 90°)$	$[0; 90°)$	50°	50°
Case 7	α	45°	45°	45°	45°	0°	90°	0°	90°
	β	0°	0°	0°	0°	$[0; 90°)$	$[0; 90°)$	60°	60°
Case 8	α	45°	45°	45°	45°	0°	90°	0°	90°
	β	0°	0°	0°	0°	$[0; 90°)$	$[0; 90°)$	70°	70°
Case 9	α	45°	45°	45°	45°	0°	90°	0°	90°
	β	0°	0°	0°	0°	$[0; 90°)$	$[0; 90°)$	80°	80°

Table B.3: The OctoMag-like configuration(Mobile coils 5 and 7).

	Angle	Coil 1	Coil 2	Coil 3	Coil 4	Coil 5	Coil 6	Coil 7	Coil 8
Case 1	α	45°	45°	45°	45°	0°	90°	0°	90°
	β	0°	0°	0°	0°	$[0; 90°)$	0°	$[0; 90°)$	0°
Case 2	α	45°	45°	45°	45°	0°	90°	0°	90°
	β	0°	0°	0°	0°	$[0; 90°)$	10°	$[0; 90°)$	10°
Case 3	α	45°	45°	45°	45°	0°	90°	0°	90°
	β	0°	0°	0°	0°	$[0; 90°)$	20°	$[0; 90°)$	20°
Case 4	α	45°	45°	45°	45°	0°	90°	0°	90°
	β	0°	0°	0°	0°	$[0; 90°)$	30°	$[0; 90°)$	30°
Case 5	α	45°	45°	45°	45°	0°	90°	0°	90°
	β	0°	0°	0°	0°	$[0; 90°)$	40°	$[0; 90°)$	40°
Case 6	α	45°	45°	45°	45°	0°	90°	0°	90°
	β	0°	0°	0°	0°	$[0; 90°)$	50°	$[0; 90°)$	50°
Case 7	α	45°	45°	45°	45°	0°	90°	0°	90°
	β	0°	0°	0°	0°	$[0; 90°)$	60°	$[0; 90°)$	60°
Case 8	α	45°	45°	45°	45°	0°	90°	0°	90°
	β	0°	0°	0°	0°	$[0; 90°)$	70°	$[0; 90°)$	70°
Case 9	α	45°	45°	45°	45°	0°	90°	0°	90°
	β	0°	0°	0°	0°	$[0; 90°)$	80°	$[0; 90°)$	80°

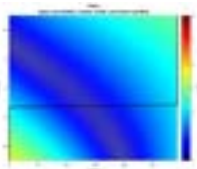

(a) Flexible fixed angle = 0

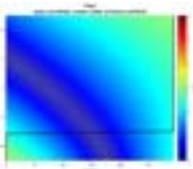

(b) Flexible fixed angle = 10

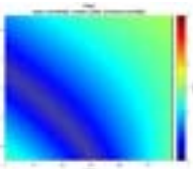

(c) Flexible fixed angle = 20

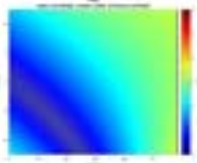

(d) Flexible fixed angle = 30

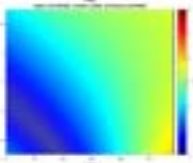

(e) Flexible fixed angle = 40

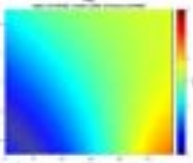

(f) Flexible fixed angle = 50

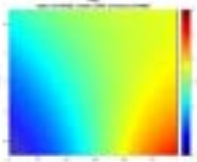

(g) Flexible fixed angle = 60

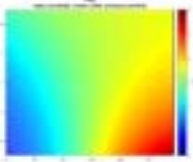

(h) Flexible fixed angle = 70

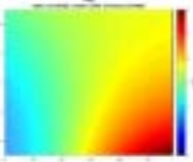

(i) Flexible fixed angle = 80

Figure B.5: Mobile coil 5 and 6 for OctoMag-like configuration

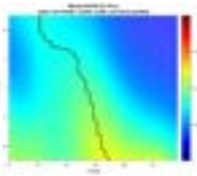

(a) Flexible fixed angle = 0

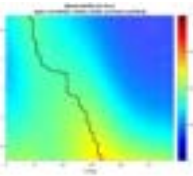

(b) Flexible fixed angle = 10

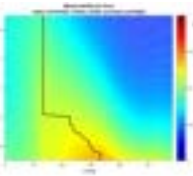

(c) Flexible fixed angle = 20

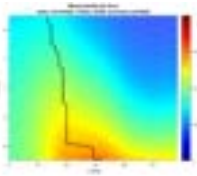

(d) Flexible fixed angle = 30

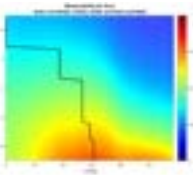

(e) Flexible fixed angle = 40

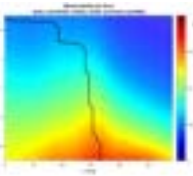

(f) Flexible fixed angle = 50

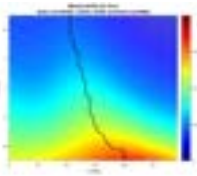

(g) Flexible fixed angle = 60

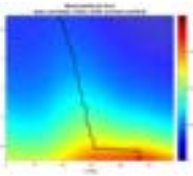

(h) Flexible fixed angle = 70

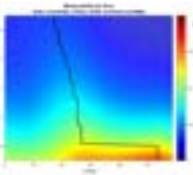

(i) Flexible fixed angle = 80

Figure B.6: (Force Manipulability) Mobile coil 5 and 6 for OctoMag-like configuration

the simulation results of magnetic field have been presented in Fig.B.8. The manipulability of force and torque have been illustrated in Figfigure B.12 and Fig.B.13, respectively.

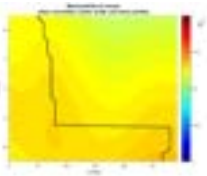

(a) Flexible fixed angle = 0

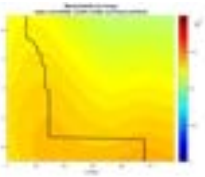

(b) Flexible fixed angle = 10

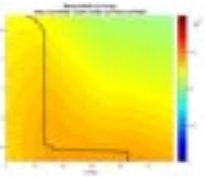

(c) Flexible fixed angle = 20

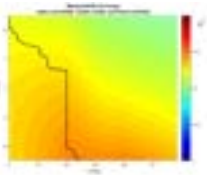

(d) Flexible fixed angle = 30

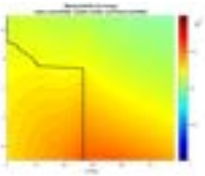

(e) Flexible fixed angle = 40

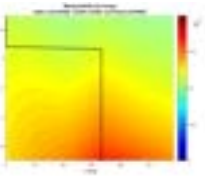

(f) Flexible fixed angle = 50

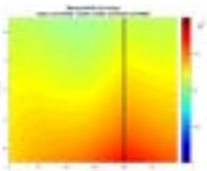

(g) Flexible fixed angle = 60

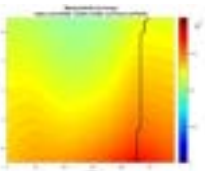

(h) Flexible fixed angle = 70

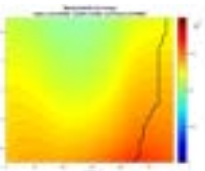

(i) Flexible fixed angle = 80

Figure B.7: (torque Manipulability) Mobile coil 5 and 6 for OctoMag-like configuration

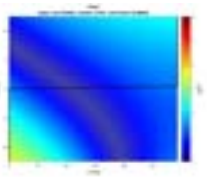

(a) Flexible fixed angle = 0

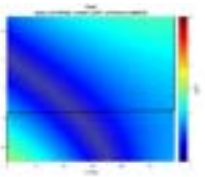

(b) Flexible fixed angle = 10

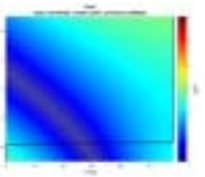

(c) Flexible fixed angle = 20

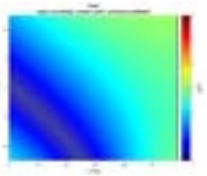

(d) Flexible fixed angle = 30

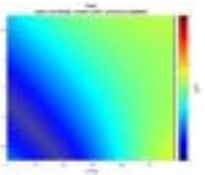

(e) Flexible fixed angle = 40

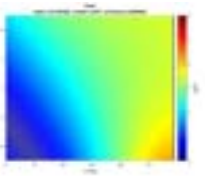

(f) Flexible fixed angle = 50

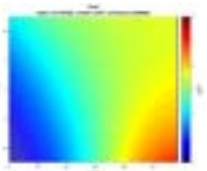

(g) Flexible fixed angle = 60

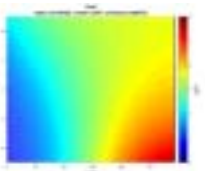

(h) Flexible fixed angle = 70

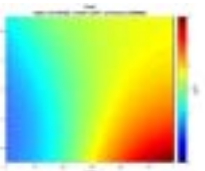

(i) Flexible fixed angle = 80

Figure B.8: Mobile coil 5 and 7 for OctoMag-like configuration

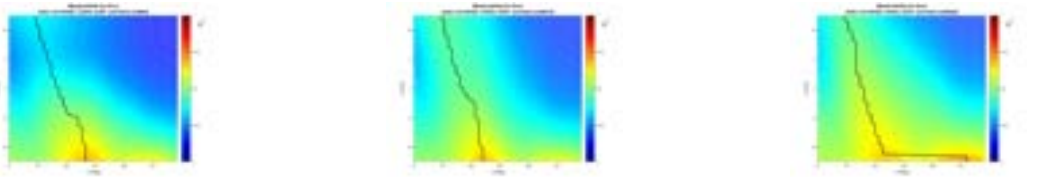

(a) Flexible fixed angle = 0 (b) Flexible fixed angle = 10 (c) Flexible fixed angle = 20

(d) Flexible fixed angle = 30 (e) Flexible fixed angle = 40 (f) Flexible fixed angle = 50

(g) Flexible fixed angle = 60 (h) Flexible fixed angle = 70 (i) Flexible fixed angle = 80

Figure B.9: (Force Manipulability) Mobile coil 5 and 7 for OctoMag-like configuration

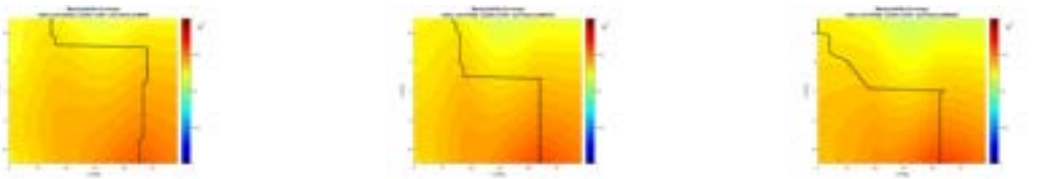

(a) Flexible fixed angle = 0 (b) Flexible fixed angle = 10 (c) Flexible fixed angle = 20

(d) Flexible fixed angle = 30 (e) Flexible fixed angle = 40 (f) Flexible fixed angle = 50

(g) Flexible fixed angle = 60 (h) Flexible fixed angle = 70 (i) Flexible fixed angle = 80

Figure B.10: (Torque Manipulability) Mobile coil 5 and 7 for OctoMag-like configuration

Table B.4: The OctoMag-like configuration(Mobile coils 5, 6 and 7).

	Angle	Coil 1	Coil 2	Coil 3	Coil 4	Coil 5	Coil 6	Coil 7	Coil 8
Case 1	α	45°	45°	45°	45°	0°	90°	0°	90°
	β	0°	0°	0°	0°	$[0; 90°)$	$[0; 90°)$	$[0; 90°)$	0°
Case 2	α	45°	45°	45°	45°	0°	90°	0°	90°
	β	0°	0°	0°	0°	$[0; 90°)$	$[0; 90°)$	$[0; 90°)$	10°
Case 3	α	45°	45°	45°	45°	0°	90°	0°	90°
	β	0°	0°	0°	0°	$[0; 90°)$	$[0; 90°)$	$[0; 90°)$	20°
Case 4	α	45°	45°	45°	45°	0°	90°	0°	90°
	β	0°	0°	0°	0°	$[0; 90°)$	$[0; 90°)$	$[0; 90°)$	30°
Case 5	α	45°	45°	45°	45°	0°	90°	0°	90°
	β	0°	0°	0°	0°	$[0; 90°)$	$[0; 90°)$	$[0; 90°)$	40°
Case 6	α	45°	45°	45°	45°	0°	90°	0°	90°
	β	0°	0°	0°	0°	$[0; 90°)$	$[0; 90°)$	$[0; 90°)$	50°
Case 7	α	45°	45°	45°	45°	0°	90°	0°	90°
	β	0°	0°	0°	0°	$[0; 90°)$	$[0; 90°)$	$[0; 90°)$	60°
Case 8	α	45°	45°	45°	45°	0°	90°	0°	90°
	β	0°	0°	0°	0°	$[0; 90°)$	$[0; 90°)$	$[0; 90°)$	70°
Case 9	α	45°	45°	45°	45°	0°	90°	0°	90°
	β	0°	0°	0°	0°	$[0; 90°)$	$[0; 90°)$	$[0; 90°)$	80°

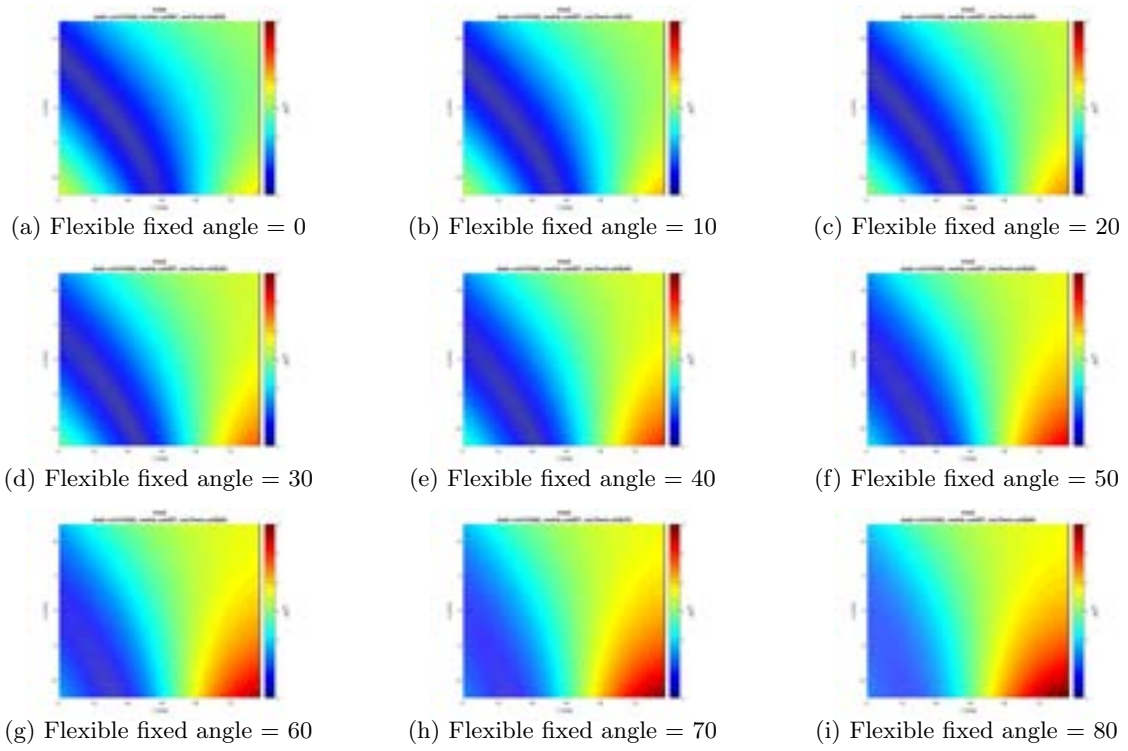

(a) Flexible fixed angle = 0 (b) Flexible fixed angle = 10 (c) Flexible fixed angle = 20

(d) Flexible fixed angle = 30 (e) Flexible fixed angle = 40 (f) Flexible fixed angle = 50

(g) Flexible fixed angle = 60 (h) Flexible fixed angle = 70 (i) Flexible fixed angle = 80

Figure B.11: Mobile coils 5, 6 and 7 for OctoMag-like configuration

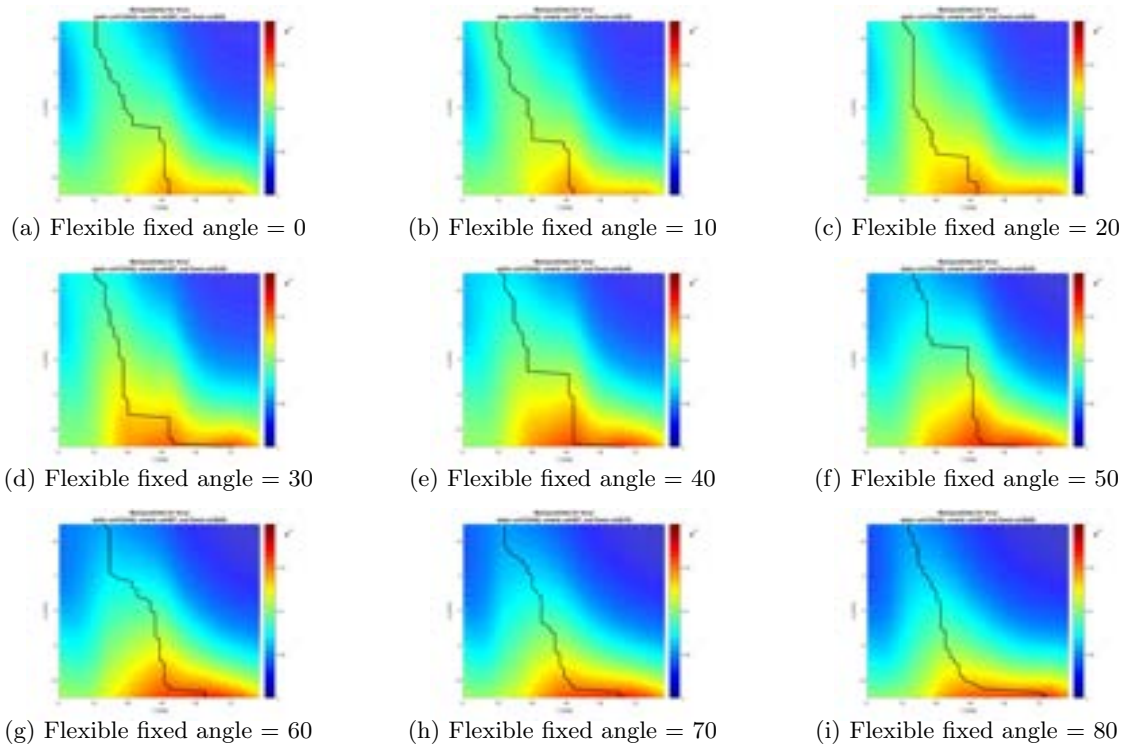

(a) Flexible fixed angle = 0 (b) Flexible fixed angle = 10 (c) Flexible fixed angle = 20

(d) Flexible fixed angle = 30 (e) Flexible fixed angle = 40 (f) Flexible fixed angle = 50

(g) Flexible fixed angle = 60 (h) Flexible fixed angle = 70 (i) Flexible fixed angle = 80

Figure B.12: (Force Manipulability) Mobile coils 5, 6 and 7 for OctoMag-like configuration

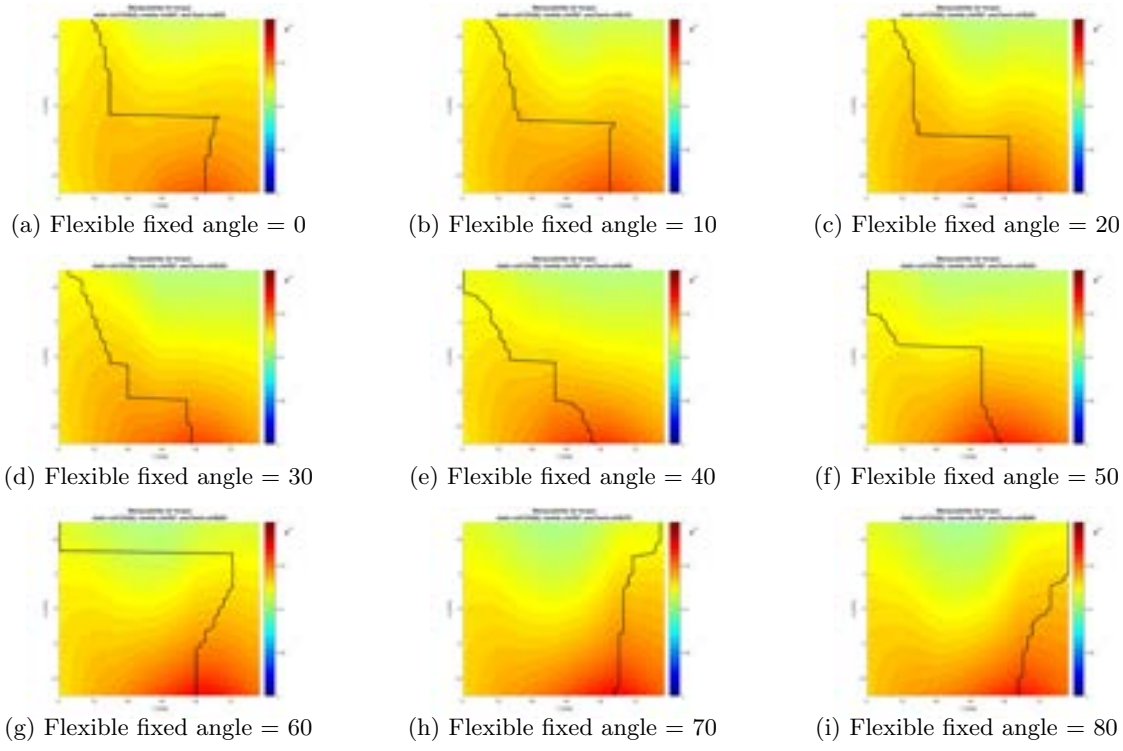

(a) Flexible fixed angle = 0 (b) Flexible fixed angle = 10 (c) Flexible fixed angle = 20

(d) Flexible fixed angle = 30 (e) Flexible fixed angle = 40 (f) Flexible fixed angle = 50

(g) Flexible fixed angle = 60 (h) Flexible fixed angle = 70 (i) Flexible fixed angle = 80

Figure B.13: (Torque Manipulability) Mobile coils 5, 6 and 7 for OctoMag-like configuration

Appendix C

The rotation and transformation matrices

C.1 Coordinate transformation

In robotics applications, many different coordinate systems can be used to define where robots, sensors, and other objects are located [186]. In general, the location of a body in 3D space can be specified by its position and orientation. There are multiple possible representations for these values, some of which are specific to certain applications.

Coordinate transformation is then a method of modeling the linkages and joints of a mechanism. Hence, a frame $\mathcal{F}_0$ is attached to each link of the robotic system. Then, homogeneous transformation is used to describe the spatial relationship between the two adjacent links. Through the sequential transformation, the pose (i.e. the position and orientation) of the end-effector relative to the reference frame $\mathcal{F}_0$ can be finally derived thereby to establish the kinematic equation of the robotic arm. Commonly, each joint of the robot can only achieve a form of motion, such as rotation or translation. Therefore, the mechanical arm joint is divided as either hinged or sliding joints. For the OctoRob EMA platform, currently, only[1] rotational motion of the robotic arm is defined. The designed electromagnetic coil is fixed on the end-effector of the robotic arm.

C.2 Definition of transformation matrices

The pose of the end-effector are obtained by Cartesian space transformation of the joints of the robotic arm. This pose of the end-effector relative to the reference $\mathcal{F}_0$ can be then computed by the given set of joint angles and links length. The direct geometric model of OctoRob robotic arm, recalled in figure C.1, includes here the following steps: First, the pose (C and F) of the fixed link is characterized in the reference $\mathcal{F}_0$. Second, the transformation matrix related to the active joint θ_1 is established. Thus, the offset angle (namely the Denavit–Hartenberg parameters) between two adjacent links should be determined. Third, the coordinate transformation can be defined by the product of each transformation matrices, including their rotation and the translation matrices. Last, the all transformation matrices are applied from the fixed pose to obtain the pose of the end-effector H in $\mathcal{F}_0$.

[1] The distance between the electromagnet and the workspace center is also affected by the rotation motion by motor.

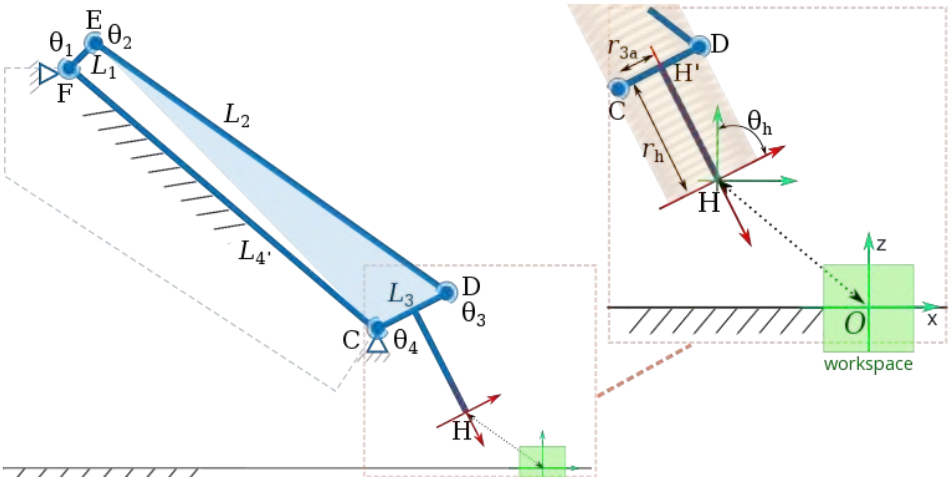

Figure C.1: Representation of the robotic arm kinematics chain with the four links L_1-L_4 and joints θ_1-θ_4.

Furthermore, the inverse geometric model means the calculation of the each joint angle θ_i of the robotic arm from the given pose of the end-effector described by Cartesian coordinate system. The inverse geometric model is actually multi-solvent, that is, a specific status of the end-effector can be achieved in various combinations of the robotic joint angles, and the solution of inverse geometric is usually difficult to determine.

Finally, the pose accuracy and repeated precision have been considered in the measure. The positioning accuracy is used as an indicator of ability for achieving a Cartesian coordinate system by the provided joint angle of robotic arm using the direct geometric model. Besides the repeatability precision presents the capability for manipulation of the end-effector in a given Cartesian coordinate system by using the inverse geometry. Usually, the repeatability precision of the robotic arm is great while the positioning accuracy is poor. Therefore, such effect of movement should be considered in the designing process of robotic arm.

C.2.1 Rotation matrix

The rotation matrix can be used to rotate the frame linked to an object in Euclidean space. The rotation matrix determines its sign by using right-hand rule, which is the positive sign produced by counterclockwise rotation along its axis. Let $\mathrm{Rot}_x(\theta)$ be a pure rotation about the axis x by an angle θ, that is basically defined as:

$$\mathrm{Rot}_x(\theta) = \begin{pmatrix} 1 & 0 & 0 \\ 0 & \cos(\theta) & -\sin(\theta) \\ 0 & \sin(\theta) & \cos(\theta) \end{pmatrix} \tag{C.1}$$

For 3D rotation transformation, it remains to define the pure rotation about the y and z-axis, and we get:

$$\mathrm{Rot}_y(\theta) = \begin{pmatrix} \cos(\theta) & 0 & \sin(\theta) \\ 0 & 1 & 0 \\ -\sin(\theta) & 0 & \cos(\theta) \end{pmatrix} \tag{C.2}$$

$$\mathrm{Rot}_z(\theta) = \begin{pmatrix} \cos(\theta) & -\sin(\theta) & 0 \\ \sin(\theta) & \cos(\theta) & 0 \\ 0 & 0 & 1 \end{pmatrix} \tag{C.3}$$

These basic rotation matrices can apply directly to the general rotations. In the 3D coordinate, the general rotation matrix can be obtained by the following equation:

$$\mathbf{R}(\alpha, \beta, \gamma) = \mathrm{Rot}_z(\alpha)\,\mathrm{Rot}_y(\beta)\,\mathrm{Rot}_x(\gamma) \tag{C.4}$$

where α, β and γ represents rotation yaw, pitch and roll angles about axes z, y and x, respectively.

Commonly, it is more convenient to define and utilize global rotation matrix $\mathbf{R}(\alpha, \beta, \gamma)$. For instance, when a vector $\mathbf{p}$ is rotated with a sole angle θ along a arbitrary vector, the following steps can be used for the computation to obtain the transformation matrix. Let consider the rotation of a vector given as $\mathbf{p} = [a_2 - a_1, b_2 - b_1, c_2 - c_1] = [a, b, c]$, that is illustrated in figure C.2a. In the figure C.2b, the rotation axis is translated to the origin coordinate o as step 1. The step 2 is the operation to rotate the rotation axis to the yoz-plane as shown in the figure C.2c. Then the axis of rotation is rotated to coincide with z-axis as step3 shown in the figure C.2d. After finishing the above three steps, the object is rotated with θ degree along z-axis. Furthermore, the reverse processes of step 3, step 2 and step 1 should be performed respectively to complete this rotation process.

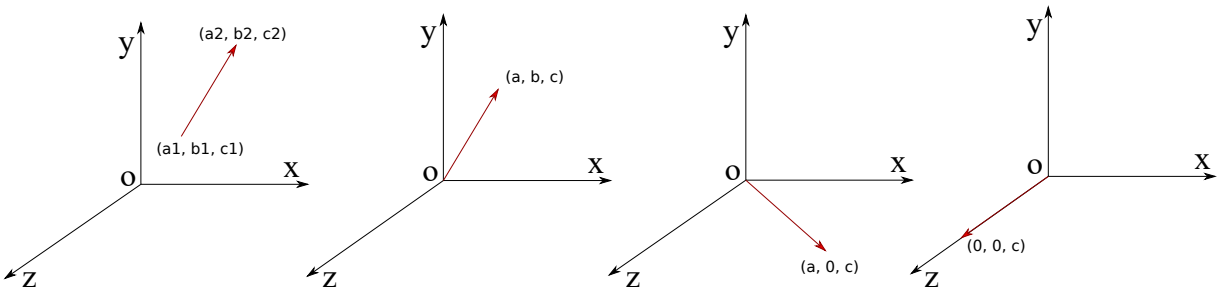

Figure C.2: Illustration of rotation step along a vector axis. A vector is referred as rotation axis in (a); (b): translate the rotation axis to origin coordinate; (c): rotate the rotation axis to yoz-plane; (d): rotate the rotation axis to coincide with z-axis. Then the object can be rotated angle θ along z-axis.

C.2.2 Transformation matrix of a pure translation

These operations can be expressed by the transformation matrix composed of translation matrix and rotation matrices. Transformation matrix of a pure translation is defined with homogeneous coordinate as:

$$\mathrm{Trans}(a, b, c) = \begin{pmatrix} 1 & 0 & 0 & a \\ 0 & 1 & 0 & b \\ 0 & 0 & 1 & c \\ 0 & 0 & 0 & 1 \end{pmatrix} \tag{C.5}$$

with a, b, and c the translation along the x, y and z axes respectively. We will also use the notation $\mathrm{Trans}_x(a)$ to denote the pure translation along the x-axis by a value a.

C.2.3 Homogeneous transformation matrices

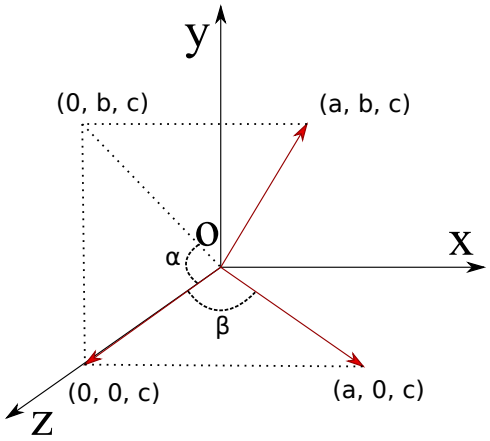

Figure C.3: The illustration of the angles between vector axis and coordinate axes.

Let $\mathbf{p} = [a, b, c]$ be a vector, as illustrated in the figure C.3. The rotation matrix $\mathrm{Rot}_x(\gamma)$ is defined for the rotational operation of the vector axis along the x-axis to the xOz-plane, that is:

$$\mathrm{Rot}_x(\theta)\,(\gamma) = \begin{pmatrix} 1 & 0 & 0 & 0 \\ 0 & \cos(\gamma) & -\sin(\gamma) & 0 \\ 0 & \sin(\gamma) & \cos(\gamma) & 0 \\ 0 & 0 & 0 & 1 \end{pmatrix} = \begin{pmatrix} 1 & 0 & 0 & 0 \\ 0 & \frac{c}{\sqrt{b^2+c^2}} & -\frac{b}{\sqrt{b^2+c^2}} & 0 \\ 0 & \frac{b}{\sqrt{b^2+c^2}} & \frac{c}{\sqrt{b^2+c^2}} & 0 \\ 0 & 0 & 0 & 1 \end{pmatrix} \tag{C.6}$$

The vector axis is then rotated along the y-axis to coincide with the z-axis on xOz-plane by the following rotation matrix:

$$\mathrm{Rot}_y(-\beta) = \begin{pmatrix} \cos(-\beta) & 0 & \sin(-\beta) & 0 \\ 0 & 1 & 0 & 0 \\ -\sin(-\beta) & 0 & \cos(-\beta) & 0 \\ 0 & 0 & 0 & 1 \end{pmatrix} = \begin{pmatrix} \frac{\sqrt{b^2+c^2}}{\sqrt{a^2+b^2+c^2}} & 0 & -\frac{a}{\sqrt{a^2+b^2+c^2}} & 0 \\ 0 & 1 & 0 & 0 \\ \frac{a}{\sqrt{a^2+b^2+c^2}} & 0 & \frac{\sqrt{b^2+c^2}}{\sqrt{a^2+b^2+c^2}} & 0 \\ 0 & 0 & 0 & 1 \end{pmatrix} \tag{C.7}$$

Let us note that the angle of rotation matrix is here negative due to vector axis is rotating clockwise around the y-axis. Finally, since the arbitrary rotation axis and z-axis coincide, the vector can be rotated with the angle α around the z-axis by applying:

$$\mathrm{Rot}_z(\alpha) = \begin{pmatrix} \cos(\alpha) & -\sin(\alpha) & 0 & 0 \\ \sin(\alpha) & \cos(\alpha) & 0 & 0 \\ 0 & 0 & 1 & 0 \\ 0 & 0 & 0 & 1 \end{pmatrix} \tag{C.8}$$

When rotation axis is connected to origin O, the rotational transformation matrix is computed from step 2, here, without translation. Wherefore the transformation matrix can be calculated as followings:

$$\mathbf{T}_{\mathrm{rot}} = \mathrm{Rot}_x(-\gamma)\,\mathrm{Rot}_y(\beta)\,\mathrm{Rot}_z(-\alpha)\,\mathrm{Rot}_x(\gamma) \tag{C.9}$$

where the matrix $\mathbf{T}$ should be used for left multiplication of the vector, that is $\mathbf{p}' = \mathbf{T}_{\text{rot}}\mathbf{p}$. The equations of each step are substituted into the eq. (C.9) to obtained the global transformation:

$$\mathbf{T}_{\text{rot}} = \begin{pmatrix} a^2 + \left(1 - a^2\right)\cos(\theta) & ab\,(1 - \cos(\theta)) - c\sin(\theta) & ac\,(1 - \cos(\theta)) + b\sin(\theta) & 0 \\ ab\,(1 - \cos(\theta)) + c\sin(\theta) & b^2 + \left(1 - b^2\right)\cos(\theta) & bc\,(1 - \cos(\theta)) - a\sin(\theta) & 0 \\ ac\,(1 - \cos(\theta)) - b\sin(\theta) & bc\,(1 - \cos(\theta)) + a\sin(\theta) & c^2 + \left(1 - c^2\right)\cos(\theta) & 0 \\ 0 & 0 & 0 & 1 \end{pmatrix} \tag{C.10}$$

If the vector $\mathbf{p}$ is not on the origin O of the frame, as in figure C.2a, the first translation and last reverse operation can not be omitted. The transformation matrice is consequently derived from:

$$\mathbf{T} = \text{Trans}\,(-a_1, -b_1, -c_1)\,\mathbf{T}_{\text{rot}}\,\text{Trans}\,(a_1, b_1, c_1) \tag{C.11}$$

where (a_1, b_1, c_1) denotes the origin of the vector $\mathbf{p}$. Therefore, the final transformation matrix is expressed as:

$$\mathbf{T} = \begin{pmatrix} a^2 + \mathfrak{bc}\cos(\theta) & ab\varsigma - c\sin(\theta) & ac\varsigma + b\sin(\theta) & (a_1\mathfrak{bc} - a\,(b_1 b + c_1 c))\,\varsigma + (b_1 c - c_1 b)\sin(\theta) \\ ab\varsigma + c\sin(\theta) & b^2 + \mathfrak{ac}\cos(\theta) & bc\varsigma - b\sin(\theta) & (b_1\mathfrak{ac} - b\,(a_1 a + c_1 c))\,\varsigma + (c_1 a - a_1 c)\sin(\theta) \\ ac\varsigma - b\sin(\theta) & bc\varsigma + a\sin(\theta) & c^2 + \mathfrak{ab}\cos(\theta) & (c_1\mathfrak{ab} - c\,(a_1 a + b_1 b))\,\varsigma + (a_1 b - b_1 a)\sin(\theta) \\ 0 & 0 & 0 & 1 \end{pmatrix} \tag{C.12}$$

with $\varsigma = (1 - \cos(\theta))$; $\mathfrak{ab} = \left(a^2 + b^2\right)$, $\mathfrak{ac} = \left(a^2 + c^2\right)$ and $\mathfrak{bc} = \left(b^2 + c^2\right)$.

The resulting homogeneous transformation matrix can be used to obtain the position and orientation of the electromagnets, for the mechanical design of the robotic arms as well.

References

[1] F. Tendick, S. S. Sastry, R. S. Fearing, and M. Cohn, "Applications of micromechatronics in minimally invasive surgery", *IEEE/ASME Transactions on Mechatronics*, vol. 3, no. 1, pp. 34–42, 1998.

[2] M. J. Mack, "Minimally invasive and robotic surgery", *Jama*, vol. 285, no. 5, pp. 568–572, 2001.

[3] M. C. Carrozza, P. Dario, and L. P. S. Jay, "Micromechatronics in surgery", *Transactions of the Institute of Measurement and Control*, vol. 25, no. 4, pp. 309–327, 2003.

[4] S. Purkayastha, T. Athanasiou, R. Casula, and S. A. Darzi, "Robotic surgery: A review", *Hospital Medicine*, vol. 65, no. 3, pp. 153–159, 2004.

[5] J. V. Joseph, M. Arya, and H. R. Patel, "Robotic surgery: The coming of a new era in surgical innovation", *Expert review of anticancer therapy*, vol. 5, no. 1, pp. 7–9, 2005.

[6] R. Bogue, "The development of medical microrobots: A review of progress", *Industrial Robot: An International Journal*, vol. 35, no. 4, pp. 294–299, 2008.

[7] I. A. Broeders and J. Ruurda, "Robotics revolutionizing surgery: The intuitive surgical "da vinci" system", *Industrial Robot: An International Journal*, vol. 28, no. 5, pp. 387–392, 2001.

[8] S. Tsuda, D. Oleynikov, J. Gould, D. Azagury, B. Sandler, M. Hutter, S. Ross, E. Haas, F. Brody, and R. Satava, "Sages tavac safety and effectiveness analysis: Da vinci® surgical system (intuitive surgical, sunnyvale, ca)", *Surgical endoscopy*, vol. 29, no. 10, pp. 2873–2884, 2015.

[9] S.-J. Baek and S.-H. Kim, "Robotics in general surgery: An evidence-based review", *Asian journal of endoscopic surgery*, vol. 7, no. 2, pp. 117–123, 2014.

[10] G. M. Grimsby, M. E. Dwyer, M. A. Jacobs, M. C. Ost, F. X. Schneck, G. M. Cannon, and P. C. Gargollo, "Multi-institutional review of outcomes of robot-assisted laparoscopic extravesical ureteral reimplantation", *The Journal of urology*, vol. 193, no. 5, pp. 1791–1795, 2015.

[11] L. Morelli, S. Guadagni, G. Di Franco, M. Palmeri, G. Di Candio, and F. Mosca, "Da vinci single site© surgical platform in clinical practice: A systematic review", *The International Journal of Medical Robotics and Computer Assisted Surgery*, vol. 12, no. 4, pp. 724–734, 2016.

[12] A. Ferreira, *The Encyclopedia of Medical Robotics*. World Scientific, 2018, vol. 2. DOI: 10.1142/10770-vol2.

[13] G.-Z. Yang, J. Bellingham, P. E. Dupont, P. Fischer, L. Floridi, R. Full, N. Jacobstein, V. Kumar, M. McNutt, R. Merrifield, *et al.*, "The grand challenges of science robotics", *Science Robotics*, vol. 3, no. 14, eaar7650, 2018.

[14] N. Simaan, R. M. Yasin, and L. Wang, "Medical technologies and challenges of robot-assisted minimally invasive intervention and diagnostics", *Annual Review of Control, Robotics, and Autonomous Systems*, vol. 1, pp. 465–490, 2018.

[15] F. Courreges, P. Vieyres, and G. Poisson, "Robotized tele-echography", in *Teleradiology*, Berlin, Heidelberg: Springer International Publishing, 2008, pp. 139–154, ISBN: 978-3-540-78871-3. DOI: 10.1007/978-3-540-78871-3_13.

[16] S. Kumar and E. Krupinski, *Teleradiology*. Springer Berlin Heidelberg, 2008, ISBN: 9783540788713. DOI: doi.org/10.1007.

[17] D. Rattner and A. Kalloo, "Asge/sages working group on natural orifice translumenal endoscopic surgery", *Surgical Endoscopy and Other Interventional Techniques*, vol. 20, no. 2, pp. 329–333, 2006.

[18] J. R. Romanelli and D. B. Earle, "Single-port laparoscopic surgery: An overview", *Surgical endoscopy*, vol. 23, no. 7, pp. 1419–1427, 2009.

[19] M. M. Tiwari, J. F. Reynoso, A. C. Lehman, A. W. Tsang, S. M. Farritor, and D. Oleynikov, "In vivo miniature robots for natural orifice surgery: State of the art and future perspectives", *World journal of gastrointestinal surgery*, vol. 2, no. 6, p. 217, 2010.

[20] D. Samarasekera and J. H. Kaouk, "Robotic single port surgery: Current status and future considerations", *Indian journal of urology: IJU: journal of the Urological Society of India*, vol. 30, no. 3, p. 326, 2014.

[21] S. U. Bae, W. K. Jeong, and S. K. Baek, "Current status of robotic single-port colonic surgery", *The International Journal of Medical Robotics and Computer Assisted Surgery*, vol. 13, no. 1, e1735, 2017.

[22] B. J. Nelson, I. K. Kaliakatsos, and J. J. Abbott, "Microrobots for minimally invasive medicine", *Annual review of biomedical engineering*, vol. 12, pp. 55–85, 2010.

[23] M. Sitti, "Miniature devices: Voyage of the microrobots", *Nature*, vol. 458, no. 7242, p. 1121, 2009.

[24] H. Ceylan, J. Giltinan, K. Kozielski, and M. Sitti, "Mobile microrobots for bioengineering applications", *Lab on a Chip*, vol. 17, no. 10, pp. 1705–1724, 2017. DOI: 10.1039/C7LC00064B.

[25] T Honda, K. Arai, and K Ishiyama, "Micro swimming mechanisms propelled by external magnetic fields", *IEEE Transactions on Magnetics*, vol. 32, no. 5, pp. 5085–5087, 1996.

[26] J. J. Abbott, K. E. Peyer, M. C. Lagomarsino, L. Zhang, L. Dong, I. K. Kaliakatsos, and B. J. Nelson, "How should microrobots swim?", *The international journal of Robotics Research*, vol. 28, no. 11-12, pp. 1434–1447, 2009.

[27] Y. Alapan, O. Yasa, O. Schauer, J. Giltinan, A. F. Tabak, V. Sourjik, and M. Sitti, "Soft erythrocyte-based bacterial microswimmers for cargo delivery", *Science Robotics*, vol. 3, no. 17, eaar4423, 2018.

[28] A. Barbot, D. Decanini, and G. Hwang, "The rotation of microrobot simplifies 3d control inside microchannels", *Scientific reports*, vol. 8, no. 1, p. 438, 2018.

[29] R. W. Carlsen, M. R. Edwards, J. Zhuang, C. Pacoret, and M. Sitti, "Magnetic steering control of multi-cellular bio-hybrid microswimmers", *Lab on a Chip*, vol. 14, no. 19, pp. 3850–3859, 2014. DOI: 10.1039/C4LC00707G.

[30] F. Carpi, N. Kastelein, M. Talcott, and C. Pappone, "Magnetically controllable gastrointestinal steering of video capsules", *IEEE Transactions on Biomedical Engineering*, vol. 58, no. 2, pp. 231–234, 2011.

[31] E. Diller, M. Sitti, *et al.*, "Micro-scale mobile robotics", *Foundations and Trends® in Robotics*, vol. 2, no. 3, pp. 143–259, 2013.

[32] A. Ghosh and P. Fischer, "Controlled propulsion of artificial magnetic nanostructured propellers", *Nano letters*, vol. 9, no. 6, pp. 2243–2245, 2009.

[33] A. Hosney, J. Abdalla, I. S. Amin, N. Hamdi, and I. S. Khalil, "In vitro validation of clearing clogged vessels using microrobots", in *IEEE International Conference on Biomedical Robotics and Biomechatronics (BioRob)*, IEEE, 2016, pp. 272–277.

[34] S. Jeon, S. Kim, S. Ha, S. Lee, E. Kim, S. Y. Kim, S. H. Park, J. H. Jeon, S. W. Kim, C. Moon, B. J. Nelson, J.-y. Kim, S.-W. Yu, and H. Choi, "Magnetically actuated microrobots as a platform for stem cell transplantation", *Science Robotics*, vol. 4, no. 30, eaav4317, 2019. DOI: 10.1126/scirobotics.aav4317.

[35] S. Kim, F. Qiu, S. Kim, A. Ghanbari, C. Moon, L. Zhang, B. J. Nelson, and H. Choi, "Fabrication and characterization of magnetic microrobots for three-dimensional cell culture and targeted transportation", *Advanced Materials*, vol. 25, no. 41, pp. 5863–5868, 2013.

[36] V. Du Nguyen, V. H. Le, S. Zheng, J. Han, and J.-O. Park, "Preparation of tumor targeting cell-based microrobots carrying nir light sensitive therapeutics manipulated by electromagnetic actuating system and chemotaxis", *Journal of Micro-Bio Robotics*, vol. 14, no. 3-4, pp. 69–77, 2018.

[37] S. Lee, S. Lee, S. Kim, C.-H. Yoon, H.-J. Park, J.-y. Kim, and H. Choi, "Fabrication and characterization of a magnetic drilling actuator for navigation in a three-dimensional phantom vascular network", *Scientific reports*, vol. 8, no. 1, p. 3691, 2018.

[38] J. Li, B. E.-F. de Ávila, W. Gao, L. Zhang, and J. Wang, "Micro/nanorobots for biomedicine: Delivery, surgery, sensing, and detoxification", *Sci. Robot*, vol. 2, no. 4, 2017.

[39] J. Li, X. Li, T. Luo, R. Wang, C. Liu, S. Chen, D. Li, J. Yue, S.-h. Cheng, and D Sun, "Development of a magnetic microrobot for carrying and delivering targeted cells", *Sci. Robot*, vol. 3, no. 19, 2018.

[40] S. Martel, "Microrobotics in the vascular network: Present status and next challenges", *Journal of Micro-Bio Robotics*, vol. 8, no. 1, pp. 41–52, 2013.

[41] B. Mitchell, J. Koo, I. Iordachita, P. Kazanzides, A. Kapoor, J. Handa, G. Hager, and R. Taylor, "Development and application of a new steady-hand manipulator for retinal surgery", in *IEEE International Conference on Robotics and Automation (ICRA)*, IEEE, 2007, pp. 623–629.

[42] S. Palagi and P. Fischer, "Bioinspired microrobots", *Nature Reviews Materials*, p. 1, 2018.

[43] S. Park, K. Cha, and J. Park, "Development of biomedical microrobot for intravascular therapy", *International Journal of Advanced Robotic Systems*, vol. 7, no. 1, p. 1, 2010.

[44] K. E. Peyer, L. Zhang, and B. J. Nelson, "Bio-inspired magnetic swimming microrobots for biomedical applications", *Nanoscale*, vol. 5, no. 4, pp. 1259–1272, 2013.

[45] F. Qiu and B. J. Nelson, "Magnetic helical micro-and nanorobots: Toward their biomedical applications", *Engineering*, vol. 1, no. 1, pp. 021–026, 2015.

[46] S. Schürle, B. E. Kratochvil, S. Pané, M. A. Zeeshan, and B. J. Nelson, "Generating magnetic fields for controlling nanorobots in medical applications", in *Nanorobotics*, Springer International Publishing, 2013, pp. 275–299.

[47] M. Sitti, H. Ceylan, W. Hu, J. Giltinan, M. Turan, S. Yim, and E. D. Diller, "Biomedical applications of untethered mobile milli/microrobots.", *Proceedings of the IEEE*, vol. 103, no. 2, pp. 205–224, 2015.

[48] H. Xie, M. Sun, X. Fan, Z. Lin, W. Chen, L. Wang, L. Dong, and Q. He, "Reconfigurable magnetic microrobot swarm: Multimode transformation, locomotion, and manipulation", *Science Robotics*, vol. 4, no. 28, eaav8006, 2019. DOI: 10.1126/scirobotics.aav8006.

[49] K. B. Yesin, P. Exner, K. Vollmers, and B. J. Nelson, "Design and control of in-vivo magnetic microrobots", in *International Conference on Medical Image Computing and Computer-Assisted Intervention*, Springer International Publishing, 2005, pp. 819–826.

[50] K. B. Yesin, K. Vollmers, and B. J. Nelson, "Modeling and control of untethered biomicrorobots in a fluidic environment using electromagnetic fields", *The International Journal of Robotics Research*, vol. 25, no. 5-6, pp. 527–536, 2006.

[51] E. B. Steager, M. Selman Sakar, C. Magee, M. Kennedy, A. Cowley, and V. Kumar, "Automated biomanipulation of single cells using magnetic microrobots", *The International Journal of Robotics Research*, vol. 32, no. 3, pp. 346–359, 2013.

[52] T. W. Fountain, P. V. Kailat, and J. J. Abbott, "Wireless control of magnetic helical microrobots using a rotating-permanent-magnet manipulator", in *IEEE International Conference on Robotics and Automation (ICRA)*, IEEE, 2010, pp. 576–581.

[53] N. A. Torres, S. Ruggeri, and D. O. Popa, "Untethered microrobots actuated with focused permanent magnet field", in *ASME 2014 International Design Engineering Technical Conferences and Computers and Information in Engineering Conference*, American Society of Mechanical Engineers, 2014, V004T09A024–V004T09A024.

[54] A. W. Mahoney and J. J. Abbott, "Five-degree-of-freedom manipulation of an untethered magnetic device in fluid using a single permanent magnet with application in stomach capsule endoscopy", *The International Journal of Robotics Research*, vol. 35, no. 1-3, pp. 129–147, 2016.

[55] G. Lucarini, G. Ciuti, M. Mura, R. Rizzo, and A. Menciassi, "A new concept for magnetic capsule colonoscopy based on an electromagnetic system", *International Journal of Advanced Robotic Systems*, vol. 12, no. 3, p. 25, 2015.

[56] P. Ryan and E. Diller, "Magnetic actuation for full dexterity microrobotic control using rotating permanent magnets", *IEEE Transactions on Robotics*, vol. 33, no. 6, pp. 1398–1409, 2017.

[57] W. Amokrane, K. Belharet, M. Souissi, A. B. Grayeli, and A. Ferreira, "Macro–micromanipulation platform for inner ear drug delivery", *Robotics and Autonomous Systems*, vol. 107, pp. 10–19, 2018.

[58] S. Schuerle, S. Erni, M. Flink, B. E. Kratochvil, and B. J. Nelson, "Three-dimensional magnetic manipulation of micro-and nanostructures for applications in life sciences", *IEEE Transactions on Magnetics*, vol. 49, no. 1, pp. 321–330, 2013. DOI: 10.1109/TMAG.2012.2224693.

[59] S. Martel, J.-B. Mathieu, O. Felfoul, A. Chanu, E. Aboussouan, S. Tamaz, P. Pouponneau, L. Yahia, G. Beaudoin, G. Soulez, *et al.*, "Automatic navigation of an untethered device in the artery of a living animal using a conventional clinical magnetic resonance imaging system", *Applied physics letters*, vol. 90, no. 11, p. 114 105, 2007.

[60] M. P. Kummer, J. J. Abbott, B. E. Kratochvil, R. Borer, A. Sengul, and B. J. Nelson, "Octomag: An electromagnetic system for 5-dof wireless micromanipulation", *IEEE Transactions on Robotics*, vol. 26, no. 6, pp. 1006–1017, 2010.

[61] B. E. Kratochvil, M. P. Kummer, S. Erni, R. Borer, D. R. Frutiger, S. Schürle, and B. J. Nelson, "Minimag: A hemispherical electromagnetic system for 5-dof wireless micromanipulation", in *Experimental Robotics*, Springer International Publishing, 2014, pp. 317–329.

[62] S. Jeong, H. Choi, J. Choi, C. Yu, J.-o. Park, and S. Park, "Novel electromagnetic actuation (ema) method for 3-dimensional locomotion of intravascular microrobot", *Sensors and Actuators A: Physical*, vol. 157, no. 1, pp. 118–125, 2010.

[63] S. Jeon, G. Jang, H. Choi, and S. Park, "Magnetic navigation system with gradient and uniform saddle coils for the wireless manipulation of micro-robots in human blood vessels", *IEEE Transactions on Magnetics*, vol. 46, no. 6, pp. 1943–1946, 2010.

[64] S. Jeon, G. Jang, H. Choi, S. Park, and J. Park, "Magnetic navigation system for the precise helical and translational motions of a microrobot in human blood vessels", *Journal of Applied Physics*, vol. 111, no. 7, 07E702, 2012.

[65] H. Choi, J. Choi, S. Jeong, C. Yu, J.-o. Park, and S. Park, "Two-dimensional locomotion of a microrobot with a novel stationary electromagnetic actuation system", *Smart Materials and Structures*, vol. 18, no. 11, p. 115 017, 2009.

[66] H. Choi, J. Choi, G. Jang, J.-o. Park, and S. Park, "Two-dimensional actuation of a microrobot with a stationary two-pair coil system", *Smart Materials and Structures*, vol. 18, no. 5, p. 055 007, 2009.

[67] J. Choi, S. Jeong, K. Cha, L. Qin, J. Li, J. Park, and S. Park, "Positioning of microrobot in a pulsating flow using ema system", in *IEEE RAS & EMBS International Conference on Biomedical Robotics and Biomechatronics*, IEEE, 2010, pp. 588–593.

[68] H. Choi, K. Cha, J. Choi, S. Jeong, S. Jeon, G. Jang, J.-o. Park, and S. Park, "Ema system with gradient and uniform saddle coils for 3d locomotion of microrobot", *Sensors and Actuators A: Physical*, vol. 163, no. 1, pp. 410–417, 2010.

[69] H. Choi, K. Cha, S. Jeong, J.-o. Park, and S. Park, "3-d locomotive and drilling microrobot using novel stationary ema system", *IEEE/ASME Transactions on Mechatronics*, vol. 18, no. 3, pp. 1221–1225, 2012.

[70] H. Choi, J.-O. Park, and S. Park, "Electromagnetic actuated micro- and nanorobots", in *The Encyclopedia of Medical Robotics*. World Scientific, 2018, vol. 2, ch. 6, pp. 113–135. DOI: 10.1142/9789813232280_0006.

[71] G. Go, H. Choi, S. Jeong, C. Lee, B. J. Park, S. Y. Ko, J.-O. Park, and S. Park, "Position-based magnetic field control for an electromagnetic actuated microrobot system", *Sensors and Actuators A: Physical*, vol. 205, pp. 215–223, 2014.

[72] G. Go, H. Choi, S. Jeong, C. Lee, S. Y. Ko, J.-O. Park, and S. Park, "Electromagnetic navigation system using simple coil structure (4 coils) for 3-d locomotive microrobot", *IEEE Transactions on Magnetics*, vol. 51, no. 4, pp. 1–7, 2015.

[73] E. Diller, J. Giltinan, P. Jena, and M. Sitti, "Three dimensional independent control of multiple magnetic microrobots", in *IEEE International Conference on Robotics and Automation (ICRA)*, IEEE, 2013, pp. 2576–2581.

[74] E. Diller, J. Giltinan, G. Z. Lum, Z. Ye, and M. Sitti, "Six-degree-of-freedom magnetic actuation for wireless microrobotics", *The International Journal of Robotics Research*, vol. 35, no. 1-3, pp. 114–128, 2016.

[75] M. Dadkhah, N. Kumar, and J. Yoon, "Design and simulation of a 3d actuation system for magnetic nano-particles delivery system", in *International Conference on Intelligent Robotics and Applications*, Springer International Publishing, 2013, pp. 177–187.

[76] Q. Fu, S. Guo, Q. Huang, H. Hirata, and H. Ishihara, "Development and evaluation of novel magnetic actuated microrobot with spiral motion using electromagnetic actuation system", *Journal of Medical and Biological Engineering*, vol. 36, no. 4, pp. 506–514, 2016.

[77] M. D. Tehrani, M. O. Kim, and J. Yoon, "A novel electromagnetic actuation system for magnetic nanoparticle guidance in blood vessels", *IEEE Transactions on Magnetics*, vol. 50, no. 7, pp. 1–12, 2014.

[78] C. Yu, J. Kim, H. Choi, J. Choi, S. Jeong, K. Cha, J.-o. Park, and S. Park, "Novel electromagnetic actuation system for three-dimensional locomotion and drilling of intravascular microrobot", *Sensors and Actuators A: Physical*, vol. 161, no. 1-2, pp. 297–304, 2010.

[79] J. J. Abbott, E. Diller, and A. J. Petruska, "Magnetic methods in robotics", *Annual Review of Control, Robotics, and Autonomous Systems*, vol. 3, 2015.

[80] S. Miyashita, S. Guitron, K. Yoshida, S. Li, D. D. Damian, and D. Rus, "Ingestible, controllable, and degradable origami robot for patching stomach wounds", in *IEEE International Conference on Robotics and Automation (ICRA)*, IEEE, 2016, pp. 909–916.

[81] G. L. Spaeth, H. Danesh-Meyer, I. Goldberg, and A. Kampik, *Ophthalmic Surgery: Principles and Practice E-Book*. Elsevier Health Sciences, 2011.

[82] D Flieger, R Keller, A May, C Ell, and W Fischbach, "Capsule endoscopy in gastrointestinal lymphomas", *Endoscopy*, vol. 37, no. 12, pp. 1174–1180, 2005.

[83] A. Moglia, A. Menciassi, M. O. Schurr, and P. Dario, "Wireless capsule endoscopy: From diagnostic devices to multipurpose robotic systems", *Biomedical microdevices*, vol. 9, no. 2, pp. 235–243, 2007.

[84] S. Fatikow and U. Rembold, *Microsystem technology and microrobotics*. Berlin Heidelberg: Springer-Verlag, 1997, ISBN: 978-3-662-03450-7. DOI: 10.1007/978-3-662-03450-7.

[85] T. Fukuda, F. Arai, and M. Nakajima, *Micro-nanorobotic manipulation systems and their applications*. Berlin Heidelberg: Springer International Publishing, 2013, ISBN: 9783642363917. DOI: 10.1007/978-3-642-36391-7.

[86] M. Sitti, *Mobile Microrobotics*, ser. Intelligent Robotics and Autonomous Agents. MIT Press, Jun. 2017, ISBN: 9780262036436.

[87] E. M. Purcell, "Life at low reynolds number", *American journal of physics*, vol. 45, no. 1, pp. 3–11, 1977.

[88] A. Vikram Singh and M. Sitti, "Targeted drug delivery and imaging using mobile milli/microrobots: A promising future towards theranostic pharmaceutical design", *Current pharmaceutical design*, vol. 22, no. 11, pp. 1418–1428, 2016.

[89] G. Dogangil, O. Ergeneman, J. J. Abbott, S. Pané, H. Hall, S. Muntwyler, and B. J. Nelson, "Toward targeted retinal drug delivery with wireless magnetic microrobots", in *IEEE/RSJ International Conference on Intelligent Robots and Systems (IROS)*, IEEE, 2008, pp. 1921–1926.

[90] S. Fusco, M. S. Sakar, S. Kennedy, C. Peters, R. Bottani, F. Starsich, A. Mao, G. A. Sotiriou, S. Pané, S. E. Pratsinis, *et al.*, "An integrated microrobotic platform for on-demand, targeted therapeutic interventions", *Advanced Materials*, vol. 26, no. 6, pp. 952–957, 2014.

[91] P. M. Devlin, *Brachytherapy: applications and techniques*. Berlin Heidelberg: Springer International Publishing, 2015.

[92] E. Gultepe, J. S. Randhawa, S. Kadam, S. Yamanaka, F. M. Selaru, E. J. Shin, A. N. Kalloo, and D. H. Gracias, "Biopsy with thermally-responsive untethered microtools", *Advanced materials*, vol. 25, no. 4, pp. 514–519, 2013.

[93] H. Zhang, D. W. Hutmacher, F. Chollet, A. N. Poo, and E. Burdet, "Microrobotics and mems-based fabrication techniques for scaffold-based tissue engineering", *Macromolecular bioscience*, vol. 5, no. 6, pp. 477–489, 2005.

[94] H.-E. Schaefer, "Nanomedicine", in *Nanoscience*, Springer International Publishing, 2010, pp. 615–735.

[95] F. Qiu, L. Zhang, S. Tottori, K. Marquardt, K. Krawczyk, A. Franco-Obregón, and B. J. Nelson, "Bio-inspired microrobots", *Materials Today*, vol. 15, no. 10, p. 463, 2012.

[96] J. Cui, Y. Wei, and H. Wang, "The study of a telemetry robot for gastrointestinal tract", in *ICMIT 2007: Mechatronics, MEMS, and Smart Materials*, International Society for Optics and Photonics, vol. 6794, 2008, 67943G.

[97] D. Jiles, *Introduction to magnetism and magnetic materials*, 3rd ed. CRC press, 2015, ISBN: 9781482238884.

[98] R. Dreyfus, J. Baudry, M. L. Roper, M. Fermigier, H. A. Stone, and J. Bibette, "Microscopic artificial swimmers", *Nature*, vol. 437, no. 7060, p. 862, 2005.

[99] A. A. Solovev, Y. Mei, E. Bermúdez Ureña, G. Huang, and O. G. Schmidt, "Catalytic microtubular jet engines self-propelled by accumulated gas bubbles", *Small*, vol. 5, no. 14, pp. 1688–1692, 2009.

[100] L. Zhang, J. J. Abbott, L. Dong, K. E. Peyer, B. E. Kratochvil, H. Zhang, C. Bergeles, and B. J. Nelson, "Characterizing the swimming properties of artificial bacterial flagella", *Nano letters*, vol. 9, no. 10, pp. 3663–3667, 2009.

[101] J. Wang and W. Gao, "Nano/microscale motors: Biomedical opportunities and challenges", *ACS nano*, vol. 6, no. 7, pp. 5745–5751, 2012.

[102] B. J. Williams, S. V. Anand, J. Rajagopalan, and M. T. A. Saif, "A self-propelled biohybrid swimmer at low reynolds number", *Nature communications*, vol. 5, p. 3081, 2014.

[103] D. Yamamoto, A. Mukai, N. Okita, K. Yoshikawa, and A. Shioi, "Catalytic micromotor generating self-propelled regular motion through random fluctuation", *The Journal of chemical physics*, vol. 139, no. 3, p. 034 705, 2013.

[104] G. Zhao, M. Viehrig, and M. Pumera, "Challenges of the movement of catalytic micromotors in blood", *Lab on a Chip*, vol. 13, no. 10, pp. 1930–1936, 2013.

[105] G. Hwang, R. Braive, L. Couraud, A. Cavanna, O. Abdelkarim, I. Robert-Philip, A. Beveratos, I. Sagnes, S. Haliyo, and S. Régnier, "Electro-osmotic propulsion of helical nanobelt swimmers", *The International Journal of Robotics Research*, vol. 30, no. 7, pp. 806–819, 2011.

[106] A. Yamazaki, M. Sendoh, K. Ishiyama, K. I. Arai, R. Kato, M. Nakano, and H. Fukunaga, "Wireless micro swimming machine with magnetic thin film", *Journal of Magnetism and Magnetic Materials*, vol. 272, E1741–E1742, 2004.

[107] D. Hyung Kim, P. Seung Soo Kim, A. Agung Julius, and M. Jun Kim, "Three-dimensional control of tetrahymena pyriformis using artificial magnetotaxis", *Applied Physics Letters*, vol. 100, no. 5, p. 053 702, 2012.

[108] V. Magdanz, S. Sanchez, and O. G. Schmidt, "Development of a sperm-flagella driven micro-bio-robot", *Advanced Materials*, vol. 25, no. 45, pp. 6581–6588, 2013.

[109] D. H. Kim, P. S. S. Kim, A. A. Julius, and M. J. Kim, "Three-dimensional control of engineered motile cellular microrobots", in *IEEE International Conference on Robotics and Automation (ICRA)*, IEEE, 2012, pp. 721–726.

[110] M. Stanton, C Trichet-Paredes, and S. Sanchez, "Applications of three-dimensional (3d) printing for microswimmers and bio-hybrid robotics", *Lab on a Chip*, vol. 15, no. 7, pp. 1634–1637, 2015.

[111] S Sudo, S Segawa, and T Honda, "Magnetic swimming mechanism in a viscous liquid", *Journal of intelligent material systems and structures*, vol. 17, no. 8-9, pp. 729–736, 2006.

[112] S. Jeong, H. Choi, K. Cha, J. Li, J.-o. Park, and S. Park, "Enhanced locomotive and drilling microrobot using precessional and gradient magnetic field", *Sensors and Actuators A: Physical*, vol. 171, no. 2, pp. 429–435, 2011.

[113] L. Zhang, J. J. Abbott, L. Dong, B. E. Kratochvil, D. Bell, and B. J. Nelson, "Artificial bacterial flagella: Fabrication and magnetic control", *Applied Physics Letters*, vol. 94, no. 6, p. 064 107, 2009.

[114] L. Zhang, K. E. Peyer, and B. J. Nelson, "Artificial bacterial flagella for micromanipulation", *Lab on a Chip*, vol. 10, no. 17, pp. 2203–2215, 2010.

[115] K. E. Peyer, S. Tottori, F. Qiu, L. Zhang, and B. J. Nelson, "Magnetic helical micromachines", *Chemistry–A European Journal*, vol. 19, no. 1, pp. 28–38, 2013.

[116] S. Tottori, L. Zhang, F. Qiu, K. K. Krawczyk, A. Franco-Obregón, and B. J. Nelson, "Magnetic helical micromachines: Fabrication, controlled swimming, and cargo transport", *Advanced materials*, vol. 24, no. 6, pp. 811–816, 2012.

[117] Z. Wu, J. Troll, H.-H. Jeong, Q. Wei, M. Stang, F. Ziemssen, Z. Wang, M. Dong, S. Schnichels, T. Qiu, *et al.*, "A swarm of slippery micropropellers penetrates the vitreous body of the eye", *Science advances*, vol. 4, no. 11, eaat4388, 2018.

[118] A. W. Mahoney, J. C. Sarrazin, E. Bamberg, and J. J. Abbott, "Velocity control with gravity compensation for magnetic helical microswimmers", *Advanced Robotics*, vol. 25, no. 8, pp. 1007–1028, 2011.

[119] B. J. Nelson and K. E. Peyer, "Micro-and nanorobots swimming in heterogeneous liquids", *Acs Nano*, vol. 8, no. 9, pp. 8718–8724, 2014.

[120] O. G. Schmidt and K. Eberl, "Nanotechnology: Thin solid films roll up into nanotubes", *Nature*, vol. 410, no. 6825, p. 168, 2001.

[121] O. Schmidt, N Schmarje, C. Deneke, C Müller, and N.-Y. Jin-Phillipp, "Three-dimensional nano-objects evolving from a two-dimensional layer technology", *Advanced Materials*, vol. 13, no. 10, pp. 756–759, 2001.

[122] G. Huang and Y. Mei, "Helices in micro-world: Materials, properties, and applications", *Journal of Materiomics*, vol. 1, no. 4, pp. 296–306, 2015.

[123] A. Servant, F. Qiu, M. Mazza, K. Kostarelos, and B. J. Nelson, "Controlled in vivo swimming of a swarm of bacteria-like microrobotic flagella", *Advanced Materials*, vol. 27, no. 19, pp. 2981–2988, 2015.

[124] M. Sendoh, K. Ishiyama, and K.-I. Arai, "Fabrication of magnetic actuator for use in a capsule endoscope", *IEEE Transactions on Magnetics*, vol. 39, no. 5, pp. 3232–3234, 2003.

[125] W. Ma, J. Li, F. Niu, H. Ji, and D. Sun, "Robust control to manipulate a microparticle with electromagnetic coil system", *IEEE Transactions on Industrial Electronics*, vol. 64, no. 11, pp. 8566–8577, 2017.

[126] Y. Ko, S. Na, Y. Lee, K. Cha, S. Y. Ko, J. Park, and S. Park, "A jellyfish-like swimming mini-robot actuated by an electromagnetic actuation system", *Smart Materials and Structures*, vol. 21, no. 5, p. 057 001, 2012.

[127] J.-B. Mathieu, S. Martel, L Yahia, G. Soulez, and G. Beaudoin, "Preliminary studies for using magnetic resonance imaging systems as a mean of propulsion for microrobots in blood vessels and evaluation of ferromagnetic artefacts", in *Canadian Conference on Electrical and Computer Engineering. Toward a Caring and Humane Technology*, IEEE, vol. 2, 2003, pp. 835–838.

[128] S Martel, J.-B. Mathieu, O Felfoul, H Macicior, G Beaudoin, G Soulez, and L. Yahia, "Adapting mri systems to propel and guide microdevices in the human blood circulatory system", in *Annual International Conference of the IEEE Engineering in Medicine and Biology Society*, IEEE, vol. 1, 2004, pp. 1044–1047.

[129] A. Bigot, C. Tremblay, G. Soulez, and S. Martel, "Magnetic resonance navigation of a bead inside a three-bifurcation pmma phantom using an imaging gradient coil insert", *IEEE Transactions on Robotics*, vol. 30, no. 3, pp. 719–727, 2014.

[130] B. Véron, A. Hubert, J. Abadie, and N. Andreff, "Geometric analysis of the singularities of a magnetic manipulation system with several mobile coils", in *IEEE/RSJ International Conference on Intelligent Robots and Systems (IROS)*, IEEE, 2013, pp. 4996–5001.

[131] L. Yang, X. Du, E. Yu, D. Jin, and L. Zhang, "Deltamag: An electromagnetic manipulation system with parallel mobile coils", in *International Conference on Robotics and Automation (ICRA)*, IEEE, 2019, pp. 9814–9820.

[132] S. Tamaz, R. Gourdeau, A. Chanu, J.-B. Mathieu, and S. Martel, "Real-time mri-based control of a ferromagnetic core for endovascular navigation", *IEEE Transactions on Biomedical Engineering*, vol. 55, no. 7, pp. 1854–1863, 2008.

[133] S. Floyd, C. Pawashe, and M. Sitti, "Microparticle manipulation using multiple untethered magnetic micro-robots on an electrostatic surface", in *IEEE/RSJ International Conference on Intelligent Robots and Systems (IROS)*, IEEE, 2009, pp. 528–533.

[134] G. Go, H. Choi, C. Lee, S. Y. Ko, J.-O. Park, and S. Park, "A multiple microrobot system with thermally responsive microclampers", in *IEEE International Conference on Biomedical Robotics and Biomechatronics (BioRob)*, IEEE, 2016, pp. 1186–1191.

[135] G. Go, H. Choi, S. Jeong, S. Y. Ko, J.-O. Park, and S. Park, "Selective microrobot control using a thermally responsive microclamper for microparticle manipulation", *Smart Materials and Structures*, vol. 25, no. 3, p. 035 004, 2016.

[136] E. Diller, S. Floyd, C. Pawashe, and M. Sitti, "Control of multiple heterogeneous magnetic microrobots in two dimensions on nonspecialized surfaces", *IEEE Transactions on Robotics*, vol. 28, no. 1, pp. 172–182, 2011.

[137] E. Diller, J. Giltinan, and M. Sitti, "Independent control of multiple magnetic microrobots in three dimensions", *The International Journal of Robotics Research*, vol. 32, no. 5, pp. 614–631, 2013.

[138] C. Elbuken, M. B. Khamesee, and M. Yavuz, "Design and implementation of a micromanipulation system using a magnetically levitated mems robot", *IEEE/ASME Transactions on Mechatronics*, vol. 14, no. 4, pp. 434–445, 2009.

[139] M. B. Khamesee, N. Kato, Y. Nomura, and T. Nakamura, "Design and control of a microrobotic system using magnetic levitation", *IEEE/ASME Transactions on Mechatronics*, vol. 7, no. 1, pp. 1–14, 2002.

[140] D. C. Meeker, E. H. Maslen, R. C. Ritter, and F. M. Creighton, "Optimal realization of arbitrary forces in a magnetic stereotaxis system", *IEEE Transactions on Magnetics*, vol. 32, no. 2, pp. 320–328, 1996.

[141] F. Ongaro, S. Pane, S. Scheggi, and S. Misra, "Design of an electromagnetic setup for independent three-dimensional control of pairs of identical and nonidentical microrobots", *IEEE Transactions on Robotics*, vol. 35, no. 1, pp. 174–183, 2018.

[142] S. Floyd, C. Pawashe, and M. Sitti, "Two-dimensional contact and noncontact micromanipulation in liquid using an untethered mobile magnetic microrobot", *IEEE Transactions on Robotics*, vol. 25, no. 6, pp. 1332–1342, 2009.

[143] D. R. Frutiger, K. Vollmers, B. E. Kratochvil, and B. J. Nelson, "Small, fast, and under control: Wireless resonant magnetic micro-agents", *The International Journal of Robotics Research*, vol. 29, no. 5, pp. 613–636, 2010.

[144] A. W. Mahoney and J. J. Abbott, "Managing magnetic force applied to a magnetic device by a rotating dipole field", *Applied Physics Letters*, vol. 99, no. 13, p. 134 103, 2011.

[145] S. Erni, S. Schürle, A. Fakhraee, B. E. Kratochvil, and B. J. Nelson, "Comparison, optimization, and limitations of magnetic manipulation systems", *Journal of Micro-Bio Robotics*, vol. 8, no. 3-4, pp. 107–120, 2013.

[146] E. P. Furlani, *Permanent magnet and electromechanical devices: materials, analysis, and applications*. Academic press, 2001, 540 pp., ISBN: 978-0-12-269951-1. DOI: 10.1016/B978-0-12-269951-1.X5000-1.

[147] M. P. Kummer, "5-dof wireless micromanipulation using soft-magnetic core electromagnets", PhD thesis, ETH Zurich, 2010.

[148] D. J. Griffiths, *Introduction to electrodynamics*. Cambridge University Press, 2017, vol. 2.

[149] A. J. Petruska and B. J. Nelson, "Minimum bounds on the number of electromagnets required for remote magnetic manipulation", *IEEE Transactions on Robotics*, vol. 31, no. 3, pp. 714–722, 2015.

[150] K Ishiyama, K. Arai, M Sendoh, and A Yamazaki, "Spiral-type micro-machine for medical applications", in *International Symposium on Micromechatronics and Human Science*, IEEE, 2000, pp. 65–69.

[151] M. N. Faddis, W. Blume, J. Finney, A. Hall, J. Rauch, J. Sell, K. T. Bae, M. Talcott, and B. Lindsay, "Novel, magnetically guided catheter for endocardial mapping and radiofrequency catheter ablation", *Circulation*, vol. 106, no. 23, pp. 2980–2985, 2002.

[152] T. Roberts, W. Hassenzahl, S. Hetts, and R. Arenson, "Remote control of catheter tip deflection: An opportunity for interventional mri", *Magnetic Resonance in Medicine: An Official Journal of the International Society for Magnetic Resonance in Medicine*, vol. 48, no. 6, pp. 1091–1095, 2002.

[153] Z. Nagy and B. J. Nelson, "Lagrangian modeling of the magnetization and the magnetic torque on assembled soft-magnetic mems devices for fast computation and analysis", *IEEE Transactions on Robotics*, vol. 28, no. 4, pp. 787–797, 2012.

[154] D. Wong, E. B. Steager, and V. Kumar, "Independent control of identical magnetic robots in a plane", *IEEE Robotics and Automation Letters*, vol. 1, no. 1, pp. 554–561, 2016.

[155] M. Etiévant, A. Bolopion, S. Régnier, and N. Andreff, "An improved control-oriented modeling of the magnetic field", in *International Conference on Robotics and Automation (ICRA)*, IEEE, 2019, pp. 6178–6184.

[156] X. Jing and W. Guo, "Modeling and configuration design of electromagnetic actuation coil for a magnetically controlled microrobot", *Chinese Journal of Mechanical Engineering*, vol. 32, no. 1, p. 63, 2019.

[157] J. K. Salisbury and J. J. Craig, "Articulated hands: Force control and kinematic issues", *The International journal of Robotics research*, vol. 1, no. 1, pp. 4–17, 1982.

[158] T. Yoshikawa, "Manipulability of robotic mechanisms", *The international journal of Robotics Research*, vol. 4, no. 2, pp. 3–9, 1985.

[159] S. Kucuk and Z. Bingul, "Comparative study of performance indices for fundamental robot manipulators", *Robotics and Autonomous Systems*, vol. 54, no. 7, pp. 567–573, 2006.

[160] J.-P. Merlet, "Jacobian, manipulability, condition number, and accuracy of parallel robots", *Journal of Mechanical Design*, vol. 128, no. 1, pp. 199–206, 2006.

[161] B. Véron, A. Hubert, J. Abadie, and N. Andreff, "Dealing with redundancy of a multiple mobile coil magnetic manipulator: A 3rpr magnetic parallel kinematics manipulator", in *Advances in Robot Kinematics 2016*, Springer, 2018, pp. 201–208.

[162] R. S. Snell and M. A. Lemp, *Clinical anatomy of the eye*. John Wiley & Sons, 2013.

[163] W. M. Tang and D. P. Han, "A study of surgical approaches to retinal vascular occlusions", *Archives of Ophthalmology*, vol. 118, no. 1, pp. 138–143, 2000.

[164] H Shahid, P Hossain, and W. Amoaku, "The management of retinal vein occlusion: Is interventional ophthalmology the way forward?", *British Journal of Ophthalmology*, vol. 90, no. 5, pp. 627–639, 2006.

[165] P. K. Gupta, P. S. Jensen, and E. de Juan, "Surgical forces and tactile perception during retinal microsurgery", in *International conference on medical image computing and computer-assisted intervention*, Springer International Publishing, 1999, pp. 1218–1225.

[166] A. D. Jagtap and C. N. Riviere, "Applied force during vitreoretinal microsurgery with handheld instruments", in *Annual International Conference of the IEEE Engineering in Medicine and Biology Society*, IEEE, vol. 1, 2004, pp. 2771–2773.

[167] S. Singhy and C. Riviere, "Physiological tremor amplitude during retinal microsurgery", in *IEEE Annual Northeast Bioengineering Conference*, IEEE, 2002, pp. 171–172.

[168] T. A. Meredith, *Atlas of retinal and vitreous surgery*. Mosby Incorporated, 1999.

[169] H. F. Fine, W. Wei, R. E. Goldman, and N. Simaan, "Robot-assisted ophthalmic surgery", *Canadian Journal of Ophthalmology*, vol. 45, no. 6, pp. 581–584, 2010.

[170] J. D. Pitcher, J. T. Wilson, T.-C. Tsao, S. D. Schwartz, and J.-P. Hubschman, "Robotic eye surgery: Past, present, and future", *Journal of Computer Science & Systems Biology*, vol. 5, no. 2, p. 1, 2012.

[171] U. Spandau and G. Scharioth, *Cutting Edge of Ophthalmic Surgery: From Refractive SMILE to Robotic Vitrectomy*. Springer International Publishing, 2017.

[172] R. Channa, I. Iordachita, and J. T. Handa, "Robotic eye surgery", *Retina (Philadelphia, Pa.)*, vol. 37, no. 7, p. 1220, 2017.

[173] A. Bonfiglio, R. Repetto, J. H. Siggers, and A. Stocchino, "Investigation of the motion of a viscous fluid in the vitreous cavity induced by eye rotations and implications for drug delivery", *Physics in Medicine & Biology*, vol. 58, no. 6, p. 1969, 2013.

[174] A. Bonfiglio, A. Lagazzo, R. Repetto, and A. Stocchino, "An experimental model of vitreous motion induced by eye rotations", *Eye and Vision*, vol. 2, no. 1, p. 10, 2015.

[175] A. F. Silva, M. A. Alves, and M. S. N. Oliveira, "Rheological behaviour of vitreous humour", *Rheologica Acta*, vol. 56, no. 4, pp. 377–386, ISSN: 1435-1528. DOI: 10.1007/s00397-017-0997-0.

[176] I. Bekerman, P. Gottlieb, and M. Vaiman, "Variations in eyeball diameters of the healthy adults", *Journal of ophthalmology*, vol. 2014, 2014.

[177] F. Amblard, B. Yurke, A. Pargellis, and S. Leibler, "A magnetic manipulator for studying local rheology and micromechanical properties of biological systems", *Review of Scientific Instruments*, vol. 67, no. 3, pp. 818–827, 1996.

[178] N. Abolhassani, R. Patel, and M. Moallem, "Needle insertion into soft tissue: A survey", *Medical Engineering & Physics*, vol. 29, no. 4, pp. 413–431, May 1, 2007, ISSN: 1350-4533. DOI: 10.1016/j.medengphy.2006.07.003.

[179] M. McCaig, *Permanent Magnets in Theory and Practice*. Pentech Press, 1977, ISBN: 9780727316042.

[180] J. Woolman and R. Mottram, *The mechanical and physical properties of the British Standard En steels*, ser. EN 40 TO EN 363. Pergamon Press, 1964, vol. 2.

[181] Z. Zhang and C.-H. Menq, "Design and Modeling of a 3-D Magnetic Actuator for Magnetic Microbead Manipulation", *IEEE/ASME Transactions on Mechatronics*, vol. 16, no. 3, Jun. 1, 2011, ISSN: 1083-4435. DOI: 10.1109/TMECH.2011.2105500.

[182] C. Haber and D. Wirtz, "Magnetic tweezers for dna micromanipulation", *Review of Scientific instruments*, vol. 71, no. 12, pp. 4561–4570, 2000.

[183] J. Giltinan, E. Diller, and M. Sitti, "Programmable assembly of heterogeneous microparts by an untethered mobile capillary microgripper", *Lab on a Chip*, vol. 16, no. 22, pp. 4445–4457, 2016.

[184] M. A. Gijs, "Magnetic bead handling on-chip: New opportunities for analytical applications", *Microfluidics and nanofluidics*, vol. 1, no. 1, pp. 22–40, 2004.

[185] Y. Moser, T. Lehnert, and M. A. Gijs, "Quadrupolar magnetic actuation of superparamagnetic particles for enhanced microfluidic perfusion", *Applied physics letters*, vol. 94, no. 2, p. 022 505, 2009.

[186] W. Khalil, "Modeling and Control of Manipulators - Part I: Geometric and Kinematic Models", Doctoral, Lecture, Centre de recherche Inria Sophia Antipolis – Méditérranée, France, Jan. 2019, [Online]. Available: https://hal.inria.fr/cel-02129939.

Ruipeng CHEN

Développement d'une Méthodologie de Conception pour Plateformes Magnétiques Microrobotisées

Résumé :

La chirurgie minimalement invasive est aujourd'hui une thématique de recherche en plein essor. Le recours à des microrobots actionnés magnétiquement à distance et naviguant dans le système cardiovasculaire ouvre de nouvelles perspectives. L'objectif de cette thèse est de proposer un socle théorique concernant la conception, la modélisation et l'optimisation de plateformes microrobotiques à base de bobines électromagnétiques pouvant manipuler magnétiquement des microrobots thérapeutiques. Tout d'abord, nous présentons les fondements théoriques de l'électromagnétisme, y compris les principes de base et les équations nécessaires. À partir de cette base théorique, nous effectuons une analyse théorique sur le nombre minimum d'électro-aimants nécessaires, leur configuration géométrique ainsi que leur disposition dans l'espace de travail pour manipuler magnétiquement des microrobots. En particulier, nous étudions des cas singuliers tels que lorsque le champ magnétique et le gradient présentent des dépendances linéaires. A partir de ces formulations de base, nous avons étudié à travers la modélisation et les simulations numériques différents arrangements d'électro-aimants. Les multiples configurations spatiales (2D et 3D) de bobines sont étudiées avec des métriques de performances définies. A partir de cette méthodologie de conception, nous avons conçu une plateforme microrobotique magnétique, appelée ***OctoRob***, dédiée aux opérations chirurgicales ophtalmologiques. Une configuration expérimentale reconfigurable à 5 degrés de liberté est proposée pour permettre un contrôle magnétique plus efficace, flexible et ingénieux des outils chirurgicaux.

Mots-clés : Microrobot, modélisation magnétique, plateforme microrobotique, conception robotique.

Design Methodology for Electromagnetic Microrobotic Platforms

Abstract :

Micromanipulation platforms that magnetically guide microrobots are of great interest in minimally surgery systems (MIS). These systems vary in their number of electromagnets, their configuration and their limitations. However, no attempts have been made to rigorously quantify, optimize and design EMA platforms. In this thesis work, we propose a holistic theoretical methodology to design EMA systems with mobile and stationary electromagnets with respect to MIS specifications. First, we present the theoretical foundation of electromagnetism including the basic principles and necessary equations. From this basis, the electromagnetic manipulation of untethered microrobot including the magnetic torque and force control is discussed. Moreover, the analysis of the minimum number of electromagnets for a EMA platform is investigated. In particular, singular cases are pointed out when magnetic field and gradient exhibit some linear dependencies. From these basic formulations, we studied through modeling and computational simulations various arrangements of electromagnetic coils. The different multiple electromagnets configurations are investigated with the defined performance metrics. Finally, we proposed the ***OctoRob*** setup design that is a specific EMA system for ophthalmic MIS. Based on the proposed methodology, the number of electromagnets and their favorable configuration are optimized through computational results. A reconfigurable 5-DoF experimental setup is then proposed to allow the magnetic control more effective, flexible and resourceful.

Key words: Magnetic microrobot, magnetic modeling, magnetic-manipulation system, robotic design.